DISSERTATION

FUNDAMENTAL INVESTIGATIONS OF HYDROCARBON PLASMA CHEMISTRY: MECHANISTIC STUDIES OF GAS-PHASE PROCESSES AND PLASMA-SURFACE INTERACTIONS

Submitted by

Tara L. Van Surksum

Department of Chemistry

In partial fulfillment of the requirements

For the Degree of Doctor of Philosophy

Colorado State University

Fort Collins, Colorado

Fall 2020

Doctoral Committee:

Advisor: Ellen R. Fisher

Alan K. Van Orden
A.R. Ravishankara
Christopher R. Weinberger

Copyright by Tara L. Van Surksum 2020
All Rights Reserved

ABSTRACT

FUNDAMENTAL INVESTIGATIONS OF HYDROCARBON PLASMA CHEMISTRY: MECHANISTIC STUDIES OF GAS-PHASE PROCESSES AND PLASMA-SURFACE INTERACTIONS

Pollution arising from industrial and vehicular combustion continues to cause increasing environmental concerns. Non-thermal plasma (NTP) technology has attracted growing interest as a pollution abatement strategy because the highly reactive chemical environment can enhance decomposition and conversion of pollutants (e.g., volatile organic compounds, nitrogen oxides) at ambient conditions. When NTP is combined with a catalyst a synergistic effect is often observed, whereby the catalyst-plasma coupling enhances the overall process; however, the implementation of plasma-assisted catalysis (PAC) is currently inhibited by a lack of knowledge on the fundamental processes contributing to observed plasma-catalyst synergies. Understanding both the roles of the catalyst and the plasma as well as the interactions occurring at the plasma-catalyst interface in a PAC system can help the community efficiently utilize plasma-catalysis systems. As such, fundamental investigations focused on gas-phase processes and plasma-surface interactions are considered vital to the future of PAC development.

The research presented within this dissertation aims to elucidate molecular-level processes in environmentally relevant low temperature plasmas (e.g., CH_4, H_2, N_2) via a suite of spectroscopic techniques and complementary materials analyses in an effort to advance plasma technologies like PAC. Plasma diagnostic tools are employed to evaluate kinetic and energetic processes for multiple molecular species in low-temperature, inductively-coupled plasma

systems with precursors of increasing complexity, including CH_4-based mixed gas systems. A primary goal of this work has been the determination of molecular temperatures [i.e., rotational (T_R) and vibrational (T_V) temperatures] within PAC systems via optical emission spectroscopy (OES). This emphasis comes from the estimation that these values collectively represent a key component to understanding the reactions that drive the chemistry and the mechanisms involved in plasma-surface interactions. Formation and destruction rates of excited state plasma species derived from time-resolved OES (TR-OES) studies are another metric used to evaluate fundamental gas phase processes and provide additional insight into formation mechanisms and decomposition pathways.

Chapter 3 includes a discussion on T_R(CH) and T_V(CH) values in 100% CH_4 and CH_4/Ar plasma systems as functions of plasma parameters (e.g., pressure, power). Yet, one important consideration with internal plasma temperature determination is that different molecular species within the same plasma system may exhibit vastly different rotational and vibrational temperatures. Thus, examining several molecular species within a plasma system provides enhanced insight into the overall plasma chemistry. Additionally, a single plasma species may be produced via different mechanisms (e.g., direct impact excitation, decomposition, recombination) and may exhibit different T_R or T_V values as a function of plasma parameters. Chapter 4 expands on the studies presented in Chapter 3 by including an evaluation of T_R(H_2) values in a 100% CH_4 plasma. Generally, T_R(CH) values (~1700 – 2100 K) are much higher than T_R(H_2) values (~500 – 700 K) in a 100% CH_4 plasma. These disparate values likely result from a combination of the differences in the species densities, radiative lifetimes, and consequently their excitation pathways. T_R(H_2) values and trends are also compared to a 100% H_2 plasma where excitation mechanisms for H_2 are expected to differ from a CH_4 plasma.

The addition of a catalyst to plasma can significantly alter the gas phase chemistry of the plasma. The impact of a TiO_2 catalyst on plasma energetics and kinetics is explored in H_2 (Chapter 5), CH_4 (Chapter 5), and N_2 (Chapter 6) discharges. The introduction of TiO_2 into the discharge has minimal effect on $T_R(H_2)$ in a 100% H_2 plasma but reduces $T_R(H_2)$ values by up to 300 K in a 100% CH_4 plasma. Time-resolved OES studies echo energy partitioning results and reveal further details about the kinetics of H_2 formation and the impact of the catalyst on gas-phase processes. Comprehensive materials analysis of the catalyst before and after plasma exposure reveals that the H_2 plasma acts as primarily an etching system whereas competing etching and deposition processes may be occurring under some conditions in CH_4 plasma system. The presence of the catalyst in the N_2 discharge resulted in a pronounced decrease of N_2 vibrational temperatures while no clear or significant impact on the rotational temperature was reported.

Gas-phase studies of increasingly complex environmentally relevant systems (i.e., mixed gas CH_4/H_2O and CH_4/N_2 plasmas) and additional molecules (i.e., CN, CO, OH) are also investigated and presented in Chapter 7 of this dissertation. Determination of rotational and vibrational temperatures for several molecular species in each plasma system demonstrate that the excited state species in our systems are not equilibrated with each other and that different species have achieved different degrees of equilibration between rotational and vibrational modes. When combined with energy partitioning results, TR-OES data provide further insight into molecule formation pathways.

The results presented within this dissertation help to establish the relationship between system parameters and the kinetic and energetic outcomes. Such information is crucial for developing systems that can potentially be implemented at the industrial level. Combined with

gas-phase analysis, complementary materials characterization of the catalyst provides a holistic approach towards understanding plasma-surface interactions and unraveling the fundamental chemical processes that occur during plasma processing. Overall, the results presented within this dissertation emphasize the intimate connections between the catalyst, plasma parameters (e.g., precursor, pressure, power), and fundamental plasma properties, all crucial components to understanding and optimizing plasma conditions for PAC.

TABLE OF CONTENTS

ABSTRACT ii

LIST OF TABLES ix

LIST OF FIGURES x

CHAPTER 1. Introduction 1
1.1. Plasma Chemistry 1
1.2. Plasma-Enhanced Chemical Vapor Deposition 4
1.3. Motivation for Research 7
1.3.1. Bridging Plasma Diagnostics and Film Properties in Plasma-Enhanced Chemical Vapor Deposition Systems 7
1.3.2. Addressing the Need for Fundamental Investigations of Plasma-Assisted Catalysis Processes 10
1.4. Research Overview 12
REFERENCES 16

CHAPTER 2. Experimental Methods 21
2.1. Plasma Systems 21
2.2. Materials Preparation 23
2.3. Materials Characterization 24
2.3.1. X-ray Photoelectron Spectroscopy 24
2.3.2. Fourier Transform Infrared Spectroscopy 24
2.3.3. Optical Profilometry 25
2.3.4. Water Contact Angle Goniometry 25
2.3.5. Scanning Electron Microscopy-Energy Dispersive Spectroscopy 25
2.3.6. Raman Spectroscopy 25
2.4. Optical Spectroscopies 26
2.5. Characteristic Plasma Temperature Determination 27
2.5.1. Electron Temperature 27
2.5.2. Determination of Rotational and Vibrational Temperatures 30
REFERENCES 35

CHAPTER 3. Determination of Rotational and Vibrational Temperatures of CH in CH_4 Plasmas 36
3.1. Introduction 36
3.2. Results 39
3.3. Discussion 53
3.4. Summary 59
REFERENCES 60
CHAPTER 4. Gas-Phase Diagnostic Studies of H_2 and CH_4 Inductively Coupled Plasmas 64

4.1. Introduction 64
4.2. Results and Discussion 68
4.3. Summary 90
REFERENCES 92

CHAPTER 5. Employing Optical Emission Spectroscopy to Elucidate the Impact of TiO_2 in Plasma Assisted Catalysis Systems 97
5.1. Introduction 97
5.2. Results 100
5.3. Discussion 127
5.4. Summary 139
REFERENCES 141

CHAPTER 6. Investigating the Impact of TiO_2 on N_2 Rotational and Vibrational Temperatures in Low Pressure Plasmas 147
6.1. Introduction 147
6.2. Results and Discussion 150
6.3. Summary 170
REFERENCES 173

CHAPTER 7. Elucidating Energetic and Kinetic Trends in Environmentally Relevant Mixed Gas Plasma Systems 176
7.1. Introduction 176
7.2. Results 179
7.2.1. CH_4/N_2 Plasma System 179
7.2.2. CH_4/H_2O Plasma System 197
7.3. Discussion 208
7.3.1. CH_4/N_2 Plasma System 208
7.3.2. CH_4/H_2O Plasma System 217
7.4. Summary 221
REFERENCES 223

CHAPTER 8. Research Summary and Perspectives 226
8.1. Research Summary 226
8.2. Future Directions 229
REFERENCES 237

APPENDIX A. The Impact of SnO_2 and ZnO Catalysts on Molecular Plasma Temperatures Within CH_4 Discharges: Preliminary Results 240
A.1. Background 240
A.2. Characteristic Plasma Temperatures 242
REFERENCES 255

APPENDIX B. Independent Research Proposal 256
B.1. Abstract 256
B.2. Background and Motivation 257

B.3. Specific Aims 261
B.4. Proposed Work...262
B.5. Summary 274
REFERENCES 275

LIST OF ABBREVIATIONS..278

LIST OF TABLES

2.1. Transitions and corresponding wavelengths used for actinometry analyses 28
2.2. Temperature determination methods for plasma species of interest....................................31
2.3. Boltzmann plot parameters for $T_R(H_2)$ determination..34

3.1. T_R(CH) and T_V(CH) values in a 100% CH_4 plasma...43
3.2. T_R(CH) and T_V(CH) values in a 3:1 CH_4/Ar plasma...49

4.1. $T_R(H_2)$ values for H_2 and CH_4 plasma systems...76
4.2. $T_R(H_2$, CH) and T_V(CH) values for CH_4/H_2 plasmas 80

5.1. Internal temperatures and trends from 100% H_2 and 100% CH_4 plasmas (sans catalyst)...101
5.2. T_R(OH) and T_V(OH) values in a 100% H_2 plasma with TiO_2 107
5.3. XPS atomic composition data for a TiO_2 substrate exposed to a 100% H_2 plasma............110
5.4. XPS atomic composition data for a TiO_2 substrate exposed to a 100% CH_4 plasma.........114
5.5. $T_R(H_2)$ values in a 100% H_2 plasma and 100% CH_4 plasma with TiO_2.............................124
5.6. T_R(CH) and T_V(CH) values in a 100% CH_4 plasma with TiO_2 126

6.1. $T_R(N_2)$ and $T_V(N_2)$ values in a 100% N_2 plasma with TiO_2 154
6.2. N_2 k_f and k_d values in a 100% N_2 plasma without and with TiO_2......................................163
6.3. XPS atomic composition data for untreated and N_2 plasma treated TiO_2 168

7.1. k_f and k_d values for N_2 and CN in CH_4/N_2 plasmas...186
7.2. T_R and T_V values for species in CH_4/N_2 plasmas 189
7.3. CO k_f and OH k_d values in CH_4/H_2O plasmas 202
7.4. T_R and T_V values for species in CH_4/H_2O plasmas..205

A.1. T_e values in a CH_4 plasma without and with substrates 244
A.2. $T_R(H_2)$ values in a CH_4 plasma without and with substrates...247
A.3. T_R(CH) values in a CH_4 plasma without and with substrates 250
A.4. T_V(CH) values in a CH_4 plasma without and with substrates 252

B.1. Selection of polymers, fillers, and fabrication and modifications approaches for MMMs 271

LIST OF FIGURES

1.1. Illustrative representation of the three distinct regions of the plasma-surface composite 5

2.1. Schematics of glass barrel ICP reactors 22
2.2. Raw TR-OES data and time-adjusted data for analysis 29
2.3. CH $A^2\Delta \rightarrow X^2\Pi$ emission spectrum in a CH_4 plasma with TiO_2 and simulated fit using LIFBASE....32

3.1. Raw OES spectrum of 100% CH_4 plasma and CH $A^2\Delta \rightarrow X^2\Pi$ band with simulated fit 40
3.2. Raw and simulated CH emission spectra with additional simulations to demonstrate change in $T_R \pm 50$ K and $T_V \pm 100$ K....41
3.3. T_R(CH) and T_V(CH) as a function of pressure in a 100% CH_4 plasma 42
3.4. T_R(CH) and T_V(CH) as a function of power in a 100% CH_4 plasma 45
3.5. Raw emission spectra of CH for CH_4 plasma with varying amount of Ar added 46
3.6. T_R(CH) and T_V(CH) as a function of power in a 3:1 CH_4/Ar plasma 48
3.7. High resolution C_{1s} XPS spectrum and FTIR spectrum for HC film deposited by a 100% CH_4 plasma 50
3.8. Optical profilometry and static WCA data for HC films deposited in a 100% CH_4 plasma 52

4.1. Emission spectra for H_2 $d^3\Pi_u \rightarrow a^3\Sigma_g^+$ in a 100% H_2 plasma with corresponding Boltzmann plot and CH $A^2\Delta \rightarrow X^2\Pi$ in a CH_4/H_2 plasma with simulated fit using LIFBASE 69
4.2. $T_R(H_2)$ in a 100% H_2 plasma and in a 100% CH_4 plasma as a function of power 72
4.3. $T_R(H_2)$ as a function of %H_2 in CH_4/H_2 plasmas 77
4.4. Relative densities of H_2 and H in H_2 and CH_4 plasmas 85
4.5. Relationship between T_R(CH) and $T_R(H_2)$ in 100% CH_4 plasmas 87
4.6. $T_R(H_2)$ as a function of %Ar in a H_2/Ar plasma system....89

5.1. Raw OES spectrum of a 100% H_2 plasma without and with TiO_2 102
5.2. Relative densities of OH, H_2, and H_α species in a 100% H_2 plasma without and with TiO_2....104
5.3. Raw and simulated OH $A^2\Sigma^+ \rightarrow X^2\Pi$ spectra in a 100% H_2 plasma with TiO_2....106
5.4. FTIR spectra of untreated and H_2 plasma treated TiO_2 109
5.5. High resolution O_{1s}, Ti_{2p}, and C_{1s} data for untreated and H_2 plasma treated TiO_2....111
5.6. High resolution O_{1s}, Ti_{2p}, and C_{1s} data for untreated and CH_4 plasma treated TiO_2 115
5.7. Raman spectra of TiO_2 substrates treated with a 100% CH_4 plasma....117
5.8. SEM images of untreated, H_2 plasma treated, and CH_4 plasma treated TiO_2....119
5.9. Temporal profiles of H_2 emission in a 100% H_2 plasma and 100% CH_4 plasma without and with TiO_2....121
5.10. $T_R(H_2)$ in a 100% H_2 and 100% CH_4 plasma without and with TiO_2 as a function of

power 122
5.11. T_R(CH) and T_V(CH) in a 100% CH_4 plasma without and with TiO_2 as a function of power 125

6.1. N_2 $C^3\Pi_u \rightarrow B^3\Pi_g$ emission spectrum in a 100% N_2 plasma with TiO_2 with corresponding Boltzmann plot and simulated fit using SpecAir 152
6.2. $T_R(N_2)$ and $T_V(N_2)$ from a 100% N_2 plasma with and without TiO_2 153
6.3. Representative emission spectrum and actinometry data for a N_2 plasma with TiO_2 158
6.4. $\Delta T_V(N_2)$ as for TiO_2 and zeolite catalysts in a 100% N_2 plasma..160
6.5. Temporal profiles of N_2 emission in an 100% N_2 plasma without and with TiO_2 162
6.6. SEM images of untreated and N_2 plasma treated TiO_2..165
6.7. High resolution O_{1s}, Ti_{2p}, and C_{1s} data for untreated and N_2 plasma treated TiO_2 167
6.8. Schematic representation of surface modification processes occurring during N_2 plasma processing 171

7.1. Raw OES spectra of 8:1 CH_4/N_2 and 1:8 CH_4/N_2 plasmas..180
7.2. Relative densities of excited state species as a function of %N_2 in CH_4/N_2 plasmas 182
7.3. Temporal profiles of CN emission in CH_4/N_2 plasmas 184
7.4. CN k_f and CN k_d as a function of %N_2 in CH_4/N_2 plasmas...185
7.5. Temporal profiles of N_2 emission in CH_4/N_2 plasmas...188
7.6. Emission spectra and simulated fits of N_2 $C^3\Pi_u \rightarrow B^3\Pi_g$ and CN $B^2\Sigma^+ \rightarrow X^2\Sigma^+$...........191
7.7. $T_R(N_2)$ and $T_V(N_2)$ as a function of %N_2 in CH_4/N_2 plasmas...193
7.8. T_R(CN) and T_V(CN) as a function of %N_2 in CH_4/N_2 plasmas 195
7.9. T_R and T_V for multiple species in an 8:1 CH_4/N_2 plasma 196
7.10. Raw OES spectra of 8:1 CH_4/H_2O and 1:8 CH_4/H_2O plasmas..198
7.11. Relative densities of excited state species as a function of %H_2O in CH_4/H_2O plasmas..199
7.12. Temporal profile of CO emission and CO k_f as a function of %H_2O in CH_4/H_2O plasmas..201
7.13. Temporal profile of OH emission and OH k_d as a function of %H_2O in CH_4/H_2O plasmas..203
7.14. Emission spectrum and simulated fit of OH $A^2\Sigma^+ \rightarrow X^2\Pi$ and T_R(OH), T_V(OH) as a function of %H_2O in CH_4/H_2O plasmas 204

8.1. BAS spectrum for CH $X^2\Pi \rightarrow A^2\Delta$ in a 100% CH_4 plasma...230
8.2. $T_V(N_2)$ in an 8:1 CH_4/N_2 plasma without and with TiO_2 233

A.1. SEM images of SnO_2 nanoparticles, ZnO nanoparticles, and ZnO microrods 243
A.2. $T_R(H_2)$ in a CH_4 plasma without and with substrates 246
A.3. T_R(CH) in a CH_4 plasma without and with substrates..249
A.4. T_V(CH) in a CH_4 plasma without and with substrates..253

B.1. Diagram illustrating challenges in MMM fabrication..259
B.2. Strategies to overcome MMM fabrication challenges 273

CHAPTER 1

INTRODUCTION

This chapter provides information on the premise and motivation behind the work detailed within this dissertation. A brief introduction to plasma chemistry and plasma deposition processes in hydrocarbon plasma systems are first presented to outline the inherent convoluted nature of the plasma systems used in this research. Plasmas are useful for a host of potential applications (e.g., materials fabrication and processing, waste gas remediation) and thus, are of significant interest to the scientific community as well as to manufacturing and industry; however, the lack of understanding of the fundamental processes occurring in plasma systems severely hinders their utility in many applications. To fully utilize the advantages of plasmas, information on energy partitioning, kinetics, plasma-surface interactions, and other mechanistic phenomena occurring in these systems must be developed and integrated into real-world applications and device design. A discussion on approaches for analyzing the inherently complex nature of these environments is included within this chapter, along with an overview of the research presented within the remainder of the dissertation.

1.1 Plasma Chemistry

The term "plasma" describes a partially-ionized gas comprising ions, electrons, radicals, and neutral atoms or molecules in ground and excited states.[1] Plasmas occur naturally (e.g., lightening, auroras) but can also be created under laboratory conditions where they are useful for a variety of commercial applications including pollution remediation, medical sterilization, and semiconductor processing, among a myriad of other surface modification applications. The

research in this dissertation aims to unravel underlying chemical processes occurring in these multi-faceted systems to further advance several technologies. Specifically, the work described within this dissertation investigates radio frequency (rf) inductively coupled non-thermal plasma (NTP) systems, wherein local thermodynamic equilibrium is not achieved. In NTP discharges, the electron temperature (T_e) exceeds the ion temperature (T_i) by up to two orders of magnitude.[1] This energy distribution is favorable in many plasma technology applications because the relatively "cold" ions and neutral species can be controlled via a range of plasma parameters to promote specific types of chemical reactions.

In general, the ignition of a plasma discharge occurs when an electric field is applied to a volume of gas causing acceleration of free electrons and sequential collisions with other gas species. In this way, a cascade of electron-mediated interactions sustains the plasma discharge. Inelastic collisions between electrons and gas species, wherein nearly all of the electron's energy is transferred to its collision partner,[1] allow a variety of reactions to take place within these discharges:

$$AB + e^- \rightarrow AB^+ + 2e^- \quad (1.1)$$

$$AB + e^- \rightarrow AB^* + e^- \quad (1.2)$$

$$AB + e^- \rightarrow A + B + e^- \quad (1.3)$$

These reactions describe electron impact ionization, excitation, and dissociation, respectively. Reaction 1.3 can also result in an electronically excited radical A or B. This dissociative excitation process is generically illustrated in reaction 1.4.

$$AB + e^- \rightarrow A^* + B + e^- \quad (1.4)$$

Plasma discharges involve many different reactions, such as the ones shown above. Even with a relatively simple precursor gas, the inherent complexity of the chemistry occurring within

these systems is apparent. In many applications, these systems are even more complicated by the use of several precursors or gas mixtures containing larger molecules. Moreover, aside from gas feed composition, additional plasma parameters (e.g., pressure, applied power, substrate identity and position) can considerably influence the chemistry occurring within the discharge.

Through plasma diagnostic techniques, characteristic plasma temperatures may be measured from the plasma to construe information on the chemical processes occurring within the discharge and aid in unraveling the mechanistic phenomena in the system. Beyond the aforementioned T_e and T_i, there are a number of characteristic energies that can be monitored within plasmas.[1] Specifically, vibrational (T_V) and rotational (T_R) temperatures of several plasma species will be discussed throughout this dissertation. Some of these temperatures are influenced by plasma parameters, including the presence and type of substrate placed within the discharge, demonstrating the significant impact of the material on plasma chemistry.

Notably, the addition of a substrate to a plasma introduces additional variables to the plasma systems as both the chemical and morphological nature of the substrate can significantly influence plasma chemistry. Indeed, the bulk of plasma applications involve etching, deposition, or functionalization of a material as routes toward surface modification, whereas other plasma applications (e.g., atmospheric remediation applications) utilize gas-surface interactions to ultimately influence the gas-phase chemistry. Although plasmas are widely employed for such applications, the gas-phase chemistry and plasma-surface interactions that lead to the desired surface modification or waste-gas conversion outcomes are often poorly understood. To more efficiently utilize plasmas for materials processing and gas-feed conversion or decomposition, an understanding of the molecular-level processes occurring in these systems is imperative.

Our efforts to unravel the chemistry of these systems focus on understanding the intricate interplay between each of the three distinct regions of the plasma-surface composite [(1) gas-phase, (2) substrate, (3) plasma-substrate interface], Figure 1.1. Each of these regions are theoretically tunable, although it requires a significant amount of fundamental knowledge of the molecular-level processes occurring throughout a wide parameter space and understanding the role that each specific parameter has on the chemistry of the system. Both the material and plasma impact the chemistry in these systems. Thus, we aim to specifically understand both the impact that the material has on the gas-phase plasma chemistry and the plasma's impact on the chemistry of material post plasma exposure. Throughout this dissertation, optical diagnostic techniques are employed as a means to elucidate key chemical processes occurring in the plasma discharge. These tools are used to identify key species and determine species kinetics and energy partitioning trends, which is of high interest to the plasma community.[2-3] In addition, thorough characterization of the substrate prior to and post plasma exposure allows us to investigate the impact that the plasma has on the substrate morphology and chemistry. Our holistic approach to plasma diagnostics and materials characterization provides insight to the chemistry occurring in the bulk plasma, at the plasma-surface interface, and within the material of interest. As such, this dissertation seeks to contribute to the plasma community by providing a foundational basis of key chemical processes occurring in low temperature plasmas.

1.2 Plasma-Enhanced Chemical Vapor Deposition

As mentioned above, the use of NTP for plasma processing of materials is of significant interest among the scientific and industrial communities because the non-thermal nature of the plasma allows for a reactive, low temperature (gas temperature < 1000 K) environment to

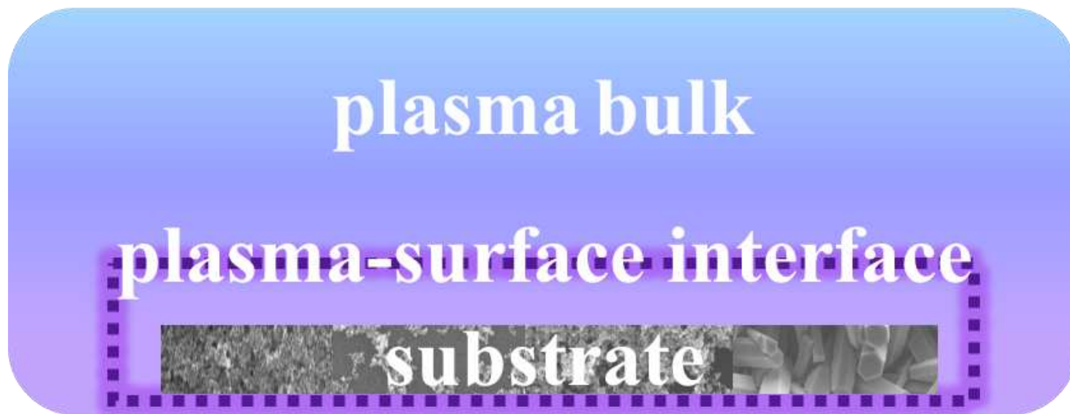

Figure 1.1. An illustrative representation of the three distinct regions of the plasma-surface composite: the plasma bulk, plasma-surface interface, and substrate.

modify materials.[1] Moreover, NTP environments typically offer a wide, tunable parameter space (e.g., precursors, pressure, power) to tailor materials properties for desired applications. As such, NTP are useful for plasma processing because they can modify surfaces via (1) etching of the material, (2) implanting functional groups with a desired chemistry, or (3) deposition of a film via plasma-enhanced chemical vapor deposition (PECVD).[1] In some cases, these modification schemes occur simultaneously and are often in competition with each other. Controlling plasma parameters offers a mechanism for potentially enhancing one process over another. PECVD is discussed here because it often dominates carbon-containing systems, such as those employed here (e.g. CH_4).

PECVD offers several advantages over other methods for thin film deposition, such as thermal CVD, which requires high (≥ 500 °C) operating temperatures and is often limited by mass transport velocity, leading to poor film quality.[4-5] Because of the non-thermal nature of low-temperature plasmas, film growth via PECVD can be performed at much lower temperatures (~100 – 500 °C), thereby, reducing the probability of substrate damage. In addition, PECVD allows conformal film deposition over larger areas making this technique suitable for a variety of substrates. For example, the Fisher group has previously shown that plasma co-polymerization can be achieved via PECVD on relatively delicate three-dimensional scaffold materials for biologically-relevant systems by producing films that conformally coat the porous structure without compromising the architecture of the material.[6] PECVD has been used to deposit a variety of materials,[7-11] but it finds the most utility in the deposition of amorphous materials, such as amorphous carbon and silicon materials. As noted above, we observe amorphous carbon film deposition in the systems studied here and although this process can be viewed as competing with the overall target of converting CH_4 through a gas-phase catalytic transformation

in plasma-assisted catalysis systems, it can also be viewed as a potential sink for the CH_4. One potential downside to the formation of carbon layers on our catalysts is that this coating could reduce or ultimately eliminate the catalytic activity of the catalytic materials being employed. Concomitant etching within the plasma systems could slow film deposition and thereby mitigate this "poisoning" of the catalyst. These ideas are further explored below and in subsequent chapters.

1.3 Motivation for Research

1.3.1. Bridging Plasma Diagnostics and Film Properties in Plasma-Enhanced Chemical Vapor Deposition Systems. Production of diamond-like carbon (DLC) films, amorphous carbon consisting of varying ratios of sp^2 and sp^3 hybridized carbon and hydrogen, is often accomplished via PECVD.[12-13] High hardness, low friction, and chemical inertness are among a few of the properties of DLC films that make them useful for applications in protective coatings, optics, and electronics.[14-16] Several hydrocarbon precursors have been used in PECVD systems for deposition of DLC films, but C_2H_2 and CH_4 are the most commonly used precursors because of their relatively simple dissociation patterns and low bias voltages required for quality DLC fabrication.[12] It is well known that DLC properties are strongly affected by the relative sp^2 and sp^3 hybridization ratios; thus, other gases, such as H_2 and Ar, are typically added to the hydrocarbon gas feed to create active sites and tune the sp^2/sp^3 ratio to tailor material properties.[12, 17]

The bulk of the research presented within this dissertation reports on CH_4 plasma chemistry; consequently, as noted above, amorphous hydrocarbon films, a type of DLC film, are deposited in nearly all of the studies described within this document. Characteristics of DLC

films deposited via PECVD have been thoroughly analyzed with respect to various plasma parameters by several researchers.[14-16, 18-19] However, the relationship between such plasma parameters and resulting film characteristics is poorly understood, making it tedious and time-consuming to reproduce similar coating technologies in different reactor set-ups.[5, 13] One approach to overcome this hurdle is to utilize plasma diagnostic techniques to elucidate the molecular-level processes occurring in the plasma bulk and correlate these plasma characteristics with resulting DLC film properties.

Several plasma diagnostic techniques have been used to study carbon-containing plasmas such as Langmuir probes,[20-22] optical absorption and emission spectroscopies,[13, 23-24] and mass spectrometry.[25-26] Each of these plasma diagnostic techniques has distinct advantages and disadvantages; thus, it is ideal to use an approach involving several of these methods to comprehensively characterize the gas-phase chemistry. For example, Langmuir probes are a common method for determining the electron energy distribution within the plasma, but it is an intrusive characterization technique that perturbs the plasma environment.[1] Optical emission spectroscopy (OES), on the other hand, is a non-intrusive diagnostic technique that can provide information on key gas-phase species, species densities, and energy partitioning trends. Such information provided by OES is essential in illuminating gas-phase mechanisms that may be crucial to the formation of key species involved in hydrocarbon film deposition. This technique is, however, limited to excited state, light-emitting species, and the emission intensity is not always directly related to species concentration.[1]

To further illustrate the importance of using plasma diagnostics, Anooshehpour *et al.* employed a partial least squares regression modelling approach to find the correlation between both deposition process parameters (i.e., bias voltage, plasma duty cycle, plasma pressure,

applied power) and OES data (i.e., FWHM of H_α line, actinometry) with DLC structural and mechanical properties.[13] Although bias voltage was an essential component to keep in any model for controlling film deposition, the authors found that all other plasma parameters studied could be replaced by OES data to predict DLC properties. This finding provides basis for using plasma diagnostic techniques to understand and control plasma processes and ultimately, overcome the hurdle of establishing the relationship between reactor-dependent plasma parameters and materials properties.

In addition to probing the gas-phase chemistry in PECVD systems, information about gas-surface interactions provides valuable insight into DLC film formation and characteristics. The Fisher research group has previously investigated the gas-surface interface in CH_4-containing plasma systems using imaging of radicals interacting with surfaces (IRIS), a laser-induced fluorescence-based technique. Zhou *et al*. reported the surface reactivity of CH radicals to be near unity with no dependence on several plasma parameters, suggesting that CH radicals have a significant impact on the properties of amorphous hydrocarbon films despite their relatively low gas phase density.[27] Such information on gas-surface interactions is currently limited but is crucial to advancing plasma technologies for PECVD applications. Furthermore, when diagnostic techniques such as OES and IRIS are used in conjunction with material characterization techniques to analyze a film's chemistry and morphology, molecular-level information essential to deciphering the relationship between such plasma parameters and resulting film characteristics can be construed. Gaining an understanding of the chemistry occurring in PECVD plasma systems, specifically those used for DLC film deposition, can allow us to provide more control over the deposition of carbon materials by creating a tunable space to tailor a material's properties for desired applications.

1.3.2. Addressing the Need for Fundamental Investigations of Plasma-Assisted Catalysis Processes. Plasma-assisted catalysis (PAC), or the coupling of a plasma with a catalyst, is a widely applicable tool that has been used for treatment of waste gas,[28-29] ammonia synthesis,[30] hydrogen production,[31-32] hydrocarbon reforming,[33-36] and fabrication of carbon nanostructures.[37-38] For example, in PECVD systems used for fabrication of carbon nanostructures, a hydrocarbon plasma is typically brought into contact with a catalyst (usually Ni, Fe, or Co).[39] The non-thermal nature of the plasma employed in PAC systems allows for access to processes that are energetically unavailable under thermal conditions and thus, has an enormous potential to increase gas feed conversion.[40-42] PAC also improves upon energy efficiency and reduces unwanted byproduct formation in waste gas conversion and decomposition of nitrogen oxides and volatile organic compounds (VOCs) compared to use of either NTP or catalysis alone.[3, 43] Regardless of the application, the future of this emerging technology resides on a more comprehensive understanding of the inherently complex plasma-catalyst system.

Optimization of PAC setups (e.g., reactor design, plasma process parameters, catalyst choice) currently remains a challenge within the community and is typically approached by trial and error processes. To date, many experimental studies have focused on parametric optimization for increasing process performance[44-47] and how plasma exposure affects the material.[48-49] Few studies have, however, focused on elucidating the influence of the catalyst on the fundamental physical characteristics of the plasma discharge, and thus, the underlying mechanistic phenomena of PAC processes are still largely unknown, reducing its overall applicability. To improve PAC applications, it is crucial to understand the underlying physiochemical mechanisms to be able to optimize processing conditions.

The combination of the plasma and catalyst can affect processes occurring in the gas phase and on the catalyst surface. For example, the plasma can modify the morphology and chemical composition of the catalyst.[37, 50] Additionally, the catalyst's properties (e.g., roughness, dielectric constant) can alter the electrical properties of the plasma and ultimately affect the physiochemical properties of the plasma [e.g., electron energy distribution (EEDF)].[37, 50] For example, Tu *et al.* demonstrated a change in discharge behavior (i.e., less filaments and more surface discharges) and an ultimate increase in the high energy tail of the EEDF upon packing their reactor bed with TiO_2 pellets.[51] Similarly, zeolites[52] and other ferroelectric materials[53] have been known to enhance the electric field. While an enhancement of the electric field is a physical effect, this can directly influence the chemistry of the plasma by altering the EEDF. Consequently, the electron impact dissociation and ionization rates are impacted, which ultimately determine the chemical composition of the plasma.

Overall, the mutual dependence of the plasma and catalyst properties results in an intricate system wherein the plasma and the catalyst can interact synergistically.[3, 40, 54] In PAC systems, feed gas conversion is often enhanced as the plasma modifies/activates both the precursor gas and the material surface, such that the plasma-catalyst combination yields improved results over either component acting alone. The origin of this synergistic environment, however, is not yet well understood.[3, 40, 50] Thus, both the chemistry in the plasma and at the surface of the catalyst are affected by the intricate interplay between the two. Given the resulting enhancement of the complexity inherent to plasma-surface interactions, fundamental investigations of gas-phase plasma species and plasma-surface interactions are required to increase the effectiveness of PAC. Knowledge of the roles of gas-phase radicals and radical-surface interactions is key to understanding overall plasma chemistry. To further illuminate the

effect of the catalyst on the plasma environment, it is vital to investigate the gas-phase chemistry of the plasma both with and without a catalyst. Specifically, an understanding of how energy is partitioned into vibrational, rotational, and translational modes provides insight into formation mechanisms, decomposition pathways, and overall plasma chemistry. Figures of merit such as T_R and T_V describe the energetics of species within the plasma system. Moreover, information gleaned from these internal temperatures and trends can expound the overall character of the plasma.

Our holistic approach towards comprehensive analyses of plasma systems aims to address the paucity of fundamental plasma information currently limiting PAC technologies. We examine the impact of the plasma on the catalyst by exploiting chemical and morphological characterization techniques to assess the material prior to and post plasma exposure. Additionally, we investigate the impact that the catalyst has on the chemistry of the plasma via optical spectroscopy techniques, which allow us to non-intrusively probe the bulk plasma region and ultimately elucidate the kinetic and energetic characteristics of the system. Understanding both the roles of the catalyst and the plasma as well as the interactions occurring at the plasma-catalyst interface in a PAC system can help the community bypass trial-and-error approaches to optimizing plasma-catalysis systems. As such, investigations focused on gas-phase processes and plasma-surface interactions are considered vital to the future of PAC development.

1.4 Research Overview

The work described within this dissertation aims to elucidate molecular-level processes in low temperature plasmas via a suite of spectroscopic techniques and complementary materials analyses in an effort to advance plasma technologies. A comprehensive investigation into each

region of a plasma-substrate system [(1) gas-phase, (2) substrate, (3) plasma-substrate interface] is critical to understanding the underlying phenomena contributing to plasma processes. A primary goal of this work has been the determination of molecular temperatures within plasma systems. This emphasis comes from the estimation that these values collectively represent a key component to understanding the reactions that drive the chemistry and the mechanisms involved in plasma-surface interactions. Moreover, these data help to establish the relationship between system parameters and energetic outcomes. Such information is crucial for developing systems that can potentially be implemented at the industrial level. Combined with gas-phase analysis, complementary materials characterization provides a holistic approach towards understanding plasma-surface interactions and unraveling the fundamental chemical processes that occur during plasma processing. Chapter 2 details the techniques utilized in this experimental approach.

Chapter 3 serves as the foundation of the work reported in this dissertation as all subsequent chapters build upon the results reported in this chapter. Chapter 3 reports on energy partitioning trends of CH $A^2\Delta \rightarrow X^2\Pi$ in 100% CH_4 and CH_4/Ar plasma systems. Here, T_R(CH) and T_V(CH) are presented with respect to plasma pressure and applied rf power parameters. In addition, chemical and morphological properties of amorphous hydrocarbon films deposited on glass slides and silicon wafers by these plasma systems are analyzed. Gas-phase analysis and material properties are linked and discussed.

The dissociation of CH_4, which has applications in several plasma technologies including the fabrication of carbon materials[55-60] and PAC systems,[61-62] has been studied extensively.[59, 61-64] Notably, a hydrogen-rich plasma environment is created during CH_4 dissociation;[65-66] thus, it is essential to consider the roles of hydrogen species when elucidating mechanistic processes occurring in CH_4 plasmas. We have measured $T_R(H_2)$ in addition to determining energy

partitioning trends for CH. These results are described in Chapter 4 where we employed OES to investigate energy partitioning in H_2 and CH_4 inductively coupled plasma systems. In 100% H_2 plasmas, $T_R(H_2)$ values are ~500 – 550 K, whereas generally higher $T_R(H_2)$ values (~500 – 700 K) are reported for 100% CH_4 plasmas. These results highlight the differences in the H_2 excitation pathways occurring in each of these two plasma systems. As such, mixed gas CH_4/H_2 plasma systems were also explored to gain further insight into these mechanistic details.

Results discussed in Chapter 5 expand upon gas-phase studies in H_2 and CH_4 plasmas by introducing a TiO_2 catalyst into the discharge. More specifically, Chapter 5 details both a gas-phase analysis of the plasma discharge and a comprehensive material analysis of the catalyst before and after plasma exposure to elucidate the contributions of both the plasma and the catalyst in a model PAC system. Energetics and kinetics of multiple excited state species are evaluated and discussed. Furthermore, materials analysis also demonstrates the impact that the plasma has on the catalyst's properties. For example, XPS data show the presence of an amorphous hydrocarbon film after exposure to the CH_4 plasma system. Additionally, Raman data reveal the presence of oxygen vacancies in the material after plasma exposure.

Additional PAC studies are presented in Chapter 6 where the impact of TiO_2 on fundamental gas phase properties is examined in a 100% N_2 plasma. The addition of the catalyst to the discharge introduces additional excited state species (e.g., NO, OH) and significantly reduces $T_V(N_2)$. XPS analysis reveals incorporation of nitrogen into the TiO_2 catalyst. Moreover, an increase in adsorbed surface oxygen and reduction of Ti are also noted post plasma exposure. Together, these results suggest the possibility of several surface modification processes that may be occurring during N_2 plasma processing.

Chapter 7 examines plasma systems of increasing complexity. Specifically, gas-phase data for mixed gas CH_4/N_2 and CH_4/H_2O plasmas provide insight on how plasma parameters affect gas-phase chemistry in these plasma systems of interest to real-world catalysis applications. OES spectra indicate the presence of key species in these systems, including the formation of CN and CO in the CH_4/N_2 and CH_4/H_2O systems, respectively. Relative densities, kinetics, and energy partitioning trends of several excited state species (e.g., CH, CN, H_2, OH, and N_2) are assessed within these mixed gas systems to illuminate mechanistic details of gas phase processes in these systems.

A summary of the entire dissertation work is presented in Chapter 8. Future avenues of investigation for this project are also briefly discussed. Overall, the results presented within this dissertation emphasize the intimate connections between the catalyst, plasma parameters (e.g., precursor, pressure, power), and fundamental plasma properties, all crucial components to understanding and optimizing plasma conditions for plasma technologies.

REFERENCES

1. Grill, A., *Cold Plasma in Materials Fabrication*. IEEE Press: New York, 1994; Vol. 151.
2. Adamovich, I.; Baalrud, S. D.; Bogaerts, A.; Bruggeman, P.; Cappelli, M.; Colombo, V.; Czarnetzki, U.; Ebert, U.; Eden, J.; Favia, P., The 2017 Plasma Roadmap: Low Temperature Plasma Science and Technology. *J. Phys. D: Appl. Phys.* **2017,** *50* (32), 323001.
3. Whitehead, J. C., Plasma–Catalysis: The Known Knowns, the Known Unknowns and the Unknown Unknowns. *J. Phys. D: Appl. Phys.* **2016,** *49* (24), 243001.
4. Jones, A. C.; Hitchman, M. L., *Overview of Chemical Vapour Deposition*. Royal Society of Chemistry: Cambridge, 2009.
5. Choy, K., Chemical Vapour Deposition of Coatings. *Prog. Mater Sci.* **2003,** *48* (2), 57-170.
6. Hawker, M. J.; Pegalajar-Jurado, A.; Hicks, K. I.; Shearer, J. C.; Fisher, E. R., Allylamine and Allyl Alcohol Plasma Copolymerization: Synthesis of Customizable Biologically-Reactive Three-Dimensional Scaffolds. *Plasma Process Polym.* **2015,** *12* (12), 1435-1450.
7. Meyyappan, M.; Delzeit, L.; Cassell, A.; Hash, D., Carbon Nanotube Growth by PECVD: A Review. *Plasma Sources Sci. Technol.* **2003,** *12* (2), 205.
8. Rath, J.; Brinza, M.; Liu, Y.; Borreman, A.; Schropp, R., Fabrication of Thin Film Silicon Solar Cells on Plastic Substrate by Very High Frequency Pecvd. *Sol. Energy Mater. Sol. Cells* **2010,** *94* (9), 1534-1541.
9. Gorin, A.; Jaouad, A.; Grondin, E.; Aimez, V.; Charette, P., Fabrication of Silicon Nitride Waveguides for Visible-Light Using Pecvd: A Study of the Effect of Plasma Frequency on Optical Properties. *Opt. Express* **2008,** *16* (18), 13509-13516.
10. Chung, C.-K.; Tsai, M.-Q.; Tsai, P.-H.; Lee, C., Fabrication and Characterization of Amorphous Si Films by PECVD for MEMs. *J Micromech Microeng.* **2004,** *15* (1), 136.
11. Zhou, K.; Ke, P.; Li, X.; Zou, Y.; Wang, A., Microstructure and Electrochemical Properties of Nitrogen-Doped DLC Films Deposited by PECVD Technique. *Appl. Surf. Sci.* **2015,** *329*, 281-286.
12. Robertson, J., Diamond-Like Amorphous Carbon. *Mater. Sci. Eng. R Rep.* **2002,** *37* (4-6), 129-281.
13. Anooshehpour, F.; Turgeon, S.; Cloutier, M.; Mantovani, D.; Laroche, G., Optical Emission Spectroscopy as a Process-Monitoring Tool in Plasma Enhanced Chemical Vapor Deposition of Amorphous Carbon Coatings-Multivariate Statistical Modelling. *Thin Solid Films* **2018,** *649*, 106-114.
14. Fedosenko, G.; Schwabedissen, A.; Engemann, J.; Braca, E.; Valentini, L.; Kenny, J., Pulsed PECVD Deposition of Diamond-Like Carbon Films. *Diamond Relat. Mater.* **2002,** *11* (3-6), 1047-1052.
15. Caschera, D.; Cossari, P.; Federici, F.; Kaciulis, S.; Mezzi, A.; Padeletti, G.; Trucchi, D., Influence of PECVD Parameters on the Properties of Diamond-Like Carbon Films. *Thin Solid Films* **2011,** *519* (12), 4087-4091.
16. Ravi, N.; Bukhovets, V.; Varshavskaya, I.; Sundararajan, G., Deposition of Diamond-Like Carbon Films on Aluminium Substrates by RF-PECVD Technique: Influence of Process Parameters. *Diamond Relat. Mater.* **2007,** *16* (1), 90-97.

17. Toro, R.; Calandra, P.; Cortese, B.; de Caro, T.; Brucale, M.; Mezzi, A.; Federici, F.; Caschera, D., Argon and Hydrogen Plasma Influence on the Protective Properties of Diamond-Like Carbon Films as Barrier Coating. *Surf. Interface* **2017,** *6*, 60-71.
18. Chao, T.; Tan, A., Dlc Deposition Parameters Optimization for Head Disk Design Interface with a Thermal Protrusion Slider from Tribological Point of View. *Mater. Des.* **2013,** *48*, 58-67.
19. Ronkainen, H.; Koskinen, J.; Varjus, S.; Holmberg, K., Experimental Design and Modelling in the Investigation of Process Parameter Effects on the Tribological and Mechanical Properties of RF-Plasma-Deposited a-C:H Films. *Surf. Coat. Technol.* **1999,** *122* (2-3), 150-160.
20. Zhou, J.; Martin, I. T.; Ayers, R.; Adams, E.; Liu, D.; Fisher, E. R., Investigation of Inductively Coupled Ar and CH_4/Ar Plasmas and the Effect of Ion Energy on DLC Film Properties. *Plasma Sources Sci. Technol.* **2006,** *15* (4), 714.
21. Corbella, C.; Vives, M.; Oncins, G.; Canal, C.; Andujar, J.; Bertran, E., Characterization of DLC Films Obtained at Room Temperature by Pulsed-DC PECVD. *Diamond Relat. Mater.* **2004,** *13* (4-8), 1494-1499.
22. Park, H. J.; Shin, J.-h.; Lee, K.-i.; Choi, Y. S.; Song, Y. I.; Suh, S. J.; Jung, Y. H., Effective Control of CH_4/H_2 Plasma Condition to Synthesize Graphene Nano-Walls with Controlled Morphology and Structural Quality. *ASCT* **2017,** *26* (6), 179-183.
23. Lombardi, G.; Hassouni, K.; Bénédic, F.; Mohasseb, F.; Röpcke, J.; Gicquel, A., Spectroscopic Diagnostics and Modeling of $Ar/H_2/CH_4$ Microwave Discharges Used for Nanocrystalline Diamond Deposition. *J. Appl. Phys.* **2004,** *96* (11), 6739-6751.
24. Naito, S.; Nomura, H.; Goto, T., Measurement of CH_3 Radical in RF Methane/Rare Gas Plasma Using Infrared Diode Laser Absorption Spectroscopy. *The Review of Laser Engineering* **1992,** *20* (9), 746-751.
25. Mutsukura, N., Deposition of Diamondlike Carbon Film and Mass Spectrometry Measurement in CH_4/N_2 RF Plasma. *Plasma Chem. Plasma Process.* **2001,** *21* (2), 265-277.
26. Zhou, H.; Watanabe, J.; Miyake, M.; Ogino, A.; Nagatsu, M.; Zhan, R., Optical and Mass Spectroscopy Measurements of $Ar/CH_4/H_2$ Microwave Plasma for Nano-Crystalline Diamond Film Deposition. *Diamond Relat. Mater.* **2007,** *16* (4-7), 675-678.
27. Zhou, J.; Fisher, E. R., Surface Reactivity and Energetics of CH Radicals During Plasma Deposition of Hydrogenated Diamondlike Carbon Films. *J. Phys. Chem. B* **2006,** *110* (43), 21911-21919.
28. Tatarova, E.; Bundaleska, N.; Sarrette, J. P.; Ferreira, C., Plasmas for Environmental Issues: From Hydrogen Production to 2D Materials Assembly. *Plasma Sources Sci. Technol.* **2014,** *23* (6), 063002.
29. Van Durme, J.; Dewulf, J.; Leys, C.; Van Langenhove, H., Combining Non-Thermal Plasma with Heterogeneous Catalysis in Waste Gas Treatment: A Review. *Appl. Catal., B* **2008,** *78* (3-4), 324-333.
30. Peng, P.; Li, Y.; Cheng, Y.; Deng, S.; Chen, P.; Ruan, R., Atmospheric Pressure Ammonia Synthesis Using Non-Thermal Plasma Assisted Catalysis. *Plasma Chem. Plasma Process.* **2016,** *36* (5), 1201-1210.
31. Chen, H. L.; Lee, H. M.; Chen, S. H.; Chao, Y.; Chang, M. B., Review of Plasma Catalysis on Hydrocarbon Reforming for Hydrogen Production—Interaction, Integration, and Prospects. *Appl. Catal., B* **2008,** *85* (1-2), 1-9.

32. Sobacchi, M.; Saveliev, A.; Fridman, A.; Kennedy, L. A.; Ahmed, S.; Krause, T., Experimental Assessment of a Combined Plasma/Catalytic System for Hydrogen Production Via Partial Oxidation of Hydrocarbon Fuels. *Int. J. Hydrogen Energy* **2002,** *27* (6), 635-642.
33. Tu, X.; Whitehead, J., Plasma-Catalytic Dry Reforming of Methane in an Atmospheric Dielectric Barrier Discharge: Understanding the Synergistic Effect at Low Temperature. *Appl. Catal., B* **2012,** *125*, 439-448.
34. Bromberg, L.; Cohn, D.; Rabinovich, A.; Alexeev, N., Plasma Catalytic Reforming of Methane. *Int. J. Hydrogen Energy* **1999,** *24* (12), 1131-1137.
35. Chung, W.-C.; Chang, M.-B., Review of Catalysis and Plasma Performance on Dry Reforming of CH_4 and Possible Synergistic Effects. *Revew. Sust. Energ. Rev.* **2016,** *62*, 13-31.
36. Kameshima, S.; Tamura, K.; Ishibashi, Y.; Nozaki, T., Pulsed Dry Methane Reforming in Plasma-Enhanced Catalytic Reaction. *Catal. Today* **2015,** *256*, 67-75.
37. Neyts, E. C.; Ostrikov, K.; Sunkara, M. K.; Bogaerts, A., Plasma Catalysis: Synergistic Effects at the Nanoscale. *Chem. Rev.* **2015,** *115* (24), 13408-13446.
38. Santhosh, N.; Filipič, G.; Tatarova, E.; Baranov, O.; Kondo, H.; Sekine, M.; Hori, M.; Ostrikov, K.; Cvelbar, U., Oriented Carbon Nanostructures by Plasma Processing: Recent Advances and Future Challenges. *Micromachines* **2018,** *9* (11), 565.
39. Meyyappan, M., Plasma Nanotechnology: Past, Present and Future. *J. Phys. D: Appl. Phys.* **2011,** *44* (17), 174002.
40. Neyts, E. C., Plasma-Surface Interactions in Plasma Catalysis. *Plasma Chem. Plasma Process.* **2016,** *36* (1), 185-212.
41. Feng, X.; Liu, H.; He, C.; Shen, Z.; Wang, T., Synergistic Effects and Mechanism of a Non-Thermal Plasma Catalysis System in Volatile Organic Compound Removal: A Review. *Catal. Sci. Technol.* **2018,** *8* (4), 936-954.
42. Puliyalil, H.; Jurković, D. L.; Dasireddy, V. D.; Likozar, B., A Review of Plasma-Assisted Catalytic Conversion of Gaseous Carbon Dioxide and Methane into Value-Added Platform Chemicals and Fuels. *RSC Adv.* **2018,** *8* (48), 27481-27508.
43. Chen, H. L.; Lee, H. M.; Chen, S. H.; Chang, M. B.; Yu, S. J.; Li, S. N., Removal of Volatile Organic Compounds by Single-Stage and Two-Stage Plasma Catalysis Systems: A Review of the Performance Enhancement Mechanisms, Current Status, and Suitable Applications. *Environ. Sci. Technol.* **2009,** *43* (7), 2216-2227.
44. Malik, M. A.; Minamitani, Y.; Schoenbach, K. H., Comparison of Catalytic Activity of Aluminum Oxide and Silica Gel for Decomposition of Volatile Organic Compounds (VOCs) in a Plasmacatalytic Reactor. *IEEE T Plasma Sci.* **2005,** *33* (1), 50-56.
45. Mizuno, A., Generation of Non-Thermal Plasma Combined with Catalysts and Their Application in Environmental Technology. *Catal. Today* **2013,** *211*, 2-8.
46. Van Durme, J.; Dewulf, J.; Sysmans, W.; Leys, C.; Van Langenhove, H., Abatement and Degradation Pathways of Toluene in Indoor Air by Positive Corona Discharge. *Chemosphere* **2007,** *68* (10), 1821-1829.
47. Nozaki, T.; Ağıral, A.; Yuzawa, S.; Gardeniers, J. H.; Okazaki, K., A Single Step Methane Conversion into Synthetic Fuels Using Microplasma Reactor. *Chem. Eng. J.* **2011,** *166* (1), 288-293.
48. Gong, X.; Zhao, R.; Qin, J.; Wang, H.; Wang, D., Ultra-Efficient Removal of NO in a MOFs-NTP Synergistic Process at Ambient Temperature. *Chem. Eng. J.* **2019,** *358*, 291-298.

49. Wu, H.; Xu, C.; Xu, J.; Lu, L.; Fan, Z.; Chen, X.; Song, Y.; Li, D., Enhanced Supercapacitance in Anodic TiO_2 Nanotube Films by Hydrogen Plasma Treatment. *Nanotechnology* **2013,** *24* (45), 455401.
50. Neyts, E.; Bogaerts, A., Understanding Plasma Catalysis through Modelling and Simulation—A Review. *J. Phys. D: Appl. Phys.* **2014,** *47* (22), 224010.
51. Tu, X.; Gallon, H. J.; Whitehead, J. C., Electrical and Spectroscopic Diagnostics of a Single-Stage Plasma-Catalysis System: Effect of Packing with TiO_2. *J. Phys. D: Appl. Phys.* **2011,** *44* (48), 482003.
52. Liu, C.-j.; Wang, J.-x.; Yu, K.-l.; Eliasson, B.; Xia, Q.; Xue, B.; Zhang, Y.-h., Floating Double Probe Characteristics of Non-Thermal Plasmas in the Presence of Zeolite. *Journal of electrostatics* **2002,** *54* (2), 149-158.
53. Holzer, F.; Kopinke, F.; Roland, U., Influence of Ferroelectric Materials and Catalysts on the Performance of Non-Thermal Plasma (NTP) for the Removal of Air Pollutants. *Plasma Chem. Plasma Process.* **2005,** *25* (6), 595-611.
54. Kim, J.; Go, D. B.; Hicks, J. C., Synergistic Effects of Plasma–Catalyst Interactions for CH_4 Activation. *Phys. Chem. Chem. Phys.* **2017,** *19* (20), 13010-13021.
55. Truscott, B. S.; Kelly, M. W.; Potter, K. J.; Ashfold, M. N.; Mankelevich, Y. A., Microwave Plasma-Activated Chemical Vapor Deposition of Nitrogen-Doped Diamond. II: $CH_4/N_2/H_2$ Plasmas. *J. Phys. Chem. A* **2016,** *120* (43), 8537-8549.
56. Li, H.; Yang, K.; Liu, H.; Zhu, X., Optical and Mass Spectroscopic Properties of Microwave $CH_4/H_2/Ar$ Plasma for Diamond Deposition in a Resonance Cavity. *Vacuum* **2018,** *147*, 45-50.
57. Ito, H.; Koshimura, K.; Onitsuka, S.; Okada, K.; Suzuki, T.; Akasaka, H.; Saitoh, H., Dissociative Excitation of C_2H_2 in the Electron Cyclotron Resonance Plasma of Ar: Production of CH ($A^2\Delta$) Radicals and Formation of Hydrogenated Amorphous Carbon Films. *Plasma Chem. Plasma Process.* **2012,** *32* (2), 231-248.
58. Pothiraja, R.; Engelhardt, M.; Bibinov, N.; Awakowicz, P., Film Deposition on the Inner Surface of Tubes Using Atmospheric-Pressure Ar–CH_4, Ar–C_2H_2 and Ar–C_2H_2–H_2 Plasmas: Interpretation of Film Properties from Plasma-Chemical Kinetics. *J. Phys. D: Appl. Phys.* **2012,** *45* (33), 335202.
59. Mohanta, A.; Lanfant, B.; Asfaha, M.; Leparoux, M., Methane Dissociation Process in Inductively Coupled $Ar/H_2/CH_4$ Plasma for Graphene Nano-Flakes Production. *Appl. Phys. Lett.* **2017,** *110* (9), 093109.
60. Okita, A.; Suda, Y.; Oda, A.; Nakamura, J.; Ozeki, A.; Bhattacharyya, K.; Sugawara, H.; Sakai, Y., Effects of Hydrogen on Carbon Nanotube Formation in CH_4/H_2 Plasmas. *Carbon* **2007,** *45* (7), 1518-1526.
61. Nozaki, T.; Muto, N.; Kado, S.; Okazaki, K., Dissociation of Vibrationally Excited Methane on Ni Catalyst: Part 1. Application to Methane Steam Reforming. *Catal. Today* **2004,** *89* (1-2), 57-65.
62. Nozaki, T.; Muto, N.; Kadio, S.; Okazaki, K., Dissociation of Vibrationally Excited Methane on Ni Catalyst: Part 2. Process Diagnostics by Emission Spectroscopy. *Catal. Today* **2004,** *89* (1-2), 67-74.
63. Tachibana, K.; Nishida, M.; Harima, H.; Urano, Y., Diagnostics and Modelling of a Methane Plasma Used in the Chemical Vapour Deposition of Amorphous Carbon Films. *J. Phys. D: Appl. Phys.* **1984,** *17* (8), 1727.

64. Legrand, J.-C.; Diamy, A.-M.; Hrach, R.; Hrachova, V., Mechanisms of Methane Decomposition in Nitrogen Afterglow Plasma. *Vacuum* **1999,** *52* (1-2), 27-32.
65. Avtaeva, S.; Lapochkina, T., Characteristics of Molecular Hydrogen and CH* Radicals in a Methane Plasma in a Magnetically Enhanced Capacitive RF Discharge. *Plasma Physics Reports* **2007,** *33* (9), 774-785.
66. Morrison, N.; William, C.; Milne, W., Methane Chemistry Involved in a Low-Pressure Electron Cyclotron Wave Resonant Plasma Discharge. *J. Appl. Phys.* **2003,** *94* (11), 7031-7043.

CHAPTER 2

EXPERIMENTAL METHODS

This chapter describes the materials, methods, and instrumentation used to complete the materials characterization and gas-phase analyses described within this dissertation. The information described within this chapter comprises five sections: plasma reactor set up and plasma conditions (2.1), materials preparation (2.2), materials characterization techniques (2.3), optical spectroscopy techniques (2.4), and characteristic plasma temperature determination (2.5).

2.1 Plasma Systems

All inductively coupled plasmas (ICP) studied herein were ignited in two different styles of glass tubular-style reactors via coupling of radio frequency (rf) power through an eight-turn Ni-plated Cu coil. Precursor gases used in this work include CH_4 (Air Products, >99.97% purity), H_2 (Airgas, 99.9%), N_2 (Airgas, >99.99%), and Ar (Airgas, >99.999% purity). A liquid precursor, deionized H_2O (Millipore, 18 mΩ cm^{-1}), was placed in a 50 mL borosilicate sidearm vacuum flask equipped with a Teflon™ stopcock and subjected to three consecutive freeze-pump-thaw cycles to remove dissolved atmospheric gases prior to use. In the experiments described Chapters 3 – 5 and Chapter 7, plasmas were ignited in a reactor created from two borosilicate glass tubes joined with a 50 mm o-ring joint allowing for easy access to the interior of the plasma reactor, Figure 2.1a.[1] The joined tubes create a reactor 35 cm in length, and the interior wall of the reactor has a diameter of 4.5 cm. In addition, a replaceable quartz window is centrally affixed to the downstream end of the reactor to allow for coaxial collection of plasma emission. In some experiments described in Chapter 5, a replaceable quartz window was also

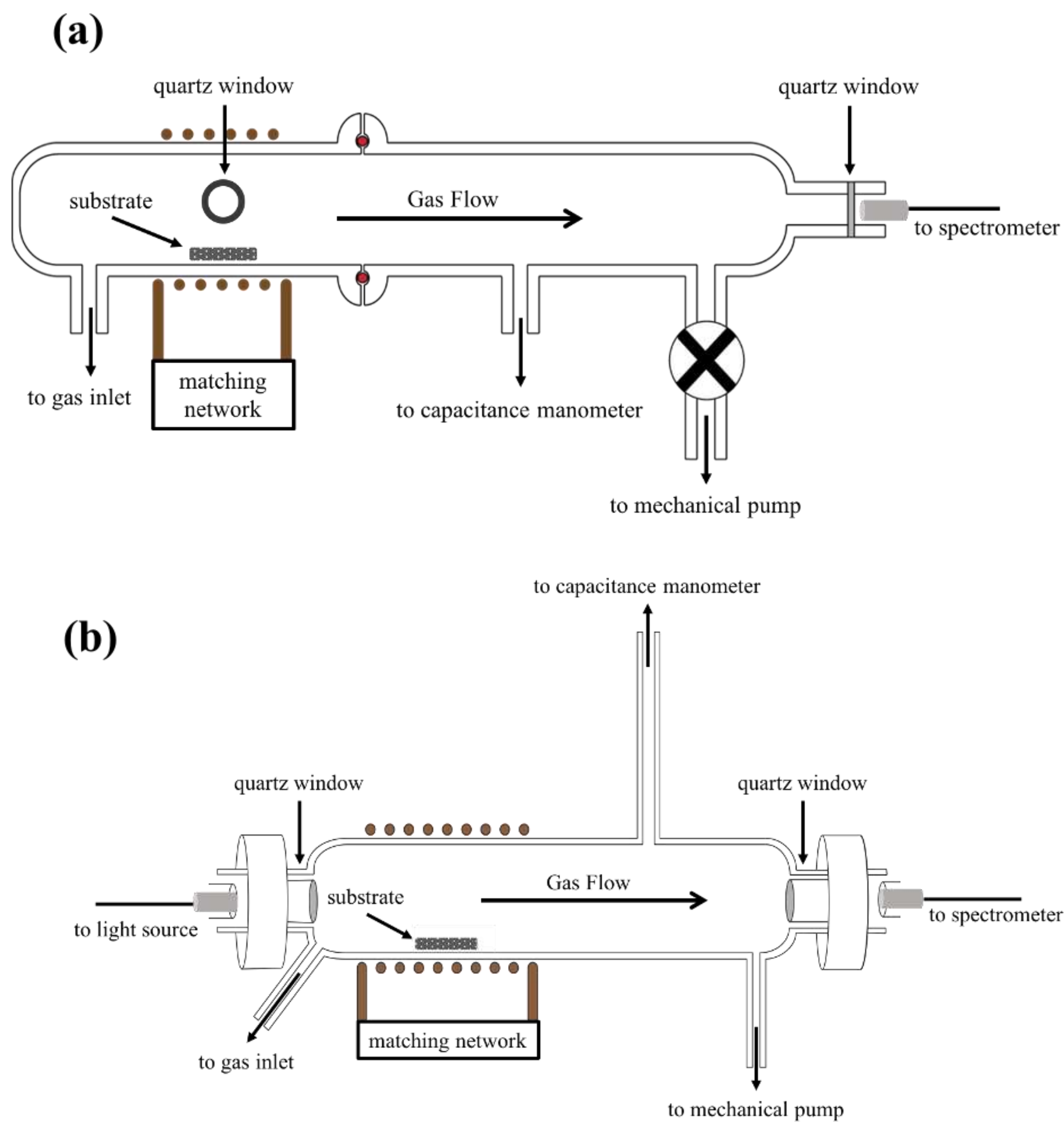

Figure 2.1. Schematics of glass barrel ICP reactors used for (a) OES and film deposition studies and (b) N_2 plasma OES and CH_4 plasma BAS data collection.

utilized on the inlet half of the reactor to monitor relative species densities directly above the substrate. For the experiments described in Chapter 6, plasmas were ignited in a separate reactor, Figure 2.1b, to reduce the possibility of hydrocarbon contamination from the interior walls of the plasma reactor. The reactor setup shown in Figure 2.1b is a modified version of the reactor in Figure 2.1a. This reactor is similar in size with a 24 cm length and 4.5 cm inner diameter.[2] With the addition of an upstream quartz window, the modified reactor allows for the collection of plasma absorption spectra in addition to emission spectra. Thus, the type of reactor shown in Figure 2.1b was also used for collection of broadband absorption spectroscopy (BAS) data in Chapter 8. Base pressure of the CH_4, H_2, and mixed gas plasma systems ranged from ~12 – 15 mTorr whereas base pressure for the 100% N_2 system was ~2 – 4 mTorr. Gas flow for these reactors was maintained by either a series of needle valves or MKS mass flow controllers, and pressure (p) ranged from 50 – 200 mTorr and was monitored by a Baratron® capacitance monometer. For all experiments, power (P) values ranged from 25 to 150 W and was applied by rf power at 13.56 MHz via a matching network.

2.2 Materials Preparation

For the purpose of characterizing the amorphous hydrocarbon (HC) films in Chapter 3, clean glass slides (VWR micro slides, plain, 1.2 mm thickness) cut to ~5 cm × 5 cm were used as the substrate material. Commercially purchased TiO_2 AEROXIDE P25 nanopowder (Acros Organics, 21 nm primary particle size) substrates were made by creating a slurry of as received nanoparticles and methanol, as described previously.[3] The nanoparticles (NP) were suspended in methanol until saturation; then the NP solution dropcast on to glass slides and p-type <100> silicon wafers (Wacker-Chemitronic GMBH, Germany) of ~3 × 3 cm. All substrates used were

placed in the coil region of the plasma reactor ~30 cm upstream from the quartz window, as shown in Figure 2.1.

2.3 Materials Characterization

2.3.1. X-ray Photoelectron Spectroscopy (XPS). Surface compositional analysis of HC films and catalytic materials prior to and after plasma exposure was performed using a PHI-5800 Electron Spectroscopy for Chemical Analysis system (Chanhassen, MN, USA) equipped with a monochromatic Al K_α X-ray source (1486.6 eV photons). Three distinct spots on at least two different samples ($n \geq 6$) were analyzed at a 45° takeoff angle. Survey spectra were collected for 5 minutes over a range of 10 – 1100 eV to obtain approximate elemental composition. High resolution spectra were collected for 20 minutes for elements present in > 1% in the survey scan including C_{1s} and O_{1s} spectra, and N_{1s} and Ti_{2p} in relevant cases. CasaXPS v2.3 was used deconvolute spectra and to determine atomic percent compositions. Charge correction of binding energies was performed by setting the C_{1s} aliphatic carbon signal to 285.0 eV. Peak FWHMs values were constrained to ≤ 2.0 eV.

2.3.2. Fourier Transform Infrared (FTIR) Spectroscopy. Film composition was also explored via FTIR spectroscopy using a Thermo Scientific Nicolet Magna 760 spectrometer (Madison, WI), with a resolution of 4 cm^{-1} and 256 averaged scans. The spectrometer was purged for > 2 hours with N_2 gas before spectra of the films deposited on pressed KBr pellets (FTIR-grade, Sigma-Aldrich, St. Louis, MO, USA) were collected. Atmospheric and baseline corrections were applied to all spectra via the onboard software (Omnic v8.2) to suppress any signals arising from water vapor or CO_2.

2.3.3. Optical Profilometry. Film morphology was assessed on HC films deposited on glass slides with a Zygo ZeScope optical profilometer (Middlefield, CT). Single scans were collected over a 250 × 350 μm area using a 20× magnification objective lens. A scan length of 100 μm in the z-axis and a signal threshold of 0.5% were used to assess the films. At least three scans were collected on three different samples ($n \geq 9$) to ensure accurate representation of the film morphology and roughness.

2.3.4. Water Contact Angle (WCA) Goniometry. A Krüss DSA 30S contact angle goniometer (Matthews, NC) was utilized to acquire surface wettability data. The static WCA for each film deposited on a clean glass slide (3 × 3 cm) was measured by capturing an image of a 2–μL drop of ultrapure water (Millipore, 18 mΩ cm^{-1}) stabilized on each substrate surface. WCAs were measured using the tangent fitting method for each film investigated. Values reported are the average and standard deviation of $n \geq 6$ where at least two measurements were acquired on three separate samples.

2.3.5. Scanning Electron Microscopy-Energy Dispersive Spectroscopy (SEM-EDS). Material morphology and chemical composition pre and post plasma exposure was evaluated via assessment of SEM-EDS images. Prior to imaging, silicon substrates were mounted on an aluminum stub with copper tape. SEM and EDS data were obtained via a JSM-6500F (JEOL, Ltd., Japan) scanning electron microscope equipped with a field emission source; an accelerating voltage of 15.0 kV and ~10 mm working distance were used.

2.3.6. Raman Spectroscopy. Raman spectroscopy was performed on TiO_2 substrates prior to and after plasma exposure on an Olympus IX-73 optical microscope with an OndaxTHz-Raman laser source (5 mW, 532 nm laser with 1.2 μm spot size). The Raman signal was collected in a backscattering geometry, passed through a Horiba iHR-550 imaging spectrometer,

and detected on a Synapse back-illuminated deep depletion charge-coupled device. Individual spectra were acquired for 30-60 seconds across a 1 mm × 1 mm sample area.

2.4 Optical Spectroscopies

Steady state optical emission spectra data reported in Chapters 3 – 5 and Chapter 7 were collected with an Avantes AvaSpec-3648-USB2 multichannel spectrometer. Four gratings (1200 lines/nm) each linked to a 3648-pixel charged-coupled device (CCD) detector over a wavelength range of 187 – 1016 nm and a 0.1 nm FWHM resolution are comprised within this spectrometer. OES and BAS data reported in Chapter 6 and Chapter 8 were collected with an Avantes AvaSpec-2048L-USB2-RM multichannel spectrometer. This spectrometer houses six gratings, each linked with a 2048-pixel CCD detector and allows for simultaneous data collection over a wavelength range of 197 – 1061 nm.

For all OES and BAS data, a fiber optic probe was placed against a quartz window downstream from the coil, allowing for coaxial data collection along the length of the reactor to maximize signal intensity. Additionally, for some experiments described in Chapter 5, emission spectra were also collected through a quartz window placed in the coil region of the reactor. For BAS experiments (Chapter 8), an AvaLight-DHS deuterium-halogen lamp was interfaced with a quartz window on the upstream end of the plasma reactor. Integration time and number of averages collected depend on the specific experiment to maximize signal-to-noise ratios. A minimum of 3 trials were executed at each plasma parameter condition.

Actinometry was utilized where described to determine relative excited electronic state densities of several emitting plasma species. In these cases, a small amount of Ar (≤10% of total gas feed pressure) was added to the plasma, and the ratio of emission intensities for the species

of interest (X) are reported relative to Ar (750.4 nm) (I_X/I_{Ar}) to allow for comparison of species densities between systems. Table 2.1 contains a concise list of the emitting species analyzed and discussed within this document as well as the associated actinometric wavelengths and transitions.

Time-resolved optical emission spectroscopy (TR-OES) data were collected to study formation and decomposition mechanisms of species within our plasma systems. For enhanced temporal resolution, an AvaSpec-ULS4096CL-EVO spectrometer (10-micron slit; 0.5 nm spectral resolution) was used to monitor emission intensity of the species of interest as a function of time. Integration times for TR-OES experiments ranged from 1.5 ms to 25 ms, depending on the experiment. Figure 2.2a demonstrates that data collection began before plasma ignition and lasted for approximately ~4 – 10 seconds after ignition. For data analysis, the first non-zero data point was set at time (t) = 0.0 s and all subsequent data points were adjusted accordingly (Figure 2.2b). The point(s) of highest intensity in the temporal profile were identified, and the rise to maximum intensity is denoted as rate constant of formation (k_f). The subsequent decrease in signal intensity to a steady state is denoted as the rate constant of destruction (k_d). A first order exponential function (e^{-kt}) was used to fit the formation and destruction curves and ultimately obtain the k_f and k_d values reported herein (Figure 2.2b). In some cases, no clear formation or destruction curves were detected on the time scale of our system.

2.5 Characteristic Plasma Temperature Determination

2.5.1. Electron Temperature. An analysis of Ar emission lines yielded mean electron temperature (T_e) values calculated via Equation 2.1,[4]

$$\frac{(E_n - E_1)}{kT_e} = \ln\left[\frac{I_1 \nu_n A_n (E_n + 2kT_e)}{I_n \nu_n A_1 (E_1 + 2kT_e)}\right] \qquad (2.1)$$

Table 2.1. Transitions and corresponding wavelengths used for actinometric analyses of selected species.

Emitting Species	Transition	Wavelength (nm)
Ar	$4p^1 \rightarrow 4s^1$	750.3
CH	$A^2\Delta \rightarrow X^2\Pi$	431.1
CN	$B^2\Sigma^+ \rightarrow X^2\Sigma^+$	388.3
H_α	$^2P^0 \rightarrow {}^2D$	656.3
H_2	$d^3\Pi_u \rightarrow a^3\Sigma_g^+$	601.8
N	$4d^4P \rightarrow 3p^4P^0$	674.0
N_2	$C^3\Pi_u \rightarrow B^3\Pi_g$	337.1
NO	$A^2\Sigma^+ \rightarrow X^2\Pi$	235.9
O	$^3S^0 \rightarrow {}^3P$	777.2
OH	$A^2\Sigma^+ \rightarrow X^2\Pi$	309.0

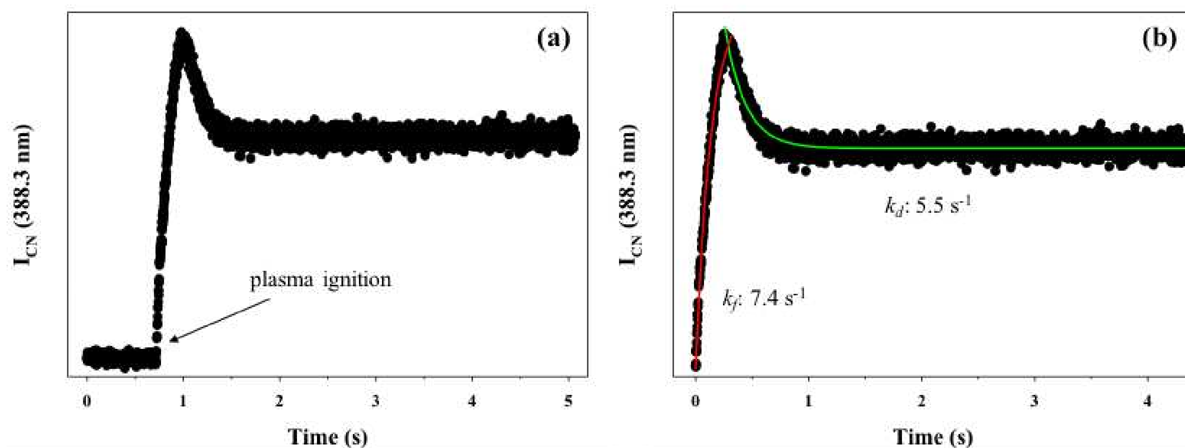

Figure 2.2. Time-resolved emission signal for CN in a 1:2 CH_4/N_2 plasma (150 mTorr, 75 W). Panel (a) displays raw emission data and highlights plasma ignition point. Panel (b) shows time-adjusted data for determination of k_f and k_d.

where E_n represents the excitation energy of arbitrarily defined transition n, I_n is the emission intensity obtained from OES, ν_n is the frequency of transition, and A_n is the transition probability. This process, summarized in greater detail previously,[4-5] involves an iterative comparison of three Ar emission lines to the 3d-4p line of Ar^+ (λ = 617.2 nm), yielding three T_e values for each OES spectrum collected. Reported T_e values are weighted averages and standard deviations from n ≥ 3 spectra.

2.5.2. Determination of Rotational and Vibrational Temperatures. Vibrational and rotational temperatures (T_V and T_R, respectively) were determined for several molecular species in the plasma systems described above from spectral data fit with SpecAir[6] and LIFBASE[7] programs or calculated via a Boltzmann plot. Details on the fitting parameters for each of these molecular species are reported in Table 2.2. Additionally, the role of the of the spectrometer grating efficiency on the emission spectra was considered. Corrections for the grating efficiency were applied to the raw data and T_R and T_V values reported herein reflect this correction.

In LIFBASE, imported spectra were evaluated by manually manipulating the vibrational histogram for a representative best fit of the vibrational state populations. These vibrational state populations were used to determine T_V(CH, CN, OH) using Equation 2.2,

$$T_V = \frac{\sum_{v_i}^{v_f} n(h\omega)(v+{}^1\!/_2)}{k_B} \tag{2.2}$$

where n represents the fractional population of an individual vibrational state, ω is the vibrational constant;[7] v is the numerical vibrational state, and k_B is Boltzmann's constant. A thermalized distribution was assumed for determination of T_R(CH, CN, OH) where the rotational temperature was adjusted within LIFBASE to best match FWHM. Figure 2.3 displays a CH $A^2\Delta \rightarrow X^2\Pi$ emission spectrum acquired under in a CH_4 plasma with a TiO_2 substrate at p = 150 mTorr and P = 50 W. For this specific spectrum, simulation via LIFBASE yields T_R(CH) = 1970 K and

Table 2.2. Temperature determination methods for plasma species of interest.

Molecule	OES Transition	Wavelength Range (nm)	Temperature Determination Method	
			T_R	T_V
CH	$A^2\Delta \rightarrow X^2\Pi$	425 – 440	LIFBASE	LIFBASE
CN	$B^2\Sigma^+ \rightarrow X^2\Sigma^+$	370 – 400	LIFBASE	LIFBASE
H_2	$d^3\Pi_u \rightarrow a^3\Sigma_g^+$	601 – 612	Boltzmann plot	--
N_2	$C^3\Pi_u \rightarrow B^3\Pi_g$	290 – 370	Specair	Boltzmann plot
OH	$A^2\Sigma^+ \rightarrow X^2\Pi$	305 – 325	LIFBASE	LIFBASE

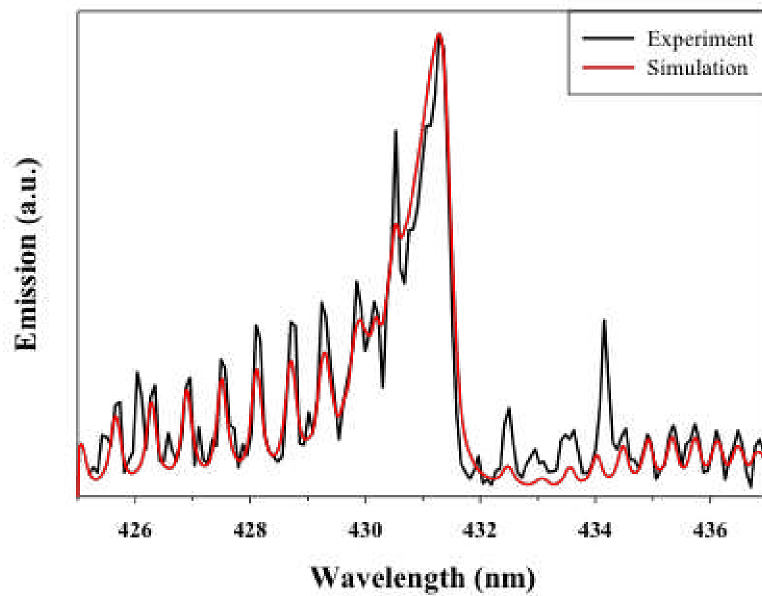

Figure 2.3. Representative emission spectrum (p = 150 mTorr, P = 50 W) for CH $A^2\Delta \rightarrow X^2\Pi$ in a CH_4 plasma with TiO_2. Simulation of the spectrum using LIFBASE yields T_R = 1970 K, T_V = 2550 K.

T_V(CH) = 2550 K. Note that error is not reported for these simulations because they were determined for a single trial. Peak correlation for all the simulations reported herein is > 80%.

A Boltzmann plot of ln (Iλ/A) as a function of vibrational energy (E) was used to calculate $T_V(N_2)$, where I and λ are the intensity (a.u.) and wavelength (nm) of a specific emission line and A (s^{-1}) is the corresponding Einstein transition probability coefficient for the transition. A typical N_2 emission spectrum acquired with a TiO_2 substrate placed in the coil region of the plasma reactor is shown in Figure 6.1. The N_2 transitions, corresponding wavelengths, and A values used to calculate $T_V(N_2)$ are reported previously.[8-10] The inset in Figure 6.1 shows a representative Boltzmann plot for a 100% N_2 plasma (with TiO_2 catalyst) created from the corresponding spectrum. The slope of the linear regression is inversely proportional to T_V, which ultimately yields $T_V(N_2)$ = 3140 ± 20 K for that particular set of conditions. $T_R(N_2)$ for the $C^3\Pi_u \rightarrow B^3\Pi_g$ transition was determined from simulated fits of experimental spectral data using the "Temperature Loop" function in SpecAir[6] by inputting the calculated $T_V(N_2)$ value obtained from the Boltzmann plot.

A Boltzmann plot was also used to calculate $T_R(H_2)$ values. For these calculations, ln ($I\lambda^4/S$) is plotted as a function of the upper state rotational energy (E), where I and λ are the intensity (a.u.) and wavelength (nm) of a specific emission line and S is the Hönl-London factor. Table 2.3 lists the selected H_2 transitions[11], corresponding wavelengths and energies, and Hönl-London factors.[12] These specific transitions for calculating $T_R(H_2)$ were selected because they have no overlap with other transitions.[11-12] All reported T_V and T_R values are the result of calculated averages and ±1 standard deviation from n ≥ 3 spectra.

Table 2.3. Parameters for selected H_2 rotational lines used to determine T_R(K) using a Boltzmann plot.

Rotational transition	(nm)	$E_{J'}$ (cm^{-1})	$S_{J'J''}$
Q_1	601.83	59.18	4.5
Q_2	602.38	177.55	2.5
Q_4	604.27	591.83	4.5
Q_6	607.20	1242.84	6.5
Q_8	611.11	2130.59	8.5

REFERENCES

1. Van Surksum, T. L.; Blechle, J. M.; Fisher, E. R., Determination of Rotational and Vibrational Temperatures of CH in CH_4 Plasmas. *J. Vac. Sci. Technol., A* **2018,** *36* (4), 041302.
2. Blechle, J. M.; Hanna, A. R.; Fisher, E. R., Determination of Internal Temperatures within Nitric Oxide Inductively Coupled Plasmas. *Plasma Process Polym.* **2017,** *14* (12), 1700041.
3. Shearer, J. C.; Fisher, M. J.; Hoogeland, D.; Fisher, E. R., Composite SiO_2/TiO_2 and Amine Polymer/TiO_2 Nanoparticles Produced Using Plasma-Enhanced Chemical Vapor Deposition. *Appl. Surf. Sci.* **2010,** *256* (7), 2081-2091.
4. Boogaard, A.; Kovalgin, A. Y.; Aarnink, A. A.; Wolters, R. A.; Holleman, J.; Brunets, I.; Schmitz, J. In *Measurement of Electron Temperatures of Argon Plasmas in a High-Density Inductively-Coupled Remote Plasma System by Langmuir Probe and Optical-Emission Spectroscopy*, Proceedings of the 9th annual workshop on Semiconductor Advances for Future Electronics and Sensors 2006, Technology Foundation (STW): 2006.
5. Hanna, A. R.; Blechle, J. M.; Fisher, E. R., Using Fundamental Spectroscopy to Elucidate Kinetic and Energetic Mechanisms within Environmentally Relevant Inductively Coupled Plasma Systems. *J. Phys. Chem. A* **2017,** *121* (40), 7627-7640.
6. Laux, C. O., Radiation and Nonequilibrium Collisional-Radiative Models. *von Karman Institute Lecture Series* **2002,** *7*.
7. Luque, J., Database and Spectral Simulation Program (Version 1.5). *SRI international report MP* **1999**, 99-009.
8. Wu, A. J.; Zhang, H.; Li, X. D.; Lu, S. Y.; Du, C. M.; Yan, J. H., Determination of Spectroscopic Temperatures and Electron Density in Rotating Gliding Arc Discharge. *IEEE T Plasma Sci.* **2015,** *43* (3), 836-845.
9. NIST, Nist Chemistry Webbook.
10. Hanna, A. R.; Van Surksum, T. L.; Fisher, E. R., Investigating the Impact of Catalysts on N_2 Rotational and Vibrational Temperatures in Low Pressure Plasmas. *J. Phys. D: Appl. Phys.* **2019,** *52* (34), 345202.
11. Garg, R.; Anderson, T.; Lucht, R.; Fisher, T.; Gore, J., Gas Temperature Measurements in a Microwave Plasma by Optical Emission Spectroscopy under Single-Wall Carbon Nanotube Growth Conditions. *J. Phys. D: Appl. Phys.* **2008,** *41* (9), 095206.
12. Shivkumar, G.; Tholeti, S.; Alrefae, M.; Fisher, T.; Alexeenko, A., Analysis of Hydrogen Plasma in a Microwave Plasma Chemical Vapor Deposition Reactor. *J. Appl. Phys.* **2016,** *119* (11), 113301.

CHAPTER 3

DETERMINATION OF ROTATIONAL AND VIBRATIONAL TEMPERATURES OF CH IN CH_4 PLASMAS

This chapter contains data from a full paper published under the same title in *Journal of Vacuum Science and Technology A* written by Tara L. Van Surksum, Joshua M. Blechle, and Ellen R. Fisher and is reproduced with permission from *J. Vac. Sci. Technol., A* 2018, *36* (4), 041302 (Copyright 2018, American Vacuum Society). These studies investigate rotational and vibrational energy partitioning trends of CH $A^2\Delta \rightarrow X^2\Pi$ in 100% CH_4 and CH_4/Ar inductively coupled plasma systems via optical emission spectroscopy. Characterization of the amorphous hydrocarbon films deposited by these plasma systems is also discussed. This work was supported by the National Science Foundation (NSF-1152963). I would also like to thank Dr. Patrick McCurdy for assistance with the XPS and the Dr. Charles Henry research group for profilometry technical support.

3.1 Introduction

Volatile organic compounds (VOCs) emitted from anthropogenic sources primarily result from fuel combustion of vehicle exhaust and various industrial processes.[1] Many VOCs are carcinogenic, and excessive exposure to them can cause headaches, dizziness, and damage to the liver, kidneys, and central nervous system.[2-4] In addition to their negative impacts on human health, VOCs also have serious undesirable environmental impacts. For example, reactions with nitrogen oxides (NO_x) result in the formation of photochemical smog and ozone.[3, 5] Thus, increasing concerns arising from deleterious pollution-related issues require effective and

efficient techniques for the abatement of toxic species such as NO_x and VOCs.

Plasma-assisted catalysis (PAC), a proposed pollutant mitigation method, couples a non-thermal plasma (NTP) with a catalyst to produce outcomes that cannot be attained by plasma or catalysis individually.[2-3, 6-8] A NTP consists of electrons, ions, radicals, and neutral and excited state species which interact with each other and in a synergistic manner with a catalyst.[7] Thus, the active species in the plasma, coupled with a catalyst, enhances selectivity and efficiency and gives rise to a plasma environment that allows for conversion and abatement of toxic pollutant species.[2, 9-10] Atmospheric pressure NTPs have shown great promise as an effective means to achieve VOC conversion and abatement because of the apparent advantages such as low cost, low operating temperatures, and wide range of applicability towards removal of VOCs and NO_x species.[9-13] However, current PAC application is limited because of selectivity issues, unwanted byproduct formation, and overall low energy efficiency.[9, 11-15] Overcoming these challenges requires a need for fundamental investigations of gas-phase plasma processes and plasma-surface interactions. Thus, emphasizing the importance of plasma diagnostic approaches in conjunction with computational strategies for plasma modeling purposes.

Knowledge of the roles of gas-phase radicals and radical-surface interactions is key to understanding fundamental plasma processes and plasma-surface chemistry. In molecular gases (e.g., methane, methane-containing mixtures), direct electron impact could lead not only to the decomposition of molecules into radicals and smaller molecules but also to the excitation of electronic, vibrational, and rotational states of species of interest.[16-17] Excited state reactions provide routes to different processes/products relative to similar processes for the same molecules or radicals in the ground state and must be taken into account when developing plasma models and elucidating overall plasma chemistry.[17] Thus, an understanding of how

energy is partitioned into vibrational, rotational, and translational modes provides insight into formation mechanisms, decomposition pathways, and overall plasma chemistry. Specifically, figures of merit such as gas temperature (T_g), vibrational temperature (T_V), and rotational temperature (T_R) describe the energetics of species within the plasma system. NTPs generally follow a relationship where $T_V > T_R \approx T_T$, yet each temperature is significantly lower than the electron temperature (T_e).[18-24] T_R and T_T are often assumed to equilibrate with each other and the T_g because of the relatively small energy separations between rotational and translational levels.[23-24] However, because of larger energy separations between vibrational levels, collisions able to produce a change in vibrational quantum number are much less frequent, and therefore, the vibrational distribution is not expected to necessarily equilibrate with the T_R or T_g.[23-24]

Here, we have chosen to examine CH_4 and CH_4/Ar plasmas as model systems because methane is a simple, model hydrocarbon representative of VOCs. Moreover, methane plasmas have been used extensively to deposit diamond and diamond-like carbon films.[25-28] Despite the extensive use of CH_4-based plasmas and several studies focused on temperature measurements under a prescribed set of conditions,[29-32] few studies report on energy partitioning trends of CH_4 discharges with catalytic substrates. Thus, a primary goal of this study is to elucidate energy partitioning trends through determination of T_R and T_V of excited state CH (CH $A^2\Delta$) in CH_4 and CH_4/Ar plasma systems as a function of system pressure (p) and applied rf power (P). We also seek to elucidate molecular-level processes occurring at the plasma-surface interface. Understanding these processes remains an important component towards elucidating more complex plasma catalyst interactions in PAC applications. Thus, in addition to characterization of the gas-phase, the chemical composition and morphology of the amorphous hydrocarbon films

deposited from the plasma were also investigated to explore the effect of the gas-phase chemistry on resulting film chemistry.

3.2 Results

The representative raw OES data depicted in Figure 3.1a for a 100% CH_4 plasma show emitting atomic and molecular hydrogen species dominate the spectrum. Emission from CH radicals is also observed at 431.1 nm. Figure 3.1b highlights the wavelength region of 425 – 437 nm, allowing for a closer examination of the CH $A^2\Delta \rightarrow X^2\Pi$ band. Emission data simulated using LIFBASE to elucidate characteristic temperatures, T_R(CH) and T_V(CH), are shown in Figure 3.1b. The simulated spectrum closely matches the experimental emission spectrum [peak correlation (PC) = 0.98]. T_R(CH) and T_V(CH) values obtained from the spectrum shown in Figure 3.1b are 1880 K and 2690 K, respectively. To demonstrate the sensitivity of the fit to changes in T_R and T_V, two additional simulations for both T_R and T_V (± 50 K and ± 100 K of the reported values, respectively) were performed for the experimental spectrum shown in Figure 3.1b and are shown in Figure 3.2. The four additional simulations also each have peak correlations of 0.98 and thus, demonstrate that the goodness of fit does not change appreciably near the upper range of our reported error.

Similar data for T_R(CH) and T_V(CH) were obtained for over the range of plasma parameters specified above. T_R(CH) values, Figure 3.3a, display a negative, linear correlation (R^2 = 0.84) with pressure in the 100% CH_4 plasma system. Table 3.1 lists all the calculated T_R(CH) values, which range from ~1750 K to ~2360 K for the studied parameter space. T_V data for CH in 100% CH_4 plasmas, Figure 3.3b, display a trend similar to the T_R(CH) data [albeit somewhat non-linear ($R^2 < 0.7$)], where an increase in pressure results in an overall decrease in

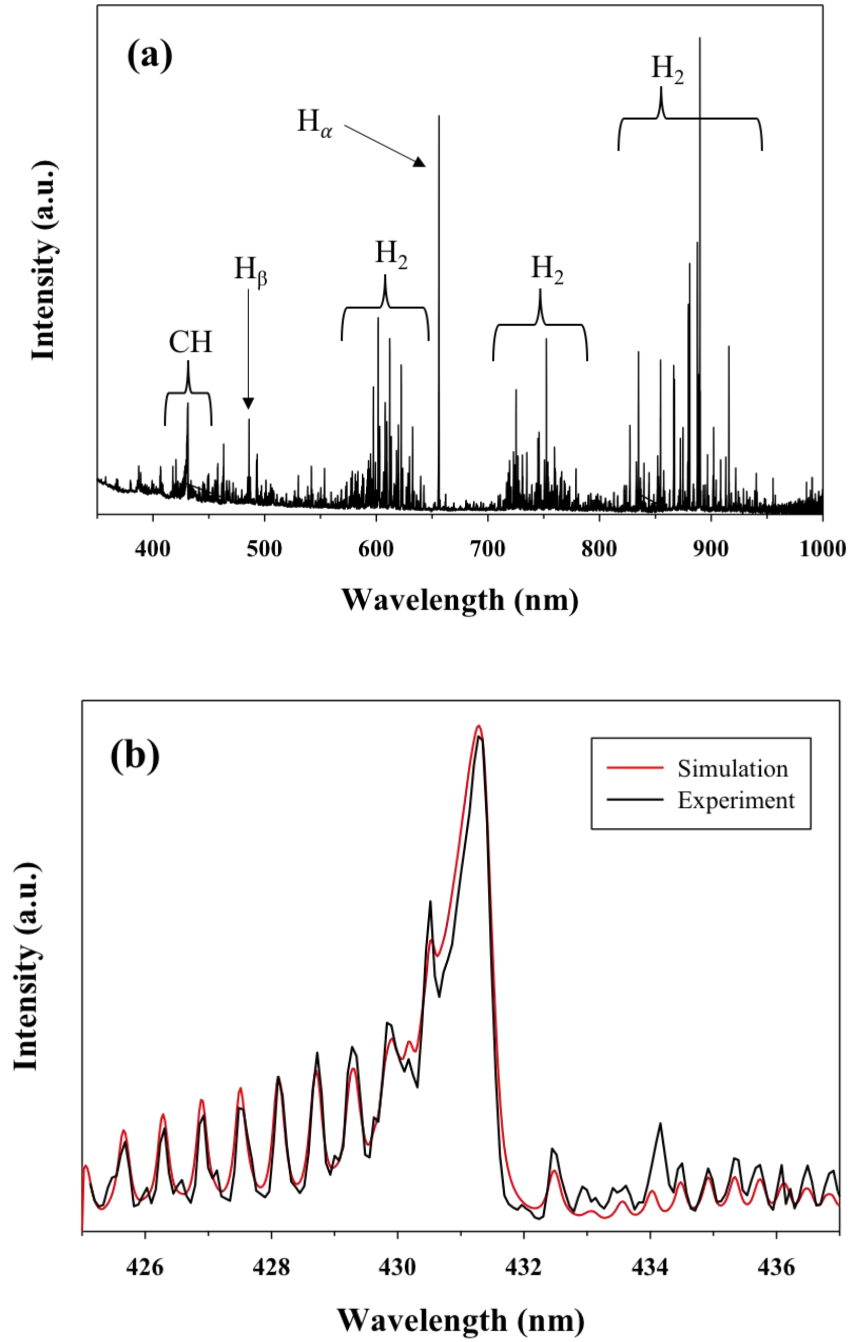

Figure 3.1. (a) Representative emission spectrum for a 100% CH_4 plasma system at p = 200 mTorr, P = 75 W. (b) Enlarged view of the CH $A^2\Delta \rightarrow X^2\Pi$ band, along with the simulated fit from LIFBASE, giving rise to T_R = 1800 K, T_V = 2690 K.

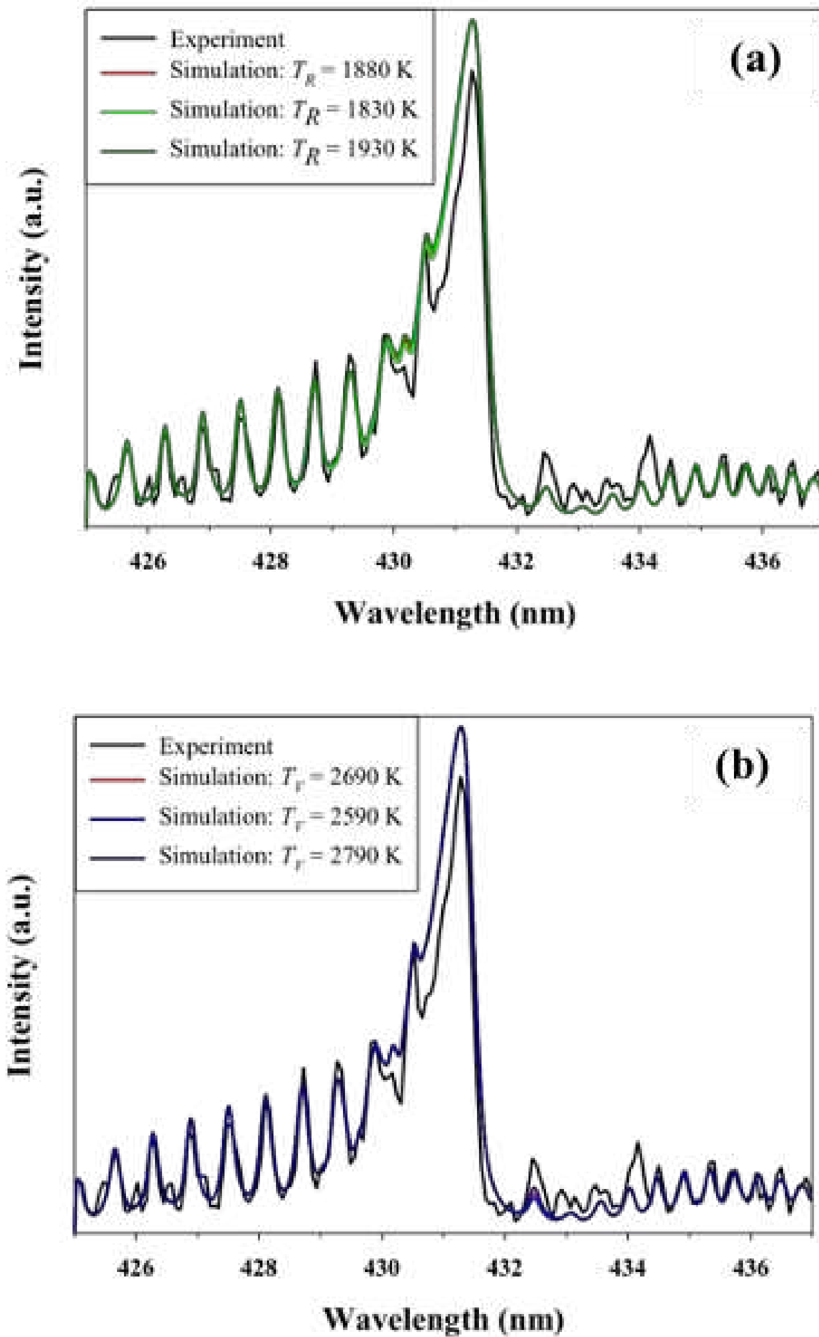

Figure 3.2. Emission spectra and reported simulated data of the CH $A^2\Delta \rightarrow X^2\Pi$ band for a 100% CH_4 plasma system at p = 200 mTorr, P = 75 W; additional simulations to demonstrate sensitivity of change in (a) $T_R \pm 50$ K and (b) $T_V \pm 100$ K.

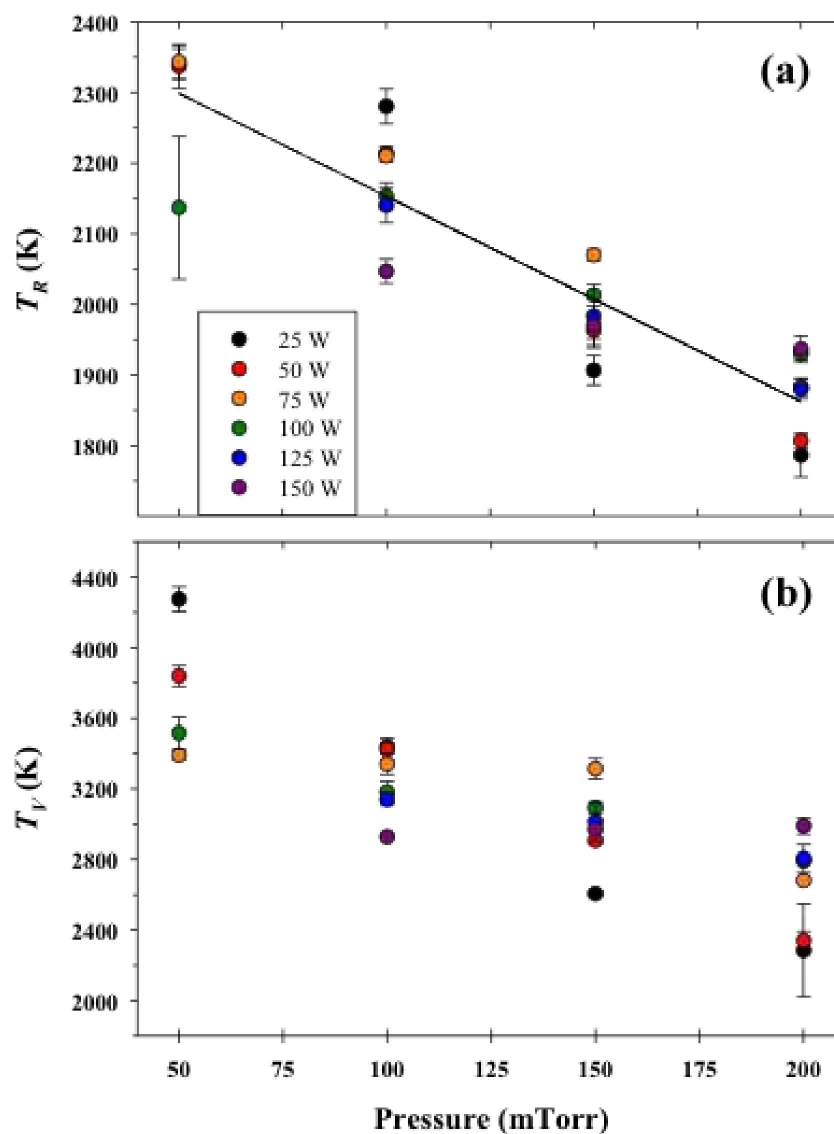

Figure 3.3. (a) CH $A^2\Delta$ T_R and (b) CH $A^2\Delta$ T_V as a function of pressure over a range of applied rf powers in a 100% CH_4 plasma system. The dependence of T_R(CH) on p was fit using a global linear regression ($R^2 = 0.84$).

Table 3.1. T_R, T_V values for CH in a 100% CH_4 plasma system.[a]

Pressure (mTorr)	Applied rf Power (W)	T_R (K)	T_V (K)
50	25	2340 (20)	4270 (70)
	50	2340 (30)	3840 (60)
	75	2340 (20)	3390 (20)
	100	2140 (100)	3520 (90)
	125	-	-
	150	-	-
100	25	2280 (20)	3440 (20)
	50	2210 (10)	3420 (60)
	75	2210 (10)	3340 (60)
	100	2150 (20)	3180 (60)
	125	2240 (20)	3140 (40)
	150	2050 (20)	2930 (10)
150	25	1910 (20)	2610 (10)
	50	1960 (10)	2910 (20)
	75	2070 (10)	3310 (60)
	100	2010 (10)	3090 (30)
	125	1980 (40)	3010 (110)
	150	1970 (30)	2970 (20)
200	25	1790 (30)	2280 (260)
	50	1810 (10)	2340 (10)
	75	1880 (10)	2680 (10)
	100	1930 (10)	2790 (10)
	125	1880 (10)	2810 (80)
	150	1940 (20)	2990 (50)

[a]Values in parentheses represent one standard deviation for the measurement.

T_V(CH) values. Notably, under all conditions T_V values are higher than T_R values, ranging from ~2020 K to ~4340 K.

The impact of applied rf power on rotational and vibrational temperatures in a 100% CH_4 plasma system was also elucidated. Figure 3.4a shows T_R(CH) plotted as a function of *P* under a range of pressure conditions. At low *P*, the *p* dependence noted above is once again clear where lower pressures are concomitant with higher T_R(CH) values and higher pressures with lower T_R(CH) values. Notably, at $P = 25$ W, the range of T_R(CH) values is larger than any other *P* condition studied, ~1750 K to ~2360 K. An interesting trend emerges at $P = 150$ W, where T_R(CH) values essentially converge to a smaller range of ~1920 K to ~2070 K, approximately halfway between the two most extreme reported rotational temperatures over the studied parameter range. Similar results are noted for T_V(CH), Figure 3.4b. At $P = 25$ W, T_V(CH) values range from ~2020 K to ~4340 K whereas at $P = 150$ W, T_V values are ~2950 K, regardless of plasma system pressure.

Diluents are often used in plasma systems for a variety of reasons, including increasing non-reactive collisions and increased precursor dissociation. To determine the potential effects that diluents have on energy partitioning in our plasmas, Ar was added to the plasma in a 3:1 CH_4/Ar ratio. Notably, the experimental spectra differed more from the calculated spectra in this system. This could arise from the formation mechanism for CH in the methane plasma, namely dissociative excitation, which can lead to non-equilibrium population of rovibrational states.[17, 33] Figure 3.5 shows emission spectra of the CH $A^2\Delta \rightarrow X^2\Pi$ band for a CH_4 plasma with 0%, 10%, and 25% Ar added to the precursor mixture. Notably, adding 10% Ar only minimally changes the emission spectrum compared to the 100% CH_4 plasma. Yet, when the Ar fraction is increased to 25%, the emission spectrum of this band changes more dramatically. Specifically,

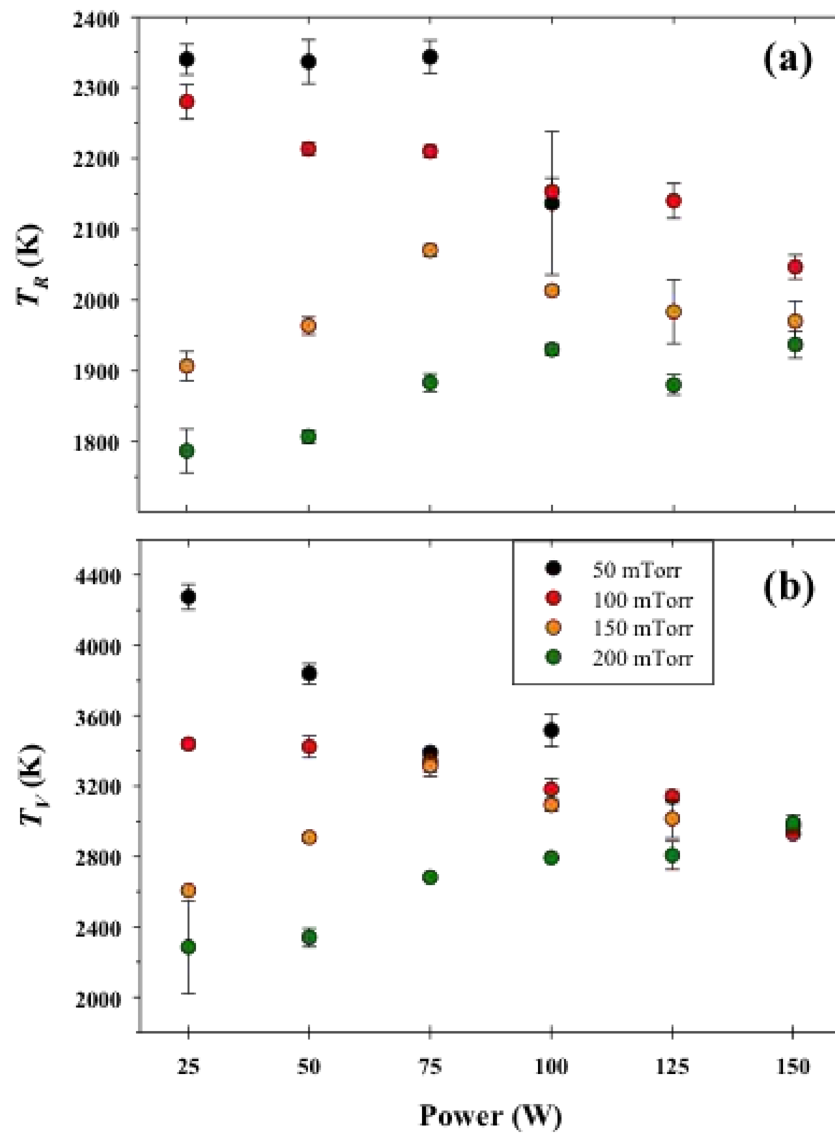

Figure 3.4. Measured CH $A^2\Delta$ internal temperatures (a) T_R and (b) T_V as a function of applied rf power over a range of pressures in a 100% CH_4 plasma.

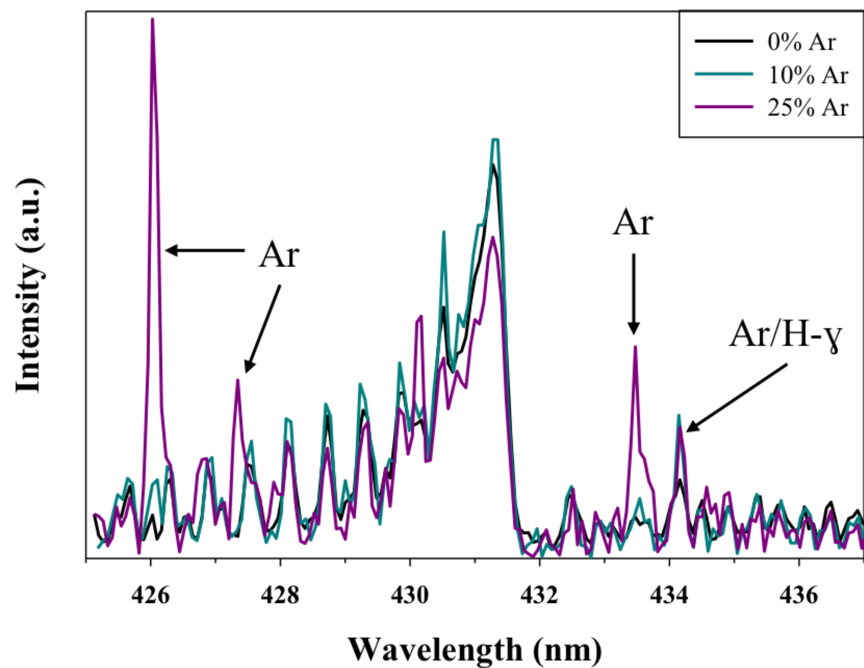

Figure 3.5. Emission spectra of the CH $A^2\Delta \rightarrow X^2\Pi$ band for a CH_4 plasma system at p = 200 mTorr, P = 75 W with varying amounts of Ar added to the precursor mixture.

Ar peaks overlap with the CH $A^2\Delta \rightarrow X^2\Pi$ band, also helping to explain the lower peak correlations when fitting these spectra.

Figure 3.6 demonstrates the impact of *P* on T_R(CH) and T_V(CH). T_R(CH) values, with specific determined values listed in Table 3.2, range from ~1700 K to ~2150 K and as demonstrated in Figure 3.6a, generally decrease as *P* increases. Under the same plasma pressure and power conditions, calculated T_V(CH) values for the mixed gas system, Table 3.2, are similar to those in the 100% CH_4 plasma system (~2050 K to ~3550 K). Unlike the 100% CH_4 plasma system, however, a different trend for the mixed gas plasma system is noted here. Figure 3.6b, demonstrates that T_V(CH) decreases linearly ($R^2 \geq 0.91$) with an increase in *P* for each studied pressure condition. A pressure dependence is also noted for vibrational temperatures in the 3:1 CH_4/Ar plasma system where higher pressures correspond to higher T_V(CH) values.

Figure 3.7 provides details on the surface and bulk chemical composition of films deposited in CH_4 plasmas. XPS data reveal the surface composition consists mainly of elemental C (~88%) and O (~12%). A representative high-resolution C_{1s} XPS spectrum for films deposited in a 100% CH_4 plasma, Figure 3.7a, displays three specific binding environments: -C-C/-C-H (285.0 eV), -C-O-C/-C-O-H (286.6 eV), and -C=O (288.7 eV) bonds with relative component percentages of 84.8 ± 3.3 %, 11.8 ± 2.8 %, and 3.4 ± 0.6 %, respectively. Notably, no appreciable differences in the high resolution C_{1s} spectra are observed between films deposited under plasma parameter conditions of varying *p* and *P*. FTIR data, Figure 3.7b, also indicate no change in chemical functionality for films deposited under different conditions. C=O and C-O stretches are noted at ~1025 cm^{-1} and ~1630 cm^{-1}, respectively. Absorption peaks attributed to C-H bending are seen in the range of 1350 – 1460 cm^{-1} and a prominent peak centered at 2923 cm^{-1} is indicative of C-H stretching. Additionally, the broad peak centered at 3442 cm^{-1} can be

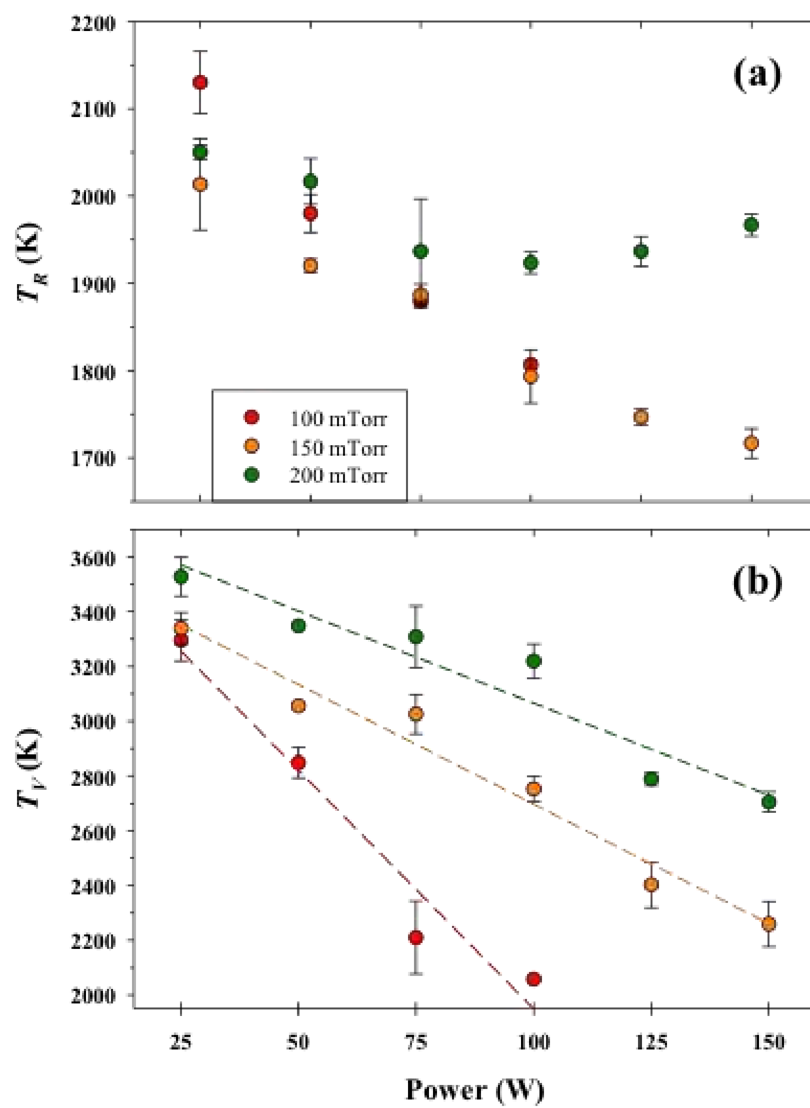

Figure 3.6. CH $A^2\Delta$ (a) T_R and (b) T_V as a function of applied rf power over a range of pressures in a 3:1 CH_4/Ar plasma. The dependence of T_V(CH) on P was fit using global linear regressions.

Table 3.2. T_R, T_V values for CH in a 3:1 CH_4/Ar plasma system.[a]

Pressure (mTorr)	Applied rf Power (W)	T_R (K)	T_V (K)
100	25	2130 (40)	3300 (80)
	50	1980 (20)	2850 (60)
	75	1880 (10)	2210 (130)
	100	1810 (10)	2060 (10)
	125	-	-
	150	-	-
150	25	2010 (50)	3340 (60)
	50	1920 (10)	3060 (10)
	75	1890 (10)	3030 (70)
	100	1790 (30)	2750 (50)
	125	1750 (10)	2400 (80)
	150	1720 (20)	2260 (80)
200	25	2050 (10)	3530 (70)
	50	2020 (30)	3350 (10)
	75	1940 (60)	3310 (110)
	100	1920 (10)	3220 (60)
	125	1940 (20)	2790 (20)
	150	1970 (10)	2700 (40)

[a]Values in parentheses represent one standard deviation for the measurement.

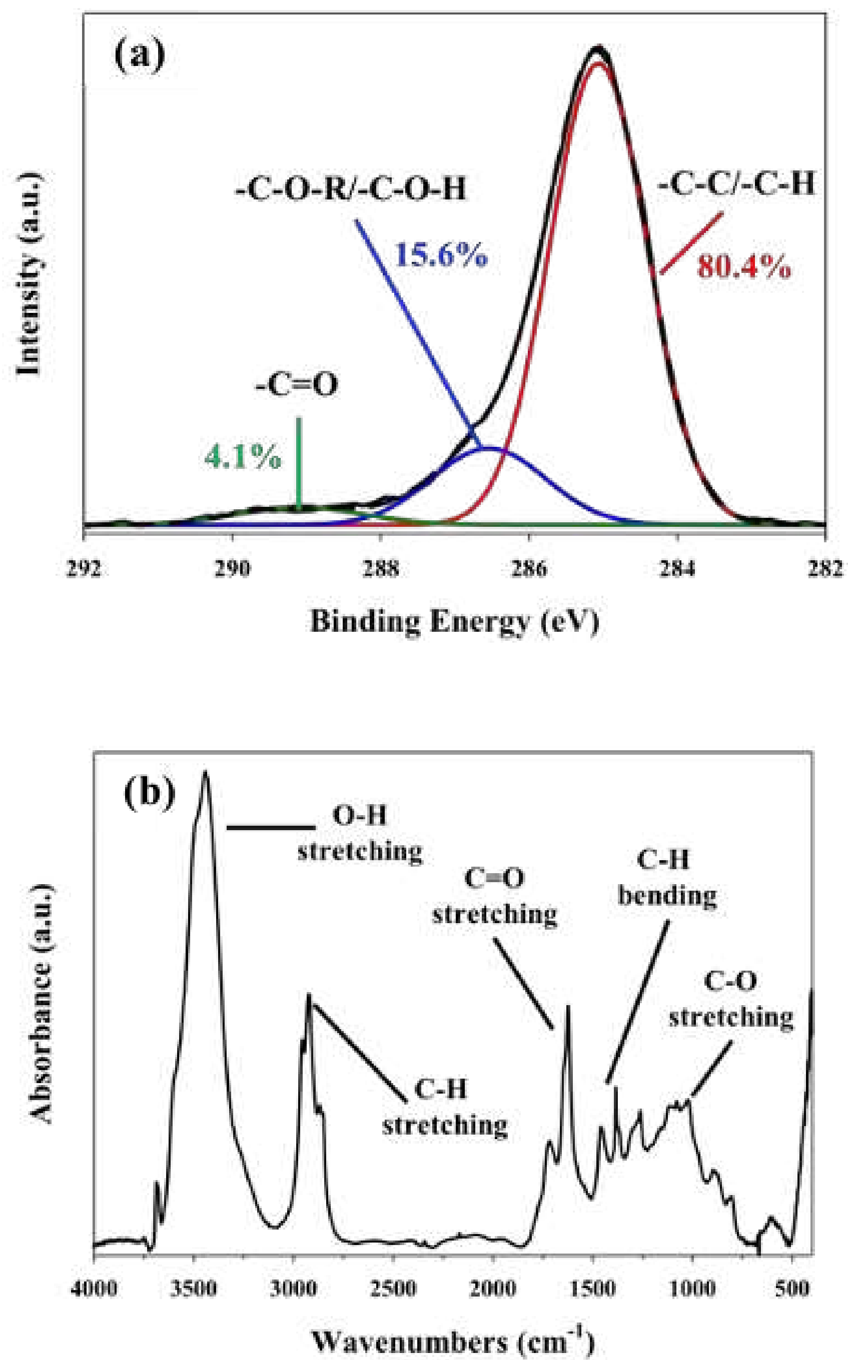

Figure 3.7. Representative (a) high-resolution C_{1s} XPS spectrum and (b) FTIR spectrum for HC film deposited by a 100% CH_4 plasma.

attributed to O-H stretching.

Optical profilometry data, Figure 3.8, display representative morphologies of HC films across designated plasma parameters. Clearly, distinct differences in HC film morphology arise between films deposited at a lower power of P = 25 W and those deposited at higher applied rf power. Differences between films deposited at P = 50 W and P = 100 W are also apparent, but subtle. For example, the morphology matrix also demonstrates that an increase in P corresponds to a general increase in the length of the cracks in the films.

Plasma system pressure also affects film morphology. As p is increased from 100 mTorr to 200 mTorr, an increase in the number of cracks in the film is generally observed, as illustrated in Figure 3.8 by films deposited at P = 25 W (Figures 3.8a, d, and g). Figure 3.8a displays an overall smooth film with several small indents whereas Figure 3.8g shows many small cracks extending across the image. At an intermediate p condition (p = 150 mTorr), Figure 3.8d, "island-like" formations of film cracking are observed. The insets in Figure 3.8 display representative WCA images and average WCA values for HC films deposited in a 100% CH_4 plasma under the specified parameter conditions. Overall, there are no appreciable differences in the measured WCA values for these films. Yet, these values tend to decrease as P increases. This is especially apparent for films deposited at the lowest applied rf power studied (P = 25 W) where WCA values are slightly higher, ~78° to ~90°, than those deposited at higher P (P = 50 W, 100 W), ~69° to ~76°. All of these values are significantly higher than the WCA value of a clean glass slide prior to CH_4 plasma exposure is ~10°, further demonstrating that a film is deposited. As one additional characterization of our deposited films, optical profilometry was performed on a few samples specifically to determine film thickness and roughness features. The thickness on these select samples ranged from ~150 – 350 nm, with roughness values ~30 –

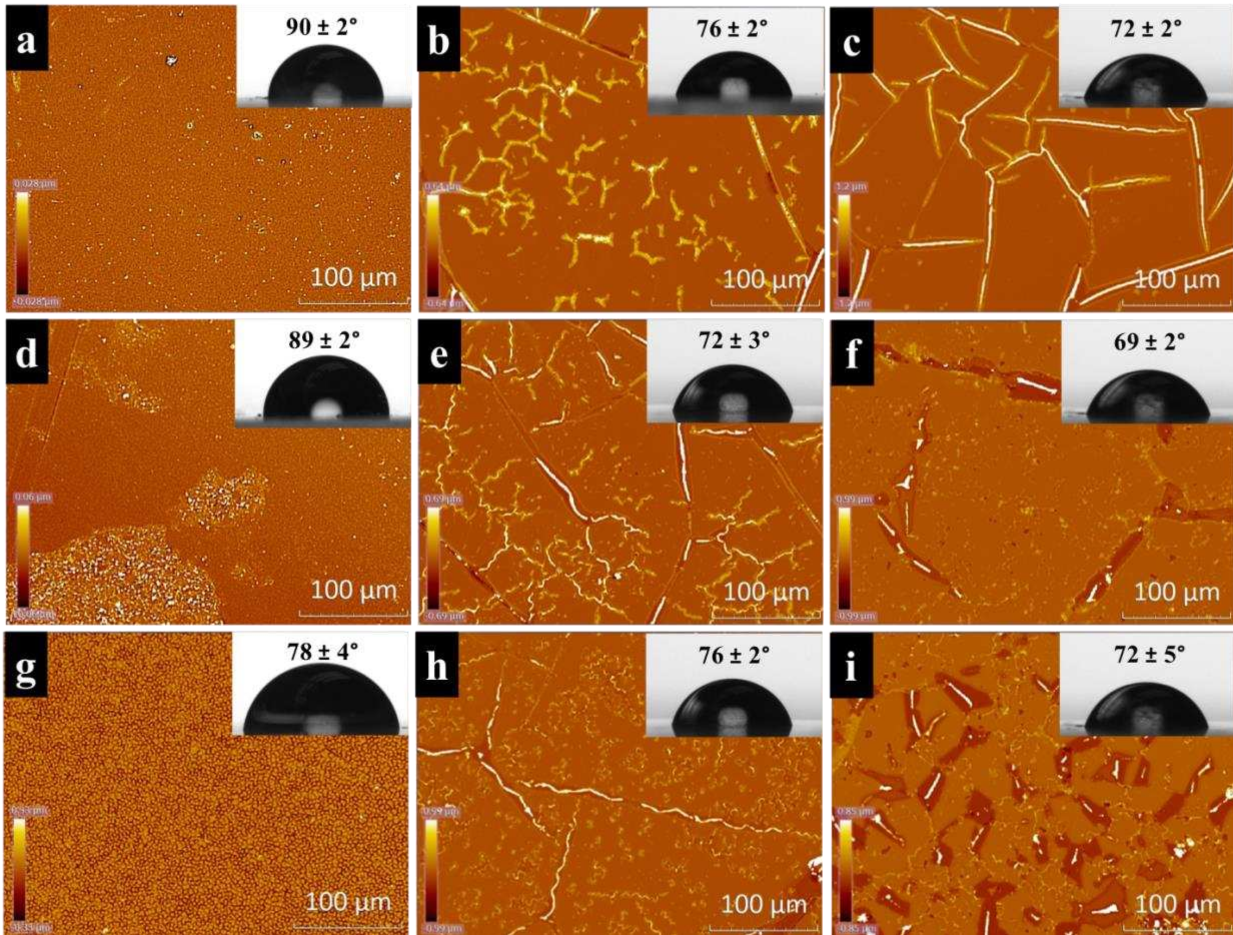

Figure 3.8. Optical profilometry images and static WCA data for HC films deposited at 100 mTorr as a function of applied rf power: (a) 25 W, (b) 50 W, and (c) 100 W; and at 150 mTorr as a function of applied rf power: (d) 25 W, (e) 50 W, and (f) 100 W; and at 200 mTorr as a function of rf power: (g) 25 W, (h) 50 W, and (i) 100 W.

150 nm, depending on conditions. These features were relatively uniform across the entire surface of a 3×3 cm substrate.

3.3 Discussion

As noted in the introduction, knowledge of key plasma processes as well as correlations between gas-phase data and resulting film properties for materials deposited via plasma enhanced chemical vapor deposition (PECVD) are important components towards elucidating a complete plasma chemistry profile. Specifically, energy partitioning trends can provide insight concerning the distribution of the upper state and potentially, may provide control over film deposition processes and chemistry.[19, 34-35] Here, trends in T_R(CH) and T_V(CH) have been investigated in CH_4 and CH_4/Ar plasma systems and potential links between these values and the properties of films deposited via PECVD in 100% CH_4 systems have been assessed.

Focusing first on the T_R and T_V data for the first excited state of CH (i.e. CH $A^2\Delta$), presented in Tables 3.1 – 3.2, we note a few interesting trends. T_R(CH) values reported herein range from ~1750 K to ~2360 K, significantly lower than the concomitant T_V(CH) values, and illustrate clear trends with respect to both system p and P. It is instructive to compare these trends with previously published data, both from our labs and from others. Similar relationships between T_R and T_V were observed by Avtaeva and Lapochkina who examined multiple molecules in rf capacitive methane discharges.[17] They found T_R(CH) < T_V(CH), similar to the results found here, but also noted that T_R(CH) decreased with increasing p whereas T_V(CH) increased. In addition, previously reported T_R values for ground state CH, acquired using laser-induced fluorescence (LIF) in our laboratory, indicated no clear trends in T_R with respect to either p or P.[36] In this previous work, T_R(CH) = ~1500 K in 100% CH_4 plasmas, significantly

lower than the T_R values reported herein for excited CH radicals. This suggests energy transfer in the ground state is fast enough to achieve some level of thermalization, relative to energy transfer in excited state species. Rotational temperatures were, however, only reported for two pressures, 50 mTorr and 110 mTorr. Indeed, the excited state T_R(CH) data reported herein (Figure 3.3a) show that at these lower pressures (p = 50 and 100 mTorr), the reported T_R(CH) values are the same within experimental error. An extension of the parameter space to p = 200 mTorr in the present work, however, reveals the expected negative dependence of T_R(CH) on p, wherein higher pressures result in lower T_R(CH). It should also be noted that ground state T_R(CH) measurements from Zhou et al. were determined from an effectively collision-free molecular beam downstream from the ignition of the plasma,[36] whereas those reported herein essentially probe the bulk of the plasma, including the coil region.

Generally, rotational relaxation can be achieved relatively quickly, typically in <10 collisions;[37] hence, T_R typically decreases as the number of collisions increase. This is exemplified in Figure 3.3a, where the increase in p from 50 mTorr to 200 mTorr concomitantly results in a decrease in T_R(CH). Ar addition to the plasma increases the probability of thermalizing conditions.[38-39] Figure 3.6 demonstrates this concept wherein the addition of Ar to the gas feed (3:1 CH_4/Ar) effectively reduces T_R(CH) values relative to the 100% CH_4 plasma system. This effect is especially notable at lower p, where there is a larger discrepancy in T_R(CH) values between the two plasma systems. As p increases from p = 100 mTorr to p = 200 mTorr, the gap between T_R(CH) values also decreases. In general, at p = 200 mTorr the values in the two systems essentially converge and are virtually the same, indicating that at p = 200 mTorr CH $A^2\Delta$ radicals are rotationally relaxed in our systems. Notably, the first excited state of CH has a lifetime of 5 x 10^{-7} s.[17] Thus, under the conditions in our plasma system, the preferred

depopulation rate is likely via emission rather than through thermalizing collisions. Additionally, as evidenced by the smaller slope for the 3:1 CH_4/Ar plasma system in Figure 3.6, the addition of Ar appears to mitigate the effect of *p* on T_R(CH), indicating that Ar indeed promotes thermalization of rotational energy in these systems.[19] Similar relationships have been observed for other radicals in a variety of plasma systems.[19, 35, 40]

Previous studies in our laboratory have demonstrated the effects of *P* on T_R and T_V on other plasma species such as NO, N_2 and CF.[19, 34-35] In these studies, T_V generally increases with increasing *P*. Interestingly, in the current work, the dependence of T_V(CH) on *P* changes as the system pressure increases. At lower *p*, the dependence appears to mimic that for T_R(CH), Figure 3.4b, decreasing as *P* increases. In contrast, at higher *p*, T_V(CH) increases with *P* up to *P* = 75-100 W, leveling out and decreasing slightly at higher *P*. Although these trends are perhaps counter intuitive, power and pressure are two plasma parameters that are intimately connected. As such, changes in one of these parameters could produce changes in the other parameter. In particular, at higher *P*, we are likely increasing the overall system pressure via formation of additional molecules in the system via additional decomposition of plasma gases. As it is difficult to achieve an accurate pressure reading when the plasma is on, this effect may not be reflected in our reported pressure values. Perusing the literature for comparable systems, we find little to directly compare with respect to the exact pressure-power parameter space used here. For comparison in a much higher pressure regime, Moon *et al.* examined the parameter dependence of the internal temperatures of both CH and CN in atmospheric discharges.[32] In these systems, they found T_V(CH) nominally increased with increasing power, but was relatively sensitive to other plasma parameters. In previous work in our laboratory,[41] we found that CH_4-containing plasmas can often be characterized by two modes. In particular, the shift from a

capacitive-coupled electrostatic pre-discharge mode (low *P*) and an inductively-coupled electromagnetic main discharge (higher *P*) occurs at ~75 W. Thus, the trend in T_V(CH) dependence on *P* may be related to this shift in plasma mode. Another explanation that could also contribute to the observed *P* dependence relies on the observation that the rovibrational states of CH $A^2\Delta$ radicals may be populated with a non-equilibrium distribution, as they are formed via a dissociative excitation process.[42] Du *et al.* noted a similar situation occurs for OH formed in H_2O based discharges and that an understanding of the mechanism(s) for formation of a particular species is critical to understanding molecular temperatures in a plasma. Similarly, Berthelot and Bogaerts,[43] examined CO_2 decomposition via computational models and concluded that vibrational excitation can dramatically impact the dissociation process. Unfortunately, this is one of the largest sources of error that contribute to less reliable plasma models. Notably, one of Berthelot and Bogaerts' recommendations is to measure kinetic rates, species densities, and temperature data as a function of plasma conditions, such as was performed here, as these data are a result of the plasma chemistry and are heavily coupled to the plasma chemistry model.

Additional insight into film deposition processes and morphological changes can be gained through consideration of internal plasma temperatures and surface reactivities. Notably, dissociation in CH_4 plasmas occurs rapidly and fairly completely, leading to an array of product species, including CH_x, H, H_2 and C_2.[28, 44] Although formation of CH has been correlated directly with the decomposition of CH_4,[29] interpretation of our energy partitioning results, must also consider the relevant amount of the discharge power that may be converted into rotational and vibrational excitation of species other than CH $A^2\Delta$. For example, hydrogen species play an important role in the production of amorphous hydrocarbon films deposited via PECVD

processes.[28, 44-46] Although not all of these examples are directly comparable, as the mechanism for plasma production is different and the operating pressures may also be different, it is still instructive to note some of the most relevant results. Avtaeva and Lapochkina examined formation of excited state H_2 and CH in rf capacitive methane plasmas. They attributed these disparate values to the differences in the molecules' excited state lifetimes and to their relative concentrations in their plasmas.[17] Likewise, Heintze *et al.* studied methane dissociation and formation of C_2 in methane pulsed microwave plasmas.[29] They found hydrogen to be an important component of methane plasma chemistry and reported T_R of both ground and excited state C_2 and H_2.[29] In particular, addition of H_2 to the methane plasma resulted in higher CH_4 conversion at a lower energy per molecule, especially under low power conditions. Notably, the rotational temperature of C_2 d $^3\Pi_g$ was considerably lower than that of either the lower electronic state of C_2 $a^3\Pi_u$ or either of the H_2 states (d $^3\Pi^-_u$ or X $^1\Sigma^+_g$). The observation that three of these four states were the same within experimental error led the authors to conclude that the gas temperature corresponded to these temperatures, nominally 1500 – 2500 K. This suggests that a similar amount of the energy being supplied to our plasmas is being partitioned into rotational and vibrational modes of a number of methane decomposition products. These results will inform our future studies, which are focused on measuring internal temperatures for C_2 and H_2 within methane and other hydrocarbon-based plasma.

As an additional consideration, we examine CH surface interactions in relation to the current results. Previous imaging of radicals interacting with surfaces (IRIS) studies for CH_4 and CH_4/Ar plasma systems reveal that the surface reactivity of CH is near unity and independent of all experimental variables studied.[36] The high CH rotational and vibrational temperature data presented herein indicate significant internal excitation of CH radicals. It is possible that this

helps promote surface reactions that lead to film formation.[47] This idea was further explored in a previously published work, wherein gas-phase energetics of several diatomic plasma species in a range of plasma systems were investigated.[40] Perhaps more importantly, the gas-phase energetics were linked to surface reaction probabilities, or surface reactivity (R). In that study, radical species with high surface reactivity values ($R > 0.8$) also had relatively high T_R, T_V, and translational temperature (T_T) values. Moreover, the reactivity of these species (CH, CN, and SiH) also appeared to be independent of plasma parameters. In contrast, species such as OH, NH, and NH_2 had moderate to low R values (depending on plasma parameters) with low T_R and T_T values. Notably, the molecules with high surface reactivity were formed in film deposition systems, whereas those with moderate reactivity were formed in systems with little to no film formation, but rather the overarching plasma process was either etching or surface modification (functional group implantation).

Such observed correlations suggest connections between gas-phase energetics and film deposition characteristics. For example, we have previously observed a correlation between vibrationally hot CF in excited electronic states and the amount of surface scatter measured for ground state CF.[35] Here, our film composition data, Figure 3.7, confirm a uniform chemical composition throughout the surface and bulk of the material, typical of previous studies of films deposited from methane-based plasmas.[25-26, 45, 48-49] Notably, film composition remains relatively uniform, regardless of system p or P. In contrast, WCA values decrease with increasing P, a phenomenon likely attributable to the observed morphological changes seen in the optical profilometry images. More importantly, the relatively high T_R and T_V values measured here for excited CH radicals along with the previously measured high surface reaction probabilities for ground state CH,[36] suggest that CH radicals play an important role in film formation processes.

Similar to what we observed with CF radicals, the higher internal energies of excited state CH may have a significant influence on the properties of the deposited films.

3.4 Summary

Energy partitioning for excited state CH radicals in CH_4 and CH_4/Ar plasmas were explored along with film formation and characterization studies. In general, T_V(CH) is higher than T_R(CH), regardless of gas mixture, system pressure or applied rf power, and T_R decreases with increasing pressure and upon addition of Ar to the system. Both T_R(CH) and T_V(CH) values are significantly above room temperature, suggesting that formation of excited state CH in the plasma happens in a non-equilibrium manner. Film characterization studies indicate that the resulting film composition does not change appreciably with plasma parameters; however, morphological changes are apparent over the studied parameter range. Ultimately, these observations provide insight towards the complexity inherent to plasma-surface interactions and fundamental energy partitioning investigations that are key to increasing the utility of PAC.

REFERENCES

1. Mannucci, P. M.; Franchini, M., Health Effects of Ambient Air Pollution in Devloping Countries. *Int. J. Environ. Res. Public Health* **2017,** *14*, 1048-1055.
2. Thévenet, F.; Sivachandiran, L.; Guaitella, O.; Barakat, C.; Rousseau, A., Plasma–Catalyst Coupling for Volatile Organic Compound Removal and Indoor Air Treatment: A Review. *J. Phys. D: Appl. Phys.* **2014,** *47* (22), 224011.
3. Chen, H. L.; Lee, H. M.; Chen, S. H.; Chang, M. B.; Yu, S. J.; Li, S. N., Removal of Volatile Organic Compounds by Single-Stage and Two-Stage Plasma Catalysis Systems: A Review of the Performance Enhancement Mechanisms, Current Status, and Suitable Applications. *Environ. Sci. Technol.* **2009,** *43* (7), 2216-2227.
4. Sarigiannis, D. A.; Karakitsios, S. P.; Gotti, A.; Liakos, I. L.; Katsoyiannis, A., Exposure to Major Volatile Organic Compounds and Carbonyls in European Indoor Environments and Associated Health Risk. *Environ. Intern.* **2011,** *37* (4), 743-765.
5. Zhang, H.; Li, H.; Zhang, Q.; Zhang, Y.; Zhang, W.; Wang, X.; Bi, F.; Chai, F.; Gao, J.; Meng, L., Atmospheric Volatile Organic Compounds in a Typical Urban Area of Beijing: Pollution Characterization, Health Risk Assessment and Source Apportionment. *Atmosphere* **2017,** *8* (3), 61.
6. Jiang, N.; Hu, J.; Li, J.; Shang, K.; Lu, N.; Wu, Y., Plasma-Catalytic Degradation of Benzene over Ag–Ce Bimetallic Oxide Catalysts Using Hybrid Surface/Packed-Bed Discharge Plasmas. *Appl. Catal., B* **2016,** *184*, 355-363.
7. Kim, J.; Go, D. B.; Hicks, J. C., Synergistic Effects of Plasma–Catalyst Interactions for CH_4 Activation. *Phys. Chem. Chem. Phys.* **2017,** *19* (20), 13010-13021.
8. Schiavon, M.; Torretta, V.; Casazza, A.; Ragazzi, M., Non-Thermal Plasma as an Innovative Option for the Abatement of Volatile Organic Compounds: A Review. *Water Air Soil Pollut.* **2017,** *228*, 388.
9. Feng, X.; Liu, H.; He, C.; Shen, Z.; Wang, T., Synergistic Effects and Mechanism of a Non-Thermal Plasma Catalysis System in Volatile Organic Compound Removal: A Review. *Catal Sci Technol.* **2018**.
10. Schmidt-Szałowski, K.; Krawczyk, K.; Sentek, J.; Ulejczyk, B.; Górska, A.; Młotek, M., Hybrid Plasma-Catalytic Systems for Converting Substances of High Stability, Greenhouse Gases and VOC. *Chem. Eng. Res. Des.* **2011,** *89* (12), 2643-2651.
11. Jiang, N.; Qiu, C.; Guo, L.; Shang, K.; Lu, N.; Li, J.; Wu, Y., Post Plasma-Catalysis of Low Concentration VOC over Alumina-Supported Silver Catalysts in a Surface/Packed-Bed Hybrid Discharge Reactor. *Water, Air, Soil Pollut.* **2017,** *228* (3), 113.
12. Michielsen, I.; Uytdenhouwen, Y.; Pype, J.; Michielsen, B.; Mertens, J.; Reniers, F.; Meynen, V.; Bogaerts, A., CO_2 Dissociation in a Packed Bed Dbd Reactor: First Steps Towards a Better Understanding of Plasma Catalysis. *Chem. Eng. J.* **2017,** *326*, 477-488.
13. Veerapandian, S. K.; Leys, C.; De Geyter, N.; Morent, R., Abatement of VOCs Using Packed Bed Non-Thermal Plasma Reactors: A Review. *Catalysts* **2017,** *7* (4), 113.
14. Adamovich, I.; Baalrud, S. D.; Bogaerts, A.; Bruggeman, P.; Cappelli, M.; Colombo, V.; Czarnetzki, U.; Ebert, U.; Eden, J.; Favia, P., The 2017 Plasma Roadmap: Low Temperature Plasma Science and Technology. *J. Phys. D: Appl. Phys.* **2017,** *50* (32), 323001.
15. Kim, H.-H.; Teramoto, Y.; Negishi, N.; Ogata, A., A Multidisciplinary Approach to Understand the Interactions of Nonthermal Plasma and Catalyst: A Review. *Catal. Today* **2015,** *256*, 13-22.

16. Biberman, L. M.; Vorob′ev, V. S.; Iakubov, I., Kinetics of Nonequilibrium Low-Temperature Plasma. *Moscow Izdatel Nauka* **1982**.
17. Avtaeva, S.; Lapochkina, T., Characteristics of Molecular Hydrogen and CH* Radicals in a Methane Plasma in a Magnetically Enhanced Capacitive RF Discharge. *Plasma Phys. Rep.* **2007,** *33* (9), 774-785.
18. Britun, N.; Gaillard, M.; Ricard, A.; Kim, Y.; Kim, K.; Han, J., Determination of the Vibrational, Rotational and Electron Temperatures in N_2 and Ar–N_2 RF Discharge. *J. Phys. D: Appl. Phys.* **2007,** *40* (4), 1022.
19. Blechle, J. M.; Hanna, A. R.; Fisher, E. R., Determination of Internal Temperatures within Nitric Oxide Inductively-Coupled Plasmas. *Plasma Process. Polym.* **2017,** *14*, e1700041.
20. Liu, W.-Y.; Xu, Y.; Liu, Y.-X.; Peng, F.; Gong, F.-P.; Li, X.-S.; Zhu, A.-M.; Wang, Y.-N., Absolute CF_2 Density and Gas Temperature Measurements by Absorption Spectroscopy in Dual-Frequency Capacitively Coupled CF_4/Ar Plasmas. *Phys. Plasmas* **2014,** *21* (10), 103501.
21. Davis, G. P.; Gottscho, R. A., Measurement of Spatially Resolved Gas-Phase Plasma Temperatures by Optical Emission and Laser-Induced Fluorescence Spectroscopy. *J. Appl. Phys.* **1983,** *54* (6), 3080-3086.
22. Zhang, Q. Y.; Shi, D. Q.; Xu, W.; Miao, C. Y.; Ma, C. Y.; Ren, C. S.; Zhang, C.; Yi, Z., Determination of Vibrational and Rotational Temperatures in Highly Constricted Nitrogen Plasmas by Fitting the Second Positive System of N_2 Molecules. *AIP Advances* **2015,** *5* (5), 057158.
23. Tonnis, E. J.; Graves, D. B., Neutral Gas Temperatures Measured within a High-Density, Inductively Coupled Plasma Abatement Device. *J. Vac. Sci. Technol. A* **2002,** *20* (5), 1787-1795.
24. Biloiu, C.; Sun, X.; Harvey, Z.; Scime, E., Determination of Rotational and Vibrational Temperatures of a Nitrogen Helicon Plasma. *Rev. Sci. Instrum.* **2006,** *77* (10), 10F117.
25. Chakrabarti, K.; Kim, J. B.; Wilson, J. I. B.; Lee, C., Effects of Ar Gas Dilution in Methane Plasma on the Properties of Diamond-Like Carbon Films. *Phys. Stat. Sol.* **2002,** *194* (1), 112-117.
26. Furlan, K. P.; Klein, A. N.; Hotza, D., Diamond-Like Carbon Films Deposited by Hydrocarbon Plasma Sources. *Rev. Adv. Mater. Sci.* **2013,** (34), 165-172.
27. Kimura, T.; Kamata, H., Preparation of Diamond-Like Carbon Films Using Reactive Ar/CH_4 High Power Impulse Magnetron Sputtering System with Negative Pulse Voltage Source for Substrate. *Jpn. J. Appl. Phys.* **2016,** *55*.
28. Truscott, B. S.; Kelly, M. W.; Potter, K. J.; Ashfold, M. N.; Mankelevich, Y. A., Microwave Plasma-Activated Chemical Vapor Deposition of Nitrogen-Doped Diamond. II: CH_4/N_2/H_2 Plasmas. *J. Phys. Chem. A* **2016,** *120* (43), 8537-8549.
29. Heintze, M.; Magureanu, M.; Kettlitz, M., Mechanism of C_2 Hydrocarbon Formation from Methane in a Pulsed Microwave Plasma. *J. Appl. Phys.* **2002,** *92* (12), 7022-7031.
30. Jonsson, M.; Borggren, J.; Alden, M.; Bood, J., Time-Resolved Spectroscopic Study of Photofragment Fluorescence in Methane/Air Mixtures And Its Diagnostic Implications. *Appl. Phys. B* **2015,** *120*, 587-599.
31. Kobayashi, H.; Kado, S.; Xiao, B.; Tanaka, S., Measurement of Rotational Populations of CH Radicals in Low-Temperature Plasmas. *Jpn. J. Appl. Phys.* **2003,** *42* (4R), 1776.
32. Moon, S. Y.; Kim, D.; Gweon, B.; Choe, W., Spectroscopic Characterization of Rovibrational Temperatures in Atmospheric Pressure He/CH_4 Plasmas. *Phys. Plasmas* **2008,** *15* (10), 103504.

33. Fantz, U., Emission Spectroscopy of Molecular Low Pressure Plasmas. *Contrib Plasm Phys.* **2004,** *44* (5-6), 508-515.
34. Hanna, A. R.; Blechle, J. M.; Fisher, E. R., Using Fundamental Spectroscopy to Elucidate Kinetic and Energetic Mechanisms within Environmentally Relevant Inductively Coupled Plasma Systems. *J. Phys. Chem. A* **2017,** *121*, 727-7640.
35. Hanna, A. R.; Cuddy, M. F.; Fisher, E. R., Energy Partitioning and Its Influence on Surface Scatter Coefficients within Fluorinated Inductively Coupled Plasmas. *J. Vac. Sci. Technol. A* **2017,** *35*, 05C308.
36. Zhou, J.; Fisher, E. R., Surface Reactivity and Energetics of CH Radicals During Plasma Deposition of Hydrogenated Diamondlike Carbon Films. *J. Phys. Chem. B* **2006,** *110*, 21911-21919.
37. Brown, M. S.; Forlines, R. A.; Ganguly, B. N., Measurement of CH Density in a Pulsed-DC Hydrocarbon-Gas-Mixture Discharge. *J. Appl. Phys.* **2005,** *97* (10), 103302.
38. Cheng, P.; Koyanagi, G. K.; Bohme, D. K., Heavy Water Reactions with Atomic Transition-Metal and Main-Group Cations: Gas Phase Room-Temperature Kinetics and Periodicities in Reactivity. *J. Phys. Chem. A* **2007,** *111* (35), 8561-8573.
39. Beckers, J.; van der Horst, R. M.; Osorio, E. A.; Kroesen, G. M. W.; Banine, V. Y., Thermalization of Electrons in Decaying Extreme Ultraviolet Photons Induced Low Pressure Argon Plasma. *Plasma Sources Sci. Technol.* **2016,** *25*, 035010 (8pp).
40. Stillahn, J. M.; Fisher, E. R., Gas Phase Energetics of CN Radicals in Radio Frequency Discharges: Influence on Surface Reaction Probability During Deposition of Carbon Nitride Films. *J. Phys. Chem. A* **2010,** *114* (16), 5287-5294.
41. McCurdy, P. R.; Truitt, J. M.; Fisher, E. R., Pulsed and Continuous Wave Plasma Deposition of Amorphous, Hydrogenated Silicon Carbide from SiH_4/CH_4 Plasmas. *J. Vac. Sci. Technol. A* **1999,** *17*, 2475-2484.
42. Du, Y.; Nayak, G.; Oinuma, G.; Ding, Y.; Peng, Z.; Bruggeman, P. J., Emission Considering Self-Absorption of OH to Simultaneously Obtain the OH Density and Gas Temperature: Validatiaon, Non-Equilibrium Effects and Limitations. *Plasma Sources Sci. Technol.* **2017,** *26*, 095007 (11 pp).
43. Berthelot, A.; Bogaerts, A., Modeling of CO_2 Plasma: Effect of Uncertainties in the Plasma Chemistry. *Plasma Sources Sci. Technol.* **2017,** *26*, 115002 (18 pp).
44. Li, H.; Yang, K.; Liu, H.-X.; Zhu, X.-D., Optical and Mass Spectroscopic Properties of Microwave CH_4/H_2/Ar Plasma for Diamond Deposition in a Resonance Cavity. *Vacuum* **2018,** *147*, 45-50.
45. Ito, H.; Koshimura, K.; Onitsuka, S.; Okada, K.; Suzuki, T.; Akasaka, H.; Saitoh, H., Dissociative Excitation of C_2H_2 in the Electron Cyclotron Resonance Plasma of Ar: Production of CH Radicals and Formation of Hydrogenated Amorphous Carbon Films. *Plasma Chem. Plasma Process.* **2012,** *32*, 231-248.
46. Pothiraja, R.; Engelhardt, M.; Bibinov, N.; Awakowicz, P., Film Deposition on the Inner Suface of Tubes Using Atmospheric Ppressure Ar-CH_4, Ar-C_2H_2 and Ar-C_2H_2-H_2 Plasmas: Interpretation of Film Properties from Plasma-Chemical Kinetics. *J. Phys. D: Appl. Phys.* **2012,** *45*, 335202-335213.
47. Juurlink, L.; Killelea, D.; Utz, A., State-Resolved Probes of Methane Dissociation Dynamics. *Prog. Surf. Sci.* **2009,** *84* (3-4), 69-134.

48. Capote, G.; Frerie, F. L. J., Production and Characterization of Hydrogenated Amorphour Carbon Thin Films Deposited in Methane Plasmas Diluted by Noble Gases. *Mater. Sci. Eng. B* **2004,** *112*, 101-105.
49. Jacobsohn, L. G.; Capote, G.; Cruz, N. C.; Zanatta, A. R.; Freire, F. L. J., Plasma Deposition of Amorphous Carbon Films from CH_4 Atmospheres Highly Diluted in Ar. *Thin Solid Films* **2002,** *419*, 46-53.

CHAPTER 4

GAS-PHASE DIAGNOSTIC STUDIES OF H_2 AND CH_4 INDUCTIVELY COUPLED PLASMAS

This chapter contains results published as a full paper under the same title in the *Journal of Vacuum Science and Technology A* written by Tara L. Van Surksum and Ellen R. Fisher and is reproduced with permission from *J. Vac. Sci. Technol., A* 2020, *38* (3), 033010 (Copyright 2020, American Vacuum Society). Optical emission spectroscopy (OES) is employed to elucidate energy partitioning information for H_2 $d^3\Pi_u \rightarrow a^3\Sigma_g^+$ and CH $A^2\Delta \rightarrow X^2\Pi$ within several plasma systems (H_2, CH_4, CH_4/H_2, H_2/Ar). Disparities in the rotational temperature trends of H_2 ($d^3\Pi_u$) between H_2 and CH_4 plasmas highlight the differences in H_2 excitation pathways occurring in each of these plasma systems. When energy partitioning trends are combined with additional information that can be obtained via OES (relative species densities, kinetics), mechanistic information can also be construed. This chapter focuses on illuminating mechanisms of H_2 formation and excitation pathways in different plasma systems using fundamental information obtained via OES. This work was supported by funding through the National Science Foundation (NSF CBET-1803067).

4.1 Introduction

Knowledge of fundamental gas-phase processes and gas-surface interactions are crucial to the advancement of numerous plasma technologies. Optical plasma diagnostics provide a non-intrusive platform for obtaining a molecular-level understanding of plasma chemistry via species identification and energy partitioning of gas phase species.[1-2] For example, an

understanding of how energy is partitioned into vibrational, rotational, and translational modes of a gas-phase molecule lends critical insight into formation mechanisms, decomposition pathways, and overall plasma chemistry. Figures of merit, such as vibrational (T_V) and rotational (T_R) temperatures, describe the energetics of molecular species within the system and are applicable to plasma modelling and estimates of gas temperature.[3-4] As such, reports on internal molecular plasma temperatures (e.g., T_V and T_R) are key to elucidating molecular-level processes that dictate overall plasma chemistry.

Nonthermal plasmas generally follow a relationship where T_V is greater than T_R and/or the translational temperature (T_T), yet each temperature is significantly lower than the electron temperature (T_e).[5-10] Interestingly, T_R values have been used as a metric to determine the gas temperature (T_g), with the assumption that T_R and T_T equilibrate with each other and thus, T_g, because of the relatively small energy separations between translational and rotational levels.[9-10] Yet, previous studies from our labs and others have demonstrated that significant differences can exist between T_R and T_T.[11-13] Bruggeman *et al.* stated that T_R equilibrates with T_T only when a nascent rotational distribution is a thermalized distribution or when rotational energy transfer occurs relatively quickly.[14] Moreover, different molecules in the same plasma system can exhibit vastly different T_R values.[4, 15-16] In addition, the same type of plasma species within a system may be formed via different mechanisms (e.g., direct-impact excitation, decomposition of the parent molecule, recombination, etc.). As a consequence of all of these potential issues, it is valuable to measure molecular plasma temperatures as a means to examine possible species formation pathways.

We have previously reported plasma temperatures for several plasma species (e.g., N_2, NO, CH) within environmentally relevant plasma systems.[6, 17-19] In one study, energy

partitioning trends of CH $A^2\Delta \rightarrow X^2\Pi$ in methane plasmas were reported as functions of plasma parameters.[18] Yet, optical emission studies have shown that methane plasma decomposition results in atomic and molecular hydrogen as well as carbon-containing products such as C_2 and CH;[18, 20-23] thus, we must also consider energy partitioned into these species as well. Avtaeva and Lapochkina determined that molecular hydrogen concentrations exceed CH concentrations in a methane-containing capacitive radio-frequency (rf) discharge.[3] In contrast, although Morrison *et al.* determined similar molecular hydrogen and CH concentrations in low-pressure CH_4 plasma systems, atomic hydrogen concentrations exceeded both of these by a few orders of magnitude.[24] These studies emphasize the hydrogen-rich plasma environment created during CH_4 dissociation. The dissociation of methane, which has applications in several plasma technologies including plasma-assisted catalysis for pollution remediation,[25-26] and the fabrication of carbon materials,[27-30] has been studied extensively.[25-27, 31-32] As such, the role of hydrogen in these systems has also been given considerable attention.[28, 33-34] Although these studies have provided significant insight into the roles of hydrogen species in CH_4 plasmas, the design and optimization of plasma systems for processing (i.e., plasma-assisted catalysis, materials fabrication) remains a challenge as fundamental properties of plasma species must be measured to accurately construe mechanistic phenomena and increase the utility of plasma technologies.

Information on molecular-level plasma processes are indispensable for understanding and optimizing plasma systems. Shivkumar *et al.* built a numerical model to analyze hydrogen plasmas in a microwave plasma enhanced chemical vapor deposition system and determine several plasma properties (electric field, electron number density, electron temperature, and the gas temperature).[35] Their results highlight the connections between these fundamental plasma

properties and plasma parameters, a key component to understanding and optimizing plasma conditions for the future development of a host of plasma technologies. Moreover, the gas temperature simulations obtained via modeling by Shivkumar *et al.* are in good agreement with $T_R(H_2)$ values determined experimentally via optical emission spectroscopy (OES).[35] For hydrogen discharges, rovibrational excitation of the H_2 molecule can have a significant impact on several molecular reaction rates;[36] thus, studies focused on determining and understanding rotational and vibrational energy partitioning of H_2 are of interest to the plasma community.

Numerous experimental studies have examined the rotational and vibrational populations of molecular hydrogen in plasmas.[37-44] Although plasmas produce rotationally excited H_2 molecules,[35-36, 39-40, 45] the influence of this excitation and the specific reactions involving rotationally excited H_2 are not well known. Consideration of rotational excitation is essential for a detailed understanding of plasmas comprising molecular hydrogen. For example, H^- ions in negative hydrogen ion sources are formed by dissociative attachment of electrons to hydrogen molecules.[46] The reaction rate for this process increases by five orders of magnitude if the H_2 molecule is vibrationally excited to a state with the vibrational quantum number $\nu = 5$.[47] Rotational excitation has an analogous effect, as the rate is dependent only on the total internal energy of the molecule rather than the fractions of energy in particular rotational and vibrational modes.[48]

As noted above, hydrogen is an important component not only to CH_4 plasma chemistry, but it is also a key component in several plasma technology applications including plasma-assisted catalysis and fabrication of carbon materials. A goal of the work described herein is to delve deeper into understanding CH_4 plasma chemistry and the contributions of hydrogen species by elucidating rotational energy distribution trends of H_2 $d^3\Pi_u \rightarrow a^3\Sigma_g^+$. Optical emission

spectroscopy (OES) was employed to measure relative species densities and determine $T_R(H_2)$ in several plasma systems comprising H_2 (i.e. CH_4, H_2, CH_4/H_2, and H_2/Ar plasmas) to elucidate the probable excitation mechanisms occurring in each of these plasma systems. These fundamental plasma investigations that uncover information about the internal energies of hydrogen plasma species are required to utilize the full potential of multiple plasma technologies.

4.2 Results and Discussion

As T_R can be affected by the mechanism for molecule formation, we determined T_R of H_2 $d^3\Pi_u \rightarrow a^3\Sigma_g^+$ and CH $A^2\Delta \rightarrow X^2\Pi$ in H_2 and CH_4 inductively coupled plasmas with the goal of illuminating mechanistic phenomena that may be key components to overall processes occurring in these systems. Figure 4.1 shows a raw emission spectrum of the Q-branch of the H_2 $d^3\Pi_u \rightarrow a^3\Sigma_g^+$ (0,0) Fulcher (α) band in a 100% H_2 plasma at p = 200 mTorr, P = 100W. The rotational transitions used to calculate $T_R(H_2)$ are labeled in the spectrum and the inset shows the corresponding Boltzmann plot, yielding $T_R(H_2)$ = 530 K, significantly higher than room temperature, but lower than T_R(CH) values measured under similar conditions (~1700 – 2300 K), reported previously.[18]

In low pressure hydrogen discharges, rotational level populations are known to be non-thermal.[37, 39, 41, 45, 49-50] Rotational states with a low rotational quantum number (J < 5) follow a Boltzmann distribution, whereas higher rotational levels may be overpopulated by several orders of magnitude, described in detail previously.[36, 39] Overpopulation of the higher rotational levels often leads to overestimated $T_R(H_2)$ values when using a single Boltzmann plot to calculate $T_R(H_2)$. Briefi *et al.* demonstrated that H_2 rotational populations can be described using a two-

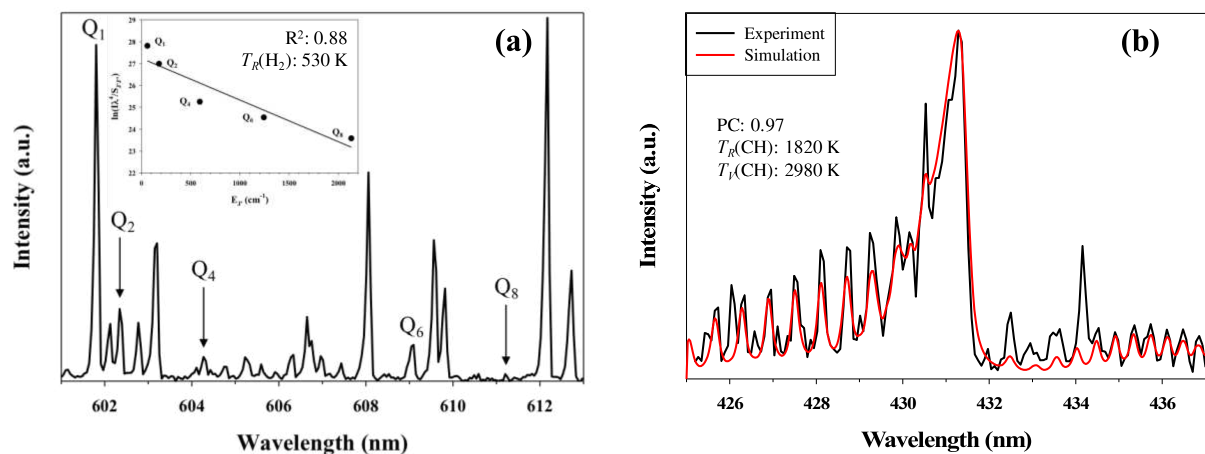

Figure 4.1. Representative emission spectra (p = 200 mTorr, P = 100 W) for (a) H_2 $d^3\Pi_u \rightarrow a^3\Sigma_g^+$ in a 100% H_2 plasma and (b) CH $A^2\Delta \rightarrow X^2\Pi$ in a CH_4/H_2 plasma (4:1 feed gas ratio). Inset in (a) shows corresponding Boltzmann plot for H_2 rotational distribution.

temperature distribution which reflects both the "cold" (lower rotational levels) and "hot" (upper rotational levels) parts of the distribution.[36] They found that by using this method, the calculated rotational temperature of H_2 in their system was reduced from 737 ± 45 K (one-temperature method) to 601 ± 12 K (two-temperature method).[36] The two-temperature method involves the use of use of several rotational lines to distinguish and ultimately fit both the "cold" and "hot" parts of the spectrum individually. Yet, the determination of the "hot temperature" can be difficult as the emission lines from the high rotational states are weak and often overlap with other species.[36]

The non-Boltzmann character of the rotational populations is evident in our own data (inset, Figure 4.1a) where Q_1, Q_2, and Q_4 follow a linear trend, but Q_6 and Q_8 appear to deviate slightly from linearity. This result mirrors what has been previously described by Briefi *et al.* in a rf inductively coupled H_2 plasma (10^{-7} mbar) where the first five rotational levels of H_2 $d^3\Pi_u \rightarrow a^3\Sigma_g^+$ (0,0) follow a linear trend; yet, the higher rotational levels deviate from linearity.[36] As noted above, however, determining $T_R(H_2)$ using the two-temperature method is challenging. In our systems, many of the higher rotational emission lines are weak, especially at low *P*. Moreover, several rotational lines are often obscured by other species. Although this is not a significant concern in 100% H_2 and 100% CH_4 plasmas, obscured rotational lines becomes a noteworthy challenge with some of the other precursor mixtures, particularly when N_2 $B^3\Pi_g \rightarrow A^3\Sigma_u^+$ is present. Using one method to calculate $T_R(H_2)$ allows comparison of $T_R(H_2)$ values and trends between all of our plasma systems. As such, we have used the Boltzmann plot method described by Garg *et al.* and Shivkumar *et al.* to calculate $T_R(H_2)$ in our systems.[35, 51] The specific rotational transitions used to calculate $T_R(H_2)$ (Q_1, Q_2, Q_4, Q_6, Q_8) were chosen as this part of the spectrum is relatively free from perturbations.[35, 51]

As discussed in Section 4.1, a goal of this work is to delve deeper into understanding CH_4 plasma chemistry. This includes interpretation of the energy partitioning trends of multiple species within our plasma systems. As such, in addition to determination of $T_R(H_2)$, we utilized LIFBASE[52] to simulate raw emission spectra of CH $A^2\Delta \rightarrow X^2\Pi$ in mixed gas CH_4/H_2 plasma systems and calculate T_R(CH) and T_V(CH). Figure 4.1b shows an experimental emission spectrum of CH $A^2\Delta \rightarrow X^2\Pi$ and the corresponding simulated fit in a mixed gas CH_4/H_2 (4:1 feed gas ratio) plasma at p = 200 mTorr, P = 100 W. For this particular spectrum, T_R(CH) = 1820 K and T_V(CH) = 2980 K; a peak correlation value (PC) of 0.97 indicates fair agreement between the raw and simulated data.

To further investigate energy partitioning in H_2 and CH_4 plasmas, a range of pressures and powers were explored. Figure 4.2 shows $T_R(H_2)$ as a function of p and P in two different plasma systems. In a 100% H_2 plasma, Figure 4.2a, $T_R(H_2)$ values are ~500 – 550 K and have minimal p or P dependence. Alternatively, $T_R(H_2)$ values are typically higher in a 100% CH_4 plasma, where values range from ~500 – 700 K, Figure 4.2b. Moreover, interesting trends with respect to both p and P are apparent in the 100% CH_4 plasma system. Here, $T_R(H_2)$ values concomitantly increase with p. We have previously determined T_R of several other excited state species (e.g., N_2, NO) in numerous plasma systems over similar pressure and applied power ranges.[6, 17] In each of these studies, we have reported an opposite trend with respect to system p, where an increase in pressure results in a decrease in T_R values to varying degrees, mostly attributing this trend to rotational cooling processes. Importantly, this is also true of CH $A^2\Delta$ molecules in a 100% CH_4 plasma, indicating opposing p trends for two molecules (CH and H_2) in the same plasma system.[18] This trend was also observed by Cruden *et al.* in a low-pressure CF_4/O_2/Ar ICP system,[15] where T_R(CO) rises with p while T_R(CF) drops as p increases. The

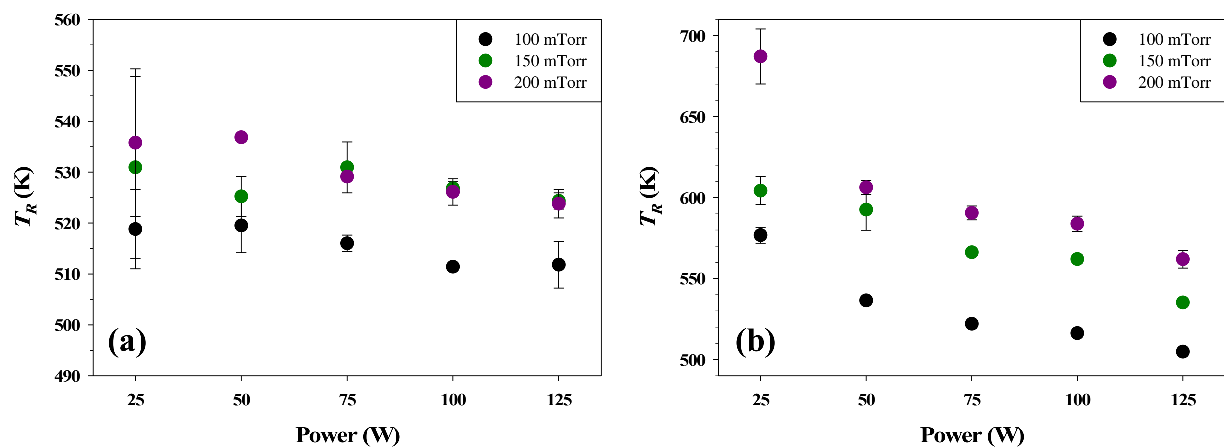

Figure 4.2. $T_R(H_2)$ in (a) 100% H_2 and (b) 100% CH_4 plasmas as a function of applied rf power at three different system pressures.

authors attribute the different p trends to differences between the kinetic energies of the species. Species possessing a kinetic energy above the mean neutral plasma temperature will experience a decrease in temperature as p increases, as a result of a higher collision rate allowing thermal equilibration of the species with the rest of the plasma.[15] Moreover, Cruden *et al.* further suggested that CF is produced with a highly rovibrationally excited nascent distribution, possibly explaining the higher rotational temperatures compared to CO in their system.[15] Similarly, CH $A^2\Delta$ is also typically produced with significant rovibrational excitation.[14, 53] This suggests that dissociative electron excitation is a likely pathway for CH excitation and may help to explain the larger T_R values for CH compared to H_2 in our plasma systems. Moreover, this may also be an important factor in determining and understanding T_R trends with respect to system pressure.

Rotational energy partitioning trends of H_2 with respect to P also differ from several of our previous studies investigating molecules in N_xO_y and fluorocarbon plasmas.[6, 17, 54] In those systems, the rotational temperature of the species of interest (e.g., N_2, NO, CF) increased with respect to applied rf P. Conversely, in the 100% CH_4 plasma system, $T_R(H_2)$ generally decreases with a concomitant increase in P, indicating opposing P trends from most of our previous studies. Nevertheless, our preceding study on rotational energy partitioning of CH $A^2\Delta$ in a 100% CH_4 plasma demonstrated a more complex relationship between T_R(CH) and P.[18] The dependence of T_R(CH) on P changed as system p increased, suggesting intimate connections between plasma parameters in this system, where a change in one parameter likely produces a change in the other parameter, both of which affect energy partitioning. For example, at higher P, we are likely increasing the overall pressure via decomposition of plasma gases and formation of additional molecules. As it is difficult to obtain an accurate pressure reading when the plasma is on, this effect may not be reflected in our reported pressure values. Moon *et al.* examined

molecular plasma temperatures in atmospheric discharges and noted that the positive *P* dependence of T_R(CH) and T_R(CN) were relatively sensitive to other plasma parameters.[55] Previous studies from our lab indicated that CH_4-containing plasmas can often be characterized by two modes.[56] Specifically, a shift from a capacitively coupled electrostatic mode at low *P* to an inductively coupled electromagnetic mode at high *P* occurs at ~ 75 W in our systems. As $T_R(H_2)$ values appear to level out at ~ 75 – 100 W and decrease slightly at higher *P*, the trend in $T_R(H_2)$ with respect to applied rf power may be related to a shift in the overall mode of the plasma.

Understanding mechanisms of formation for a particular species is critical to comprehending molecular plasma temperatures. In a 100% H_2 plasma, H_2^* is formed primarily through direct electron impact excitation from the ground state,[3, 36, 57] Reaction 4.1,

$$H_2 + e^- \rightarrow H_2^* + e^- \qquad (4.1)$$

whereas in CH_4 plasmas, numerous additional pathways for H_2^* formation exist. Importantly, in 100% CH_4 plasmas, H_2^* must be formed through decomposition of the precursor, a process that can occur in a single step or multiple steps.

Similar to a hydrogen plasma, electron impact excitation of H_2 from the ground state is also the main pathway for H_2^* formation in methane plasmas,[3] Reaction 4.2.

$$CH_4 + e^- \rightarrow CH + H + H_2 + e^- \qquad (4.2a)$$

$$H_2 + e^- \rightarrow H_2^* + e^- \qquad (4.2b)$$

Besides direct electron impact excitation of hydrogen molecules that may be produced via decomposition and/or recombination reactions, dissociative excitation of methane molecules via collisions with electrons may also contribute to the production of H_2^* in 100% CH_4 plasmas, Reactions 4.3 – 4.5.

$$CH_4^* + e^- \rightarrow CH_2 + H_2^* + e^- \quad (4.3)$$

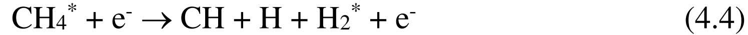

$$CH_4^* + e^- \rightarrow CH + H + H_2^* + e^- \quad (4.4)$$

$$2H + e^- \rightarrow H_2^* + e^- \quad (4.5)$$

The discernable differences between the $T_R(H_2)$ values, listed in Table 4.1, and p and P trends in these two plasma systems prompted us to further investigate these systems by combining H_2 and CH_4 in various gas mixtures.

Mixed gas CH_4/H_2 plasmas with varying precursor ratios were investigated via OES to decipher how $T_R(H_2)$ changes as a function of %H_2 in the feed gas. Figure 4.3 shows $T_R(H_2)$ in a CH_4/H_2 plasma as a function of %H_2 in the gas feed at p = 200 mTorr and two different powers. Notably, there is an inverse linear relationship between $T_R(H_2)$ and %H_2 in CH_4/H_2 plasmas. The P trend for $T_R(H_2)$ in 100% CH_4 plasmas (0% H_2) is again highlighted in Figure 4.3 where there is a >100 K difference in $T_R(H_2)$ values between P = 25 W and P = 125 W plasmas. As more H_2 is added to the system, however, the P dependence essentially disappears as $T_R(H_2)$ values at P = 25 W and P = 125 W are within error of each other in a 100% H_2 plasma. Moreover, at p = 200 mTorr, the dependence on % H_2 decreases by nearly a factor of 4 as P is increased from 25 W to 125 W, highlighting the significant effects of P and precursor ratio on fundamental plasma processes and, consequently, $T_R(H_2)$.

At P = 125 W, $T_R(H_2)$ values are only ~ 35 K higher in the 100% CH_4 plasma system than in the 100% H_2 plasma system. This subtle difference in $T_R(H_2)$ values between the two plasma systems at P = 125 W, suggests that similar excitation mechanisms for H_2^* may be occurring under these plasma conditions. Thus, in the CH_4 plasma system, at high P, we hypothesize that direct electron impact of molecular hydrogen, Reaction 4.2, is the predominant route for excitation. In contrast, at low P, dissociative excitation, Reactions 4.3 – 4.4, may

Table 4.1. $T_R(H_2)$ values for H_2 and CH_4 plasma systems.[a]

Pressure (mTorr)	Applied rf Power (W)	100% H_2	100% CH_4	75% CH_4/ 25% Ar
50	25	--	560 (5)	--
	50	--	545 (5)	--
	75	--	535 (5)	--
	100	--	540 (5)	--
100	25	520 (10)	575 (5)	540 (10)
	50	520 (5)	535 (5)	525 (5)
	75	515 (5)	520 (5)	525 (5)
	100	510 (5)	515 (5)	520 (5)
	125	510 (5)	505 (5)	535 (10)
150	25	530 (20)	605 (10)	590 (10)
	50	525 (5)	590 (15)	550 (5)
	75	530 (5)	565 (5)	540 (5)
	100	525 (5)	560 (5)	535 (10)
	125	525 (5)	535 (5)	530 (5)
200	25	535 (15)	690 (20)	635 (20)
	50	535 (5)	605 (5)	580 (20)
	75	530 (5)	590 (5)	580 (10)
	100	525 (5)	585 (5)	565 (5)
	125	525 (5)	560 (5)	545 (5)

[a]Values in parentheses represent standard deviation calculated from the mean of $n \geq 3$ trials.

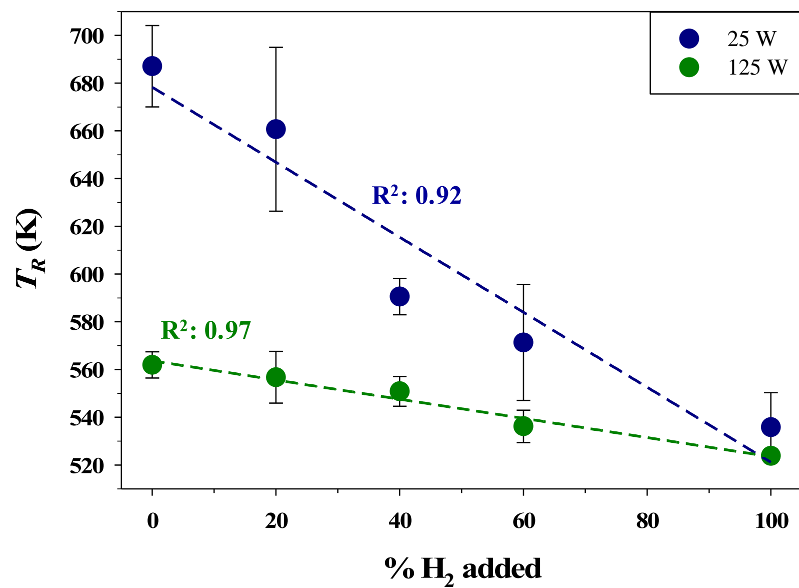

Figure 4.3. $T_R(H_2)$ as a function of % H_2 in CH_4/H_2 plasmas (p = 200 mTorr) at two applied rf powers (25 and 125 W).

become a more prominent mechanism for H_2^* formation, ultimately resulting in the higher $T_R(H_2)$ values observed at low P.

Furthermore, additional routes for H_2^* formation can occur in CH_4/H_2 gas mixtures. NASA groups have focused on gas phase reactions crucial to deposition processes and have noted that the CH_4 dissociation process is not only the result of electron impact dissociation but also to the hydrogen abstraction mechanism, Reaction 4.6, where the hydrogen atom can be sourced from either precursor.[58-61]

$$CH_4 + H \rightarrow CH_3 + H_2 \qquad (4.6)$$

The molecular hydrogen product is subsequently excited via electron impact. In 100% CH_4 plasmas, methane is initially dissociated via collisions with energetic electrons. As soon as H atoms are formed, however, hydrogen abstraction becomes an important channel for further dissociation of methane. Previous studies of hydrogen-hydrocarbon mixtures (e.g., H_2/CH_4, H_2/C_2H_2) agree that hydrogen abstraction from methane by atomic hydrogen dominates over electron impact dissociation, except at low pressures.[62-66] Specifically, a study on methane dissociation in low-pressure plasmas described the likelihood of hydrogen abstraction contributing to methane dissociation at pressures of 1 Torr and 6 Torr.[66] Several plasma properties (e.g., electron temperature, electron density, atomic hydrogen density, T_g) contribute to the ratio between the two main processes involved in methane dissociation, electron impact and hydrogen abstraction.[20, 66] Consequently, each of these plasma properties is dependent on the gas pressure. Reaction rates reported by Mechold *et al.* suggest that electron impact is the predominate route to methane dissociation at 1 Torr whereas hydrogen abstraction dominates methane dissociation processes at 6 Torr.[66] Thus, in our systems, we believe Reaction 4.6 does

not significantly contribute to production of molecular hydrogen, even as H-alpha density increases with *P*.

T_R(CH) and T_V(CH) were also measured in the CH_4/H_2 plasma systems at p = 200 mTorr, Table 4.2. T_R(CH) values range from ~ 1700 – 2100 K over the studied parameter space, with no clear trends relating to applied rf power or precursor ratio. Reported T_V(CH) values are higher than T_R values, a well-documented phenomenon,[67] and range from ~ 2000 to 3000 K. Similar to T_R(CH) results, there are no clear trends corresponding to *P* or precursor ratio. Overall, T_R(CH) and T_V(CH) values are similar to previously reported values from our lab in a 100% CH_4 plasma, discussed in Chapter 3.[18] These results indicate that H_2 does not appreciably affect CH formation mechanisms or vibrational excitation pathways.

Notably, $T_R(H_2)$ values are significantly lower than what is observed for T_R(CH) in CH_4-containing plasma systems where T_R(CH) is ~ 1700 – 2400 K, Table 4.2.[18] Similarly, Avtaeva and Lapochkina observed disparate ground state $T_R(H_2\ X^1\Sigma)$ and excited state $T_R(\mathrm{CH}\ A^2\Delta)$ values in a methane-containing rf capacitive discharge, which they attributed to the molecules' radiative lifetimes and concentrations in the plasma.[3] The concentration of molecular hydrogen in methane discharges is fairly high, especially when compared to CH $A^2\Delta$ concentration.[3] As such, direct electron impact excitation of H_2 from the ground state tends to dominate over dissociative excitation of H_2 from a methane molecule, corresponding to the relatively low reported $T_R(H_2\ X^1\Sigma)$ values (487 – 564 K) reported by Avtaeva and Lapochkina.[3, 36]

In another study, Heintze *et al.* examined methane plasma dissociation and formation of C_2 and H_2 in pulsed microwave discharges.[20] Notably, they determined T_R of both ground and excited states species for C_2 ($a^3\Pi_u$, $d^3\Pi_g$) and H_2 ($X^1\Sigma_g^+$, $d^3\Pi_u^-$) and found the rotational temperature of excited state H_2 ($d^3\Pi_u^-$) (~800 – 1500 K) was significantly lower than that for

Table 4.2. T_R and T_V values for CH_4/H_2 plasma at p = 200 mTorr.[a]

Applied rf Power (W)	% H_2	$T_R(H_2)$	T_R(CH)	T_V(CH)
25 W	0	690 (20)	1790 (30)	2280 (260)
	20	660 (30)	1720 (70)	2250 (120)
	40	590 (10)	1890 (50)	2060 (10)
	60	570 (25)	2090 (120)	2700 (50)
	100	535 (15)	--	--
75 W	0	590 (5)	1880 (10)	2680 (10)
	20	570 (10)	1790 (30)	2770 (140)
	40	560 (5)	1780 (70)	2060 (10)
	60	550 (15)	1870 (50)	2700 (210)
	100	530 (5)	--	--
125 W	0	560 (5)	1880 (10)	2810 (80)
	20	555 (10)	1770 (30)	2910 (100)
	40	550 (5)	1730 (70)	2060 (10)
	60	535 (5)	1840 (50)	2700 (40)
	100	525 (5)	--	--

[a]Values in parentheses represent standard deviation calculated from the mean of n ≥ 3 trials.

ground state H_2 ($X^1\Sigma_g^+$) and either of the C_2 electronic states ($d^3\Pi_g$ or $a^3\Pi_u$) (all were ~1500–2500 K).[20] The authors attributed the lower rotational temperature of H_2 $d^3\Pi_u^-$ to the short radiative lifetime (40 ns)[68] of the upper state, which does not allow for sufficient time to achieve thermal equilibrium of rotational level populations.[20] Furthermore, the observation that three of the four electronic states had similar rotational temperatures led the authors to assume that the gas temperature corresponded to these temperatures (~1500 – 2500 K).[20] This suggests that a similar amount of energy may be partitioned into the rotational and vibrational modes of all methane decomposition products. Our studies, however, demonstrate disparate $T_R(H_2)$ and $T_R(CH)$ values are obtained in our methane-based plasma systems. Possible explanations for the differences between rotational temperature values in these systems may be related to the disparities in the plasma systems studied and the production mechanisms and nascent rotational distributions of the molecules of interest. Emission intensity within a plasma is influenced by several factors including the electron energy distribution function (EEDF), formation mechanisms, cascade processes, radiation transport, and collisions.[69] Importantly, the operation frequency (microwave vs. rf) may further affect this as frequency can alter the shape of EEDF and thereby control electron-molecule reaction channels.[70-71] Moreover, our system operates in the mTorr pressure range (~0.13 – 0.26 mbar), whereas the system used by Heintze *et al.* operates at 30 mbar.[20] The much lower pressures used in our system increases the mean free path, reducing the possibility of thermalizing collisions. In their system, Heintze *et al.* demonstrate that C_2 is mainly formed via dimerization of CH_x species and subsequent dehydrogenization via hydrogen abstraction from atomic hydrogen present in the discharge.[20] Furthermore, they believe excited state C_2 $d^3\Pi_g$ is formed via electron impact excitation from the ground state. In our systems, we believe CH $A^2\Delta$ is produced via dissociative excitation of a

CH_x parent molecule. Previous studies showed that CH $X^2\Pi$ radicals typically react very quickly with residual gas molecules;[3, 31, 72] thus, in CH_4 plasmas, CH $A^2\Delta$ is primarily formed via dissociative excitation of CH_4 rather than electron impact excitation of CH from the ground state. Furthermore, the excited state lifetime of CH $A^2\Delta$ is relatively short, ~ 5×10^{-7} seconds,[3] so the rotational distribution formed in the course of dissociative excitation has little time to relax to an equilibrium distribution with a temperature close to the gas temperature.[3] This may explain the much higher T_R(CH) values compared to $T_R(H_2)$ as reported herein and by Avtaeva and Lapochkina.[3]

In a related system, Cruden *et al.* determined rotational temperatures of multiple diatomic species in a low pressure (30 mTorr), inductively coupled CF_4 plasma to examine the accuracy of using T_R to estimate the neutral gas temperature.[4] Four different rotational temperatures were obtained for five molecular species ranging from ~1200 – 2300 K. Species produced in the plasma bulk (CF and CN) yielded the lowest T_R values (~1250 K), whereas SiF, an etch product from plasma interaction with the quartz window in the reactor, had the highest T_R values (~2300 K). C_2 and CO, produced both in the plasma bulk and via plasma-surface interactions had intermediate T_R values (1600 K and 1800 K, respectively). Their results demonstrate a thermal nonequilibrium between molecular species and further imply that formation mechanisms play a significant role in rotational temperature determination. A follow up study by Cruden *et al.* focused on determination of T_R(CF) and T_R(CO) in a CF_4/O_2/Ar ICP.[15] In this study, T_R(CF) was elevated in comparison to T_R(CO). The difference between T_R(CF) and T_R(CO) was attributed to an incomplete equilibration of T_R(CF) with the average neutral gas temperature. The authors stated that CF created via CF_4 dissociation will possess a kinetic energy above that of other neutral species in the discharge because of Franck-Condon heating.[15] Franck-Condon heating

occurs when an electron strikes a neutral molecule with sufficient energy to raise the molecule to a dissociative state, usually greater than the dissociation energy of the molecule resulting in extra kinetic energy being distributed to the dissociated fragments.[73]

Few other studies have investigated energy partitioning of multiple species in low temperature plasmas. As discussed in the Section 4.1, insight into fundamental plasma processes can be gained through consideration of energy partitioning trends of multiple species. Such information is crucial to advancing plasma technologies (e.g., plasma-assisted catalysis, film/coating technologies) which rely on knowledge of fundamental chemical processes in systems of interest to optimize plasma conditions for plasma processing. As such, a goal of this work is to examine the energetics of multiple species in low temperature plasma systems to gain a deeper understanding of the molecular-level processes occurring in these systems. Although we have reported on both T_R(H_2 $d^3\Pi_u$) and T_R(CH $A^2\Delta$) herein, these are only two of the many possible products in methane plasma dissociation, and as such, future investigations should include the use of other plasma diagnostic techniques to elucidate additional underlying processes in these plasma systems. For example, our lab has previously investigated energy partitioning of N_2 $B^3\Pi_g \leftrightarrow C^3\Pi_u$ and NO $X^2\Pi \leftrightarrow A^2\Sigma^+$ in N_xO_y plasma systems using broadband absorption spectroscopy (BAS) to probe energetics of ground state molecules as a complimentary technique to OES.[6, 17] T_R(NO) was almost exclusively higher for the ground state ($X^2\Pi$) compared to the excited state ($A^2\Sigma^+$) in a 100% NO plasma suggesting that energy transfer in the excited state may be fast enough to achieve some level of thermalization.[6] Similar investigations in CH_4 and CH_4/H_2 plasmas may illuminate further mechanistic details. As such, future studies shall include employing BAS in conjunction with OES to obtain energy partitioning information on ground state species as well as excited state species.

Further spectral analysis allows us to monitor changes in species densities as functions of plasma parameters, which can help elucidate reaction mechanisms, especially when combined with characteristic plasma temperatures (e.g., T_R and T_V). Within this chapter, we utilized inert gas actinometry to determine relative densities of several gas-phase species of interest. In these cases, a small amount of Ar (~5 – 10%) was added as an actinometer to the H_2 and CH_4 plasmas, allowing for species comparisons across systems. Relative densities of H_2 and H_α within H_2 and CH_4 plasma systems are shown in Figure 4.4 as a function of P (p = 200 mTorr). H_2 density increases with respect to P in a CH_4 plasma system but has virtually no dependence on P in a H_2 plasma. Similarly, in a 100% H_2 plasma, $T_R(H_2)$ has no P dependence and is relatively constant among changes in plasma system p and P. Conversely, there is a clear, linear ($R^2 = 0.91$) P dependence for $T_R(H_2)$ in a 100% CH_4 plasma where $T_R(H_2)$ concomitantly decreases with increasing P. As H_2^* concentration increases in the plasma, direct electron impact excitation, Reaction 4.2, may become a more dominant process because of the increasing concentration of molecular hydrogen in the discharge.[3] Ultimately, this may correspond to the lower $T_R(H_2)$ values observed at high P in the CH_4 plasma system.

Conversely, in the 100% H_2 plasma system, precursor gas flow is continuous, and molecular hydrogen does not have to be formed from the precursor through decomposition reactions. Thus, direct electron impact excitation, Reaction 4.1, is the primary route to H_2 excitation. Furthermore, H_2 density remains relatively constant as a function of P. Together, these may help explain the lack of pressure or power dependence of $T_R(H_2)$ observed in a 100% H_2 plasma. However, H_2^* may not be formed exclusively via Reaction 4.1 in a H_2 plasma, as other possible routes to H_2^* formation exist. For example, atomic hydrogen may also recombine

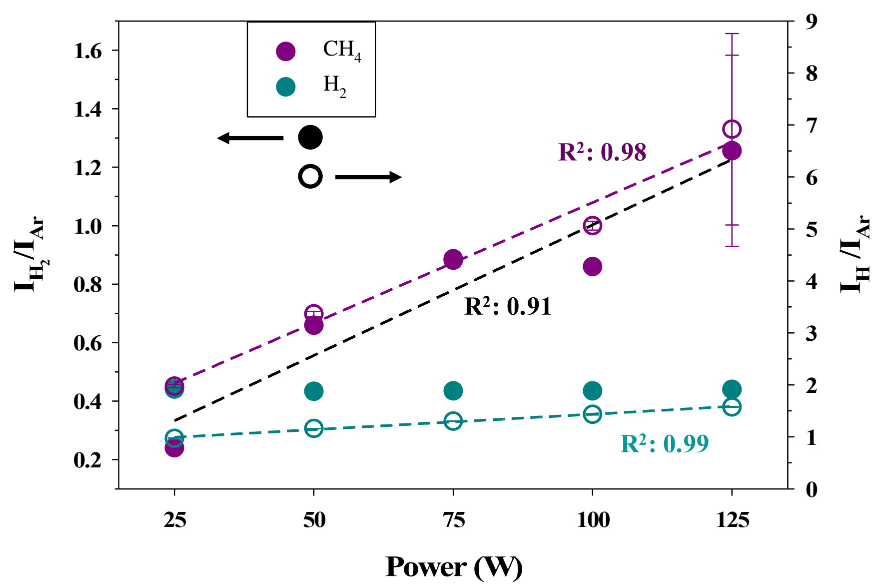

Figure 4.4. Relative density of H_2 (closed circles, left axis) and H_α (open circles, right axis) as a function of applied rf power in CH_4 and H_2 plasmas (each with 10% Ar, p = 200 mTorr). Dashed lines represent linear regression analyses for: H_2 (black, slope: 0.0089) and H_α (purple, slope: 0.0463) in a CH_4 plasma, and H_α (cyan, slope: 0.0059) in a H_2 plasma.

to form H_2, Reaction 4.7, where either one or both hydrogen atoms may already be in an excited state:

$$H^* + H^* \rightarrow H_2^* \qquad (4.7)$$

Reaction 4.7 may occur in either the 100% CH_4 or the 100% H_2 plasma system, and as such, the atomic hydrogen density in the plasma may also be an important consideration for determining the likelihood of Reaction 4.7. Figure 4.4 also shows the relative densities of H_α^*, revealing H_α^* increases with increasing *P* in both systems, indicating the probability of Reaction 4.4 may rise at higher *P*. Although H_α density increases with increasing *P* in both CH_4 and H_2 plasma systems, the *P* dependence is ~5 times greater in the CH_4 plasma relative to the H_2 plasma. These results highlight the significant role of *P* in hydrogen species concentrations in CH_4 plasmas whereas this role is significantly less important in H_2 plasmas.

As one additional way to visualize the relationships between different molecular temperatures in this system, Figure 4.5 shows the relationship between T_R(CH) and $T_R(H_2)$ in a 100% CH_4 plasma at different *p* and *P*. As reported previously, T_R(CH) generally decreases with increasing *p* with values decreasing from ~ 2350 K at 50 mTorr to ~ 1750 K at 200 mTorr.[18] Although the pressure dependence for $T_R(H_2)$ is not as dramatic, it is still evident. $T_R(H_2)$ values range from ~500 to ~600 K at lower pressures (*p* = 50 – 100 mTorr) compared to the slightly higher values (~550 – 700 K) measured at higher pressures (*p* = 150 – 200 mTorr). The *P* dependence of T_R(CH) in a 100% CH_4 plasma is complex and appears to also depend on other plasma parameters and thus, is not as apparent in Figure 4.5.[18] Nevertheless, these data clearly display a *P* dependence for $T_R(H_2)$. High applied rf power (125 W) results in lower $T_R(H_2)$ values (~500 – 570 K) for a CH_4 plasma, whereas lower applied rf power (25 W) results in higher $T_R(H_2)$ values (~570 – 700 K).

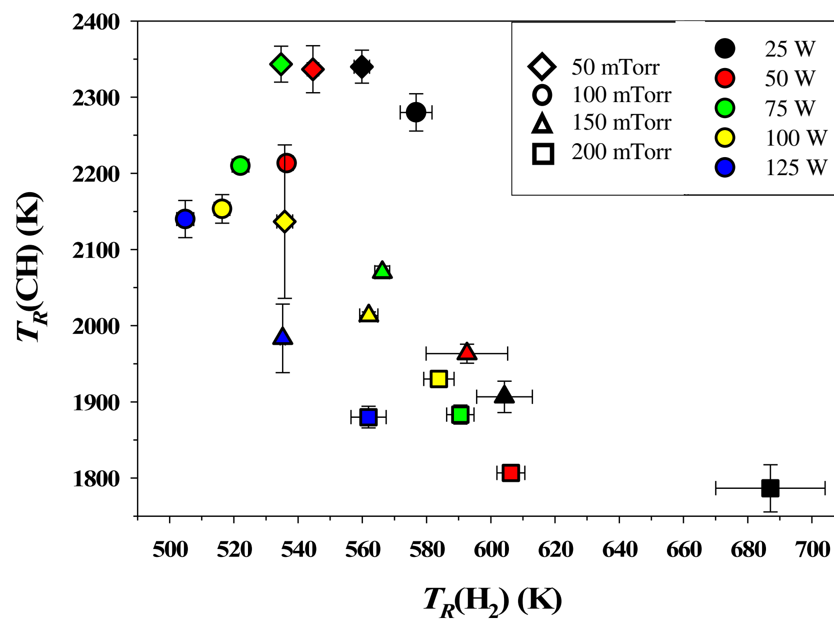

Figure 4.5. Relationship between T_R(CH) (y-axis) and T_R(H_2) (x-axis) over a range of pressures and applied rf powers in 100% CH_4 plasmas. Each shape corresponds to a different *p* and each color corresponds to a different *P*.

Based on the T_R(CH, H_2) measurements in the mixed gas CH_4/H_2 system and the results displayed in Figure 4.5, it is apparent that T_R(CH, H_2) depend heavily on p and P of the plasma system in a 100% CH_4 plasma. By more closely examining these energy portioning trends we observe that at low p and low P, both T_R(CH) and T_R(H_2) values are generally high. For example, at p = 50 mTorr, P = 25 W T_R(CH) = ~2350 K and T_R(H_2) = ~580 K; both of these values are on the higher end of the reported ranges for the investigated parameter space. Conversely, at high p and high P, T_R(CH) and T_R(H_2) values are both on the lower end of the reported ranges for the investigated parameter space. For instance, at p = 200 mTorr, P = 125 W, T_R(CH) = ~1900 K and T_R(H_2) = ~560 K.

Previously, we studied the effect of Ar in the plasma on T_R(CH) and T_V(CH) energy partitioning trends in CH_4 plasmas.[18] Addition of Ar as a precursor gas changed the emission spectrum of the CH $A^2\Delta$ band.[18] This, in turn, had a profound effect on the energy partitioning trends for CH $A^2\Delta$ compared to a 100% CH_4 plasma. As such, here we further investigated the effect of Ar addition on T_R(H_2) in CH_4 and H_2 plasmas. T_R(H_2) values were calculated for a CH_4/Ar (3:1) system, Table 4.1. Notably, T_R(H_2) values and trends in the CH_4/Ar mixed gas system do not differ appreciably from the 100% CH_4 plasma system. Similarly, in H_2/Ar plasmas, T_R(H_2) was unaffected by addition of Ar as a precursor gas. Figure 4.6 shows T_R(H_2) in H_2/Ar plasmas comprising up to 60% Ar at a total pressure of 150 mTorr. At greater than 60% Ar, some H_2 Fulcher rotational band emissions were either very weak or obscured so the Boltzmann plot method was ineffective at calculating T_R(H_2). T_R(H_2) values range from ~ 500 to 550 K, Figure 4.6, and appear to be independent of both P and % Ar in the gas feed. Similarly, this trend was documented for all studied pressures (p = 100 – 200 mTorr).

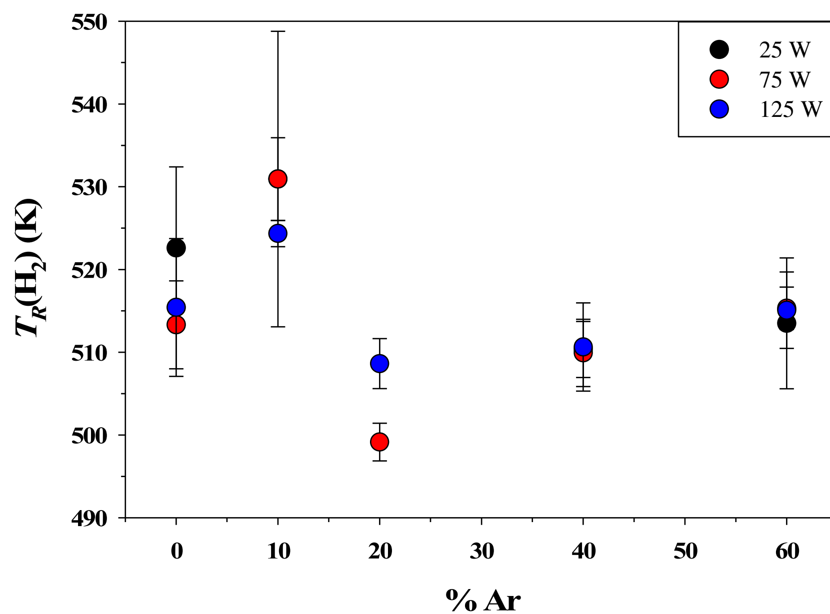

Figure 4.6. $T_R(H_2)$ as a function of % Ar in a H_2/Ar plasma system at three different *P* (p = 150 mTorr).

Adding an inert precursor like Ar increases the number of nonreactive gas-phase collisions and thus, can be used to distinguish between the effects of collision environment and formation mechanisms of species of interest. Studies from Stillahn and Fisher measured the effect of Ar addition on T_R(CN $X^2\Sigma^+$) in CH_3CN plasmas.[74] In a CH_3CN/Ar plasma, T_R(CN) remained unaffected by an increase in the %Ar in the feed gas mixture.[74] Yet, a negative dependence of T_R(CN) on system p in their study suggests that collisional cooling effects are dependent on the frequency of collisions rather than the nature of them. In a 100% H_2 plasma system, there is no p dependence for $T_R(H_2)$ (Figure 4.2), suggesting that H_2 is not rotationally thermalized via collisions in this system. Excited H_2 ($d^3\Pi_u^-$) has a short radiative lifetime of 40 ns[68] and is depopulated rather quickly via radiative decay, reducing the likelihood of thermalizing collisions with other species.[3, 36] Ultimately, we believe that the work presented herein demonstrates the significance of employing optical plasma diagnostics as a tool to determine molecular temperature trends and elucidate probable mechanistic information. Yet, significant additional work must be done to more fully elucidate the fundamental chemical processes in the gas phase and at the gas-surface interface to address the current limitations of plasma technologies.

4.3 Summary

Plasma species can be produced via a variety of mechanisms (direct-impact excitation, decomposition, recombination, etc.); therefore, fundamental investigations of the energetics of plasma species are crucial components to understanding and optimizing plasma conditions for the future development of a host of plasma technologies. OES was employed to elucidate energy partitioning trends of H_2 $d^3\Pi_u \rightarrow a^3\Sigma_g^+$ and CH $A^2\Delta \rightarrow X^2\Pi$ in H_2 and CH_4 plasma systems.

Generally, T_R(CH) values (~1700 – 2100 K) are much higher than $T_R(H_2)$ values (~500 – 700 K) in a 100% CH_4 plasma. These disparate values likely result from a combination of the differences in the species densities, radiative lifetimes, and consequently their excitation pathways. Direct electron impact excitation is indicated as the primary H_2^* formation pathway in a 100% H_2 plasma, but elevated $T_R(H_2)$ values in a 100% CH_4 plasma suggest that other excitation mechanisms are likely contributing to the production of H_2^*. Additionally, studies of CH_4/H_2 mixed gas plasma systems highlight the significant effects of plasma parameters (e.g., applied rf power, feed gas composition) on $T_R(H_2)$ values and trends. Nevertheless, T_R(CH) and T_V(CH) do not change appreciably as function of feed gas composition in mixed gas CH_4/H_2 plasmas indicating that H_2 does not appreciably affect CH formation mechanisms or vibrational excitation pathways. Ultimately, these data provide information that may lend critical insight into the overall character of the plasma and aid in understanding key mechanistic phenomena occurring during plasma processing.

REFERENCES

1. Stillahn, J. M.; Trevino, K. J.; Fisher, E. R., Plasma Diagnostics for Unraveling Process Chemistry. *Annu. Rev. Anal. Chem.* **2008,** *1*, 261-291.
2. Hanna, A. R.; Fisher, E. R., Investigating Recent Developments and Applications of Optical Plasma Spectroscopy: A Review. *J. Vac. Sci. Technol., A* **2020,** *38* (2), 020806.
3. Avtaeva, S.; Lapochkina, T., Characteristics of Molecular Hydrogen and CH* Radicals in a Methane Plasma in a Magnetically Enhanced Capacitive RF Discharge. *Plasma Phys. Rep.* **2007,** *33* (9), 774-785.
4. Cruden, B. A.; Rao, M.; Sharma, S. P.; Meyyappan, M., Neutral Gas Temperature Estimates in an Inductively Coupled CF_4 Plasma by Fitting Diatomic Emission Spectra. *J. Appl. Phys.* **2002,** *91* (11), 8955-8964.
5. Britun, N.; Gaillard, M.; Ricard, A.; Kim, Y.; Kim, K.; Han, J., Determination of the Vibrational, Rotational and Electron Temperatures in N_2 and Ar–N_2 RF Discharge. *J. Phys. D: Appl. Phys.* **2007,** *40* (4), 1022.
6. Blechle, J. M.; Hanna, A. R.; Fisher, E. R., Determination of Internal Temperatures within Nitric Oxide Inductively Coupled Plasmas. *Plasma Process. Polym.* **2017,** *14* (12), 1700041.
7. Liu, W.-Y.; Xu, Y.; Liu, Y.-X.; Peng, F.; Gong, F.-P.; Li, X.-S.; Zhu, A.-M.; Wang, Y.-N., Absolute CF_2 Density and Gas Temperature Measurements by Absorption Spectroscopy in Dual-Frequency Capacitively Coupled CF_4/Ar Plasmas. *Phys. Plasmas* **2014,** *21* (10), 103501.
8. Davis, G. P.; Gottscho, R. A., Measurement of Spatially Resolved Gas-Phase Plasma Temperatures by Optical Emission and Laser-Induced Fluorescence Spectroscopy. *J. Appl. Phys.* **1983,** *54* (6), 3080-3086.
9. Tonnis, E. J.; Graves, D. B., Neutral Gas Temperatures Measured within a High-Density, Inductively Coupled Plasma Abatement Device. *J. Vac. Sci. Technol., A* **2002,** *20* (5), 1787-1795.
10. Biloiu, C.; Sun, X.; Harvey, Z.; Scime, E., Determination of Rotational and Vibrational Temperatures of a Nitrogen Helicon Plasma. *Rev. Sci. Instrum.* **2006,** *77* (10), 10F117.
11. McCurdy, P. R.; Venturo, V. A.; Fisher, E. R., Velocity Distributions of NH_2 Radicals in an NH_3 Plasma Molecular Beam. *Chem. Phys. Lett.* **1997,** *274* (1-3), 120-126.
12. Bogart, K.; Cushing, J.; Fisher, E. R., Effects of Plasma Processing Parameters on the Surface Reactivity of OH ($X^2\Pi$) in Tetraethoxysilane/O_2 Plasmas During Deposition of SiO_2. *J. Phys. Chem. B* **1997,** *101* (48), 10016-10023.
13. Kessels, W.; McCurdy, P. R.; Williams, K. L.; Barker, G.; Venturo, V. A.; Fisher, E. R., Surface Reactivity and Plasma Energetics of Sih Radicals During Plasma Deposition of Silicon-Based Materials. *J. Phys. Chem. B* **2002,** *106* (10), 2680-2689.
14. Bruggeman, P. J.; Sadeghi, N.; Schram, D.; Linss, V., Gas Temperature Determination from Rotational Lines in Non-Equilibrium Plasmas: A Review. *Plasma Sources Sci. Technol.* **2014,** *23* (2), 023001.
15. Cruden, B. A.; Rao, M.; Sharma, S. P.; Meyyappan, M., Neutral Gas Temperature Estimate in CF_4/O_2/Ar Inductively Coupled Plasmas. *Appl. Phys. Lett.* **2002,** *81* (6), 990-992.
16. André, P.; Barinov, Y. A.; Faure, G.; Shkol'nik, S., Modelling Radiation Spectrum of a Discharge with Two Liquid Non-Metallic (Tap-Water) Electrodes in Air at Atmospheric Pressure. *J. Phys. D: Appl. Phys.* **2011,** *44* (37), 375203.

17. Hanna, A. R.; Blechle, J. M.; Fisher, E. R., Using Fundamental Spectroscopy to Elucidate Kinetic and Energetic Mechanisms within Environmentally Relevant Inductively Coupled Plasma Systems. *J. Phys. Chem. A* **2017,** *121* (40), 7627-7640.
18. Van Surksum, T. L.; Blechle, J. M.; Fisher, E. R., Determination of Rotational and Vibrational Temperatures of CH in CH_4 Plasmas. *J. Vac. Sci. Technol., A* **2018,** *36* (4), 041302.
19. Hanna, A. R.; Van Surksum, T. L.; Fisher, E. R., Investigating the Impact of Catalysts on N_2 Rotational and Vibrational Temperatures in Low Pressure Plasmas. *J. Phys. D: Appl. Phys.* **2019,** *52* (34), 345202.
20. Heintze, M.; Magureanu, M.; Kettlitz, M., Mechanism of C_2 Hydrocarbon Formation from Methane in a Pulsed Microwave Plasma. *J. Appl. Phys.* **2002,** *92* (12), 7022-7031.
21. Bišćan, M.; Kregar, Z.; Krstulović, N.; Milošević, S., Time Resolved Spectroscopic Characterization of a-C:H Deposition by Methane and Removal by Oxygen Inductively Coupled RF Plasma. *Plasma Chem. Plasma Process.* **2010,** *30* (3), 401-412.
22. Anooshehpour, F.; Turgeon, S.; Cloutier, M.; Mantovani, D.; Laroche, G., Optical Emission Spectroscopy as a Process-Monitoring Tool in Plasma Enhanced Chemical Vapor Deposition of Amorphous Carbon Coatings-Multivariate Statistical Modelling. *Thin Solid Films* **2018,** *649*, 106-114.
23. Hassan, M. K.; Pramanik, B. K.; Hatta, A., Comparative Study on Chemical Vapor Deposition of Diamond-Like Carbon Films from Methane and Acetylene Using RF Plasma. *Jpn. J. Appl. Phys.* **2006,** *45* (10S), 8398.
24. Morrison, N.; William, C.; Milne, W., Methane Chemistry Involved in a Low-Pressure Electron Cyclotron Wave Resonant Plasma Discharge. *J. Appl. Phys.* **2003,** *94* (11), 7031-7043.
25. Nozaki, T.; Muto, N.; Kado, S.; Okazaki, K., Dissociation of Vibrationally Excited Methane on Ni Catalyst: Part 1. Application to Methane Steam Reforming. *Catal. Today* **2004,** *89* (1-2), 57-65.
26. Nozaki, T.; Muto, N.; Kadio, S.; Okazaki, K., Dissociation of Vibrationally Excited Methane on Ni Catalyst: Part 2. Process Diagnostics by Emission Spectroscopy. *Catal. Today* **2004,** *89* (1-2), 67-74.
27. Mohanta, A.; Lanfant, B.; Asfaha, M.; Leparoux, M., Methane Dissociation Process in Inductively Coupled $Ar/H_2/CH_4$ Plasma for Graphene Nano-Flakes Production. *Appl. Phys. Lett.* **2017,** *110* (9), 093109.
28. Okita, A.; Suda, Y.; Oda, A.; Nakamura, J.; Ozeki, A.; Bhattacharyya, K.; Sugawara, H.; Sakai, Y., Effects of Hydrogen on Carbon Nanotube Formation in CH_4/H_2 Plasmas. *Carbon* **2007,** *45* (7), 1518-1526.
29. Liu, Y.; Liu, J.; Zhu, C.; Liu, W., Effects of Gas Pressure and Plasma Power on the Growth of Carbon Nanostructures. *Appl. Surf. Sci.* **2010,** *256* (7), 1996-1999.
30. Hsu, J.-S.; Tzeng, S.-S.; Wu, Y.-J., Influence of Hydrogen on the Mechanical Properties and Microstructure of Dlc Films Synthesized by RF-PECVD. *Vacuum* **2008,** *83* (3), 622-624.
31. Tachibana, K.; Nishida, M.; Harima, H.; Urano, Y., Diagnostics and Modelling of a Methane Plasma Used in the Chemical Vapour Deposition of Amorphous Carbon Films. *J. Phys. D: Appl. Phys.* **1984,** *17* (8), 1727.
32. Legrand, J.-C.; Diamy, A.-M.; Hrach, R.; Hrachova, V., Mechanisms of Methane Decomposition in Nitrogen Afterglow Plasma. *Vacuum* **1999,** *52* (1-2), 27-32.
33. Mesbahi, A.; Silva, F., Study of the Influence of Gas Flow on PECVD Diamond Growth: Influence of the Separate Injection of Gases. *J. Phys. D: Appl. Phys.* **2017,** *50* (47), 475203.

34. Vlassiouk, I.; Regmi, M.; Fulvio, P.; Dai, S.; Datskos, P.; Eres, G.; Smirnov, S., Role of Hydrogen in Chemical Vapor Deposition Growth of Large Single-Crystal Graphene. *ACS Nano* **2011,** *5* (7), 6069-6076.
35. Shivkumar, G.; Tholeti, S.; Alrefae, M.; Fisher, T.; Alexeenko, A., Analysis of Hydrogen Plasma in a Microwave Plasma Chemical Vapor Deposition Reactor. *J. Appl. Phys.* **2016,** *119* (11), 113301.
36. Briefi, S.; Rauner, D.; Fantz, U., Determination of the Rotational Population of H_2 and D_2 Including High-N States in Low Temperature Plasmas Via the Fulcher-α Transition. *J. Quant. Spectrosc. Radiat. Transfer* **2017,** *187*, 135-144.
37. Mosbach, T.; Katsch, H.-M.; Döbele, H., In Situ Diagnostics in Plasmas of Electronic-Ground-State Hydrogen Molecules in High Vibrational and Rotational States by Laser-Induced Fluorescence with Vacuum-Ultraviolet Radiation. *Phys. Rev. Lett.* **2000,** *85* (16), 3420.
38. Vankan, P.; Heil, S.; Mazouffre, S.; Engeln, R.; Schram, D.; Döbele, H., A Vacuum-UV Laser-Induced Fluorescence Experiment for Measurement of Rotationally and Vibrationally Excited H_2. *Rev. Sci. Instrum.* **2004,** *75* (4), 996-999.
39. Vankan, P.; Schram, D.; Engeln, R., High Rotational Excitation of Molecular Hydrogen in Plasmas. *Chem. Phys. Lett.* **2004,** *400* (1-3), 196-200.
40. Vankan, P.; Schram, D.; Engeln, R., Relaxation Behavior of Rovibrationally Excited H_2 in a Rarefied Expansion. *J. Chem. Phys.* **2004,** *121* (20), 9876-9884.
41. Meulenbroeks, R.; Engeln, R.; Van der Mullen, J.; Schram, D., Coherent Anti-Stokes Raman Scattering Performed on Expanding Thermal Arc Plasmas. *Phys. Rev. E: Stat. Phys., Plasmas, Fluids,* **1996,** *53* (5), 5207.
42. Gabriel, O.; Schram, D.; Engeln, R., Formation and Relaxation of Rovibrationally Excited H_2 Molecules Due to Plasma-Surface Interaction. *Phys. Rev. E: Stat. Phys., Plasmas, Fluids,* **2008,** *78* (1), 016407.
43. Xiao, B.; Kado, S.; Kajita, S.; Yamasaki, D.; Tanaka, S., Rovibrational Distribution of H_2 in Low Temperature Plasma: The Dependence on the Plasma Parameters. *J. Nucl. Mater.* **2005,** *337*, 1082-1086.
44. Iordanova, S. In *Spectroscopic Temperature Measurements in Hydrogen Inductively-Driven Plasmas at Low Pressures*, Journal of Physics: Conference Series, IOP Publishing: 2008; p 012005.
45. Stutzin, G.; Young, A.; Döbele, H.; Schlachter, A. S.; Leung, K.; Kunkel, W., In Situ Density and Temperature Measurements of Vibrationally Excited Hydrogen Molecules in Ion Source Plasmas. *Rev. Sci. Instrum.* **1990,** *61* (1), 619-621.
46. Capitelli, M.; Gorse, C., Open Problems in the Physics of Volume H/Sup-//D/Sup-/Sources. *IEEE T Plasma Sci.* **2005,** *33* (6), 1832-1844.
47. Celiberto, R.; Janev, R.; Laricchiuta, A.; Capitelli, M.; Wadehra, J.; Atems, D., Cross Section Data for Electron-Impact Inelastic Processes of Vibrationally Excited Molecules of Hydrogen and Its Isotopes. *At. Data Nucl. Data Tables* **2001,** *77* (2), 161-213.
48. Wadehra, J., Dissociative Attachment to Rovibrationally Excited H_2. *Phys. Rev. A: At. Mol. Opt. Phys.* **1984,** *29* (1), 106.
49. Bonnie, J.; Eenshuistra, P.; Hopman, H., Scaling Laws for Atomic and Molecular Hydrogen in a Multicusp Ion Source. *Phys. Rev. A: At. Mol. Opt. Phys.* **1988,** *37* (4), 1121.
50. Stutzin, G.; Young, A.; Schlachter, A.; Leung, K.; Kunkel, W., In Situ Measurement of Rovibrational Populations of H_2 Ground Electronic State in a Plasma by VUV Laser Absorption. *Chem. Phys. Lett.* **1989,** *155* (4-5), 475-480.

51. Garg, R.; Anderson, T.; Lucht, R.; Fisher, T.; Gore, J., Gas Temperature Measurements in a Microwave Plasma by Optical Emission Spectroscopy under Single-Wall Carbon Nanotube Growth Conditions. *J. Phys. D: Appl. Phys.* **2008,** *41* (9), 095206.
52. Luque, J.; Crosley, D. R., Lifbase: Database and Spectral Simulation Program (Version 1.5). *SRI International Report MP* **1999,** *99* (009).
53. Luque, J.; Kraus, M.; Wokaun, A.; Haffner, K.; Kogelschatz, U.; Eliasson, B., Gas Temperature Measurement in CH_4/CO_2 Dielectric-Barrier Discharges by Optical Emission Spectroscopy. *J. Appl. Phys.* **2003,** *93* (8), 4432-4438.
54. Hanna, A. R.; Cuddy, M. F.; Fisher, E. R., Energy Partitioning and Its Influence on Surface Scatter Coefficients within Fluorinated Inductively Coupled Plasmas. *J. Vac. Sci. Technol., A* **2017,** *35* (5), 05C308.
55. Moon, S. Y.; Kim, D.; Gweon, B.; Choe, W., Spectroscopic Characterization of Rovibrational Temperatures in Atmospheric Pressure He/CH_4 Plasmas. *Phys. Plasmas* **2008,** *15* (10), 103504.
56. McCurdy, P. R.; Truitt, J. M.; Fisher, E. R., Pulsed and Continuous Wave Plasma Deposition of Amorphous, Hydrogenated Silicon Carbide from SiH_4/CH_4 Plasmas. *J. Vac. Sci. Technol., A* **1999,** *17* (5), 2475-2484.
57. Farley, D.; Stotler, D.; Lundberg, D.; Cohen, S. A., Modeling of Hydrogen Ground State Rotational and Vibrational Temperatures in Kinetic Plasmas. *J. Quant. Spectrosc. Radiat. Transfer* **2011,** *112* (5), 800-819.
58. Delzeit, L.; McAninch, I.; Cruden, B. A.; Hash, D.; Chen, B.; Han, J.; Meyyappan, M., Growth of Multiwall Carbon Nanotubes in an Inductively Coupled Plasma Reactor. *J. Appl. Phys.* **2002,** *91* (9), 6027-6033.
59. Meyyappan, M.; Delzeit, L.; Cassell, A.; Hash, D., Carbon Nanotube Growth by PECVD: A Review. *Plasma Sources Sci. Technol.* **2003,** *12* (2), 205.
60. Hash, D.; Meyyappan, M., Model Based Comparison of Thermal and Plasma Chemical Vapor Deposition of Carbon Nanotubes. *J. Appl. Phys.* **2003,** *93* (1), 750-752.
61. Hash, D.; Bose, D.; Govindan, T.; Meyyappan, M., Simulation of the DC Plasma in Carbon Nanotube Growth. *J. Appl. Phys.* **2003,** *93* (10), 6284-6290.
62. Hsu, W. L., Gas-Phase Kinetics During Microwave Plasma-Assisted Diamond Deposition: Is the Hydrocarbon Product Distribution Dictated by Neutral-Neutral Interactions? *J. Appl. Phys.* **1992,** *72* (7), 3102-3109.
63. Schwärzler, C.; Schnabl, O.; Laimer, J.; Störi, H., On the Plasma Chemistry of the C/H System Relevant to Diamond Deposition Processes. *Plasma Chem. Plasma Process.* **1996,** *16* (2), 173-185.
64. Lang, T.; Laimer, J.; Störi, H., Quasi-Equilibria of Gaseous Species in the CH System. *Diamond Relat. Mater.* **1994,** *3* (4-6), 470-475.
65. Hassouni, K.; Leroy, O.; Farhat, S.; Gicquel, A., Modeling of H_2 and H_2/CH_4 Moderate-Pressure Microwave Plasma Used for Diamond Deposition. *Plasma Chem. Plasma Process.* **1998,** *18* (3), 325-362.
66. Mechold, L.; Röpcke, J.; Duten, X.; Rousseau, A., On the Hydrocarbon Chemistry in a H_2 Surface Wave Discharge Containing Methane. *Plasma Sources Sci. Technol.* **2001,** *10* (1), 52.
67. Fridman, A., *Plasma Chemistry*. Cambridge University Press: 2008.
68. Astashkevich, S.; Käning, M.; Käning, E.; Kokina, N.; Lavrov, B.; Ohl, A.; Röpcke, J., Radiative Characteristics of 3p Σ, Π; 3d$\pi-$, $\Delta-$ States of H_2 and Determination of Gas

Temperature of Low Pressure Hydrogen Containing Plasmas. *J. Quant. Spectrosc. Radiat. Transfer* **1996,** *56* (5), 725-751.
69. Meichsner, J.; Schmidt, M.; Schneider, R.; Wagner, H.-E., *Nonthermal Plasma Chemistry and Physics*. CRC Press: 2012.
70. Moisan, M.; Barbeau, C.; Claude, R.; Ferreira, C.; Margot, J.; Paraszczak, J.; Sá, A.; Sauvé, G.; Wertheimer, M., Radio Frequency or Microwave Plasma Reactors? Factors Determining the Optimum Frequency of Operation. *J. Vac. Sci. Technol., B* **1991,** *9* (1), 8-25.
71. Flamm, D. L., Frequency Effects in Plasma Etching. *J. Vac. Sci. Technol., A* **1986,** *4* (3), 729-738.
72. Pastol, A.; Catherine, Y., Optical Emission Spectroscopy for Diagnostic and Monitoring of CH_4 Plasmas Used for a-C:H Deposition. *J. Phys. D: Appl. Phys.* **1990,** *23* (7), 799.
73. Kiehlbauch, M. W.; Graves, D. B., Temperature Resolved Modeling of Plasma Abatement of Perfluorinated Compounds. *J. Appl. Phys.* **2001,** *89* (4), 2047-2057.
74. Stillahn, J. M.; Fisher, E. R., CN Surface Interactions and Temperature-Dependent Film Growth During Plasma Deposition of Amorphous, Hydrogenated Carbon Nitride. *J. Phys. Chem. C* **2009,** *113* (5), 1963-1971.

CHAPTER 5

EMPLOYING OPTICAL EMISSION SPECTROSCOPY TO ELUCIDATE THE IMPACT OF TITANIUM DIOXIDE IN PLASMA ASSISTED CATALYSIS SYSTEMS

This chapter contains results to be submitted as a full paper under the same title to *Applied Catalysis B* by Tara L. Van Surksum and Ellen R. Fisher. Optical emission spectroscopy (OES) was employed to investigate gas-phase processes in H_2 and CH_4 plasma systems in the presence of a catalytic TiO_2 substrate. The introduction of TiO_2 into the discharge has minimal effect on the rotational temperature of H_2 [$T_R(H_2)$] in a 100% H_2 plasma but reduces $T_R(H_2)$ values by up to 300 K in a 100% CH_4 plasma. TR-OES studies echo energy partitioning results and reveal further details about the kinetics of H_2 formation and the impact of the catalyst on gas-phase processes. Comprehensive materials analysis of the catalyst before and after plasma exposure reveals that the H_2 plasma acts as primarily an etching system whereas competing etching and deposition processes may be occurring under some conditions in CH_4 plasma system. This work was supported by funding through the National Science Foundation (NSF CBET – 1803067) and the American Chemical Petroleum Research Fund (ACS PRF 59776 – ND6). I also thank the staff of the CSU Analytical Resources Core for assistance with the XPS and SEM analyses and the Dr. Justin Sambur research group for support with the Raman spectroscopy analyses.

5.1 Introduction

Plasma-assisted catalysis (PAC) has recently gained attention in the plasma community because of its enormous potential to enhance feed gas conversion.[1-3] Generally, PAC describes the coupling of a plasma with a catalyst for enhanced processing of the input gas stream to either

convert the feed gas mixture to another gas mixture or to grow a material from the precursor gas. For example, in plasma-enhanced chemical vapor deposition (PECVD) systems used for fabrication of carbon nanostructures, a hydrocarbon plasma is typically brought into contact with a catalyst (usually Ni, Fe, or Co).[4] PAC, however, is more traditionally used to describe waste gas stream processing such as for the abatement of volatile organic compounds[5-7] or hydrocarbon reforming for the production of value-added chemicals such as syngas or methanol.[8-10] Regardless of the end application, the underlying fundamental phenomena in PAC systems are still not well understood, reducing its overall utility.

To improve the utility of PAC, it is crucial to understand and optimize the underlying physicochemical mechanisms for their desired applications. Although many studies have focused on parametric optimization for increasing gas conversion efficiency,[11-14] relationships between plasma parameters and performance are ultimately poorly understood, making it tedious and time-consuming to try to reproduce similar results in different reactor setups. Few studies have actually addressed fundamental aspects of PAC systems. Specifically, the need for fundamental insight in this field requires an understanding of plasma generation and general operating conditions, catalyst selection (including consideration of both chemical and physical properties), and the interactions between the plasma and catalyst. Importantly, an understanding of how the plasma affects the catalyst properties and vice versa must also be construed to address current challenges with implementing PAC technologies. As such, fundamental investigations that probe the molecular-level processes in PAC are central to improving PAC processes.

Knowledge of the roles of gas-phase radicals and radical-surface interactions is key to understanding overall plasma chemistry. To further illuminate the effect of the catalyst on the plasma environment, it is vital to investigate the gas-phase chemistry of the plasma both with and

without a catalyst. Specifically, an understanding of how energy is partitioned into vibrational, rotational, and translational modes provides insight into formation mechanisms, decomposition pathways, and overall plasma chemistry. Figures of merit such as rotational and vibrational temperatures (T_R and T_V, respectively) describe the energetics of species within the plasma system. One study that examined the impact of a catalyst on internal plasma temperatures measured T_R and T_V of CH $A^2\Delta \rightarrow X^2\Pi$ in a packed bed dielectric barrier discharge (DBD) using optical emission spectroscopy (OES).[15] Nozaki *et al.* found that although T_R(CH) was dependent on the catalyst bed temperature, T_R(CH) remained unchanged upon addition of the catalyst to the reactor.[15] The explanation for this observation lies in the assumption that the rotational equilibrium of CH $A^2\Delta$ is reached within its radiative lifetime and that the *R* branches display a similar intensity distribution with or without the catalyst. In contrast, T_V(CH) increased significantly with bed temperature only when the Ni catalyst was present. Specifically, the relative intensity of the $\nu(2, 2)$ vibrational band remained independent of bed temperature but decreases in the $\nu(0, 0)$ and $\nu(1, 1)$ vibrational bands were observed as bed temperature increased only with the catalyst present. Consequently, the decreased contributions of the $\nu(0,0)$ and $\nu(1,1)$ vibrational bands to the overall spectral structure results in the observed increase in vibrational temperature in the presence of the catalyst. As the electric and optical properties (e.g., reduced field strength, average electron density, rotational temperature) were not affected by the presence of the Ni catalyst,[15-16] the authors hypothesize that the CH $A^2\Delta$ $\nu(0, 0)$ and $\nu(1, 1)$ states selectively react on the Ni surface.

We have previously investigated energy partitioning trends of CH $A^2\Delta \rightarrow X^2\Pi$ and H_2 $d^3\Pi_u \rightarrow a^3\Sigma_g^+$ in CH_4-based low pressure, inductively-coupled plasmas as functions of plasma parameters (Chapters 3 and 4, respectively).[17-18] An overview of the internal temperature values

and parameter trends determined from 100% H_2 and 100% CH_4 plasmas sans catalyst are displayed in Table 5.1. Notably, T_V(CH) was higher than T_R(CH) regardless of gas mixture, pressure, or power, and both T_V(CH) and T_R(CH) decreased with increasing pressure, suggesting collisional quenching. T_R(CH) values were also nominally much higher than T_R(H_2) values in a 100% CH_4 plasma system, Table 5.1. Moreover, studies using a 100% H_2 plasma reveal relatively low T_R(H_2) values (~500 – 550 K) with virtually no trends with respect to system pressure and power.[18] These disparate values and trends may be attributed to a combination of the differences in species densities, radiative lifetimes, and their excitation pathways. In this work, we expand on these fundamental studies by introducing a TiO_2 catalyst to H_2 and CH_4 plasmas. We examine the impact of the plasma on the catalyst by exploiting chemical and morphological characterization techniques to assess the material prior to and post plasma exposure. Additionally, we investigate the impact of the catalyst on gas phase chemistry via OES, which allows us to non-intrusively probe the energetic and kinetic characteristics of the system. T_R and T_V are measured for three excited state species (CH, H_2, OH) and are discussed in comparison to values obtained without a catalyst.

5.2 Results

A major focus of this work is to investigate fundamental plasma-catalyst interactions in environmentally relevant systems. Our multi-pronged approach towards unravelling complex PAC environments involves an investigation of both the gas phase processes and an analysis of the catalyst's chemical and morphological properties. Raw OES spectra of a H_2 plasma (10% Ar) show emission arising from atomic and molecular hydrogen species and Ar species, Figure 5.1a. With a TiO_2 substrate present, additional spectral peaks are observed, arising from OH and CO emission, Figure 5.1b. As these species are not detected above experimental noise in the

Table 5.1. Internal temperature values and trends from 100% H_2 and 100% CH_4 plasmas sans catalyst (reported previously).[17-18]

	100% H_2	100% CH_4		
	$T_R(H_2)$	$T_R(H_2)$	$T_R(CH)$	$T_V(CH)$
internal temperature value range (K)	~500 – 550	~500 – 700	~1750 – 2350	~2280 – 3440
pressure increase (100 mTorr → 200 mTorr)	no trend	increases	decreases	decreases
power increase (25 W → 125 W)	no trend	decreases	trend dependent on system pressure	trend dependent on system pressure

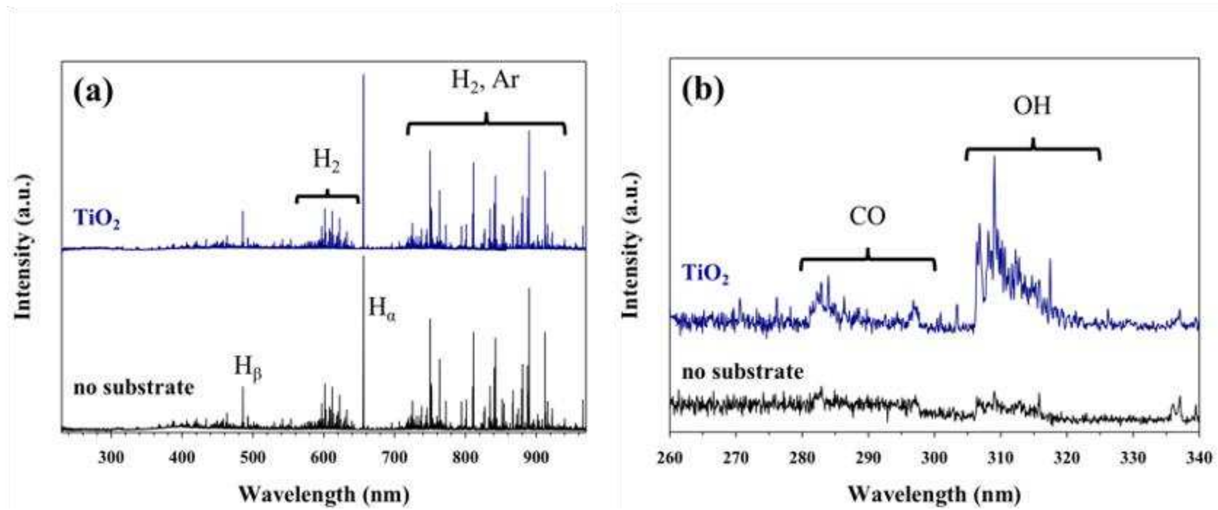

Figure 5.1. Raw OES spectra of H_2 plasma (*p* = 100 mTorr, *P* = 100 W, *t* = 30 s) collected coaxially without a substrate and with a TiO_2 substrate: (a) full spectral range and (b) expanded view of the 260 – 340 nm range.

substrate-free system, OH production likely occurs through removal of oxygen from the TiO_2 catalyst and the small amounts of $CO_{(g)}$ also likely arise via interaction of gas-phase species with adventitious carbon on the catalyst surface.

Further spectral comparison via inert gas actinometry elucidates details about relative densities of excited state species (denoted here with brackets, e.g. [OH]). For these studies, emissions from OH (309.0 nm), H_α (656.5 nm), H_2 (601.8 nm), and Ar (750.4 nm) were monitored. Actinometry studies were performed for several power conditions in H_2 plasmas (p = 100 mTorr) both with and without TiO_2 for 5 min immediately following plasma ignition. Measurements were made at two locations, in the coil region directly above the substrate (cross-sectional) and downstream (coaxial). Figure 5.2a shows [OH] as a function of time (p = 100 mTorr, P = 100 W) with and without TiO_2 present in the reactor. Notably, [OH] is nearly zero without the substrate; however, when TiO_2 is introduced into the plasma [OH] is initially greater than the no substrate system, then decreases as a function of time. After ~2 min of plasma on time, the [OH] is within error of the no substrate system and essentially zero for all P studied. Actinometry results from the coil region demonstrate that [OH] may be only slightly elevated compared to the coaxially collected data, suggesting that when OH is formed from plasma-substrate substrate interactions it likely remains intact as it travels downstream in the reactor.

Actinometric analysis of hydrogen species in the plasma provides insight on the impact of TiO_2 on gas phase properties. [H_2] remained relatively constant as a function of time (Figure 5.2b), and both the addition of the catalyst and the measurement location essentially has no effect on [H_2]. Yet, the atomic hydrogen density is significantly elevated in the coil region compared to the coaxially collected data, Figure 5.2c. This is expected given the constant source of H_2 gas, which can dissociate to form H in the coil region of the reactor. Moreover, [H] does not change

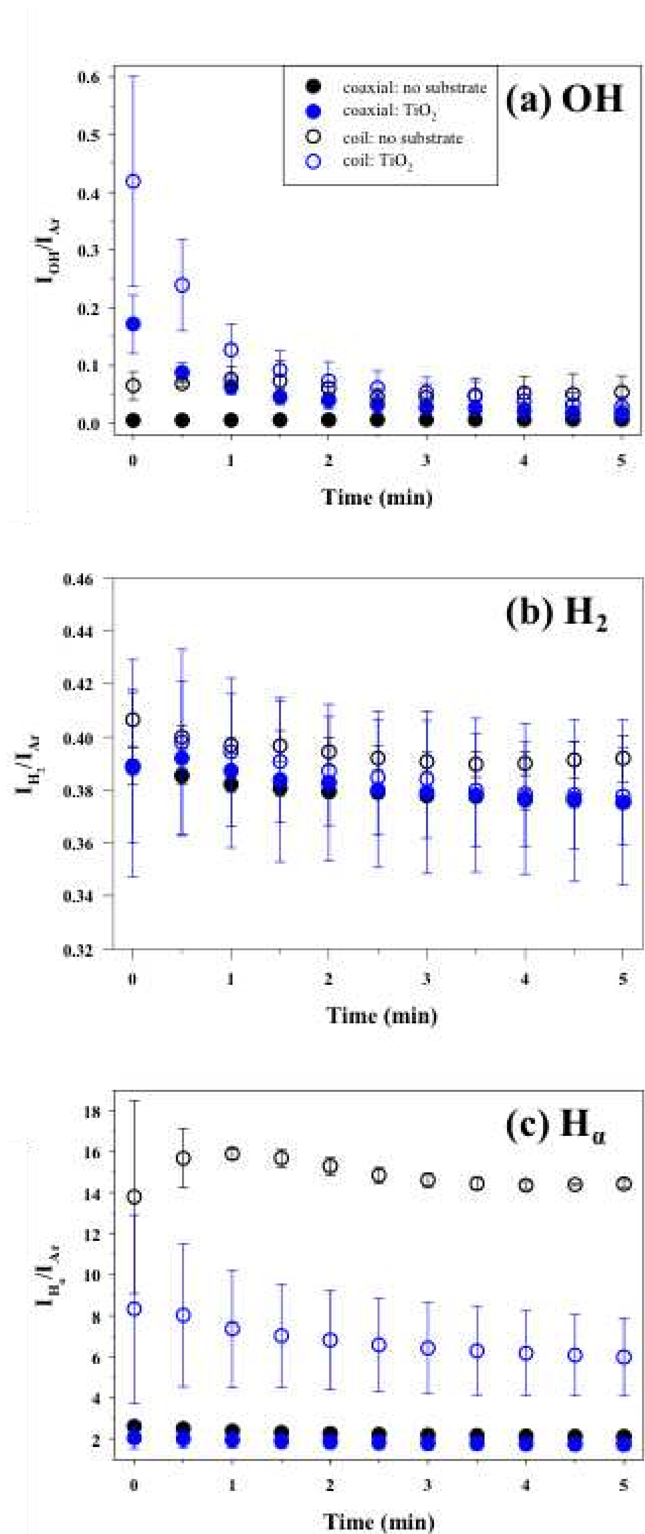

Figure 5.2. Relative density from OES spectra collected coaxially and in the coil region of the reactor as a function of time in an H_2 plasma (p = 100 mTorr, P = 125 W) with and without a TiO_2 substrate for (a) OH (b) H_2, and (c) H_α.

appreciable during the 5-min data collection time. This suggests that H_2 decomposes in the coil region and H is not likely to recombine to form H_2 there, but it may undergo deexcitation or other recombination processes as it continues downstream, leading to the lower density observed with coaxially collected OES data, Figure 5.2c. With the TiO_2 substrate, [H] measured coaxially (i.e. downstream) is slightly lower than the substrate-free system, albeit within error. In the coil region, however, [H] is significantly lower in the presence of the catalyst, indicating that H atoms are likely interacting with the substrate (e.g. to produce the observed $OH_{(g)}$).

To gain further insight into the plasma-substrate interactions and gas-phase processes, the energetics of plasma species can be evaluated as functions of plasma parameters. T_R(OH) and T_V(OH) values were determined via spectral simulation with LIFBASE, where all fits had peak correlation (PC) values ≥ 0.89. OES data collected 30 s after plasma ignition was used for determination of T_R(OH) and T_V(OH) because OH emission signal was prominent at this time point. Unfortunately, raw OH data could not be analyzed at low P (P = 25–50 W) or high p (p = 200 mTorr) because of limited signal intensity under these conditions. Figure 5.3 shows a representative fit of the OH $A^2\Sigma^+ \rightarrow X^2\Pi$ transition (p = 100 mTorr, P = 100 W), giving rise to T_R(OH) = 2550 K and T_V(OH) = 4600 K and with a PC value of 0.96. Although PC values are fairly high for each individual spectrum, indicating reasonable agreement between the experimental data and corresponding simulation, standard deviation weighs in as high as 16% in some cases, as listed in Table 5.2. Although challenging to illicit trends from these data, we are able to ascertain an order of magnitude for T_R(OH) and T_V(OH) and can compare these values to $T_R(H_2)$ in the same plasma system and other T_R(OH) and T_V(OH) values reported in the literature.[19-22]

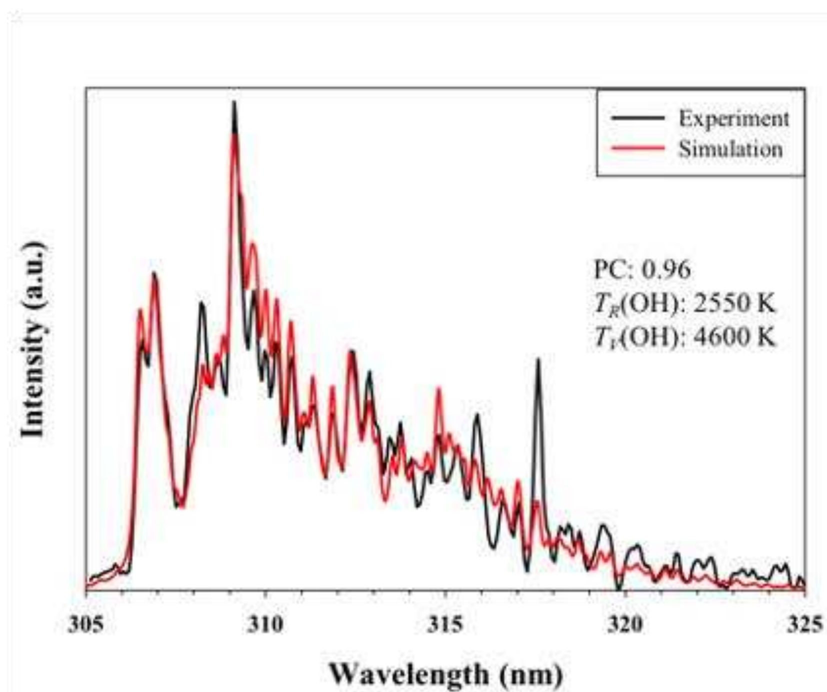

Figure 5.3. Representative emission spectrum collected coaxially for OH $A^2\Sigma^+ \rightarrow X^2\Pi$ in a H_2 plasma with a TiO_2 substrate (p = 100 mTorr, P = 100 W).

Table 5.2. T_R(OH) and T_V(OH) values obtained from a H_2 plasma with a TiO_2 substrate.[a]

p (mTorr)	P (W)	T_R (K)	T_V (K)
100	75	3680 (150)	4020 (40)
	100	2940 (480)	4430 (250)
	125	3370 (290)	4360 (180)
150	75	3740 (130)	4110 (40)
	100	3520 (450)	4310 (220)
	125	3680 (230)	4150 (20)

[a]Values in parentheses represent standard deviation calculated from the mean of n ≥ 3 trials.

To better understand these gas phase trends and the impact of plasma processing on the catalyst, the substrates were analyzed before and after plasma exposure. Figure 5.4 shows representative FTIR spectra of untreated (UT) and H_2 plasma treated (p = 100 mTorr, P = 100 W, t = 5 min) TiO_2 substrates. The adsorption bands at 3400 cm^{-1} and 1630 cm^{-1} are assigned to stretching bands for O-H surface hydroxyl groups and H-O-H physically adsorbed water, respectively.[23] Symmetric and asymmetric stretching of $-CH_2$ is observed in the 2830 – 2990 cm^{-1} region for the UT material.[24] The large absorption band below 1000 cm^{-1} is assigned to Ti-O-Ti stretching vibration of the interconnected octahedral [TiO_6].[23] Some differences worth noting appear when comparing the two spectra. First, the disappearance of the $-CH_2$ peaks and the significant reduction of the O-H stretching band after plasma exposure suggests removal of impurities or cleaning of the material surface by the plasma. Moreover, narrowing of the Ti-O-Ti stretching absorption band post plasma exposure suggests the creation of a more uniform lattice environment and removal of excess impurities.

We employed XPS to further investigate the chemical composition of the surface of our catalysts before and after H_2 plasma exposure. Survey scans conducted on all of the substrates showed the presence of titanium, oxygen, and carbon prompting the collection of high-resolution data for the Ti_{2p}, O_{1s}, and C_{1s} binding environments for each spot. Elemental compositions, listed in Table 5.3, show a decrease in the amount of carbon after H_2 plasma exposure. The amount of titanium decreases slightly at high P and longer plasma exposure times (P = 100 W, 125 W, t = 5 min and P = 125 W, t = 10 min). Additionally, an increase in %O is noted after H_2 plasma exposure at all conditions except for P = 25 W, t = 5 min. Representative high resolution Ti_{2p}, O_{1s}, and C_{1s} XPS spectra prior to and post H_2 plasma exposure (p = 100 mTorr, P = 150 W, t = 1 min) are shown in Figure 5.5. High resolution Ti_{2p} spectra of the UT TiO_2 material, Figure

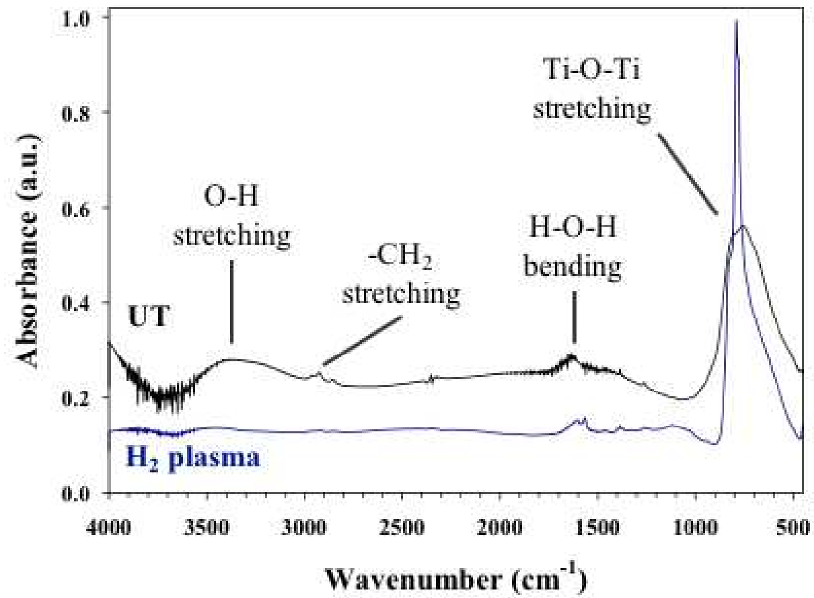

Figure 5.4. FTIR spectra of untreated and H_2 plasma treated (p = 100 mTorr, P = 100 W, t = 5 min) TiO_2 substrates.

Table 5.3. XPS atomic composition data for a TiO_2 substrate exposed to a 100% H_2 plasma (p = 100 mTorr).[a]

Plasma Exposure Time	*P* (W)	C [%]	O [%]	Ti [%]
—	—	10.9 (2.3)	63.6 (1.4)	25.5 (1.2)
1 min	125	5.6 (0.4)	68.7 (0.9)	25.7 (0.6)
5min	25	9.6 (1.9)	65.0 (1.4)	25.3 (0.6)
	75	5.2 (0.5)	70.3 (0.9)	24.5 (0.9)
	100	4.8 (0.9)	72.0 (1.1)	23.2 (0.8)
	125	3.4 (0.6)	75.9 (3.5)	20.7 (2.9)
10 min	125	3.2 (0.5)	76.2 (1.5)	20.6 (1.5)

[a] Errors are the standard deviation of the mean of 3 measurements on n ≥ 2 samples.

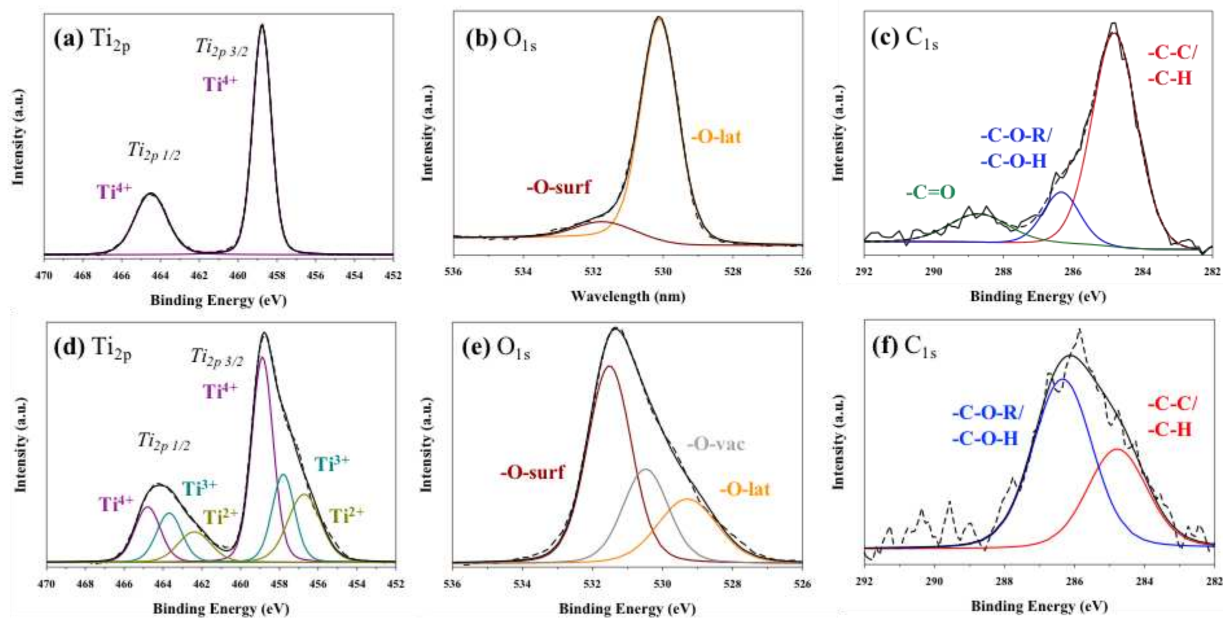

Figure 5.5. High resolution Ti_{2p} (a,d), O_{1s} (b,e), and C_{1s} (c,f) XPS spectra for untreated (top row) and H_2 plasma treated (bottom row) TiO_2 substrates (p = 100 mTorr, P = 125 W, t = 1 min).

5.5a, show peaks for $Ti_{2p3/2}$ and $Ti_{2p1/2}$ at binding energies of 458.8 eV and 464.7 eV, respectively, corresponding to surface titanium in the Ti^{4+} oxidation state.[25-26] In some cases, Ti^{4+} was reduced (i.e., Ti^{3+} or Ti^{3+} and Ti^{2+} binding environments noted in addition to Ti^{4+}) after H_2 plasma exposure whereas in other cases, the Ti_{2p} binding environment remained nominally unchanged post H_2 plasma exposure (i.e., only Ti^{4+} binding environments present). Reduction of Ti^{4+} was not dependent on plasma parameters and was somewhat inconsistent between spots on a single sample and/or different samples produced under the same plasma conditions. Figure 5.5d shows an example Ti_{2p} high resolution spectrum of a spot where Ti^{4+} is reduced to Ti^{3+} (457.8 eV and 463.6 eV) and Ti^{2+} (456.7 eV and 462.4 eV) oxidation states. The primary contribution to the O_{1s} spectra in the UT TiO_2 arises from lattice bound oxygen (or bound to Ti^{4+}) (529.2 eV), Figure 5.5b, with a smaller peak assigned to oxygen adsorbed to the material surface, such as hydroxyl species (531.5 eV).[25, 27] When Ti is reduced, an additional binding environment appears after hydrogen plasma exposure at 530.5 eV, corresponding to oxygen vacancies (e.g., Ti_2O_3).[27] Here, an increase of adsorbed surface oxygen post H_2 plasma processing, Figure 5.5e, is also observed, presumably as a result of the plasma creating oxygen vacancies within the TiO_2 lattice, which ultimately decreases the relative contribution of bound oxygen.[25, 28] High resolution C_{1s} spectra for the UT material, Figure 5.5c, show binding environments for -C-C/-C-H (284.8 eV), -C-O-R/-C-O-H (286.3 eV), and -C=O (288.7 eV). The reduction in percent carbon after plasma exposure suggests removal of adventitious carbon, Table 5.3. Although it is difficult to elucidate specific binding environments with the low C signal, we believe binding environments attributed to -C-C/-C-H (284.8 eV) and -C-O-R/-C-O-H (286.3 eV) are still present in the H_2 plasma treated material (Figure 5.5f).

As H_2 plasmas are generally considered etching systems, we also investigated the impact of a clearly depositing system (i.e. 100% CH_4 plasmas) on the catalyst. XPS atomic composition data, Table 5.4, demonstrate a significant increase in %C post CH_4 plasma exposure. Moreover, the %C on the surface is highly dependent on plasma parameters. For example, a TiO_2 substrate exposed to a 100% CH_4 plasma at fairly mild conditions (p = 100 mTorr, P = 25 W, t = 30 s) results in 51.2% C whereas 91.7% C is measured under more intense depositing conditions (p = 200 mTorr, P = 125 W, t = 2 min). Consequently, this drastically changes the O and Ti atomic compositions at the material surface. Interestingly, a slight increase in %Ti is observed from the samples treated for 30 s compared to those exposed to the plasma for 2 min, except at p = 200 mTorr, P = 125 W where no Ti was detected. This likely indicates competing etching and depositing regimes occurring in this system, with deposition winning out as the process time lengthens and/or the applied rf power and system pressure are increased.

Further details about the types of films deposited or the possible etching processes occurring in CH_4 plasmas can be elucidated from the high resolution XPS spectra. Figure 5.6a shows high resolution Ti_{2p} spectra of an UT TiO_2 substrate and TiO_2 substrates after a 2 min exposure to a 100% CH_4 plasma under several pressure and power conditions. As stated above, binding energies for $Ti_{2p3/2}$ and $Ti_{2p1/2}$ are present at 458.6 eV and 464.2 eV, respectively, corresponding to surface titanium in the Ti^{4+} oxidation state.[25-26] Additionally, contributions from the Ti^{3+} binding environment are noted at 457.9 eV and 462.5 eV for materials treated at p = 200 mTorr, P = 25 W.[25] High resolution O_{1s} spectra, Figure 5.6b, show contributions from lattice bound oxygen at 530.2 eV and adsorbed oxygen species at 532.1 eV for the UT material and after CH_4 plasma exposure.[29-30] The TiO_2 substrates exposed to a CH_4 plasma have an additional peak at 533.3 eV, corresponding to oxygen singly bound to carbon in ethers.[30]

Table 5.4. XPS atomic composition data for a TiO_2 substrate exposed to a 100% CH_4 plasma.[a]

Plasma Exposure Time	*p* (mTorr)	*P* (W)	C [%]	O [%]	Ti [%]
—	—	—	10.9 (2.3)	63.6 (1.4)	25.5 (1.2)
30 sec	100	25	51.2 (4.4)	48.1 (4.3)	< 1%
		125	87.9 (2.8)	9.1 (2.0)	3.0 (0.8)
	200	25	84.8 (1.2)	14.9 (0.8)	< 1%
		125	91.3 (2.1)	7.7 (1.6)	< 1%
2 min	100	25	77.4 (6.4)	17.6 (4.4)	5.1 (2.0)
		125	61.9 (12.8)	27.8 (8.7)	10.3 (4.2)
	200	25	78.4 (2.4)	18.1 (1.3)	3.6 (1.3)
		125	91.7 (0.4)	8.4 (0.4)	—

[a] Errors are the standard deviation of the mean of 3 measurements on $n \geq 2$ samples.

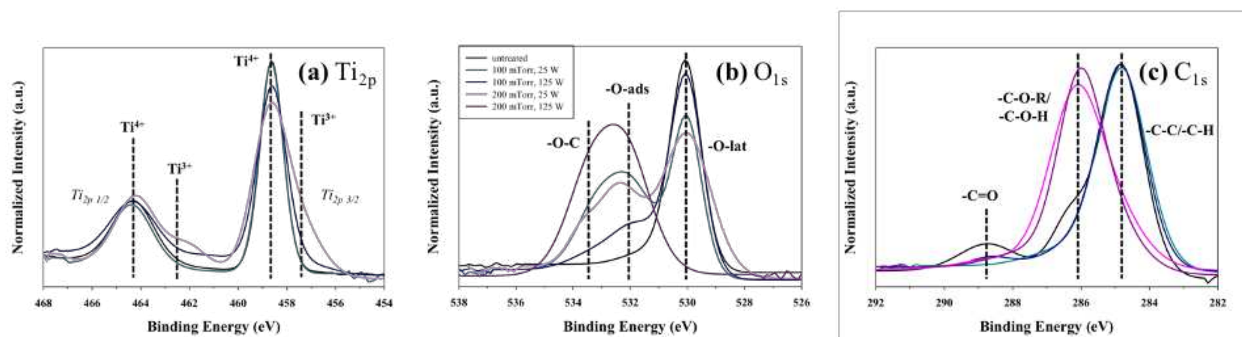

Figure 5.6. High resolution (a) C_{1s}, (b) O_{1s}, and (c) Ti_{2p} spectra of TiO_2 substrates prior and post CH_4 plasma exposure ($t = 2$ min).

Notably, the spectrum acquired under conditions with no detectable Ti in the elemental composition data (p = 200 mTorr, P = 125 W) shows no lattice bound oxygen species, only adsorbed oxygen species and oxygen bound to carbon. High resolution C_{1s} spectra, Figure 5.6c, display three specific binding environments corresponding to -C-C/-C-H (284.8 eV), -C-O-C/-C-O-H (286.6 eV), and -C=O (288.7 eV).[29] After CH_4 plasma exposure, the -C=O contribution decreases significantly, regardless of treatment parameters. Moreover, with p = 200 mTorr, the -C-O-R/-C-O-H contribution increases dramatically relative to the p = 100 mTorr treatment, dominating the spectra for both low and high P treatments.

Raman data, Figure 5.7, also demonstrate the presence of an amorphous hydrocarbon film on the TiO_2 after CH_4 plasma exposure. Figure 5.7a shows Raman spectra for UT TiO_2 and TiO_2 treated with a 100% CH_4 plasma (p = 200 mTorr) at different P. Anatase TiO_2 has six Raman active modes (3 E_g + 2 B_{1g} + 1 A_{1g}).[31-32] The three E_g modes correspond to the high intensity band at 136 cm^{-1} and the lower intensity bands at 196 and 638 cm^{-1}. Additionally, the doublet band at 515 cm^{-1} corresponds to the A_{1g} and B_{1g} modes, and the band at ~396 cm^{-1} belongs to the B_{1g} mode.[31-32] Peaks at 429 cm^{-1}, 608 cm^{-1}, and 1100 cm^{-1} arise from the glass substrate. Figure 5.7a demonstrates carbon deposition via the appearance of the D-band and G-band for plasma parameters associated with the most intense deposition conditions in our CH_4 plasma systems (high p, high P). In conjunction with the presence of the D-band and G-band, the more intense deposition parameters also appear to coincide with overall minimized TiO_2 bands.

Figure 5.7b displays an expanded view of the E_g band at ~135 cm^{-1}. The E_g peaks correlate to the symmetric stretching vibration of O-Ti-O in TiO_2;[33-34] thus, they are very sensitive to local oxygen coordination surrounding the metal ion. Here, we note a general shift

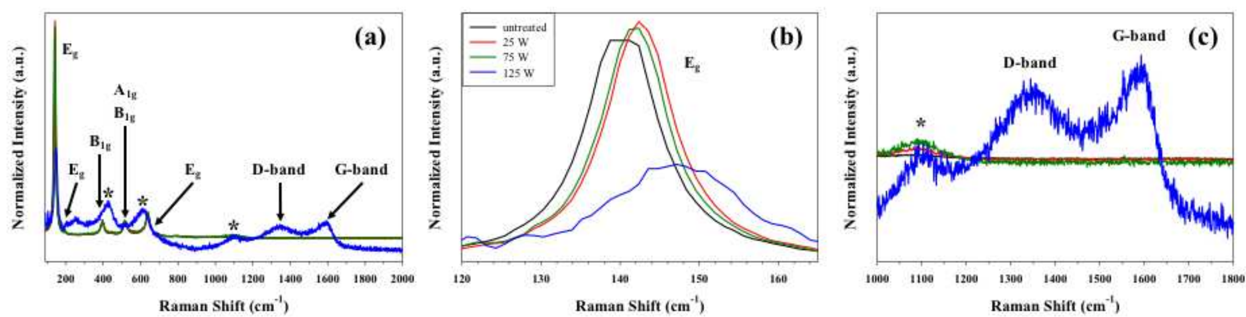

Figure 5.7. (a) Raman spectra of TiO_2 substrates [untreated and treated with a 100% CH_4 plasma at three applied rf powers (p = 200 mTorr, t = 2 min)]. Expanded views of the (b) E_g peak and the (c) D-band/G-band region. Asterisk (*) represents signal from glass slide substrate.

and broadening of the E_g peak at ~135 cm^{-1} to higher wavenumbers for the plasma treated substrate relative to the untreated TiO_2. For example, the higher *P* plasma treatment (*P* = 125 W) results in the largest E_g peak shift, 7 cm^{-1}, whereas the milder plasma treatments (*P* = 25 W and *P* = 50 W) result in less peak shifting, 1 – 3 cm^{-1}, relative to the untreated TiO_2. Nevertheless, these data demonstrate that CH_4 plasma exposure affects the underlying material beyond deposition of an amorphous hydrocarbon film over the surface of the material.

Figure 5.7a further demonstrates that carbon deposition throughout the material is observed via the appearance of the D-band and G-band for plasma parameters associated with the most intense deposition conditions (high *p*, high *P*). In conjunction with the presence of the D-band and G-band, these deposition parameters also appear to coincide with overall minimized TiO_2 bands. Figure 5.7c shows an expanded view of the D-band/G-band region for untreated TiO_2 and TiO_2 post CH_4 plasma exposure at *p* = 200 mTorr and several *P* conditions. Notably, the D-band and G-band are only present in the spectra acquired from the *P* = 125 W plasma treated substrate.

As substrate morphology can impact overall PAC interactions, we used SEM to evaluate material morphology of the UT and plasma treated TiO_2 materials. A representative SEM image of the UT material, Figure 5.8a, highlights the porous morphological nature of the TiO_2 nanoparticle agglomerates. Figures 5.8b and 5.8c show representative SEM images of the catalyst after exposure to 100% H_2 (*p* = 100 mTorr, *P* = 100 W, *t* = 5 min) and 100% CH_4 (*p* = 150 mTorr, *P* = 125 W, *t* = 2 min) plasmas, respectively. The morphology characteristic of the UT TiO_2 material does not change appreciably after exposure plasma, regardless of *p* or *P*, for the parameter space reported herein.

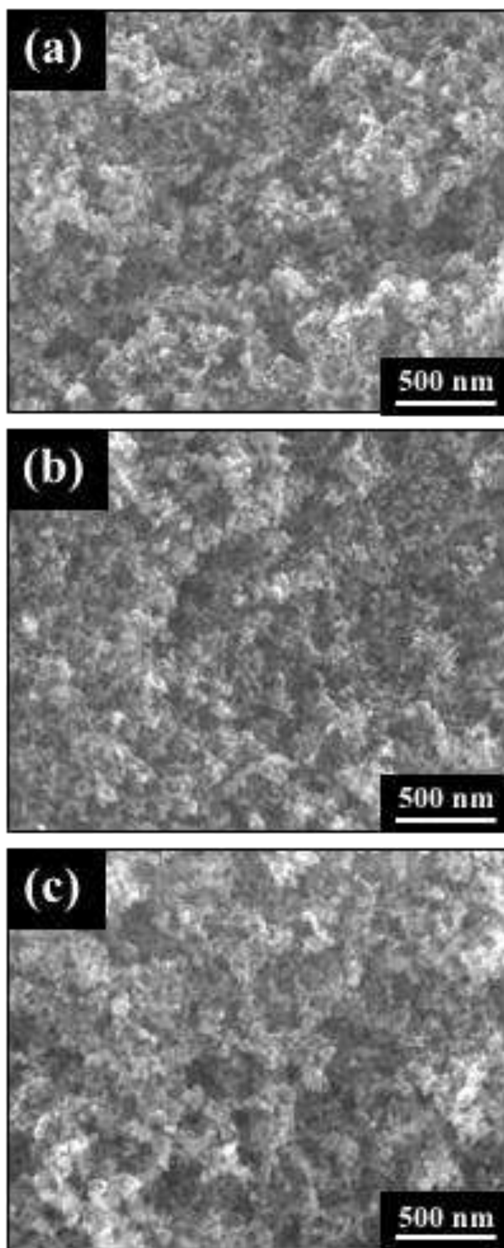

Figure 5.8. Representative SEM images (50000x) of (a) untreated (b) H_2 plasma treated (p = 100 mTorr, P = 125 W, t = 5 min) and (c) CH_4 plasma treated (p = 150 mTorr, P = 125 W, t = 2 min) TiO_2 substrates.

Clearly, H_2 and CH_4 plasmas differentially impact the resulting catalyst chemistry; thus, we compare and contrast the impact of the catalyst on gas phase chemistry in these two systems. We have previously investigated energy partitioning trends of $T_R(H_2)$ in H_2 and CH_4 plasmas (no substrate) to elucidate probable mechanisms of H_2 formation.[18] Here, we utilized TR-OES to further delve into these fundamental processes by studying the first few seconds immediately following plasma ignition in H_2 and CH_4 plasmas with and without TiO_2. Figure 5.9 shows a comparison of the temporal emission profiles of H_2 in the two plasma systems with and without a catalyst. In a 100% H_2 plasma, the rise to maximum intensity and subsequent steady state emission for H_2 (Figure 5.9a) occurs within the first 0.1 s of plasma ignition. Conversely, the rise to a steady state for H_2 takes several seconds in a CH_4 plasma without a substrate. The overall characteristics of the temporal profiles do not change appreciably upon the addition of a TiO_2 substrate to the 100% H_2 plasma (Figure 5.9c). In contrast, the TiO_2 dramatically alters the temporal profile of H_2 emission in the 100% CH_4 plasma (Figure 5.9d). Here, the temporal profile mirrors the 100% H_2 plasma system, with a sharp rise within < 0.1 s. These TR-OES data provide essential insight into plasma ignition processes and potential species formation mechanisms; however, evaluation of species energetics is also a key component to understanding fundamental plasma processes during PAC.

T_R values of excited state H_2 are plotted in Figure 5.10 as a function of P for both H_2 and CH_4 plasmas with and without TiO_2. At $p = 100$ mTorr, Figure 5.10a, $T_R(H_2)$ values have a narrow range of ~500 – 550 K, display minimal power dependence, and remain constant with and without a TiO_2 catalyst in the 100% H_2 plasma system. Conversely, the $T_R(H_2)$ values in a 100% CH_4 plasma without a substrate at $p = 100$ mTorr, Figure 5.10a, decrease with increasing P, with $T_R(H_2)$ = ~580 K and ~500 K at P = 25 W and 125 W, respectively. Addition of the

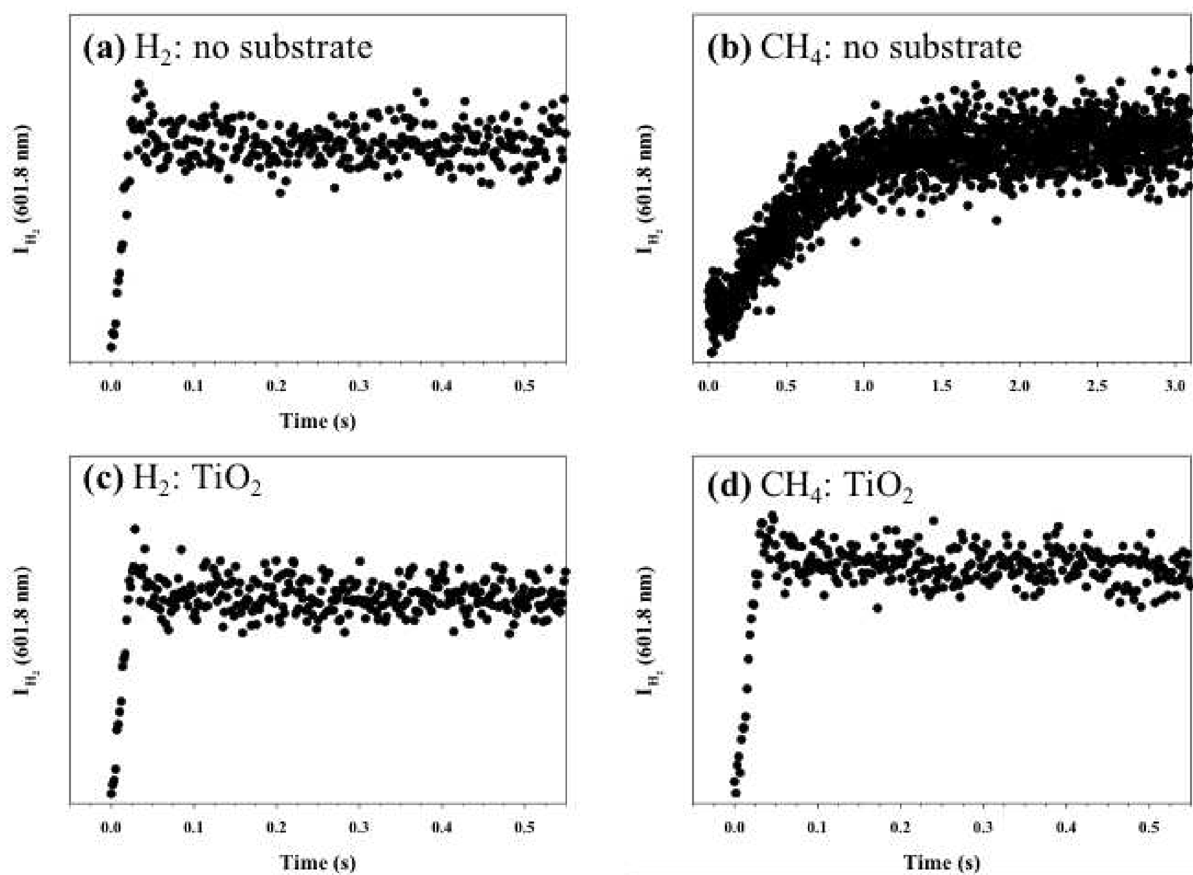

Figure 5.9. Temporal profiles of H_2 emission in a H_2 plasma (a,c) and a CH_4 plasma (b,d) without a substrate (a,b) and with a TiO_2 substrate (c,d) at *p* = 100 mTorr, *P* = 125 W.

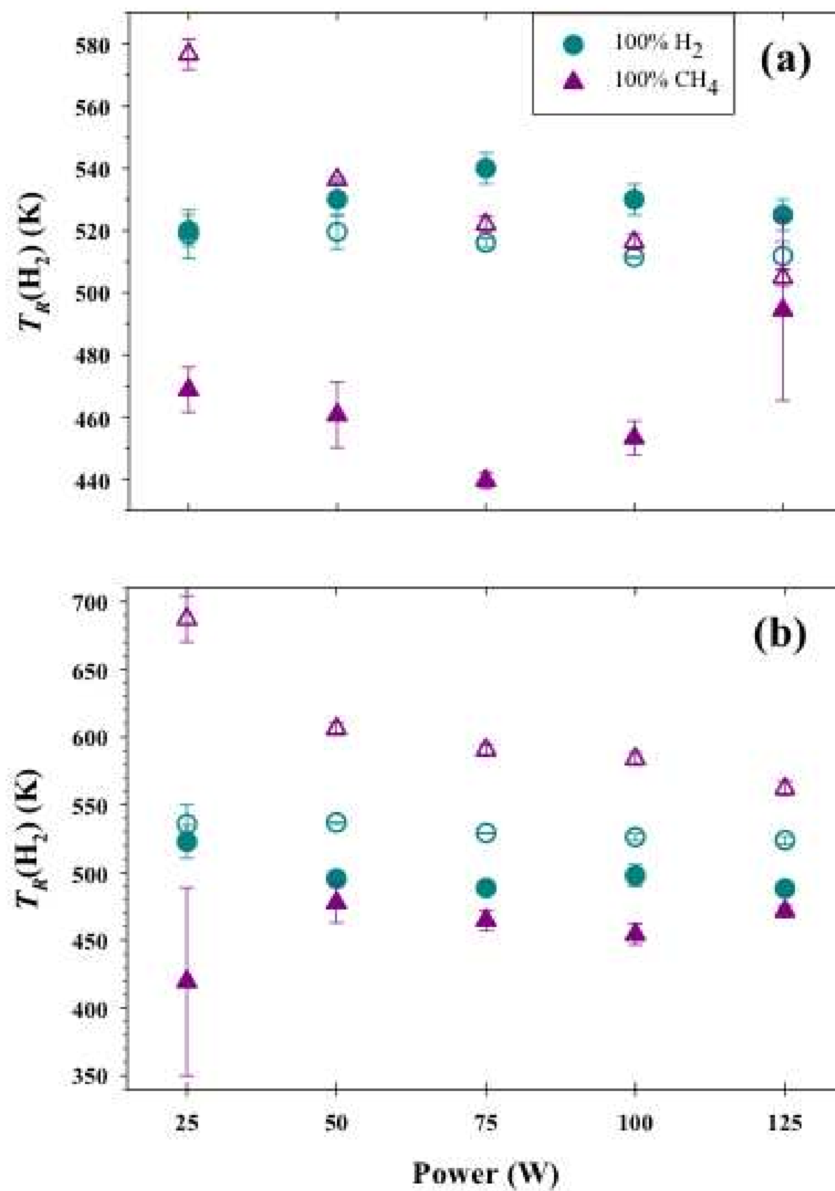

Figure 5.10. $T_R(H_2)$ data as a function of applied rf power for 100% H_2 and 100% CH_4 plasma systems without (open symbols) and with (closed symbols) a TiO_2 substrate at (a) p = 100 mTorr and (b) p = 200 mTorr. Values for $T_R(H_2)$ without substrate were previously reported.[18]

catalyst results in a notable decrease in $T_R(H_2)$, with values of ~400 – 480 K and minimal P dependence at p = 100 mTorr. Similar trends are noted in the higher-pressure system (p = 200 mTorr), Figure 5.10b, with $T_R(H_2)$ values elevated somewhat by ~100 – 200 K for the CH_4 plasma system (no substrate). Overall, $T_R(H_2)$ values at p = 200 mTorr for a 100% H_2 plasma are similar to those at p = 100 mTorr. Nevertheless, at $P \geq 50$ W, $T_R(H_2)$ values are reduced slightly compared to the no substrate system. Numerical values for all conditions studied with TiO_2 are listed in Table 5.5 and range from ~400 – 700 K over the entire parameter space. $T_R(H_2)$ values for the no substrate systems (both H_2 and CH_4) have been previously reported.[18]

To further demonstrate the impact of the catalyst on energy partitioning, T_R(CH) is plotted as a function of P at two different pressures in Figure 5.11a, and T_R(CH) values for the entire parameter space are reported in Table 5.6. At p = 100 mTorr, T_R(CH) values are decreased by ~100 – 200 K with a TiO_2 catalyst except at P = 50 W. Interestingly, an increase in system pressure to ≥150 mTorr, results in T_R(CH) values comparable to those in the no substrate system. Notably, T_R(CH) values also decrease concomitantly with an increase in system pressure, a trend we previously reported for 100% CH_4 plasmas without a substrate.[17] These results demonstrate the significant impact that catalysts can have on rotational energy partitioning in PAC systems.

Additionally, we determined T_V(CH) for the same parameter space, Table 5.6, where values range from ~2000 – 3100 K. Figure 5.11b shows T_V(CH) for a CH_4 plasma system without and with a TiO_2 substrate at two different pressures. At p = 100 mTorr, T_V(CH) is significantly reduced (~300 K – 1200 K) upon addition of the catalyst to the discharge. This trend generally holds true at each pressure (p = 100 – 200 mTorr). Pressure and power trends for T_V(CH) are also worth noting here as T_V(CH) values generally decrease with increasing p for CH_4 plasmas. The P dependence demonstrates a more complex trend wherein T_V(CH) decreases

Table 5.5. $T_R(H_2)$ (K) values in 100% H_2 and 100% CH_4 plasma systems.[a]

p (mTorr)	*P* (W)	H_2 plasma		CH_4 plasma	
		no substrate[b]	TiO_2	no substrate[b]	TiO_2
100	25	520 (10)	520 (5)	575 (5)	470 (10)
	50	520 (5)	530 (5)	535 (5)	460 (10)
	75	515 (5)	540 (5)	520 (5)	440 (5)
	100	510 (5)	530 (5)	515 (5)	455 (10)
	125	510 (5)	525 (5)	505 (5)	495 (30)
150	25	530 (20)	540 (20)	605 (10)	460 (20)
	50	525 (5)	545 (10)	590 (15)	450 (10)
	75	530 (5)	550 (15)	565 (5)	470 (5)
	100	525 (5)	525 (5)	560 (5)	455 (15)
	125	525 (5)	525 (5)	535 (5)	450 (10)
200	25	535 (15)	520 (15)	690 (20)	420 (70)
	50	535 (5)	500 (10)	605 (5)	480 (15)
	75	530 (5)	490 (5)	590 (5)	465 (10)
	100	525 (5)	500 (10)	585 (5)	455 (10)
	125	525 (5)	490 (5)	560 (5)	470 (5)

[a]Values in parentheses represent standard deviation calculated from the mean of $n \geq 3$ trials.
[b]"No substrate" values reported previously.[18]

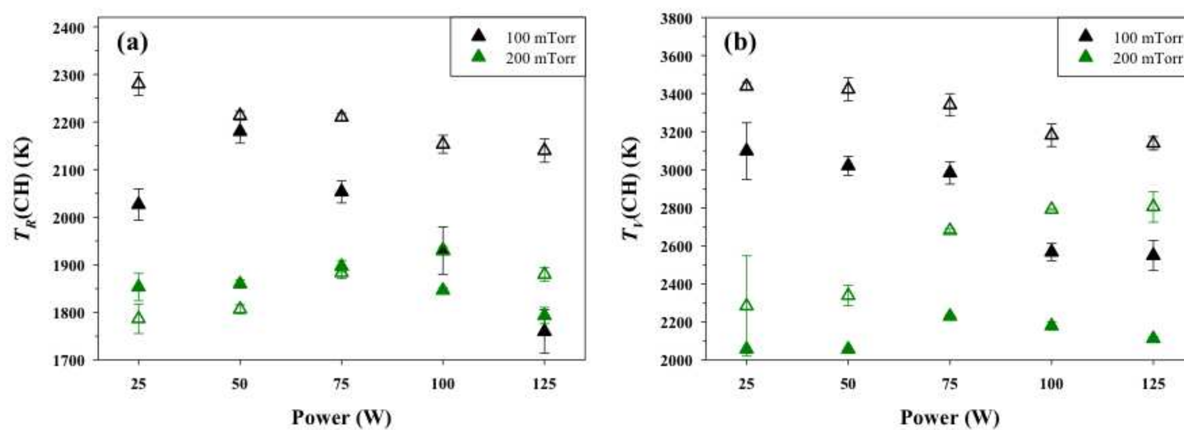

Figure 5.11. (a) T_R(CH) and (b) T_V(CH) as a function of *P* for a 100% CH_4 plasma without (open triangles) and with a TiO_2 substrate (closed triangles). Values for T_R(CH) and T_V(CH) without substrate were previously reported.[17]

Table 5.6. T_R(CH) and T_V(CH) values in a 100% CH_4 plasma with a TiO_2 substrate.[a]

p (mTorr)	P (W)	T_R (K)		T_V (K)	
		no substrate[b]	TiO_2	no substrate[b]	TiO_2
100	25	2280 (20)	2030 (30)	3440 (20)	3100 (150)
	50	2210 (10)	2180 (20)	3420 (60)	3020 (50)
	75	2210 (10)	2050 (20)	3340 (60)	2980 (60)
	100	2150 (20)	1930 (50)	3180 (60)	2570 (50)
	125	2240 (20)	1760 (50)	3140 (40)	2550 (80)
150	25	1910 (20)	2030 (30)	2610 (10)	2680 (70)
	50	1960 (10)	1980 (20)	2910 (20)	2480 (50)
	75	2070 (10)	1970 (10)	3310 (60)	2620 (40)
	100	2010 (10)	1930 (40)	3090 (30)	2690 (30)
	125	1980 (40)	1880 (20)	3010 (110)	2680 (120)
200	25	1790 (30)	1850 (30)	2280 (260)	2060 (10)
	50	1810 (10)	1860 (10)	2340 (10)	2060 (10)
	75	1880 (10)	1900 (10)	2680 (10)	2230 (10)
	100	1930 (10)	1850 (10)	2790 (10)	2180 (20)
	125	1880 (10)	1790 (20)	2810(80)	2110 (10)

[a]Values in parentheses represent standard deviation calculated from the mean of $n \geq 3$ trials.
[b]"No substrate" values reported previously.[17]

with increasing P at low p (p = 100 mTorr) but increases with P at high p (p = 200 mTorr). This trend has been discussed previously.[17]

5.3 Discussion

As noted in the Introduction, the applicability of PAC is limited by a lack of knowledge of the fundamental processes contributing to plasma-catalyst synergy. Understanding the roles of both the catalyst and plasma as well as the interactions occurring at the plasma-catalyst interface in a PAC system can help the community bypass trial-and-error approaches towards optimizing plasma-catalysis systems and establish a more informed method for optimization towards a desired application. Thus, the goal of this work is to elucidate both the impact of the catalyst on the fundamental properties of the plasma discharge and to understand the effect of plasma exposure on the catalyst's properties. Here, we utilize a nanostructured TiO_2 catalyst to report on effects on fundamental plasma processes in low pressure, inductively coupled H_2 and CH_4 plasmas. Chemical and morphological properties of the catalyst prior to and post plasma exposure were assessed in addition to the gas-phase studies as a more holistic approach towards elucidating the molecular level processes occurring in these inherently complex PAC systems.

A previous study from our lab employed OES to examine the gas phase of H_2 plasmas during processing of SnO_2 nanomaterials.[19] In that study, excited state OH and Sn species were observed in the gas phase only when a substrate was placed in the discharge. Similar observations are reported here where raw OES spectra of H_2 plasmas show the presence of OH and CO species when a TiO_2 substrate is placed in the discharge, Figure 5.1b. XPS atomic composition data, Table 5.3, also show a significant reduction of carbon post H_2 plasma exposure, suggesting that adventitious carbon is removed from the material surface during

plasma processing and is likely the source for the gas phase CO species. Given that we do not see OH^* without a substrate, OH^* formation likely occurs through removal of oxygen from the substrate. To elucidate further details about these plasma-surface interactions, we utilized inert gas actinometry to measure relative species densities as functions of plasma parameters, Figure 5.2, revealing that [H] is not affected by the catalyst when emission is collected coaxially along the length of the reactor. Conversely, [H] in the coil region shows an overall increase compared to the coaxially collected data, presumably resulting from the continuous flow of H_2 that can dissociate to H^* in the coil. Interestingly, when a TiO_2 substrate is placed in the discharge [H] is significantly reduced only in the coil region of the reactor. Shirazi *et al.* found that H atoms originating either from dissociative adsorption of H_2 or CH_4 or from H atoms produced in the bulk plasma can be readily adsorbed on a Ni catalyst.[35] Thus, the significant decrease of [H] directly above the substrate may be a result of adsorption of H atoms on the TiO_2 catalyst surface. Conversely, [OH] was similar in both the coil and coaxial data, indicating that once OH^* forms in the coil region it persists as it continues downstream in the reactor. One additional noteworthy observation from the Figure 5.2 actinometry data is that [OH] decreases to nearly zero over the 5-min treatment time. In H_2 plasmas, the only source of oxygen is the TiO_2 substrate, thereby serving as a limiting reagent for OH species production, especially if surface oxygen were removed from the substrate through plasma processes.

FTIR and XPS results further corroborate the H_2 plasma OES data. For example, FTIR data (Figure 5.4) suggest the creation of a more uniform lattice environment and removal of carbon and oxygen species. Additionally, high resolution XPS data demonstrate increases in the $-O_{vac}$ and $-O_{surf}$ binding environments (Figures 6b and 6e) and reduction of Ti^{4+} (Figures 6a and 6d) after plasma exposure. Although Ti^{4+} was not always reduced, an increase in the $-O_{vac}$ and -

O_{surf} binding environments was always observed post plasma treatment. Changes in atomic composition (Table 5.3) are noted after 1 and 5 minutes of plasma exposure (P = 125 W), but atomic compositions are within error for the 5 and 10 min plasma treatments, indicating significant changes to the catalyst's surface chemistry likely occur within the first few minutes of plasma exposure. Together, the OES and materials characterization data suggest etching of surface oxygen by the hydrogen plasma. It is thus useful to consider which gas phase species act as etchants in this system to further illuminate potential etching mechanisms.

Both hydrogen and argon plasma treatments have been used widely as a preparation method for catalyst reduction; consequently, several investigations of the primary etching pathways within these systems have been reported.[36-39] For example, one study suggests the products of electron-mediated reactions with ethanol may be the primary reducing agents in Ar plasmas.[38] Moreover, a recent review of plasma catalyst preparation states that both hydrogen radicals and electrons are strong reducing agents for metal catalysts in H_2 plasmas.[39] A previous study from our lab provided a discussion on the potential etchants of SnO_2 nanomaterials in low pressure, inductively coupled rf H_2/Ar plasmas, concluding that H^* acted as the primary etchant.[19] Given the similar parameters utilized in this study, we believe H^* acts as the primary etchant here as well. Moreover, the significant decrease in [H] when the catalyst is in the plasma, Figure 5.2b, indicates that hydrogen atoms interact with the substrate to form OH or other species (e.g., H_2).

One approach to discerning key mechanistic processes occurring in our plasma systems includes determination of internal molecular plasma temperatures and trends. For example, T_R(OH) and T_V(OH) were calculated for the 100% H_2 plasma system with TiO_2 as OH is an etch product that also changes with plasma parameters. Importantly, a non-Boltzmann distribution

behavior is expected for OH $A^2\Sigma^+$, H_2 $d^3\Pi_u$, and CH $A^2\Delta$ in low pressure plasmas because the collisional timeframe is on the same order as the radiative lifetime.[21, 40-41] As such, the rotational states have no time to relax before undergoing radiative decay. Thus, T_R values measured in our systems can be used to elucidate formation mechanisms because T_R becomes an image of the formation process rather than the kinetic temperature. Furthermore, some formation mechanisms can favor production of high or low rotational excited states which can drastically change T_R and ultimately provide insight into understanding mechanistic phenomena occurring in our systems.[21]

T_R(OH) values cover a fairly large range (~2900 K to 3700 K), and T_V(OH) values are routinely higher (~4000 – 4400 K). Although the representative emission spectrum of the OH $A^2\Sigma^+ \rightarrow X^2\Pi$ transition in Figure 5.3, shows a high PC value (0.96), our associated experimental error does not allow clear conclusions regarding energy partitioning trends from these data. Nevertheless, we can compare the range of these values to those reported in the literature. Stuckert *et al.* determined T_R(OH) and T_V(OH) in H_2O and H_2 plasmas with SnO_2 nanomaterials under similar pressure and power ranges.[19] Reported T_V(OH) values were ~3450 – 4020 K, and T_R(OH) values ranged from ~ 1800 to 5400 K, with typically higher T_R(OH) values reported in the H_2 system compared to the H_2O system. Notably, these values generally align with those reported herein. A study by Sarani *et al.* suggests vibrational-rotational populations of OH can be formed via different mechanisms of generation for excited state species with different J levels.[20] The authors suggest lower rotational states ($J < 13$) are produced in their system (atmospheric pressure DBD plasma jet, Ar/water vapor mixtures) through a combination of direct electron impact excitation from the ground state and dissociative excitation, resulting in T_R(OH) = 625 K. Meanwhile the $13 < J < 25$ states, are characterized by a higher rotational temperature [T_R(OH) = 5000 K], suggesting dissociative excitation as the main pathway for OH

$A^2\Sigma^+$ formation. Other reported T_R(OH $A^2\Sigma^+$) values range from ~450 K – 3700 K with T_V(OH $A^2\Sigma^+$) = ~6000 K.[21-22] A critical review of T_R(OH) determination by Bruggeman and coworkers demonstrates that even at atmospheric pressure, rotational population distributions of OH $A^2\Sigma^+$ provide an image of its formation process.[21] Thus, although many of these literature values arise from atmospheric pressure plasma systems, the wide range of T_R(OH) values reported likely evolve from different formation processes.

Notably, T_R(OH) values are also much larger than $T_R(H_2)$ or T_R(CH) values reported herein. In a related study by Cruden *et al.*, rotational temperatures of five molecular species (i.e., CF, CN, CO, C_2, SiF) were measured in a low pressure (30 mTorr) inductively coupled CF_4-based plasma.[42] The authors determined that SiF, produced solely from plasma-surface interactions with the reactor wall, had a higher rotational temperature (~2300 K) than those for molecules produced primarily from gas phase reactions (e.g. CF and CN, ~1250 K). Species produced via a combination of gas-phase and plasma-surface interactions (identified as CO and C_2) exhibited intermediate T_R values of 1600 K and 1800 K, respectively. Their results suggest that species produced as etch products leave the surface with significant internal energies and further supports the elevated T_R(OH) values measured in our systems.

Based on our materials analyses and the measured T_R(OH) and T_V(OH) values in our plasmas, we determined probable mechanistic pathways for OH^* formation, depicted in Reactions 5.1 – 5.2, where "•" represents an active site on the material surface.

$$H_2^* (g) \rightarrow 2H^* (g) \quad (5.1)$$

$$H^* (g) + TiO_2 (s) \rightarrow OH (g) + \bullet TiO (s) + e^- \quad (5.2a)$$

$$OH (g) + e^- \rightarrow OH^* (g) + e^- \quad (5.2b)$$

One reason we included H_2 plasmas in our PAC studies is that hydrogen species comprise a significant component of CH_4 plasma decomposition. As such, it is important to determine how these species interact with the catalyst. Precursor dissociation in CH_4 plasma discharges generally leads to an array of product species such as CH_x, H, H_2, and C_2.[43-44] Consequently, several groups have previously reported on energy partitioning of CH or C_2 in CH_4 plasmas.[45-48] Electron impact dissociation of CH_4 is the dominant pathway for generating these species in the plasma with either subsequent radical recombination reactions to form higher order hydrocarbons or further electron impact dissociation.[9, 49] Specifically, Reactions 5.3 – 5.5 are hypothesized to be the primary routes for CH_4 decomposition. Simulation of DBD methane plasma conversion showed that Reaction 5.3 accounts for ~79% of electron impact dissociation of CH_4 and Reactions 5.4 – 5.5 account for ~15% and ~5%, respectively.[50]

$$CH_4 + e^- \rightarrow CH_3 + H + e^- \qquad (5.3)$$

$$CH_4 + e^- \rightarrow CH_2 + H_2 + e^- \qquad (5.4)$$

$$CH_4 + e^- \rightarrow CH + H + H_2 + e^- \qquad (5.5)$$

Although formation of CH has been directly related to CH_4 decomposition,[48] interpretation of energy partitioning results should also consider the relevant amount of discharge power converted to rotational and vibrational excitation of other species in the plasma. For example, H_2 is an important component to CH_4 plasma chemistry utilized for production of amorphous hydrocarbon films deposited via PECVD.[43-44, 51-52] Furthermore, hydrogen production via hydrocarbon reforming has received much attention as an alternative energy source;[53-54] thus, we sought to combine $T_R(H_2)$ values with energy partitioning trends for CH in CH_4 systems.

Our proceeding study included investigations of $T_R(H_2)$ trends and discussion on probable excitation mechanisms for H_2 in 100% H_2 and 100% CH_4 plasmas sans catalyst.[18] These data are

depicted by the open symbols in Figure 5.10. Notably, $T_R(H_2)$ values (no substrate) are typically higher in 100% CH_4 plasmas (~500 – 700 K) compared to 100% H_2 plasmas (~500 – 550 K). Although discernable differences between $T_R(H_2)$ values and trends in these two plasma systems have been discussed in detail previously,[18] the TR-OES studies performed here lend additional insight into formation mechanisms. Temporal profiles of H_2 emission in a 100% H_2 plasma and a 100% CH_4 plasma without TiO_2, Figures 10a and 10b, respectively, demonstrate clear differences in formation rates. With a TiO_2 substrate in the system, little changes for the 100% H_2 plasma, whereas a dramatic change in the H_2 temporal profile is observed for the CH_4 system (Figure 5.9d). The H_2 energetics in these two systems with the catalyst support these TR-OES results. Specifically, in the 100% H_2 plasmas, $T_R(H_2)$ values are not significantly altered by the presence of the TiO_2 (Figure 5.10), suggesting TiO_2 does not affect H_2 excitation pathways in H_2 plasmas. Contrarily, $T_R(H_2)$ values in the 100% CH_4 plasma decrease by ~100 – 200 K in the presence of the catalyst, strongly indicating the catalyst plays a significant role in H_2^* formation processes in CH_4 plasmas.

Density functional theory calculations have recently been used to investigate the interactions of hydrogen species with catalysts and hydrogenation mechanisms in PAC systems.[35, 55-56] In one such study, Shirazi *et al.* examined the diffusion of H atoms to the surface and into the bulk of Ni(111) for different amounts of H atom surface coverage.[35] Their results suggest the H atom coverage on the catalyst can strongly influence reaction kinetics. For example, when a threshold H atom surface coverage is surpassed, adsorption of H atoms or dissociative adsorption of H_2 or CH_4 becomes an endothermic, and thus, unfavorable process. In this case, associative desorption of H_2 or the consumption of surface bound H atoms by another reactant will occur to release active sites for further adsorption of species. A higher rate of H

atom diffusion to a subsurface also gives rise to a higher H atom adsorption on the surface, resulting in the reduction of surface bound H atoms and increases the rate of hydrogenation. Indeed, another study by these authors showed that catalytic hydrogenation reactions proceed faster in the presence of high H-coverage.[55] Furthermore, the adsorbate surface coverage is highly dependent on PAC reaction conditions. Thus, changes in plasma parameters can result in significant changes to the surface chemistry and ultimately modify the reaction kinetics at the catalyst surface.

Similar to $T_R(H_2)$ in the 100% CH_4 plasma, T_R(CH) also decreases upon the addition of a TiO_2 catalyst, Figure 5.11a (100 mTorr). Here, T_R(CH) values are reduced by ~100 – 200 K except at P = 50 W where T_R(CH) values are within error for the no substrate and TiO_2 substrate systems. The addition of a substrate to the plasma may impact rotational cooling pathways by providing an extra surface for collisional cooling, leading to the lower $T_R(H_2)$ and T_R(CH) values. Rotational relaxation is a relatively fast process as fewer than ten collisions are typically required to reach equilibrium.[57] Thus, although T_R(CH) decreases with the addition of the catalyst to the discharge at p = 100 mTorr, at p = 150 – 200 mTorr T_R(CH) values for the catalyst systems are generally within experimental error of the no catalyst system, indicating that gas-phase rotational cooling processes are likely the principal processes occurring at these increased pressures.

Our data clearly demonstrate the impact of a TiO_2 catalyst on rotational energy partitioning for H_2 $d^3\Pi_u$ and CH $A^2\Delta$ in CH_4 plasmas; yet, rotational excitation pathways via electron impact have threshold energies (~0.01 – 0.1 eV) much lower than activation energies of heterogenous catalysis reactions.[58] Consequently, the internal energy of rotationally excited species is too low to induce thermal catalysis in plasma. Vibrationally excited species, on the other hand, have threshold energies (~0.1 – 1 eV) close to or greater than activation energies in

catalysis reactions and are typically not de-excited before they reach the catalyst surface (unlike ions and electronically excited species).[58-60] As such, vibrationally excited species can strongly influence plasma-surface interactions in PAC systems. Numerous studies have focused on elevating the vibrational energy of reactants to enhance dissociative adsorption in catalytic reactions. To date, these studies have mainly focused on CH_4[61-65] and N_2[66-69] because of their applications in H_2 generation via methane reforming and NH_3 synthesis, respectively. Since dissociative adsorption of CH_4 and N_2 becomes the rate-limiting steps in catalytic reactions,[58] an understanding of how energy is partitioned into vibrational degrees of freedom and how to ultimately control that energy is key to enhancing conversion rates in PAC systems.

T_V(CH) measured in our plasmas without and with a TiO_2 substrate in the discharge indicate T_V(CH) is significantly decreased (~2550 – 3100 K) upon addition of the catalyst. We have previously illustrated a similar trend in 100% N_2 plasmas, where $T_V(N_2)$ was measured without and with two different catalysts, TiO_2 and zeolite NaY.[70] In these studies, $T_V(N_2)$ decreased by ~400 – 1000 K with either catalyst in the discharge. Moreover, when our reactor was lined with multiple catalytic zeolite substrates, the observed decrease in $T_V(N_2)$ was profoundly enhanced. These results suggest that vibrationally excited molecules leave the surface with some energy loss, resulting in the observed reduced $T_V(N_2)$ values.

Notably, an important piece of surface relaxation mechanisms involves the adsorption of the excited species onto the catalyst surface.[1, 71] Dombrowski *et al.* described a precursor-mediated mechanism in which vibrationally excited methane molecules first trap on the catalyst surface via physisorption before chemisorption or desorption occurs.[72] Depending on the vibrational lifetime and nature of the adsorbate/catalyst interaction, the molecule may either desorb with increased vibrational energy from energy exchange with the catalytic surface or the

molecule may become vibrationally quenched by the surface interaction. Several studies have shown that vibrationally excited methane molecules interact more favorably with catalytic Ni surfaces than ground state molecules, and that ultimately, these plasma-catalyst interactions lower the reaction barrier for C-H dissociation of CH_4.[15-16, 73] One of these studies measured T_R and T_V of CH $A^2\Delta$ in a packed bed DBD reactor filled with SiO_2 pellets only and SiO_2 with 3 wt% loading of Ni catalyst to elucidate a better understanding of plasma-catalyst synergies in CH_4 reforming systems.[15-16] Their OES results show that although T_R(CH) remains unchanged by the introduction of the catalyst, the Ni catalyst significantly increases T_V(CH) with catalyst bed temperatures, but was essentially independent of bed temperature without the catalyst. Specifically, a close examination of the emission spectra for the CH $A^2\Delta \rightarrow X^2\Pi$ band reveals the intensity of the $v(0, 0)$ and $v(1, 1)$ vibrational bands are decreased at elevated bed temperatures, whereas the relative intensity of the $v(2, 2)$ vibrational band is independent of bed temperature. These results suggest that vibrationally excited CH reacts selectively on the catalyst surface, resulting in intensity changes of the $v(0, 0)$ and $v(1, 1)$ vibrational bands and consequently, the observed elevated T_V(CH) values.[15] This synergistic effect, however, was only observed when the catalyst bed temperature exceeded 400 °C.

Another study by Tu *et al.* examined the impact of TiO_2 on $T_R(N_2)$ and $T_V(N_2)$ in a N_2 packed bed DBD.[74] Similar to the results presented in the Nozaki *et al.* study on T_V(CH),[15] Tu *et al.* found that $T_V(N_2)$ increased from ~2300 – 2800 K to ~3200 – 4100 K with the catalyst in the discharge.[74] Upon catalyst packing, the authors also observed a change in the discharge behavior from a filamentary discharge to a combination of surface discharges on the catalyst and micro discharges generated in void spaces between TiO_2 pellets. The authors suggest changes in discharge behavior and concomitant increase in $T_V(N_2)$ from catalyst packing coincide with

changes in the electron energy distribution function, wherein there is nominally a shift in the distribution to higher energy electrons.

Our results differ from the studies by Nozaki *et al.*[15] and Tu *et al.*[74] in that T_V displays the opposite behavior when the catalyst is placed in the discharge (i.e. T_V decreases upon catalyst introduction). Possible explanations for these differences may be related primarily to the differences between the two plasma systems. The DBD systems operate at atmospheric pressure whereas our system operates at much lower pressures. At atmospheric pressure the collisional time is typically shorter than the radiative lifetime of the species of interest.[21] Thus, in our systems fewer collisions are likely to occur compared to the DBD systems. With the addition of a substrate, there is a greater likelihood of productive plasma-surface collisions, effectively quenching the CH excited states.

Furthermore, the catalyst in our system occupies only a small amount of the total volume, whereas the DBD reactors are packed with pellets, allowing more surface area for plasma-catalyst interactions. These interactions can be complex when the catalysts lie within the discharge zone as a variety of species can interact with catalyst. Interactions between the plasma and the catalyst can be viewed from two perspectives: (1) the influence of the catalyst on plasma characteristics and (2) the influence of the plasma on the catalyst. The presence of a catalyst could significantly enhance the electric field, especially around contact points between the pellets/electrodes.[58, 75] Several simulation studies have verified that a packed bed reactor could achieve a higher electric field compare with a non-packed one.[76-77] A higher electric field generally leads to a higher electron energy, which could promote decomposition. Additionally, if the catalyst does indeed enhance the average electron energy, then this enhancement could depend on the amount of catalyst in the discharge. Electron temperature (T_e) measured from

OES lines in our system (described previously[78]) indicate that T_e ranged from ~2.4 – 2.7 eV in CH_4 plasmas (Table A.1), independent of pressure and power. Moreover, the presence of the TiO_2 catalyst does not appreciably affect T_e, further suggesting the change in T_V(CH) noted in our systems may not arise from a change to the plasma discharge, but rather may be related to vibrational quenching from plasma-surface interactions. Similarly, Nozaki *et al.* noted that the reduced field and electron density were not affected by the presence of a Ni catalyst in their simulations, indicating that plasma-catalyst reactions were the primary cause for the observed changes in T_V(CH).[16]

Herrera *et al.* further explored synergistic behavior of plasma-catalysis systems in a N_2/H_2 packed-bed DBD reactor with three types of transition metal catalysts on Al_2O_3 support (i.e., Fe/Al_2O_3, Ni/Al_2O_3, CO/Al_2O_3).[79] Their results demonstrate the metal-on-oxide support catalysts had no significant effect on the plasma's electrical or optical properties compared to the same system with just the Al_2O_3 support substrate. These results bolster the argument that the observed synergy results from plasma modification of the catalyst surface rather than catalyst modification of the bulk plasma properties. Indeed, plasmas can significantly alter the chemical and morphological properties of catalytic materials in PAC systems; thus, changes to the catalyst properties will, in turn, have an effect on the overall PAC processes.

Our XPS (Table 5.4, Figure 5.6) and Raman data (Figure 5.7) from catalysts exposed to CH_4 plasma indicate that although amorphous carbon film deposition occurs, the plasma also modifies the underlying substrate under some parameter conditions. High resolution Ti_{2p} spectra show reduction of Ti from Ti^{4+} to Ti^{3+} at p = 200 mTorr, P = 25 W (Figure 5.6a) and Raman spectra (Figure 5.7b) indicate the presence of oxygen vacancies within the material. Indeed, high resolution O_{1s} data (Figure 5.6b) show an increase in adsorbed oxygen species after CH_4 plasma

exposure also indicative of oxygen vacancies.[25, 28] Overall, these results imply concomitant etching and deposition processes occur within the CH_4 plasma system. Interestingly, some studies suggest carbon deposition is significantly reduced by synergistic effects during PAC[58, 80] and plasma treatment has been used as a preparation method for catalysts to reduce coke formation.[39, 81-82] This plasma treatment step serves to reduce the metal catalyst and results in higher metal dispersion and catalyst reactivity.[80] Plasma treatment for catalyst preparation in PAC systems has been studied primarily with respect to selectivity and conversion efficiencies;[80] thus, fundamental questions regarding the synergistic effects remain unanswered. These ideas could be further explored via a more holistic experimental approach utilizing gas-phase diagnostics and materials analysis to gain additional insight into synergistic plasma-catalyst interactions.

5.4 Summary

As evidenced from our data, the presence of a catalytic material can drastically alter the gas phase chemistry of the plasma. Within a CH_4 plasma, differences in species energetics and kinetics are observed with the introduction of a TiO_2 catalyst. Although the catalyst did not affect $T_R(H_2)$ in H_2 plasmas, pronounced decreases in $T_R(CH, H_2)$ and $T_V(CH)$ are observed in the CH_4 plasmas. Materials characterization reveals an amorphous hydrocarbon film is deposited in the CH_4 plasma, although competing etching processes may also be occurring under some conditions. Conversely, materials analysis post H_2 plasma exposure reveals that the plasma acts primarily as an etching system. As PAC systems are extremely complex and convoluted, it is difficult to determine whether the catalyst has more influence on the plasma characteristics or the plasma's impact on the catalyst promotes changes. Ultimately, much work remains to be done to

deconvolute plasma-catalyst synergies. Although this work emphasized the importance of analyzing both the gas phase and catalyst in PAC systems, additional data on gas-surface interactions is vital to the future of this emerging technology. For example, our imaging of radicals interacting with surfaces (IRIS) technique measures a molecule's propensity to scatter from substrates may provide more evidence for how plasma species interact synergistically with catalysts. Future work should include a holistic experimental approach focused on elucidating interactions at the plasma-surface interface by combining gas-phase diagnostics, IRIS, and comprehensive materials characterization.

REFERENCES

1. Neyts, E. C., Plasma-Surface Interactions in Plasma Catalysis. *Plasma Chem. Plasma Process.* **2016,** *36* (1), 185-212.
2. Feng, X.; Liu, H.; He, C.; Shen, Z.; Wang, T., Synergistic Effects and Mechanism of a Non-Thermal Plasma Catalysis System in Volatile Organic Compound Removal: A Review. *Catal. Sci. Technol.* **2018,** *8* (4), 936-954.
3. Puliyalil, H.; Jurković, D. L.; Dasireddy, V. D.; Likozar, B., A Review of Plasma-Assisted Catalytic Conversion of Gaseous Carbon Dioxide and Methane into Value-Added Platform Chemicals and Fuels. *RSC Adv.* **2018,** *8* (48), 27481-27508.
4. Meyyappan, M., Plasma Nanotechnology: Past, Present and Future. *J. Phys. D: Appl. Phys.* **2011,** *44* (17), 174002.
5. Kim, H.-H.; Ogata, A.; Futamura, S., Oxygen Partial Pressure-Dependent Behavior of Various Catalysts for the Total Oxidation of VOCs Using Cycled System of Adsorption and Oxygen Plasma. *Appl. Catal., B* **2008,** *79* (4), 356-367.
6. Mustafa, M. F.; Fu, X.; Liu, Y.; Abbas, Y.; Wang, H.; Lu, W., Volatile Organic Compounds (VOCs) Removal in Non-Thermal Plasma Double Dielectric Barrier Discharge Reactor. *J. Hazard. Mater.* **2018,** *347*, 317-324.
7. Pan, K. L.; Chang, M. B., Plasma Catalytic Oxidation of Toluene over Double Perovskite-Type Oxide Via Packed-Bed DBD. *Environ. Sci. Pollut. Res.* **2019,** *26* (13), 12948-12962.
8. Shang, S.; Liu, G.; Chai, X.; Tao, X.; Li, X.; Bai, M.; Chu, W.; Dai, X.; Zhao, Y.; Yin, Y., Research on Ni/Γ-Al_2O_3 Catalyst for CO_2 Reforming of CH_4 Prepared by Atmospheric Pressure Glow Discharge Plasma Jet. *Catal. Today* **2009,** *148* (3-4), 268-274.
9. Tu, X.; Whitehead, J., Plasma-Catalytic Dry Reforming of Methane in an Atmospheric Dielectric Barrier Discharge: Understanding the Synergistic Effect at Low Temperature. *Appl. Catal., B* **2012,** *125*, 439-448.
10. Li, D.; Rohani, V.; Fabry, F.; Ramaswamy, A. P.; Sennour, M.; Fulcheri, L., Direct Conversion of CO_2 and CH_4 into Liquid Chemicals by Plasma-Catalysis. *Appl. Catal., B* **2020,** *261*, 118228.
11. Malik, M. A.; Minamitani, Y.; Schoenbach, K. H., Comparison of Catalytic Activity of Aluminum Oxide and Silica Gel for Decomposition of Volatile Organic Compounds (VOCs) in a Plasmacatalytic Reactor. *IEEE Trans. Plasma Sci.* **2005,** *33* (1), 50-56.
12. Mizuno, A., Generation of Non-Thermal Plasma Combined with Catalysts and Their Application in Environmental Technology. *Catal. Today* **2013,** *211*, 2-8.
13. Van Durme, J.; Dewulf, J.; Sysmans, W.; Leys, C.; Van Langenhove, H., Abatement and Degradation Pathways of Toluene in Indoor Air by Positive Corona Discharge. *Chemosphere* **2007,** *68* (10), 1821-1829.
14. Nozaki, T.; Ağıral, A.; Yuzawa, S.; Gardeniers, J. H.; Okazaki, K., A Single Step Methane Conversion into Synthetic Fuels Using Microplasma Reactor. *Chem. Eng. J.* **2011,** *166* (1), 288-293.
15. Nozaki, T.; Muto, N.; Kadio, S.; Okazaki, K., Dissociation of Vibrationally Excited Methane on Ni Catalyst: Part 2. Process Diagnostics by Emission Spectroscopy. *Catal. Today* **2004,** *89* (1-2), 67-74.

16. Nozaki, T.; Muto, N.; Kado, S.; Okazaki, K., Dissociation of Vibrationally Excited Methane on Ni Catalyst: Part 1. Application to Methane Steam Reforming. *Catal. Today* **2004,** *89* (1-2), 57-65.
17. Van Surksum, T. L.; Blechle, J. M.; Fisher, E. R., Determination of Rotational and Vibrational Temperatures of CH in CH_4 Plasmas. *J. Vac. Sci. Technol., A* **2018,** *36* (4), 041302.
18. Van Surksum, T. L.; Fisher, E. R., Gas-Phase Diagnostic Studies of H_2 and CH_4 Inductively Coupled Plasmas. *J. Vac. Sci. Technol., A* **2020,** *38* (3), 033010.
19. Stuckert, E. P.; Miller, C. J.; Fisher, E. R., Gas-Phase Diagnostics During H_2 and H_2O Plasma Treatment of SnO_2 Nanomaterials: Implications for Surface Modification. *J. Vac. Sci. Technol., B* **2017,** *35* (2), 021802.
20. Sarani, A.; Nikiforov, A. Y.; Leys, C., Atmospheric Pressure Plasma Jet in Ar and Ar/H_2O Mixtures: Optical Emission Spectroscopy and Temperature Measurements. *Phys. Plasmas* **2010,** *17* (6), 063504.
21. Bruggeman, P.; Schram, D. C.; Kong, M. G.; Leys, C., Is the Rotational Temperature of OH (A–X) for Discharges in and in Contact with Liquids a Good Diagnostic for Determining the Gas Temperature? *Plasma Process. Polym.* **2009,** *6* (11), 751-762.
22. Mukasa, S.; Nomura, S.; Toyota, H.; Maehara, T.; Abe, F.; Kawashima, A., Temperature Distributions of Radio-Frequency Plasma in Water by Spectroscopic Analysis. *J. Appl. Phys.* **2009,** *106* (11), 113302.
23. Bezrodna, T.; Puchkovska, G.; Shymanovska, V.; Baran, J.; Ratajczak, H., IR-Analysis of H-Bonded H_2O on the Pure TiO_2 Surface. *J. Mol. Struct.* **2004,** *700* (1-3), 175-181.
24. León, A.; Reuquen, P.; Garín, C.; Segura, R.; Vargas, P.; Zapata, P.; Orihuela, P. A., FTIR and Raman Characterization of TiO_2 Nanoparticles Coated with Polyethylene Glycol as Carrier for 2-Methoxyestradiol. *Appl. Sci.* **2017,** *7* (1), 49.
25. Wu, H.; Xu, C.; Xu, J.; Lu, L.; Fan, Z.; Chen, X.; Song, Y.; Li, D., Enhanced Supercapacitance in Anodic TiO_2 Nanotube Films by Hydrogen Plasma Treatment. *Nanotechnology* **2013,** *24* (45), 455401.
26. Ahn, K.; Lee, H.-U.; Jeong, S.-Y.; Kim, J.-P.; Jin, J. S.; Ahn, H.-S.; Kim, H.-S.; Cho, C.-R., Plasma Treatment Effect on Dye-Sensitized Solar Cell Efficiency of Hydrothermal-Processed TiO_2 Nanorods. *J. Nanosci. Nanotechnol.* **2012,** *12* (7), 6022-6025.
27. Achour, A.; Islam, M.; Solaymani, S.; Vizireanu, S.; Saeed, K.; Dinescu, G., Influence of Plasma Functionalization Treatment and Gold Nanoparticles on Surface Chemistry and Wettability of Reactive-Sputtered TiO_2 Thin Films. *Appl. Surf. Sci.* **2018,** *458*, 678-685.
28. Han, J.-B.; Wang, X.; Wang, N.; Wei, Z.-H.; Yu, G.-P.; Zhou, Z.-G.; Wang, Q.-Q., Effect of Plasma Treatment on Hydrophilic Properties of TiO_2 Thin Films. *Surf. Coat. Technol.* **2006,** *200* (16-17), 4876-4878.
29. Jensen, H.; Soloviev, A.; Li, Z.; Søgaard, E. G., XPS and FTIR Investigation of the Surface Properties of Different Prepared Titania Nano-Powders. *Appl. Surf. Sci.* **2005,** *246* (1-3), 239-249.
30. Kundu, S.; Wang, Y.; Xia, W.; Muhler, M., Thermal Stability and Reducibility of Oxygen-Containing Functional Groups on Multiwalled Carbon Nanotube Surfaces: A Quantitative High-Resolution XPS and TPD/TPR Study. *J. Phys. Chem. C* **2008,** *112* (43), 16869-16878.
31. Choudhury, B.; Choudhury, A., Dopant Induced Changes in Structural and Optical Properties of Cr^{3+} Doped TiO_2 Nanoparticles. *Mater. Chem. Phys.* **2012,** *132* (2-3), 1112-1118.

32. Chen, G.; Britun, N.; Godfroid, T.; Georgieva, V.; Snyders, R.; Delplancke-Ogletree, M., Efficient CO_2 Conversion in Microwave Plasma Via Plasma Catalysis. *J. Phys. D: Appl. Phys* **2017,** *50*, 084001.
33. Tian, F.; Zhang, Y.; Zhang, J.; Pan, C., Raman Spectroscopy: A New Approach to Measure the Percentage of Anatase TiO_2 Exposed (001) Facets. *J. Phys. Chem. C* **2012,** *116* (13), 7515-7519.
34. Sarkar, A.; Khan, G. G., The Formation and Detection Techniques of Oxygen Vacancies in Titanium Oxide-Based Nanostructures. *Nanoscale* **2019,** *11* (8), 3414-3444.
35. Shirazi, M.; Bogaerts, A.; Neyts, E. C., A DFT Study of H-Dissolution into the Bulk of a Crystalline Ni (111) Surface: A Chemical Identifier for the Reaction Kinetics. *Phys. Chem. Chem. Phys.* **2017,** *19* (29), 19150-19158.
36. Zhang, Y.; Chu, W.; Cao, W.; Luo, C.; Wen, X.; Zhou, K., A Plasma-Activated Ni/α-Al_2O_3 Catalyst for the Conversion of CH_4 to Syngas. *Plasma Chem. Plasma Process.* **2000,** *20* (1), 137-144.
37. Ihara, T.; Miyoshi, M.; Ando, M.; Sugihara, S.; Iriyama, Y., Preparation of a Visible-Light-Active TiO_2 Photocatalyst by RF Plasma Treatment. *J. Mater. Sci.* **2001,** *36* (17), 4201-4207.
38. Di, L.; Li, Z.; Lee, B.; Park, D.-W., An Alternative Atmospheric-Pressure Cold Plasma Method for Synthesizing Pd/P25 Catalysts with the Assistance of Ethanol. *Int. J. Hydrogen Energy* **2017,** *42* (16), 11372-11378.
39. Wang, Z.; Zhang, Y.; Neyts, E. C.; Cao, X.; Zhang, X.; Jang, B. W.-L.; Liu, C.-j., Catalyst Preparation with Plasmas: How Does It Work? *ACS Catal.* **2018,** *8* (3), 2093-2110.
40. Vankan, P.; Schram, D.; Engeln, R., Atomic and Molecular Hydrogen Densities in a Plasma Expansion. *Plasma Sources Sci. Technol.* **2005,** *14* (4), 744.
41. Luque, J.; Kraus, M.; Wokaun, A.; Haffner, K.; Kogelschatz, U.; Eliasson, B., Gas Temperature Measurement in CH_4/CO_2 Dielectric-Barrier Discharges by Optical Emission Spectroscopy. *J. Appl. Phys.* **2003,** *93* (8), 4432-4438.
42. Cruden, B. A.; Rao, M.; Sharma, S. P.; Meyyappan, Neutral Gas Temperature Estimates in an Inductively Coupled CF_4 Plasma by Fitting Diatomic Emission Spectra. *J. Appl. Phys.* **2002,** *91* (11), 8955-8964.
43. Truscott, B. S.; Kelly, M. W.; Potter, K. J.; Ashfold, M. N.; Mankelevich, Y. A., Microwave Plasma-Activated Chemical Vapor Deposition of Nitrogen-Doped Diamond. II: $CH_4/N_2/H_2$ Plasmas. *J. Phys. Chem. A* **2016,** *120* (43), 8537-8549.
44. Li, H.; Yang, K.; Liu, H.; Zhu, X., Optical and Mass Spectroscopic Properties of Microwave CH_4/H_2/Ar Plasma for Diamond Deposition in a Resonance Cavity. *Vacuum* **2018,** *147*, 45-50.
45. Zhang, S.; Gao, Y.; Sun, H.; Bai, H.; Wang, R.; Shao, T., Time-Resolved Characteristics and Chemical Kinetics of Non-Oxidative Methane Conversion in Repetitively Pulsed Dielectric Barrier Discharge Plasmas. *J. Phys. D: Appl. Phys.* **2018,** *51* (27), 274005.
46. Wang, X.; Gao, Y.; Zhang, S.; Sun, H.; Li, J.; Shao, T., Nanosecond Pulsed Plasma Assisted Dry Reforming of CH_4: The Effect of Plasma Operating Parameters. *Appl. Energy* **2019,** *243*, 132-144.
47. Duten, X.; Rousseau, A.; Gicquel, A.; Leprince, P., Rotational Temperature Measurements of Excited and Ground States of C_2 ($d^3\Pi_g - a^3\Pi_u$) Transition in a H_2/CH_4 915 Mhz Microwave Pulsed Plasma. *J. Appl. Phys.* **1999,** *86* (9), 5299-5301.

48. Heintze, M.; Magureanu, M.; Kettlitz, M., Mechanism of C_2 Hydrocarbon Formation from Methane in a Pulsed Microwave Plasma. *J. Appl. Phys.* **2002,** *92* (12), 7022-7031.
49. Nair, S.; Nozaki, T.; Okazaki, K., Methane Oxidative Conversion Pathways in a Dielectric Barrier Discharge Reactor—Investigation of Gas Phase Mechanism. *Chem. Eng. J.* **2007,** *132* (1-3), 85-95.
50. De Bie, C.; Verheyde, B.; Martens, T.; van Dijk, J.; Paulussen, S.; Bogaerts, A., Fluid Modeling of the Conversion of Methane into Higher Hydrocarbons in an Atmospheric Pressure Dielectric Barrier Discharge. *Plasma Process. Polym.* **2011,** *8* (11), 1033-1058.
51. Ito, H.; Koshimura, K.; Onitsuka, S.; Okada, K.; Suzuki, T.; Akasaka, H.; Saitoh, H., Dissociative Excitation of C_2H_2 in the Electron Cyclotron Resonance Plasma of Ar: Production of CH ($A^2\Delta$) Radicals and Formation of Hydrogenated Amorphous Carbon Films. *Plasma Chem. Plasma Process.* **2012,** *32* (2), 231-248.
52. Pothiraja, R.; Engelhardt, M.; Bibinov, N.; Awakowicz, P., Film Deposition on the Inner Surface of Tubes Using Atmospheric-Pressure Ar–CH_4, Ar–C_2H_2 and Ar–C_2H_2–H_2 Plasmas: Interpretation of Film Properties from Plasma-Chemical Kinetics. *J. Phys. D: Appl. Phys.* **2012,** *45* (33), 335202.
53. Chung, W.-C.; Chang, M.-B., Review of Catalysis and Plasma Performance on Dry Reforming of CH_4 and Possible Synergistic Effects. *Renew. Sust. Energ. Rev.* **2016,** *62*, 13-31.
54. Gao, Y.; Jiang, J.; Meng, Y.; Yan, F.; Aihemaiti, A., A Review of Recent Developments in Hydrogen Production Via Biogas Dry Reforming. *Energy Convers. Manage.* **2018,** *171*, 133-155.
55. Shirazi, M.; Neyts, E. C.; Bogaerts, A., DFT Study of Ni-Catalyzed Plasma Dry Reforming of Methane. *Appl. Catal., B* **2017,** *205*, 605-614.
56. Somers, W.; Bogaerts, A.; Van Duin, A.; Neyts, E., Plasma Species Interacting with Nickel Surfaces: Toward an Atomic Scale Understanding of Plasma-Catalysis. *J. Phys. Chem. C* **2012,** *116* (39), 20958-20965.
57. Brown, M. S.; Forlines, R. A.; Ganguly, B. N., Measurement of CH Density in a Pulsed-DC Hydrocarbon-Gas-Mixture Discharge. *J. Appl. Phys.* **2005,** *97* (10), 103302.
58. Chen, H. L.; Lee, H. M.; Chen, S. H.; Chao, Y.; Chang, M. B., Review of Plasma Catalysis on Hydrocarbon Reforming for Hydrogen Production—Interaction, Integration, and Prospects. *Appl. Catal., B* **2008,** *85* (1-2), 1-9.
59. Gicquel, A.; Cavadias, S.; Amouroux, J., Heterogeneous Catalysis in Low-Pressure Plasmas. *J. Phys. D: Appl. Phys.* **1986,** *19* (11), 2013.
60. Rapakoulias, D.; Cavadias, S.; Mataras, D., Heterogeneous Catalysis in Interaction of Plasma Excited Species with Surfaces. *High Temp. Chem. Process.* **1993,** *2*, 231-246.
61. Holmblad, P. M.; Wambach, J.; Chorkendorff, I., Molecular Beam Study of Dissociative Sticking of Methane on Ni (100). *J. Chem. Phys.* **1995,** *102* (20), 8255-8263.
62. Walker, A.; King, D., Dynamics of Dissociative Methane Adsorption on Metals: CH_4 on Pt {110}(1× 2). *J. Chem. Phys.* **2000,** *112* (10), 4739-4748.
63. Higgins, J.; Conjusteau, A.; Scoles, G.; Bernasek, S., State Selective Vibrational ($2\nu_3$) Activation of the Chemisorption of Methane on Pt (111). *J. Chem. Phys.* **2001,** *114* (12), 5277-5283.
64. Beck, R. D.; Maroni, P.; Papageorgopoulos, D. C.; Dang, T. T.; Schmid, M. P.; Rizzo, T. R., Vibrational Mode-Specific Reaction of Methane on a Nickel Surface. *Science* **2003,** *302* (5642), 98-100.

65. Jackson, B.; Nave, S., The Dissociative Chemisorption of Methane on Ni (111): The Effects of Molecular Vibration and Lattice Motion. *J. Chem. Phys.* **2013,** *138* (17), 174705.
66. Rettner, C.; Stein, H., Effect of Vibrational Energy on the Dissociative Chemisorption of N_2 on Fe (111). *J. Chem. Phys.* **1987,** *87* (1), 770-771.
67. Romm, L.; Katz, G.; Kosloff, R.; Asscher, M., Dissociative Chemisorption of N_2 on Ru (001) Enhanced by Vibrational and Kinetic Energy: Molecular Beam Experiments and Quantum Mechanical Calculations. *J. Phys. Chem. B* **1997,** *101* (12), 2213-2217.
68. Mehta, P.; Barboun, P.; Herrera, F. A.; Kim, J.; Rumbach, P.; Go, D. B.; Hicks, J. C.; Schneider, W. F., Overcoming Ammonia Synthesis Scaling Relations with Plasma-Enabled Catalysis. *Nat. Catal.* **2018,** *1* (4), 269-275.
69. Rouwenhorst, K. H.; Kim, H.-H.; Lefferts, L., Vibrationally Excited Activation of N_2 in Plasma-Enhanced Catalytic Ammonia Synthesis: A Kinetic Analysis. *ACS Sustain. Chem. Eng.* **2019,** *7* (20), 17515-17522.
70. Hanna, A. R.; Van Surksum, T. L.; Fisher, E. R., Investigating the Impact of Catalysts on N_2 Rotational and Vibrational Temperatures in Low Pressure Plasmas. *J. Phys. D: Appl. Phys.* **2019,** *52* (34), 345202.
71. Whitehead, J. C., Plasma–Catalysis: The Known Knowns, the Known Unknowns and the Unknown Unknowns. *J. Phys. D: Appl. Phys.* **2016,** *49* (24), 243001.
72. Dombrowski, E.; Peterson, E.; Del Sesto, D.; Utz, A., Precursor-Mediated Reactivity of Vibrationally Hot Molecules: Methane Activation on Ir (1 1 1). *Catal. Today* **2015,** *244*, 10-18.
73. Kim, J.; Abbott, M. S.; Go, D. B.; Hicks, J. C., Enhancing C–H Bond Activation of Methane Via Temperature-Controlled, Catalyst–Plasma Interactions. *ACS Energy Lett.* **2016,** *1* (1), 94-99.
74. Tu, X.; Gallon, H. J.; Whitehead, J. C., Electrical and Spectroscopic Diagnostics of a Single-Stage Plasma-Catalysis System: Effect of Packing with TiO_2. *J. Phys. D: Appl. Phys.* **2011,** *44* (48), 482003.
75. Neyts, E. C.; Ostrikov, K.; Sunkara, M. K.; Bogaerts, A., Plasma Catalysis: Synergistic Effects at the Nanoscale. *Chem. Rev.* **2015,** *115* (24), 13408-13446.
76. Van Laer, K.; Bogaerts, A., Fluid Modelling of a Packed Bed Dielectric Barrier Discharge Plasma Reactor. *Plasma Sources Sci. Technol.* **2015,** *25* (1), 015002.
77. Kruszelnicki, J.; Engeling, K. W.; Foster, J. E.; Xiong, Z.; Kushner, M. J., Propagation of Negative Electrical Discharges through 2-Dimensional Packed Bed Reactors. *J. Phys. D: Appl. Phys.* **2016,** *50* (2), 025203.
78. Hanna, A. R.; Blechle, J. M.; Fisher, E. R., Using Fundamental Spectroscopy to Elucidate Kinetic and Energetic Mechanisms within Environmentally Relevant Inductively Coupled Plasma Systems. *J. Phys. Chem. A* **2017,** *121* (40), 7627-7640.
79. Herrera, F. A.; Brown, G. H.; Barboun, P.; Turan, N.; Mehta, P.; Schneider, W. F.; Hicks, J. C.; Go, D. B., The Impact of Transition Metal Catalysts on Macroscopic Dielectric Barrier Discharge (DBD) Characteristics in an Ammonia Synthesis Plasma Catalysis Reactor. *J. Phys. D: Appl. Phys.* **2019,** *52* (22), 224002.
80. Chen, H. L.; Lee, H. M.; Chen, S. H.; Chang, M. B.; Yu, S. J.; Li, S. N., Removal of Volatile Organic Compounds by Single-Stage and Two-Stage Plasma Catalysis Systems: A Review of the Performance Enhancement Mechanisms, Current Status, and Suitable Applications. *Environ. Sci. Technol.* **2009,** *43* (7), 2216-2227.

81. Yan, X.; Zhao, B.; Liu, Y.; Li, Y., Dielectric Barrier Discharge Plasma for Preparation of Ni-Based Catalysts with Enhanced Coke Resistance: Current Status and Perspective. *Catal. Today* **2015,** *256*, 29-40.
82. Chen, G.; Britun, N.; Godfroid, T.; Georgieva, V.; Snyders, R.; Delplancke-Ogletree, M.-P., An Overview of CO_2 Conversion in a Microwave Discharge: The Role of Plasma-Catalysis. *J. Phys. D: Appl. Phys.* **2017,** *50* (8), 084001.

CHAPTER 6

INVESTIGATING THE IMPACT OF TiO_2 ON N_2 ROTATIONAL AND VIBRATIONAL TEMPERATURES IN LOW PRESSURE PLASMAS

This chapter is based on work published in *Journal of Physics D: Applied Physics* by Angela R. Hanna, Tara L. Van Surksum, and Ellen R. Fisher, and is reproduced with permission. The published study describes the impact of two catalytic materials (nano-structured TiO_2 and micro-structured zeolite) on N_2 rotational and vibrational temperatures in low pressure N_2 plasmas. Note that a portion of this work was previously presented in Dr. Angela R. Hanna's dissertation. Dr. A. R. Hanna established the Boltzmann plot method for determination of $T_V(N_2)$ within the Fisher group. She also collected and analyzed the data pertaining to N_2 plasma without substrates and performed the study on zeolite materials. As such, the results and discussion presented herein have been excerpted and adapted for this dissertation to represent my direct contributions to this work. Specifically, the results described in this chapter include the determination of $T_R(N_2)$ and $T_V(N_2)$ in a 100% N_2 plasma with a TiO_2 substrate. Morphological and chemical characterization of the catalyst before and after plasma exposure were also assessed and presented herein. The work included in this chapter was supported by the National Science Foundation (NSF CBET-1803067). I would like to thank Dr. Patrick McCurdy for assistance with SEM and XPS analyses.

6.1 Introduction

Plasma assisted catalysis (PAC) generally describes the coupling of a plasma and catalytic material for enhanced decomposition of a waste stream. In PAC systems, the plasma state can provide high energy species that help reactants reach their dissociation energies and/or

activation energies, and the catalyst can aid in targeted product synthesis by enhancing selectivity.[1-2] This results in a synergistic environment wherein both the plasma and catalyst can be chemically or physically altered by each other. Currently, limited understanding of the underlying phenomena contributing to plasma-catalyst synergy inhibits the implementation of PAC as a viable technology. As such, fundamental investigations regarding gas-phase processes and plasma-surface interactions are considered vital to the future of PAC development.[1, 3-5]

The combination of the plasma and the catalyst can affect processes occurring both in the gas phase and on the catalyst surface. The plasma can inherently modify catalyst properties to alter its morphology and chemical composition.[6] Several studies have examined how the plasma affects the material in PAC systems.[7-8] Few studies, however, have explored how the catalyst modifies the fundamental plasma properties. Catalyst properties, such as roughness and dielectric constant, can modify the electrical properties of the plasma and ultimately affect physiochemical properties of the plasma such as the electron energy distribution.[1] This, in turn, can affect energy partitioning and rates of gas phase processes.

Although it is generally understood that catalyst particle size can influence overall rate and efficiency of PAC processes,[9-10] little is understood about how low temperature plasmas (LTPs) interact with micro- and nano-structured materials. For PAC to become an efficient, working technology, it is vital to understand how the material affects gas-phase properties and the interactions occurring at the plasma-surface interface. Currently, optimization of plasma-catalysis setups (e.g., reactor design, plasma process conditions, catalyst choice) are determined through trial-and-error approaches. Elucidating fundamental gas phase processes by measuring species kinetics and internal plasma temperatures [i.e., rotational temperature (T_R) and vibrational temperature (T_V)] can afford insights into the underlying mechanisms at work in PAC

systems. Furthermore, by examining both the impact of the catalyst on gas-phase properties and how the plasma affects materials properties, information on gas-surface interface processes can be inferred.

Two studies that examined energy partitioning of N_2 plasma species in model PAC systems measured T_V and T_R of N_2 utilizing TiO_2 in a packed bed atmospheric dielectric barrier discharge (DBD) system [system pressure (p) of ~101 Pa][11] and Co-ZSM-5 in a radio frequency (rf) plasma, operated near atmospheric pressure (p = 90 Pa).[12] Tu *el al.* found that $T_V(N_2)$ increased dramatically from ~2300 – 2800 K to ~3200 – 4100 K when TiO_2 pellets were placed in the plasma and attributed this to an increase in electron temperature (T_e) as a result of the catalyst.[11] Interestingly, the TiO_2 catalyst had no effect on $T_R(N_2)$ at the lowest applied discharge power (P) of 40 W and removed all the positive linear dependence of $T_R(N_2)$ on P observed without TiO_2 (P = 40 – 70 W). Although Tu *et al.* noted some of these changes may indicate heating of the substrate, the true origin of these effects remains unclear. Niu *et al.* also observed differences in $T_V(N_2)$ and $T_R(N_2)$ when employing a Co-ZSM-5 catalyst in a N_2 discharge.[12] Here, however, $T_V(N_2)$ was ~3100 – 3400 K with the catalyst, more than 1000 K lower than that measured without the Co-ZSM-5 (~4300 – 5000 K). A slight decrease was observed as a function of rf power with the catalyst whereas the opposite trend was observed without the catalyst. Notably, all of the measurements made in the Niu *et al.* study were at P = 5 – 25 W,[12] discharge powers considerably lower than the lowest used by Tu *et al.*.[11] Although no explanation was provided for the differences between these internal temperature values and those measured by Tu *et al.*, variations in P and the catalyst type could account for the observed dissimilarities.

We have further explored all these phenomena by examining the effect of adding catalysts to an inductively coupled N_2 plasma (ICP) operated at relatively low pressure (~50 – 150 mTorr or ~7 – 20 Pa). TiO_2 nanoparticles were employed as the catalyst for a direct comparison to the Tu *et al.* study.[11] Furthermore, the published study included results and analysis for micro-structured NaY zeolite with additional discussion on the differences noted between the nano- and micro-structured catalysts employed.[13] $T_R(N_2)$ and $T_V(N_2)$ were measured with the catalyst in the discharge as functions of *p* and *P* using optical emission spectroscopy (OES). Time-resolved OES (TR-OES) was also employed to measure rates of N_2 formation and decay. N_2 kinetics and energetics are discussed in comparison to previously reported results for an N_2 plasma with no substrate.[14] We have also examined the morphology and chemical composition of the catalysts using scanning electron microscopy (SEM) and X-ray photoelectron spectroscopy (XPS) both before and after plasma exposure to determine the impact of the plasma on the catalyst. Our holistic approach to plasma diagnostics and comprehensive materials characterization enables us to more thoroughly investigate potential synergisms arising from the coupling of low temperature plasma and catalytic materials.

6.2 Results and Discussion

Energy partitioning within N_2 plasmas has been extensively studied over the past few decades.[14-23] As a result, a wide range of plasma operating parameters have been explored, creating an array of reported $T_R(N_2)$ and $T_V(N_2)$ values. Prior to the PAC studies described within this chapter, the Fisher group measured rotational and vibrational temperatures for N_2 in a 100% N_2 plasma (no substrate).[14] This previous work allows for direct comparison between our N_2 plasma systems (no substrate and catalyst) and serves as a reference point to many of the

results described throughout this chapter. Figure 6.1 shows a typical N_2 emission spectrum acquired with a TiO_2 substrate placed in the coil region of the reactor. $T_R(N_2)$ for the $C^3\Pi_u \rightarrow B^3\Pi_g$ transition was determined from simulated fits of experimental spectral data using SpecAir[24] whereas a Boltzmann plot was used to calculate $T_V(N_2)$. For $T_V(N_2)$ calculations, $\ln(I\lambda/A)$ is plotted as a function of vibrational energy (E) where I and λ are the intensity (a.u.) and wavelength (nm) of a specific emission line and A (s^{-1}) is the corresponding Einstein transition probability coefficient for the transition. The N_2 vibrational transitions, corresponding wavelengths, and A values used here are reported previously.[21, 25] The inset in Figure 6.1 shows the Boltzmann plot created from the corresponding displayed N_2 emission spectrum. The slope of the linear regression is inversely proportional to T_V, which ultimately yields $T_V = 3140 \pm 20$ K for the particular set of conditions shown in Figure 6.1.

Rotational and vibrational temperatures were determined under several sets of plasma conditions. Figure 6.2 shows T_R and T_V data for N_2 with and without a TiO_2 substrate in a 100% N_2 plasma (p = 100 mTorr) as a function of P. Numerical values for $T_R(N_2)$ and $T_V(N_2)$ measured under all conditions studied here are listed in Table 6.1. The $T_R(N_2)$ data in the 100% N_2 plasma (no substrate), reported previously[14], show a small, but fairly linear increase with increasing P, with values near room temperature (~310 – 340 K), Figure 6.2a. Addition of a TiO_2 substrate does not appreciably change the overall values, but the P dependence has largely disappeared, within experimental error. In contrast, the T_V values shown in Figure 6.2b show a strong linear dependence on P, both with and without the TiO_2 catalyst in the plasma. Interestingly, with the catalyst, the measured temperatures decrease by ~400 – 1000 K and the dependence on P decreases by approximately a factor of 2. This decrease in $T_V(N_2)$ was documented at all pressures studied herein (50 – 150 mTorr), Table 6.1. Notably, $T_V(N_2)$ reaches

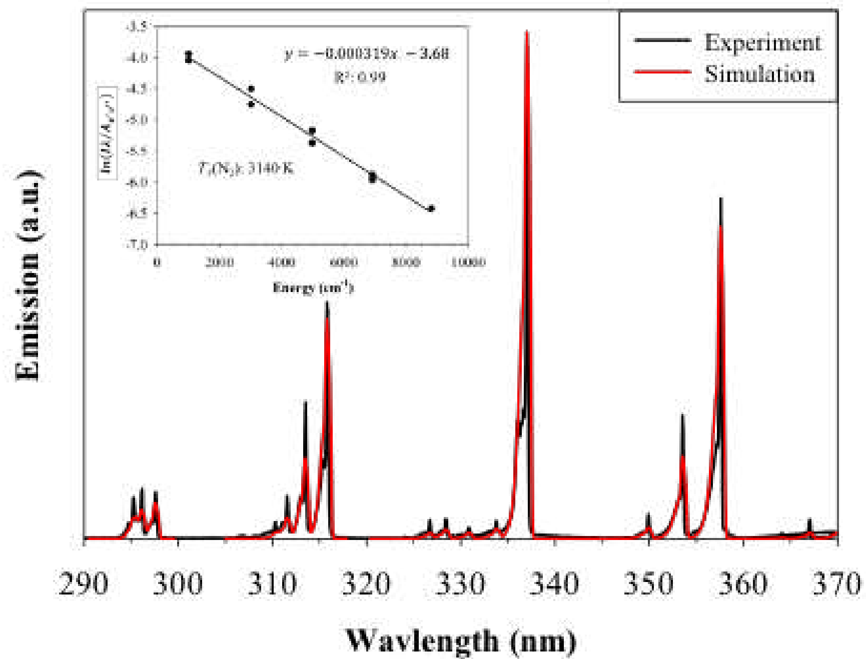

Figure 6.1. Representative emission spectrum at p = 100 mTorr, P = 100 W for N_2 ($C^3\Pi_u \rightarrow B^3\Pi_g$) in a N_2 plasma with TiO_2. Simulation of the spectrum using SpecAir yields T_R = 350 K. Inset shows a Boltzmann plot of N_2 vibrational distribution in a 100% N_2 plasma under the same conditions with a TiO_2 catalyst.

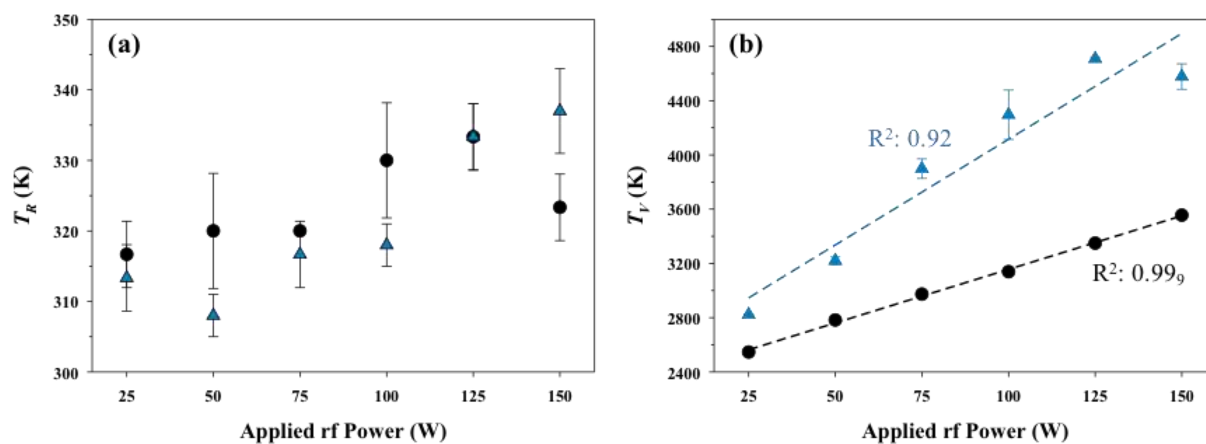

Figure 6.2. (a) $T_R(N_2)$ and (b) $T_V(N_2)$ from a N_2 plasma system at p = 100 mTorr with (black circles) and without (blue triangles) a TiO_2 substrate. Values for T_R without a substrate were previously reported.[14]

Table 6.1. $T_R(N_2)$, $T_V(N_2)$ values in a N_2 plasma system with TiO_2.[a]

p (mTorr)	P (W)	T_R (K)	T_V (K)
50	25	300 (10)	2310 (20)
	50	300 (10)	2560 (10)
	75	310 (10)	2780 (10)
	100	320 (10)	3120 (120)
	125	320 (10)	3700 (270)
	150	370 (10)	4620 (70)
100	25	320 (10)	2550 (10)
	50	320 (10)	2780 (10)
	75	320 (10)	2970 (20)
	100	330 (10)	3140 (20)
	125	330 (10)	3350 (10)
	150	320 (10)	3560 (20)
150	25	300 (10)	2520 (20)
	50	300 (10)	2770 (10)
	75	330 (10)	3010 (10)
	100	330 (10)	3150 (10)
	125	330 (10)	3310 (20)
	150	340 (10)	3480 (10)

[a]Values in parentheses represent standard deviation calculated from the mean of $n \geq 3$ trials.

values nearly an order of magnitude higher than $T_R(N_2)$, suggesting that rotational relaxation is more efficient than vibrational relaxation. Within N_2 plasmas containing a TiO_2 substrate, as *p* increases from 50 mTorr to 150 mTorr, some interesting trends emerge. At lower *P* (25 – 75 W), $T_V(N_2)$ at 100 and 150 mTorr are within experimental error but are elevated compared to the 50 mTorr data. At higher *P*, as pressure is increased to 150 mTorr, there is significant quenching of the vibrational excited states, resulting in a decrease in $T_V(N_2)$ as a function of *p*.

Our results clearly demonstrate that the presence of a TiO_2 catalyst within the plasma can impact $T_V(N_2)$ and agree to a certain extent with the results reported by Tu *et al.* for a TiO_2 packed bed DBD system.[11] Overall, both $T_R(N_2)$ values (~300 – 600 K) and $T_V(N_2)$ values (~2500 – 4500 K) are similar to the Tu *et al.* system. In the DBD system, however, opposite trends with respect to $T_V(N_2)$ are reported. Namely, Tu *et al.* described a decrease in $T_V(N_2)$ with increasing *P* and an increase of $T_V(N_2)$ upon packing with TiO_2.[11] They attributed this behavior to greater vibrational-translation relaxation at higher *P*, and the increase in $T_V(N_2)$ was attributed to an enhancement of the average electron energy in the plasma.

Possible explanations for the disparities between these reported trends and the results reported herein may be attributed to inherent differences between the two types of plasma systems used. First, the DBD reactor operates at atmospheric pressure, whereas our systems operate in a much lower pressure regime (50 – 150 mTorr), with a concomitant much longer the mean free path in our system. At atmospheric pressure, electronic quenching (the process by which a collision with species *M* removes energy from excited state species towards any other final product[26]) determines the lifetime of the excited electronic state, occurring on a longer timescale compared to radiative decay. As such, fewer collisions are likely to occur in our systems than in the DBD system. Upon the addition of a substrate, there is a greater likelihood

of productive plasma-surface collisions, effectively quenching N_2 excited states. Furthermore, plasma processing time is an important consideration, as the DBD system studied by Tu *et al.* operated on the μs timescale,[11] whereas our temperature studies investigate steady-state emissions from N_2 molecules on the timescale of minutes. Arguably, there can be vast differences in long-lived and short-lived species within plasma discharges;[27] therefore, future studies probing plasma internal temperatures as a function of time may be useful to understanding species' evolution during plasma processing.

Second, the catalyst in our system occupies only a small fraction of the total plasma volume, whereas Tu *et al.*'s reactor is completely packed with TiO_2 nanoparticles.[11] Thus, the surface area of catalyst available for interaction with the plasma is much larger in the DBD system. Moreover, the packed reactor reduces the plasma volume and gives rise to changes in the discharge mode which could promote decomposition or non-uniform electric fields in the system.[28] If the hypothesis that the catalyst enhances the average electron energy in the plasma is true, then this enhancement could be dependent on the amount of catalyst present. We have previously used the OES spectra acquired in our system to measure T_e in our plasmas, reporting T_e ~1.6 eV in a 100% N_2 plasma (no substrate), regardless of P.[14] Here, we measured T_e ~1.8 eV for the same system with a TiO_2 substrate, also independent of P at p = 50 and 100 mTorr. The lack of significant dependence on P suggests increasing the overall energy of the system preferentially results in increasing the internal energy of neutrals or positive ions, rather than heating the electrons. Nevertheless, T_e appears to be slightly elevated in the presence of the TiO_2 catalytic material, indicating this catalyst does indeed slightly enhance the average T_e in our systems.

Additional OES analysis reveals that not only does a TiO_2 catalyst affect energy partitioning within a N_2 plasma, but the presence of new gas-phase species is also observed when the catalyst is placed in the discharge. A representative raw emission spectrum of 100% N_2 plasma (p = 100 mTorr, P = 75 W) features the observed N_2 $C^3\Pi_u \rightarrow B^3\Pi_g$, NO $A^2\Sigma^+ \rightarrow X^2\Pi$, and OH $A^2\Sigma^+ \rightarrow X^2\Pi$ bands when TiO_2 is placed in the coil region of the reactor space, Figure 6.3a. Comparatively, when no substrate is present in the discharge, little to no emissions from NO or OH are observed,[13] highlighting the significant impact of the catalyst on the gas phase of the plasma. The presence of oxygen-containing gas phase species arises as the plasma interacts with the TiO_2 catalyst, resulting in removal of surface oxygen species. Additionally, the decrease in $T_V(N_2)$ in the presence of the catalyst suggests that within our systems, vibrationally excited molecules interact with the substrates and rebound with some energy loss.

To further explore this impact, relative species' densities were calculated using inert gas actinometry where molecular emissions of N_2 (337.1 nm), OH (309.0 nm), and NO (235.9 nm) were monitored. Figure 6.3b shows the relative amount of N_2 present remains nearly constant with increasing P. This P dependence is similar to observations in a N_2 plasma with a zeolite substrate where the N_2 density is within error from P = 50 – 150 W.[13] In an N_2 plasma with a TiO_2 substrate, OH density also remains constant as a function of P. Conversely, NO density remains fairly constant at low applied rf power until P = ~75 – 100 W, where it begins to decrease. Moreover, the P trends of the oxygen-containing gas phase species differ from the N_2 zeolite PAC system, where OH and NO densities both increase with respect to P.[13] In another study from the Fisher research group, the impact of a zeolite catalyst on gas phase chemistry in an N_2O plasma was examined.[29] In that work, a sharp decrease in NO density is observed at P = 75 W with a simultaneous increase in N_2 and atomic oxygen, suggesting that NO may react with

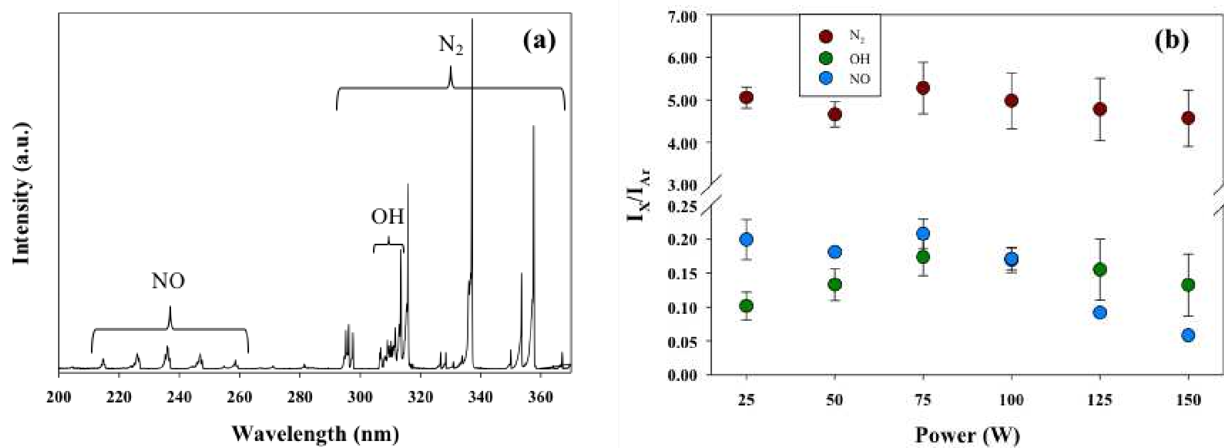

Figure 6.3. (a) Representative emission spectrum (P = 75 W) and (b) relative species density as a function of applied rf power in a 100 mTorr N_2 plasma system with TiO_2.

atomic nitrogen species to form N_2 and O. Because OH density remains fairly constant as a function of P in this system, it is likely that NO is also still being formed from interactions between the plasma and the substrate, but is being decomposed in the gas phase at high P. In this system, however, we do not observe atomic oxygen species or an increase in N_2 density. To gain further insight into the processes occurring in this system, future investigations could include actinometry studies of TiO_2 in other types of N_xO_y plasma systems. Additionally, gas phase investigations with multiple TiO_2 substrates in the plasma would allow for a larger surface area for gas-surface interactions and may help to illuminate clearer density trends or expound the presence of additional gas phase species, such as atomic oxygen.

The interactions between the plasma and the catalyst are obviously imperative to PAC synergy. Thus, choosing an appropriate catalyst is an essential consideration when constructing a viable PAC system. Catalyst pore size and geometry are a couple of important factors to consider in PAC systems as these structural characteristics can have a substantial impact on the fundamental plasma properties. For example, Zhang *et al.* demonstrated that pore shape and size had a significant effect on the electric field within a plasma resulting in changes to the electron density and temperature.[30] Our published report compared the impacts of both nano-structured TiO_2 and micro-structured zeolites on N_2 rotational and vibrational temperatures.[13] To illustrate the impact of these two catalysts on $T_V(N_2)$, ΔT_V was calculated via equation 6.1 and the error reported was appropriately propagated.

$$\Delta T_V = [T_V(\text{catalyst}) - T_V(\text{no substrate})] \qquad (6.1)$$

Notably, Figure 6.4 demonstrates that vibrational cooling of N_2 occurs with either catalyst present in the discharge. A similar observation was also made in N_2O plasma where decreased $T_V(N_2)$ values were also documented for three different catalysts (Pt foil, nano-

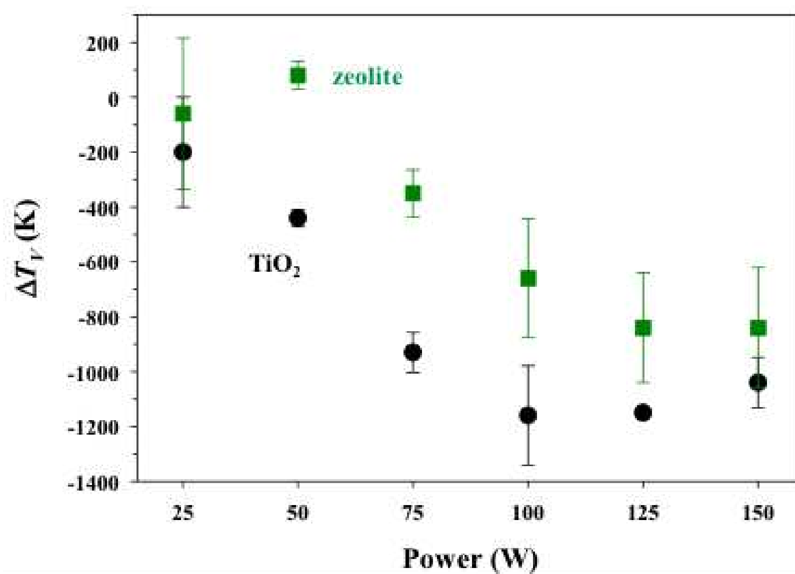

Figure 6.4. ΔT_V for N_2 as a function of applied rf power in a 100% N_2 plasma (p = 100 mTorr) with a TiO_2 substrate (black circles) and a zeolite substrate (green squares). Zeolite data were collected and analyzed by A. R. Hanna.

structured Pt powder, and micro-structured zeolite).[29] Here, although decreased $T_V(N_2)$ values were also documented in the presence of a micro-structured zeolite pellet, the difference compared to a substrate-less system was not as drastic as with a nano-structured TiO_2 substrate. Similarly, in the N_2O plasma system, the nano-structured Pt powder catalyst resulted in markedly decreased $T_V(N_2)$ values compared to the flat Pt and micro-structured zeolite substrates.[29] In our systems, the TiO_2 substrates have significantly smaller pores than the zeolite, suggesting that plasma generation near the pores of the TiO_2 substrate may be heightened, ultimately leading to more vibrational quenching interactions with the catalyst surface. TiO_2 is also a known photocatalyst, and the UV light generated from the plasma may further activate these materials and also contribute to vibrational quenching. Evaluating steady state emission spectroscopy provides valuable information regarding species densities and energetics; however, TR-OES data can help to elucidate additional details about the entangled dynamics in PAC-relevant systems.

Emission intensity of N_2 (337.0 nm) was monitored as a function of time and rate constants of formation (k_f) and destruction (k_d) were determined by fitting the resulting intensity curve with first order exponentials (e^{-kt}). As evidenced in Figure 6.5a, the system with no substrate reaches a steady state with no subsequent decay, hence k_d is not reported. The addition of a TiO_2 catalyst to the discharge, however, significantly changes the gas-phase chemistry and a subsequent decay to a steady state is evident at high powers ($P \geq 100$ W), Figure 6.5b. To further assess kinetic trends, TR-OES data were collected as a function of P at $p = 100$ mTorr, Table 6.2. Without a catalyst present, k_f values decrease as a function of P. Upon addition of a TiO_2 substrate, k_f values are lower, except at $P = 125$ W where k_f values of the two systems are within error of each other. At $P = 150$ W, a clear formation curve followed by a subsequent decay curve were present in some cases, whereas in other cases only a decay curve was present

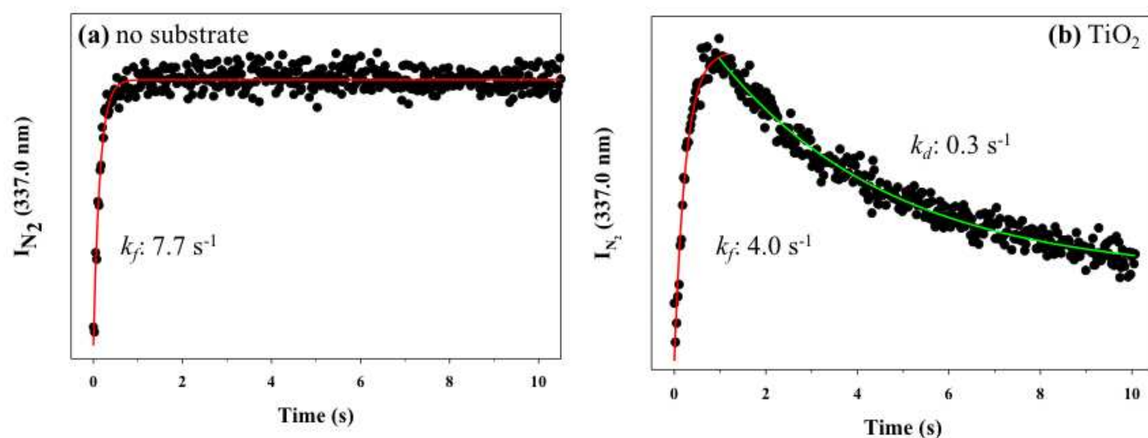

Figure 6.5. Intensity of N_2 emission plotted as a function of time at (a) p = 100 mTorr, P = 50 W with no substrate; (b) p = 100 mTorr, P = 150 W with a TiO_2 substrate. Rate constants of formation and destruction were determined by fitting a first order exponential to each curve (red and green lines, respectively). The no substrate data were collected and analyzed by A. R. Hanna.

Table 6.2. k_f (s^{-1}) and k_d (s^{-1}) values in a 100% N_2 plasma without and with a TiO_2 substrate.[a]

P (W)	no substrate[b] k_f (s^{-1})	TiO_2 k_f (s^{-1})	TiO_2 k_d (s^{-1})
25	10.0 (5.8)	3.1 (0.4)	—
50	8.1 (1.6)	5.7 (0.6)	—
75	5.3 (2.9)	0.71 (0.17)	—
100	4.8 (0.4)	3.5 (0.4)	0.28 (0.014)
125	2.4 (0.3)	3.7 (2.4)	0.27 (0.028)
150	1.3 (0.06)	—	0.29 (0.094)

[a] Values in parentheses represent standard deviation calculated from the mean of $n \geq 3$ trials.
[b] No substrate data collected and analyzed by A. R. Hanna.

at the integration time utilized (25 ms). Thus, a k_f value is not reported for the P = 150 W with TiO_2 substrate system. Comparatively, when a zeolite catalyst (single substrate and multiple substrates) was added to plasma, k_f values differed from the no substrate system except at high power.[13] The plasma discharge mode switches between operating in E-mode [capacitively-coupled electrostatic pre-discharge mode (low P)] and H-mode [inductively-coupled electromagnetic main discharge mode (high P)] between 125 W and 150 W, such that at 150 W the plasma is operating in H-mode. These results suggest that catalysts may have a greater impact on the reaction kinetics when the discharge is operating in E-mode.

Differences in kinetic trends between the two catalyst systems are also worth noting here. The documented k_d values for a TiO_2, Table 6.2, remain constant at ~0.28 s^{-1} regardless of P. Conversely, in the zeolite system, k_d values increase with P and are lower than the TiO_2 system.[13] Mehta *et al.* argue the gas-phase is heavily influenced by active nitrogen species (i.e., N, N_2^+, and vibrationally excited N_2) and increased reaction rates in the presence of catalysts arise from N_2 molecules in low vibrational states on the surface.[31] Notably, $T_V(N_2)$ values are lower (i.e. less vibrationally active) for the TiO_2 catalyst system relative to the zeolite system. Regardless of the catalyst material or morphology, it is clear that the catalyst alters the gas-phase of the plasma. Consequently, we have also investigated how the catalysts were changed through gas-surface interactions.

N_2 plasmas have been used to create metal nitrides and other materials as nitrogen is known to readily replace oxygen in metal oxide lattices.[32-33] Thus, we have examined the morphology and surface composition of our catalyst prior to and after N_2 plasma exposure using SEM and XPS. Figure 6.6 highlights the approximate sizes of the TiO_2 nanoparticles and pores. The commercially purchased TiO_2 material agglomerates into nanoparticle clusters with a porous

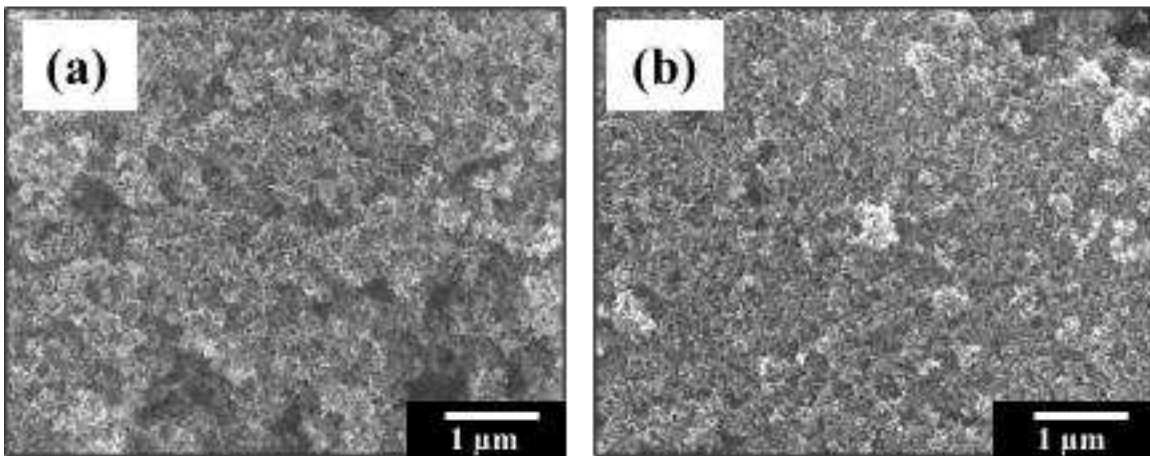

Figure 6.6. Representative SEM images (x20000) of TiO_2 (a) as prepared on Si wafer substrate and (b) post N_2 plasma exposure (*P* = 150 W; *p* = 100 mTorr; *t* = 10 min).

structure when pasted onto the glass substrate, Figure 6.6a. Notably, the morphological features do not change appreciably upon exposure to the N_2 plasma, Figure 6.6b, regardless of *P* or *p* over the parameter space explored herein.

Figure 6.7 contains high-resolution O_{1s} and Ti_{2p} spectra for TiO_2 prior to and post N_2 plasma exposure (p = 100 mTorr, P = 150 W, t = 10 min). The primary contribution to the O_{1s} spectra in untreated TiO_2 arises, as expected, from oxygen bound to Ti^{4+} (530.2 eV),[8] Figure 6.7a, with a smaller peak assigned to oxygen adsorbed to the material surface, such as hydroxyl species (532.1 eV).[8, 34] An increase of adsorbed surface oxygen post N_2 plasma processing, Figure 6.7d, is likely the result of the plasma creating oxygen vacancies within the TiO_2 lattice, which ultimately decreases the relative contribution of the bound oxygen.[8, 35] High resolution Ti_{2p} spectra of the untreated TiO_2 material, Figure 6.7b, show binding energies for $Ti_{2p3/2}$ and $Ti_{2p1/2}$ at 458.6 eV and 464.2 eV, respectively, corresponding to surface titanium in the Ti^{4+} oxidation state.[8] Additional binding environments at 457.9 eV and 462.5 eV corresponding to Ti^{3+} exist in the spectrum of the TiO_2 substrates post N_2 plasma exposure, Figure 6.7e, suggesting nitrogen doping.[8, 33] Specifically, the formation of an O-Ti-N binding environment by substitution of an O atom in the TiO_2 lattice with a N atom is attributed to a shift toward lower binding energy.[36] High-resolution C_{1s} spectra, Figure 6.7c and 6.7f, show binding environments for -C-C/-C-H (284.8 eV), -C-O-R/-C-O-H (286.3 eV), and -C=O (288.7 eV) for the TiO_2 substrate before and after plasma treatment. From these spectra and the corresponding elemental composition, Table 6.3, exposure to the N_2 plasma does not appear to significantly change the nature or amount of carbon on the TiO_2 nanoparticle surface. We do, however, observe a small, but non-negligible amount of nitrogen incorporated into the TiO_2 catalyst surface. Similarly, Lu *et al.* utilized Fourier transform infrared spectroscopy and XPS to

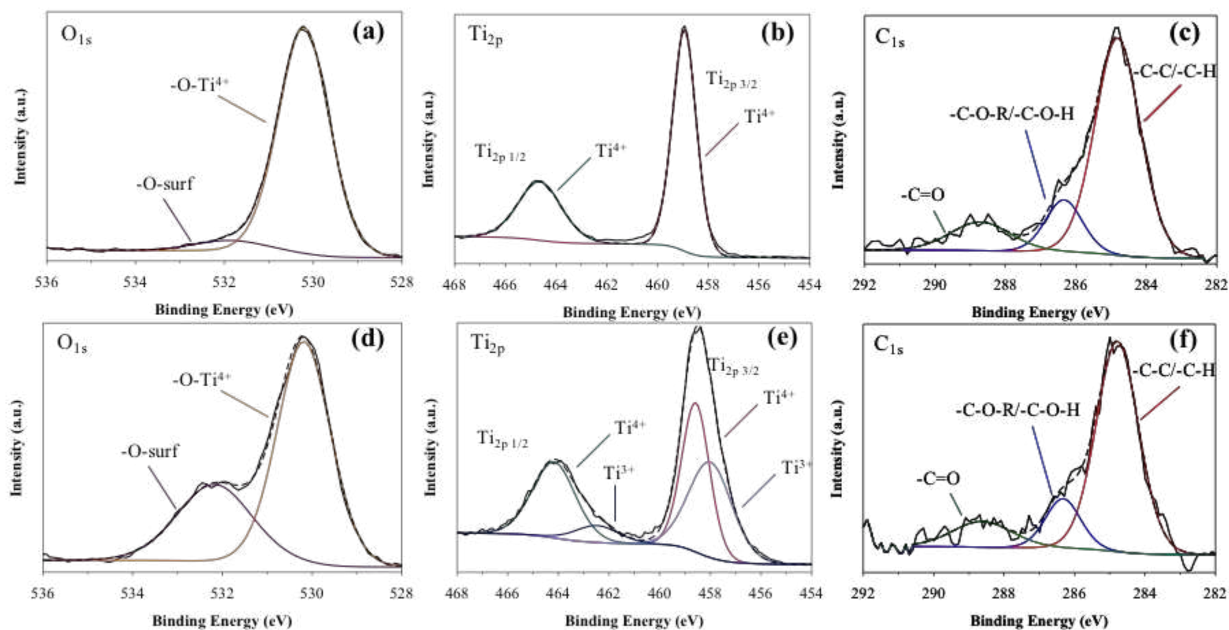

Figure 6.7. XPS high resolution O_{1s}, Ti_{2p}, and C_{1s} data for TiO_2 prior to plasma exposure (a, b, c) and after N_2 plasma (p = 100 mTorr, P = 150 W, t = 10 min) exposure (d, e, f).

Table 6.3. XPS atomic composition data for TiO_2.[a,b]

	Untreated	N_2 plasma
Ti [%]	25.5 (1.2)	19.1 (2.1)
O [%]	63.6 (1.4)	58.8 (1.8)
C [%]	10.9 (2.3)	9.5 (2.3)
N [%]	--	6.6 (1.8)
Si [%]	--	6.0 (2.2)

[a]Values in parentheses represent one standard deviation for the measurement.
[b]Treatment conditions: p = 100 mTorr, P = 150 W, t = 10 min

document nitrogen doping into the structure of TiO_2 coated dielectric of their parallel-plate DBD reactor.[36] Pulsipher *et al.* also observed nitrogen incorporation into TiO_2 substrates upon exposure to a range of nitrogen-containing plasmas, including N_2-based systems.[37]

As discussed throughout this chapter, we sought to not only examine the impact of the catalyst on fundamental gas-phase processes in the plasma but are also to understand the plasma's impact on catalyst properties. Elucidating the entangled impact of both the plasma and the material on each other helps to unravel the synergistic effects and complex chemical processes and work needed to ultimately improve the performance of these processes for practical applications. Hueso *et al.* also noted the importance of examining both the gas-phase of the plasma and the catalyst to deconvolute plasma-catalyst synergies for improving process performance.[38] They studied conversion of NO and CH_4 in mixed gas plasma systems with two catalytic materials, a perovskite-type catalyst and SiO_2. In addition to gas conversion calculations, they utilized OES to identify the prominent gas-phase species in their plasma systems and XPS to evaluate surface chemistry of their catalysts before and after plasma exposure. Interestingly, in their systems, decreased NO removal efficiency was observed in the presence of either catalyst. XPS results from Hueso *et al.* show the presence of adsorbed nitrogen species [$–NO_x$ ($x \leq 2$) and $–NO_2$] on the perovskite-type catalyst after plasma exposure.[38] The adsorbed species pass through a maximum concentration as a function of time and then decrease when steady-state conditions are reached. The authors attribute this to a high concentration of NO^* shown in their OES results. NO^* can be reactive towards oxide surfaces and give rise to the $–NO_x$ and $–NO_2$ adsorbed species corroborated by their XPS results.[38-40] Removal and decomposition of these species from the surface can ultimately yield NO, possibly explaining the reduced NO removal efficiency. These results are important in that they consider

both the gas-phase and material in PAC systems in an effort to elucidate plasma-catalyst synergies; yet, the authors did not monitor the gas-phase via OES with a catalyst present in the plasma. Results presented throughout this chapter demonstrate that plasma chemistry can change significantly upon addition of a catalyst to the discharge. Thus, a thorough analysis of the plasma with and without a catalyst is an essential consideration when investigating inherently complex PAC systems.

Our experimental approach allows us to gain further insight into the mechanistic phenomena and plasma-catalyst synergies in PAC systems. Figure 6.8 depicts the gas-surface interactions that we believe are the most prevalent in our system. XPS data reveal nitrogen doping into the TiO_2 lattice under some parameters. The etching of lattice oxygen can occur when excited state nitrogen impinges and reacts to form additional gas-phase species (i.e., NO, OH) as depicted in Figure 6.8 and reaction 6.2.

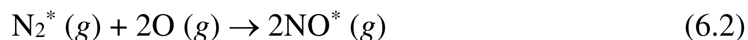

$$N_2^* \, (g) + 2O \, (g) \rightarrow 2NO^* \, (g) \qquad (6.2)$$

Ultimately, there is still much work to be done to understand the underlying mechanisms involved in PAC. Nevertheless, the work presented herein clearly demonstrates that catalytic materials can alter energy partitioning with the gas-phase of the plasma.

6.3 Summary

Evaluation of energy partitioning and materials characterization data reveal a synergistic nature between the plasma and TiO_2 catalyst wherein the material impacts the gas-phase of the plasma and the plasma alters chemical characteristics of the catalyst. The presence of the catalyst in the N_2 discharge resulted in a pronounced decrease of N_2 vibrational temperatures while no clear or significant impact on the rotational temperature was reported. For PAC to

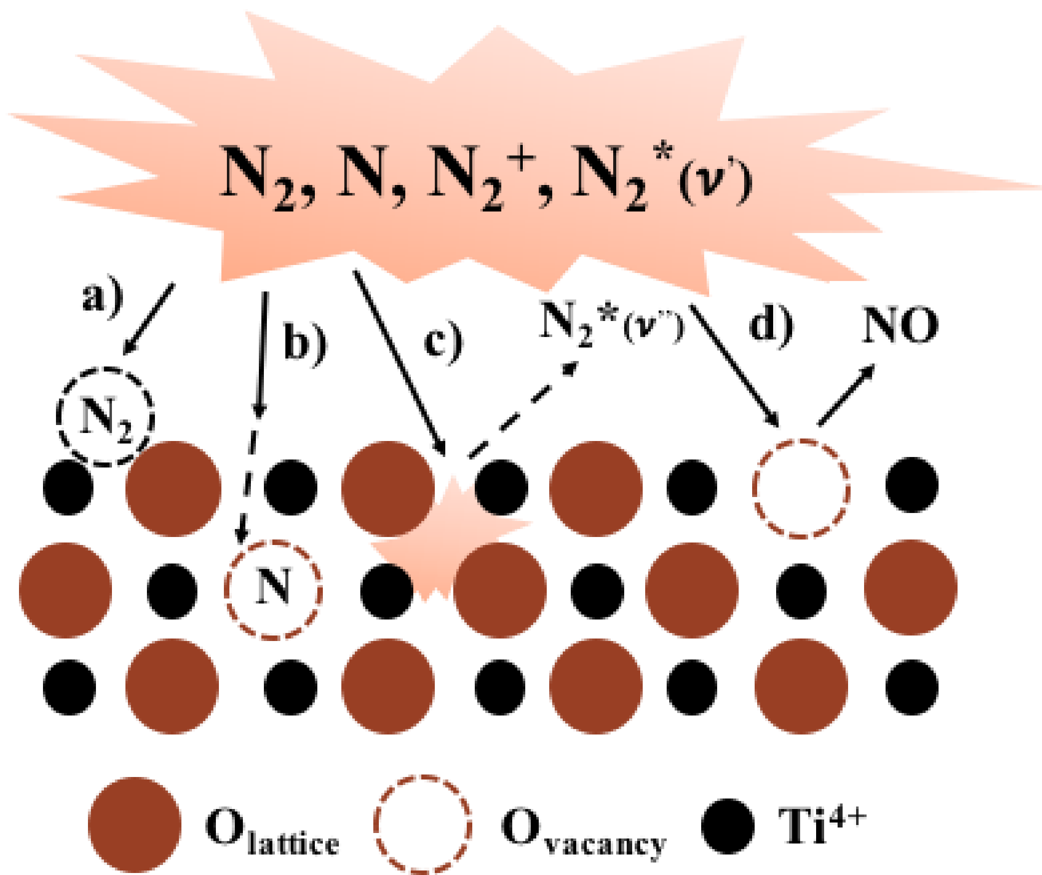

Figure 6.8. Schematic representation of various surface modification process occurring during N_2 plasma processing: (a) surface adsorption; (b) N-doping of the substrate; (c) energetic bombardment resulting in vibrational quenching; (d) etching and formation of new gaseous species. This figure has been modified from the published version (original version created by A. R. Hanna) to reflect the new information presented within this chapter.[13]

become a viable tool for pollution control, fundamental plasma characteristics must first be examined to elucidate mechanistic phenomena that control PAC synergies. Specifically, investigations into plasma-surface interactions are vital to the future of this technology. Employing our unique imaging radicals interacting with surfaces (IRIS) technique to determine a molecule's propensity to scatter from catalytic surfaces could provide insight into gas-surface interactions and will be used in future work. A holistic experimental approach employing gas-phase, gas-surface interface, and materials analyses will be essential to increasing the potential for utilizing PAC as a pollution remediation tool.

REFERENCES

1. Neyts, E.; Bogaerts, A., Understanding Plasma Catalysis through Modelling and Simulation—A Review. *J. Phys. D: Appl. Phys.* **2014,** *47* (22), 224010.
2. Whitehead, J. C., Plasma-Catalysis: The Known Knowns, the Known Unknowns, and the Unknown Unknowns. *J. Phys. D: Appl. Phys.* **2016,** *49*, 243001 (24pp).
3. Neyts, E. C., Plasma-Surface Interactions in Plasma Catalysis. *Plasma Chem. Plasma Process.* **2016,** *36*, 185-212.
4. Kim, H.-H.; Teramoto, Y.; Ogata, A.; Takagi, H.; Nanba, T., Plasma Catalysis for Environmental Treatment and Energy Applications. *Plasma Chem. Plasma Process.* **2016,** *36* (1), 45-72.
5. Adamovich, I.; Baalrud, S. D.; Bogaerts, A.; Bruggeman, P. J.; Cappelli, M.; Colombo, V.; Czarnetzki, U.; Ebert, U.; Eden, J. G.; Favia, P.; Graves, D. B.; Hamaguchi, S.; Hieftje, G.; Hori, M.; Kaganovich, I. D.; Kortshagen, U.; Kushner, M. J.; Mason, N. J.; Mazouffre, S.; Thagard, S. M.; Metelmann, H. R.; Mizuno, A.; Moreau, E.; Murphy, A. B.; Niemira, B. A.; Oehrlein, G. S.; Petrovic, Z. L.; Pitchford, L. C.; Pu, Y. K.; Rauf, S.; Sakai, O.; Samukawa, S.; Starikovskaia, S.; Tennyson, J.; Terashima, K.; Turner, M. M.; Sanden, M. C. M. v. d.; Vardelle, A., The 2017 Plasma Roadmap: Low Temperature Plasma Science and Technology. *J. Phys. D: Appl. Phys.* **2017,** *50* (32), 323001.
6. Neyts, E. C.; Ostrikov, K.; Sunkara, M. K.; Bogaerts, A., Plasma Catalysis: Synergistic Effects at the Nanoscale. *Chem. Rev.* **2015,** *115* (24), 13408-13446.
7. Gong; Zhao, R.; Qin, J.; Wang, H.; Wang, D., Ultra-Efficient Removal of NO in a MOFs-NTP Synergistic Process at Ambient Temperature. *Chem. Eng. J.* **2019,** *358*, 291-298.
8. Wu, H.; Xu, C.; Xu, J.; Lu, L.; Fan, Z.; Chen, X.; Song, Y.; Li, D., Enhanced Supercapacitance in Anodic TiO_2 Nanotube Films by Hydrogen Plasma Treatment. *Nanotechnology* **2013,** *24* (45), 455401.
9. Feng, X.; Liu, H.; He, C.; Shen, Z.; Wang, T., Synergistic Effects and Mechanism of a Non-Thermal Plasma Catalysis System in Volatile Organic Compound Removal: A Review. *Catal. Sci. Technol.* **2018,** *8* (4), 936-954.
10. Puliyalil, H.; Jurkovic, D. L.; Dasireddy, V. D. B. C.; Likozar, B., A Review of Plasma-Assisted Catalytic Conversion of Gaseous Carbon Dioxide and Methane into Value-Added Platform Chemicals and Fuels. *RSC Adv.* **2018,** *8*, 27481-27508.
11. Tu, X.; Gallon, J.; Whitehead, J. C., Electrical and Spectroscopic Diagnostics of a Single-Stage Plasma-Catalysis System: Effect of Packing with TiO_2. *J. Phys. D: Appl. Phys.* **2011,** *44*, 482003.
12. Niu, J.; Peng, B.; Yang, Q.; Cong, Y.; Liu, D.; Fan, H., Spectroscopic Diagnostics of Plasma-Assisted Catalytic Systems for NO Removal from $NO/N_2/O_2/C_2H_4$ Mixtures. *Cat. Today* **2013,** *211*, 58-65.
13. Hanna, A. R.; Van Surksum, T. L.; Fisher, E. R., Investigating the Impact of Catalysts on N_2 Rotational and Vibrational Temperatures in Low Pressure Plasmas. *J. Phys. D: Appl. Phys.* **2019,** *52* (34), 345202.
14. Hanna, A. R.; Blechle, J. M.; Fisher, E. R., Using Fundamental Spectroscopy to Elucidate Kinetic and Energetic Mechanisms within Environmentally Relevant Inductively Coupled Plasma Systems. *J. Phys. Chem. A* **2017,** *121* (40), 7627-7640.
15. Porter, R. A.; Harshbarger, W. R., Gas Rotational Temperature in an RF Plasma. *J. Electrochem. Soc.* **1979,** *126* (3), 460-464.

16. Cernogora, G.; Ferreira, C. M.; Hochard, L.; Touzeau, M.; Loureiro, J., Vibrational Populations of $N_2(A^3\Sigma_u^+)$ in a Pure Nitrogen Glow Discharge. *J. Phys. B: At., Mol. Opt. Phys.* **1984,** *17* (21), 4429-4437.
17. Zhang, J.; Liu, L.; Ma, T.; Deng, X., Rotational Temperature of Nitrogen Glow Discharge Obtained by Optical Emission Spectroscopy. *Spectrochim. Acta, Part A* **2002,** *58* (9), 1915-1922.
18. Masoud, N.; Martus, K.; Figus, M.; Becker, K., Rotational and Vibrational Temperature Measurements in a High-Pressure Cylindrical Dielectric Barrier Discharge (C-DBD). *Contrib. Plasm. Phys.* **2005,** *45* (1), 32-39.
19. Britun, N.; Gaillard, M.; Ricard, A.; Kim, Y. M.; Kim, K. S.; Han, J. G., Determination of the Vibrational, Rotational and Electron Temperatures in N_2 and Ar–N_2 RF Discharge. *J. Phys. D: Appl. Phys.* **2007,** *40* (4), 1022-1029.
20. Gangoli, S. P.; Gutsol, A. F.; Fridman, A. A., A Non-Equilibrium Plasma Source: Magnetically Stabilized Gliding Arc Discharge: I. Design and Diagnostics. *Plasma Sources Sci. Technol.* **2010,** *19* (6), 065003.
21. Wu, A. J.; Zhang, H.; Li, X. D.; Lu, S. Y.; Du, C. M.; Yan, J. H., Determination of Spectroscopic Temperatures and Electron Density in Rotating Gliding Arc Discharge *IEEE Trans. Plasma Sci.* **2015,** *43* (3), 836-845.
22. Yang, F.; Mu, Z.; Zhang, J., Discharge Modes Suggested by Emission Spectra of Nitrogen Dielectric Barrier Discharge with Wire-Cylinder Electrodes. *Plasma Sources Sci. Technol.* **2016,** *18* (1), 79-85.
23. Gröger, S.; Ramakers, M.; Hamme, M.; Medrano, J. A.; Bibinov, N.; Gallucci, F.; Bogaerts, A.; Awakowicz, P., Characterization of a Nitrogen Gliding Arc Plasmatron Using Optical Emission Spectroscopy and High-Speed Camera. *J. Phys. D: Appl. Phys.* **2018,** *52* (6), 065201.
24. Laux, C. O. In *Radiation and Nonequilibrium Collisional-Radiative Models*, von Karman Institute Lecture Series, Physico-Chemical Modeling of High Enthalpy and Plasma Flows, Rhode-Saint-Gense, Belgium), Fletcher, D.; Charbonnier, J.-M.; Sarma, G. S. R.; Magin, T., Eds. Rhode-Saint-Gense, Belgium), 2002.
25. NIST. *Nist Chemistry Webbook*. http://webbook.nist.gov/chemistry (accessed October 12, 2018).
26. Dilecce, G., Optical Spectroscopy Diagnostics of Discharges at Atmospheric Pressure. *Plasma Sources Sci. Technol.* **2014,** *23* (1), 015011.
27. Grill, A., *Cold Plasma Materials Fabrications: From Fundamentals to Applications*. IEEE Press: Piscataway, NJ, 1994.
28. Feng, X.; Liu, H.; Hi, C.; Shen, Z.; Wang, T., Synergistic Effects and Mechanism of a Non-Thermal Plasma Catalysis System in Volatile Organic Compound Removal: A Review. *Catal. Sci. Technol.* **2018,** *8*, 936-954.
29. Hanna, A. R.; Fisher, E. R., Efforts toward Unraveling Plasma-Assisted Catalysis: Determination of Kinetics and Molecular Temperatures within N_2O Discharges. *ACS Catal.* **2020,** *10*, 6546-6560.
30. Zhang, Y.-R.; Neyts, E. C.; Bogaerts, A., Enhancement of Plasma Generation in Catalyst Pores with Different Shapes. *Plasma Sources Sci. Technol.* **2018,** *27* (5), 055008.
31. Mehta, P.; Barboun, P.; Go, D. B.; Hicks, J. C.; Schneider, W. F., Catalysis Enabled by Plasma Activation of Strong Chemical Bonds: A Review. *ACS Energy Lett.* **2019**, 1115-1133.

32. Antonczak, A. J.; Skowronski, L.; Trzcinski, M.; Kinzhybalo, V. V.; Lazarek, L. K.; Abramski, K. M., Laser-Induced Oxidation of Titanium Substrate: Analysis of the Physicochemical Structure of the Surface and Sub-Surface Layers. *Appl. Surf. Sci.* **2015,** *325*, 217-226.
33. Kollbek, K.; Szkudlarek, A.; Marzec, M. M.; Lyson-Sypien, B.; Cecot, M.; Bernasik, A.; Radecka, M.; Zakrzewska, Optical and Electrical Properties of Ti(Cr)O_2:N Thin Films Deposted by Magnetron Co-Sputtering. *Appl. Surf. Sci.* **2016,** *380*, 73-82.
34. Cao, Y.; Meng, Q.; Yang, W.; Yao, J.; Shu, Y.; Wang, W.; Chen, G., Effect of Plasma Treatment on Surface Properties of TiO_2 Nanoparticulate Films. *Colloids Surf., A* **2005,** *262* (1-3), 181-186.
35. Han, J.-B.; Wang, X.; Wang, N.; Wei, Z.-H.; Yu, G.-P.; Zhou, Z.-G.; Wang, Q.-Q., Effect of Plasma Treatment on Hydrophilic Properties of TiO_2 Thin Films. *Surf. Coat. Technol.* **2006,** *200* (16-17), 4876-4878.
36. Lu, N.; Hui, Y.; Shang, K.; Jiang, N.; Li, J.; Wu, Y., Diagnostics of Plasma Behavior and TiO_2 Properties Based on DBD/TiO_2 Hybrid System. *Plasma Chem. Plasma Process.* **2018,** *38* (6), 1239-1258.
37. Pulsipher, D. J. V.; Martin, I. T.; Fisher, E. R., Controlled Nitrogen Doping and Film Colorimetrics in Porous TiO_2 Materials Using Plasma Processing. *ACS Appl. Mater. Interfaces* **2010,** *2*, 1743-1753.
38. Hueso, J.; Cotrino, J.; Caballero, A.; Espinós, J.; González-Elipe, A., Plasma Catalysis with Perovskite-Type Catalysts for the Removal of NO and CH_4 from Combustion Exhausts. *J. Catal.* **2007,** *247* (2), 288-297.
39. Hueso, J.; González-Elipe, A.; Cotrino, J.; Caballero, A., Plasma Chemistry of NO in Complex Gas Mixtures Excited with a Surfatron Launcher. *J. Phys. Chem. A* **2005,** *109* (22), 4930-4938.
40. Hueso, J. L.; González-Elipe, A. R.; Cotrino, J.; Caballero, A., Removal of NO in NO/N_2, NO/N_2/O_2, NO/CH_4/N_2, and NO/CH_4/O_2/N_2 Systems by Flowing Microwave Discharges. *J. Phys. Chem. A* **2007,** *111* (6), 1057-1065.

CHAPTER 7

ELUCIDATING ENERGETIC AND KINETIC TRENDS IN ENVIRONMENTALLY RELEVANT MIXED GAS PLASMA SYSTEMS

The studies presented within this chapter employ optical spectroscopy techniques to elucidate energetic and kinetic trends of several molecular species (i.e., CH, CN, CO, H_2, OH, N_2) in CH_4/N_2 and CH_4/H_2O plasma systems. Time-resolved optical emission spectroscopy results suggest formation of CN may be related to the excited nitrogen species available in a CH_4/N_2 plasma. Moreover, there are vast differences in rotational and vibrational temperatures between different plasma species. This indicates that the rotational and vibrational temperatures of the excited state species in our system are not equilibrated with each other and that different species have achieved different degrees of equilibration between rotational and vibrational modes. Mechanistic phenomena regarding molecule formation in these plasma systems will be discussed. This work was supported by funding through the National Science Foundation (NSF CBET – 1803067) and the American Chemical Petroleum Research Fund (ACS PRF 59776 – ND6).

7.1 Introduction

Nonthermal, low temperature plasmas (LTPs) comprise a variety of electrons, ions, atoms and molecular species that are not in equilibrium with each other and can have significantly different kinetic energies.[1] Specifically, the translational energy of the electrons in LTPs are much larger than the heavy species in the plasma (i.e., ions, neutrals, radicals).[1] Consequently, the electron temperature (T_e) is much higher than the gas temperature (T_g), and the highly

energetic electrons initiate numerous reactions through electron impact collisions.[1] Because reactive species generated in the plasma lead to complex physical and chemical reactions, an LTP is a highly promising approach to surface modification, etching, deposition, or synthesis of new molecules. An example of the last instance can be found in plasma assisted catalysis (PAC) applications, which generally describes the coupling of a plasma and catalyst for enhanced processing of the input gas stream to either convert the feed gas mixture to another gas mixture or to grow a material from the precursor gas. For example, carbon deposition from CH_4 or C_2H_2 produces a significant amount of H_2.[2] Additionally, the conversion of volatile organic compounds and NO_x emissions into harmless constituents via PAC is of particular interest to the plasma community.[3] Regardless of the end application, a thorough understanding of the molecular formation processes is critical to the advancement of plasma technology.

Optical spectroscopy diagnostics have been widely employed to examine molecule formation processes in LTPs because of their relatively simple configuration and the nonintrusive nature of the technique.[4] For example, Wang *et al.* used optical emission spectroscopy (OES) to better understand the formation and role of active gas-phase species in the plasma-enhanced synthesis of ammonia.[5] The authors examined emission intensities of several excited state species (i.e., N_2^+, N, H_α, NH) in a N_2/H_2 dielectric barrier discharge (DBD) without and with catalyst packing. Identification of atomic N and the H_α Balmer line via OES suggests dissociation of the precursor gases. Furthermore, with catalyst packing, the increase in NH_3 yield in conjunction with the increased intensity for each of the studied gas phase species suggests that the generation of these species may help promote NH_3 formation. Another recent OES study examined the effects of pulsed plasma parameters during the reforming process in a 50% CH_4/50% CO_2 dielectric barrier discharge (DBD).[6] The authors noted that the emission

spectrum comprised CH, C_2, H_α, CO, and CO_2^+ species and determined the rotational (T_R) and vibrational (T_V) temperatures of CH $A^2\Delta \rightarrow X^2\Pi$ in their system. The large difference between T_V(CH) (6500 ± 1000 K) and T_R(CH) (547 ± 10 K) indicates a significant internal non-equilibrium in the plasma which the authors hypothesize ultimately facilitated temperature control and enhanced the conversion process.[6]

Although these studies provide useful information on the excited state species in the plasma, OES is a powerful diagnostic tool that can also be used to probe kinetics and energy distributions.[4] Indeed, the future of plasma technology relies on a deeper understanding of gas phase kinetic and energetic pathways.[3] Such information is crucial to accurate plasma modelling and the development of efficient PAC systems. In this work, species formation (k_f) and destruction (k_d) rates are determined by employing time-resolved OES (TR-OES). Additional insight into molecule formation mechanisms and decomposition pathways is gained via the rotational and vibrational temperatures of molecular species within our plasma systems. One important consideration with internal plasma temperature determination is that different molecular species within the same plasma system may exhibit vastly different rotational and vibrational temperatures. Thus, examining several molecular species within a plasma system provides enhanced insight into the overall plasma chemistry. Additionally, a single plasma species may be produced via different mechanisms (e.g., direct impact excitation, decomposition, recombination) and may exhibit different T_R or T_V values as a function of plasma parameters. Indeed, plasma temperatures tend to be highly dependent on plasma parameters.[7-9] For example, Raud *et al.* calculated $T_R(N_2)$ and T_R(OH) in a 2 Torr Ar/0.5% O_2 rf discharge as a function of power density, demonstrating that T_R(OH) increased with growing power density whereas $T_R(N_2)$ displayed the opposite trend.[8] In addition, $T_R(N_2)$ was consistently higher than T_R(OH) over the

parameter range studied, suggesting that $T_R(N_2)$ was not directly related to the gas temperature in their system. Thus, a more complete understanding of the relationship between plasma parameters and kinetic and energetic outcomes can provide prolific insights into the roles of the reactive species in physical or chemical catalytic reactions and can ultimately provide reference for the optimization of plasma devices and the efficiency of PAC systems.

In this work, we investigated the kinetics and energy partitioning trends of several molecular species (i.e., CH, CN, CO, H_2, N_2, OH) in two CH_4-containing plasma mixtures as functions of feed gas composition and applied rf power (P) using steady state OES and TR-OES. Note that all experiments described within this chapter were performed at a total system pressure of 150 mTorr. CH_4/N_2 and CH_4/H_2O gas mixtures were chosen these studies because of their environmental relevance for PAC applications. For all steady state experiments (e.g., actinometry, internal temperature determination), a small amount of Ar (10%) was added to the precursor mixture. The remaining 90% of the feed gas comprised of CH_4/N_2 or CH_4/H_2O mixtures at different ratios. TR-OES experiments used the same ratio mixtures, but no Ar was added to these experiments. Some of the results in this report are compared to our previous energy partitioning studies of 100% N_2 and 100% CH_4.[10-12] By coupling kinetic and energy partitioning data for multiple species within our plasmas systems, we can begin to unravel the complex chemical processes responsible for plasma behavior.

7.2 Results

a. *CH_4/N_2 plasma system.* Representative raw OES spectra for two different gas ratios of a CH_4/N_2 plasma system (with 10% Ar added) are shown in Figure 7.1. Emission peaks arising from Ar transitions appear in both spectra, although many of these lines are obscured by

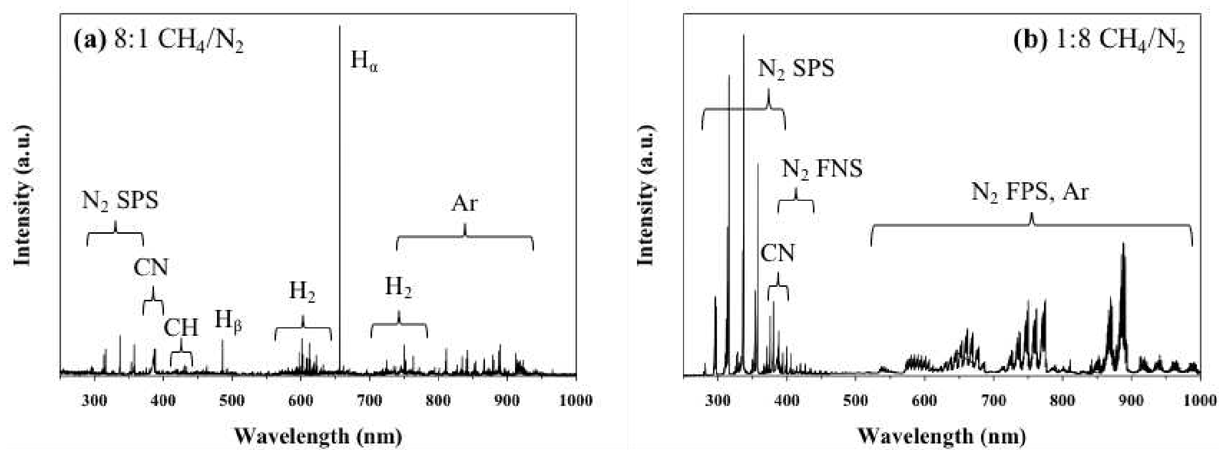

Figure 7.1. Raw OES spectra (P = 125 W) of a (a) 8:1 CH_4/N_2 plasma and a (b) 1:8 CH_4/N_2 plasma. Emission lines and bands attributed to the major emitting species are labeled.

the N_2 first positive system (FPS) ($B^3\Pi_g \rightarrow A^3\Sigma_u^+$) in the 1:8 CH_4/N_2 plasma (Figure 7.1b). Emission corresponding to H_α (656.2 nm), H_β (486.1 nm), and H_2 molecular bands centered at ~610 nm and ~740 nm is observed in the spectrum of the 8:1 CH_4/N_2 plasma system (Figure 7.1a). Emission bands for the CH $A^2\Delta \rightarrow X^2\Pi$ (431.1 nm) and the CN $B^2\Sigma^+ \rightarrow X^2\Sigma^+$ (388.3 nm) transitions are also observed. Although only the N_2 second positive system (SPS) ($C^3\Pi_u \rightarrow B^3\Pi_g$) is clearly seen in the spectrum of the 8:1 CH_4/N_2 ratio mixture, the N_2 FPS ($B^3\Pi_g \rightarrow A^3\Sigma_u^+$) and N_2^+ first negative system (FNS) ($B^2\Sigma_u^+ \rightarrow X^2\Sigma_g^+$) are also observed in the spectrum for the 1:8 CH_4/N_2 system, Figure 7.1b. In addition to the N_2 molecular bands, CN emission is also noted in the 1:8 CH_4/N_2 system.

The emission spectra for a CH_4/N_2 plasma (Figure 7.1) can comprise different plasma species and display noticeable variations in species intensities depending on the feed gas ratio. Inert gas actinometry was used to determine how relative species densities (denoted here with brackets, e.g., "[CN]") changed as a function of the precursor ratio. Depicted in Figure 7.2, relative densities were derived for CH (431.1 nm), CN (388.3 nm), H_α (656.2 nm), H_2 (601.1 nm), and N_2 (337.0 nm) at several feed gas ratios for a CH_4/N_2 plasma. As expected, the densities of species resulting primarily from CH_4 decomposition (CH, H_α, and H_2) decrease while [N_2] increases with a concomitant increase of N_2 fraction in the feed gas. [CN] initially increases with N_2 feed gas fraction before reaching a maximum density at a 1:1 CH_4/N_2 ratio. As the N_2 fraction becomes greater than the CH_4 fraction, a subsequent decrease in [CN] is observed. Notably, these data were collected at a 50 ms integration time with 150 averages per scan over the course of several minutes. Thus, these data provide us with an effectively steady-state snapshot of the plasma. These steady state concentrations provide us with valuable information regarding the gas-phase species in the plasma; however, TR-OES can be used to

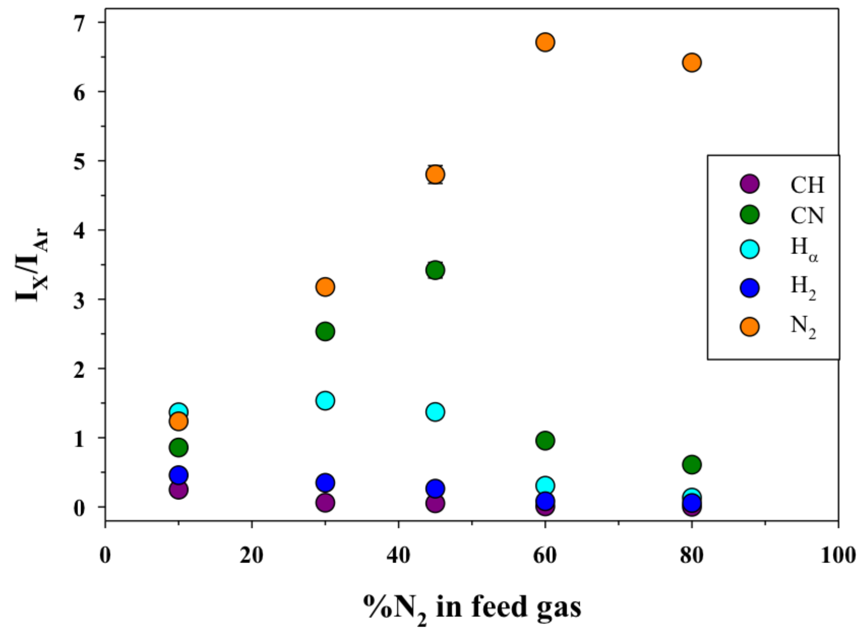

Figure 7.2. Relative densities of excited state species in CH_4/N_2 plasma as a function of $\%N_2$ in the feed gas mixture (P = 75 W).

examine the temporal evolution of plasma species, yielding kinetic insight into possible mechanisms of species formation and destruction.

Figure 7.3 shows the intensity of CN emission as a function of time for each gas ratio explored. Notably, there are significant differences in the temporal profiles between each of the feed gas ratios. When the feed gas composition comprises mostly CH_4 (8:1 and 2:1 CH_4/N_2 ratios), only a rise in emission intensity to a steady state is observed. As more N_2 is added to the feed gas, however, the rise to maximum emission intensity is followed by a subsequent decay in intensity until a steady state is reached. Although a temporal decay for CN is observed at all powers in the 1:8 CH_4/N_2 system, the 1:1 and 1:2 CH_4/N_2 systems display a decomposition curve only at $P \geq 75$ W. By fitting the intensity curves with a first order exponential (e^{-kt}), we obtain information about the rates of formation (k_f) and destruction (k_d) for CN. Figure 7.4a shows CN k_f values as a function of %N_2 in the feed gas at P = 25 W, 75 W, 125 W. At low N_2 fraction (<50%), CN k_f ranges from ~1.5 – 2.9 s^{-1} and does not appear to be dependent on P. As the percent N_2 in the feed gas increases (≥50%), however, the observed CN kinetic trends change significantly. Specifically, CN k_f increases concomitantly with the percent N_2 and with P. At ≥50% N_2 in the feed gas, CN k_f values range from ~1.5 – 21.0 s^{-1}, changing dramatically with plasma parameters. Notably, no CN k_f value is reported for P = 25 W in the 8:1 CH_4/N_2 plasma system because of low CN emission intensity. Likewise, at P = 125 W in the 1:8 CH_4/N_2 plasma, a fit for CN k_d could not be obtained because no formation curve was observable even at the fastest integration times used for these experiments (1.5 ms). CN k_d was also measured where decay curves were present, Figure 7.4b. Overall, CN k_d trends are similar to those for CN k_f as k_d also increases concomitantly with percent N_2 and with P, ranging from ~2.9 – 15.4 s^{-1}. All k_f and k_d values are listed in Table 7.1 for reference.

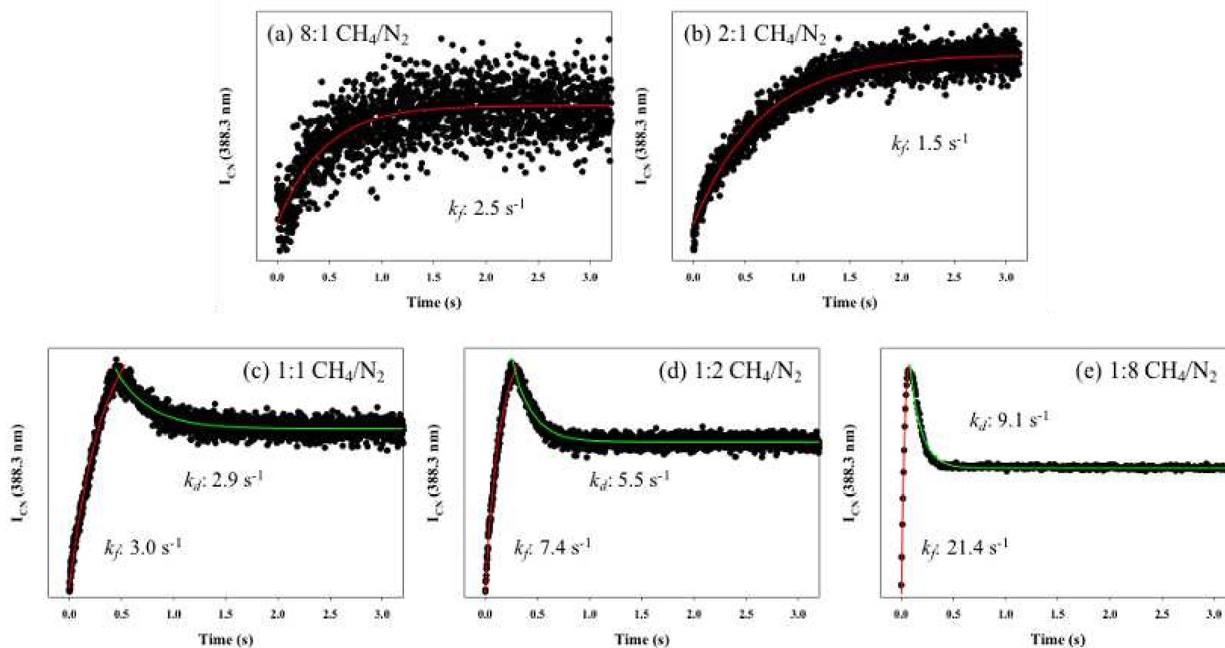

Figure 7.3. Intensity of CN emission plotted as a function of time (P = 75 W) in (a) 8:1 CH_4/N_2, (b) 2:1 CH_4/N_2, (c) 1:1 CH_4/N_2, (d) 1:2 CH_4/N_2, and (e) 1:8 CH_4/N_2 plasmas. Rate constants of formation and destruction were determined by fitting a first order exponential to each portion of the curve (solid lines). Y-axes are intensities of the selected CN emission line in arbitrary units.

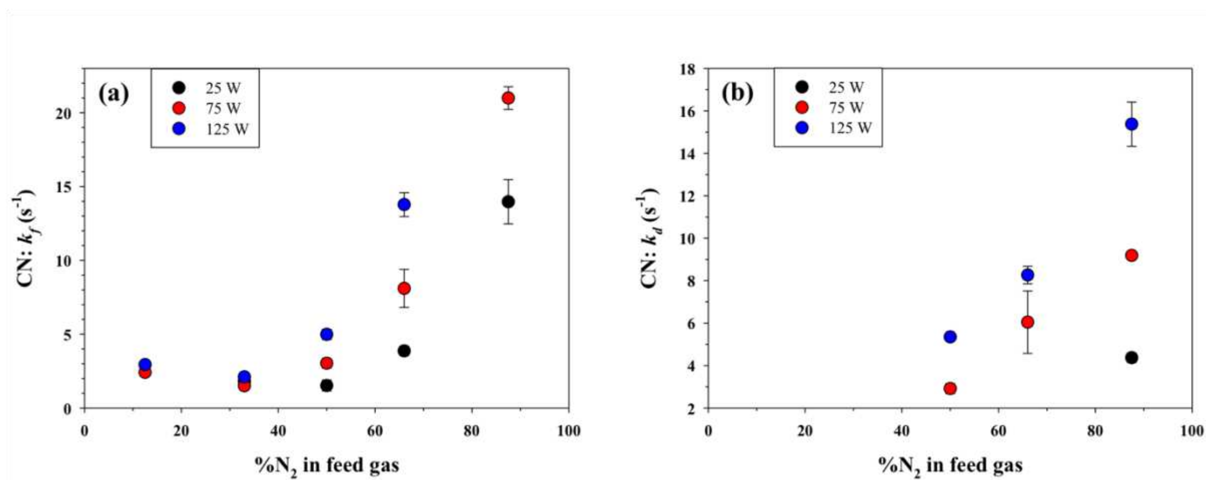

Figure 7.4. (a) CN k_f (s^{-1}) and (b) CN k_d (s^{-1}) values as a function of %N_2 in CH_4/N_2 plasmas at three applied rf powers (25 W, 75 W, and 125 W).

Table 7.1. Calculated k_f and k_d values for N_2 and CN.[a,b]

P (W)	N_2: k_f	CN: k_f	CN: k_d
8:1 CH_4/N_2			
25	—	—	—
75	—	2.4 (0.2)	—
125	—	2.9 (0.1)	—
2:1 CH_4/N_2			
25	—	1.8 (0.2)	—
75	—	1.5 (0.1)	—
125	—	2.1 (0.1)	—
1:1 CH_4/N_2			
25	1.7 (1.2)	1.5 (0.4)	—
75	2.0 (0.1)	3.0 (0.3)	2.9 (0.2)
125	3.0 (0.1)	5.0 (0.3)	5.4 (0.1)
1:2 CH_4/N_2			
25	1.1 (0.1)	3.9 (0.3)	—
75	3.0 (0.2)	8.1 (1.3)	6.0 (1.5)
125	4.1 (0.2)	13.8 (0.8)	8.3 (0.4)
1:8 CH_4/N_2			
25	2.1 (0.1)	14.0 (1.5)	4.4 (0.2)
75	10.0 (0.4)	21.0 (0.8)	9.2 (0.1)
125	14.9 (6.0)	—	15.4 (1.0)

[a] Values in parentheses represent the standard deviation calculated from the mean of n≥3 trials.

Table 7.1 also lists k_f values for N_2 for feed gas conditions comprising ≥50% N_2. At low N_2 content (<50%), only a decay to steady state is observed (i.e. no formation curve was present) and destruction rates could not be reliably obtained from these data. Representative temporal profiles highlighting N_2 decay for low N_2 content plasmas are shown in Figures 7.5a and 7.5b. For the 1:1 and 1:2 CH_4/N_2 systems (Figures 7.5c and 7.5d, respectively), N_2 temporal emission profiles also show a clear destruction curve immediately following plasma ignition. Following the initial destruction curve, however, a formation curve to a steady state also occurs with these two feed gas ratios. Although an N_2 destruction curve is not observed in the 1:8 CH_4/N_2 plasma system, the first 1–2 data points immediately following plasma ignition were consistently elevated relative to the formation curve. We have previously observed and discussed this phenomenon in pulsed 100% Ar and 100% N_2 discharges, attributing it to "hot electrons" which tend to overshoot steady state values at the beginning of the active glow.[4] Overall, N_2 k_f trends are similar to the those for CN k_f and k_d. N_2 k_f increases concomitantly with both P and %N_2 in the feed gas, and values range from ~1.1 – 14.9 s^{-1} across the parameter space. Evaluation of plasma kinetics can provide insight into plasma ignition and initial plasma processes; yet, steady-state energetics is also a critical component to a comprehensive evaluation of fundamental plasma processes.

As noted in Section 7.1, we also determined rotational and vibrational temperatures for several species in our plasma systems. All T_R and T_V values measured for diatomic gas-phase species in the CH_4/N_2 system are listed in Table 7.2 for reference. Figure 7.6a shows a representative N_2 emission spectrum for a 1:2 CH_4/N_2 plasma (P = 75 W) along with the corresponding Boltzmann plot used to determine $T_V(N_2)$ for that particular spectrum. As

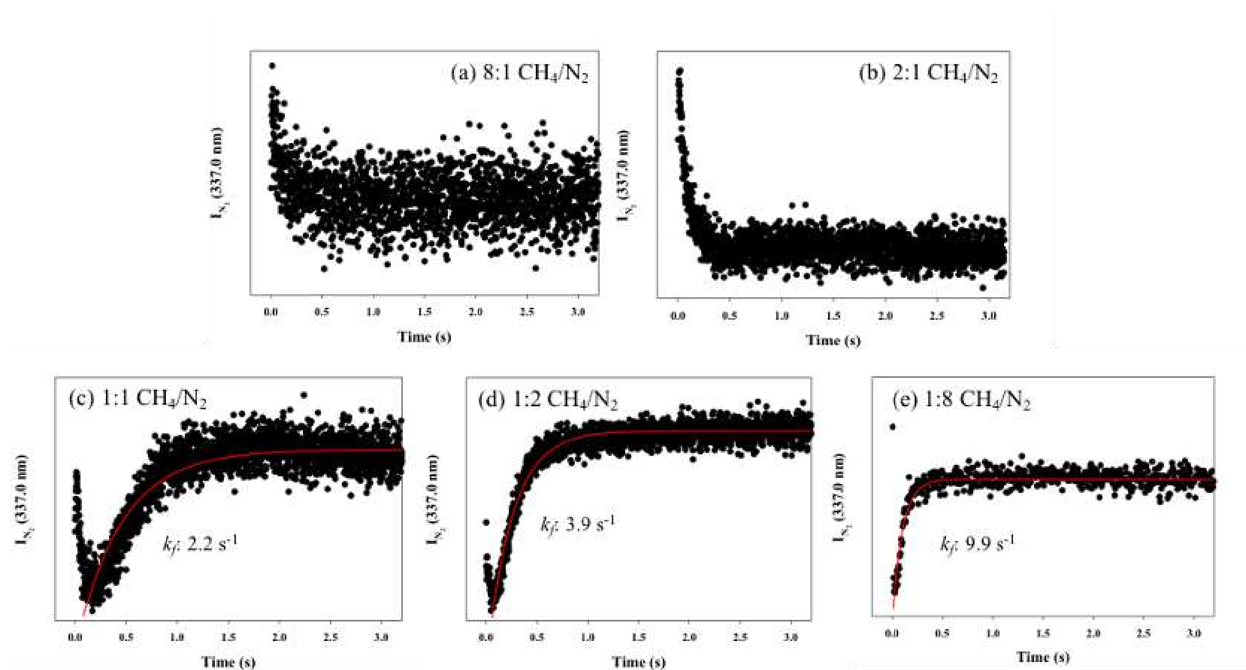

Figure 7.5. Intensity of N_2 emission plotted as a function of time (P = 75 W) in (a) 8:1 CH_4/N_2, (b) 2:1 CH_4/N_2, (c) 1:1 CH_4/N_2, (d) 1:2 CH_4/N_2, and (e) 1:8 CH_4/N_2 plasmas. Rate constants of formation and destruction were determined by fitting a first order exponential to each portion of the curve (solid lines). Y-axes are intensities of the selected N_2 emission line in arbitrary units.

Table 7.2. T_R (K) and T_V (K) values for CH_4/N_2 plasma systems.[a,b]

P (W)	T_R(CH)	T_V(CH)	T_R(CN)	T_V(CN)	$T_R(H_2)$	$T_R(N_2)$	$T_V(N_2)$
8:1 CH_4/N_2							
25	1700 (10)	2830 (190)	1140 (10)	3200 (220)	700 (30)	320 (20)	2910 (250)
50	1640 (20)	2190 (10)	1180 (20)	3970 (80)	640 (30)	380 (20)	4700 (290)
75	1720 (30)	2170 (30)	1180 (20)	4160 (30)	600 (20)	280 (20)	5840 (380)
100	1600 (20)	2120 (30)	1180 (10)	4230 (20)	590 (10)	330 (20)	6600 (540)
125	1640 (30)	2230 (30)	1180 (10)	4230 (80)	540 (20)	320 (20)	6920 (530)
2:1 CH_4/N_2							
P (W)	T_R(CH)	T_V(CH)	T_R(CN)	T_V(CN)	$T_R(H_2)$	$T_R(N_2)$	$T_V(N_2)$
25	—	—	1080 (30)	4020 (30)	—	260 (20)	4420 (10)
50	—	—	1070 (10)	4570 (10)	—	270 (10)	5780 (20)
75	—	—	1030 (10)	4760 (20)	—	290 (10)	6910 (20)
100	—	—	990 (10)	4870 (10)	—	290 (10)	7680 (40)
125	—	—	990 (10)	4930 (10)	—	290 (10)	8240 (40)
1:1 CH_4/N_2							
P (W)	T_R(CH)	T_V(CH)	T_R(CN)	T_V(CN)	$T_R(H_2)$	$T_R(N_2)$	$T_V(N_2)$
25	—	—	950 (10)	4010 (50)	—	280 (10)	4400 (20)
50	—	—	930 (10)	4510 (20)	—	280 (10)	5670 (20)
75	—	—	860 (10)	4740 (20)	—	300 (10)	6440 (140)
100	—	—	870 (10)	4640 (20)	—	310 (10)	7120 (30)
125	—	—	920 (10)	4360 (180)	—	300 (10)	7560 (110)

1:2 CH_4/N_2							
P (W)	T_R(CH)	T_V(CH)	T_R(CN)	T_V(CN)	T_R(H_2)	T_R(N_2)	T_V(N_2)
25	—	—	870 (20)	3370 (100)	—	280 (10)	3660 (20)
50	—	—	820 (10)	3470 (20)	—	310 (30)	4470 (10)
75	—	—	810 (10)	3520 (40)	—	300 (10)	5040 (40)
100	—	—	800 (10)	3600 (20)	—	300 (10)	5340 (70)
125	—	—	790 (10)	3670 (30)	—	290 (10)	5470 (90)
1:8 CH_4/N_2							
P (W)	T_R(CH)	T_V(CH)	T_R(CN)	T_V(CN)	T_R(H_2)	T_R(N_2)	T_V(N_2)
25	—	—	880 (10)	3910 (20)	—	270 (10)	3030 (40)
50	—	—	1000 (30)	3770 (10)	—	290 (10)	3550 (10)
75	—	—	990 (10)	3800 (10)	—	300 (10)	4040 (20)
100	—	—	960 (10)	3900 (10)	—	290 (10)	4610 (40)
125	—	—	950 (10)	3910 (20)	—	300 (10)	5220 (50)

[a] Values in parentheses represent the standard deviation calculated from the mean of n≥3 trials.

[b] "—" represents conditions where species is not present above experimental noise.

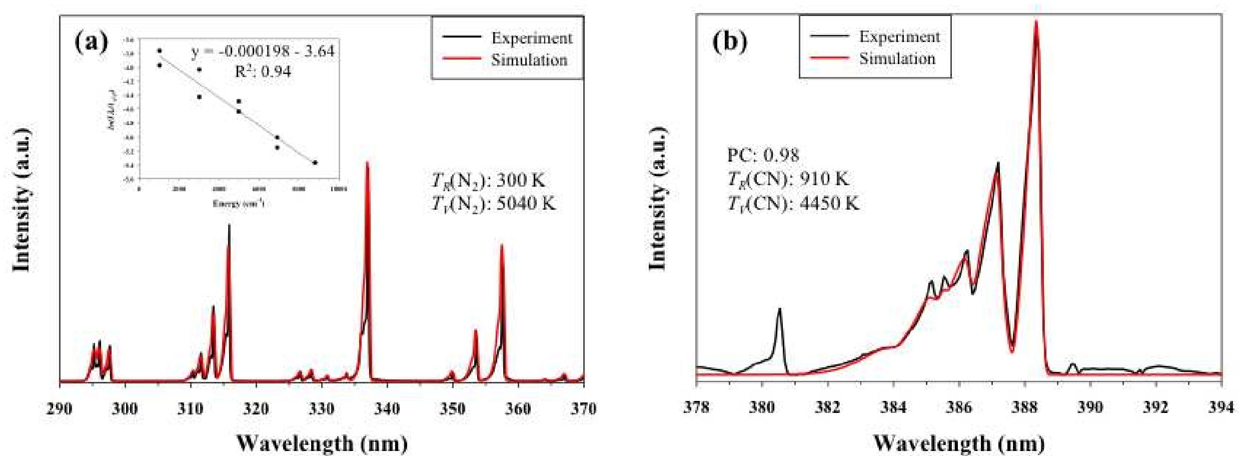

Figure 7.6. Representative emission spectra and simulated fits of the (a) N_2 $C^3\Pi_u \rightarrow B^3\Pi_g$ (1:2 CH_4/N_2 plasma, P = 75 W) and (b) CN $B^2\Sigma^+ \rightarrow X^2\Sigma^+$ (1:1 CH_4/N_2 plasma, P = 125 W) transitions. Inset in (a) is the corresponding Boltzmann plot of the N_2 vibrational distribution.

discussed in Chapter 2, $T_R(N_2)$ was determined from simulated fits of the experimental spectrum with SpecAir.[13] Select $T_R(N_2)$ and $T_V(N_2)$ values as a function of %N_2 in the feed gas for a CH_4/N_2 plasma are displayed in Figures 7.7a and 7.7b, respectively. $T_R(N_2)$ values range from ~280 – 350 K with no clear dependence on P or feed gas composition. Previous studies from our lab have also reported similar $T_R(N_2)$ values in several feed gas systems (e.g., N_2, NO, N_2O, N_2/O_2).[10-11] In those studies, $T_R(N_2)$ remained independent of several plasma parameters (e.g., pressure, power, feed gas, catalyst presence), indicating that $T_R(N_2)$ efficiently thermalizes to approximately room temperature regardless of parameter conditions. In contrast, $T_V(N_2)$ clearly demonstrates dependence on both P and feed gas composition. Specifically, $T_V(N_2)$ generally increases as the CH_4 content in the CH_4/N_2 plasma also increases. $T_V(N_2)$ also increases as P increases at all the feed gas compositions explored, ranging from ~2910 K at P = 25 W to ~6920 K at P = 125 W in the 8:1 CH_4/N_2 system. A slight increase in $T_V(N_2)$ at each P is noted as the feed gas ratio is changed to 2:1 CH_4/N_2, and further increases in N_2 content results in a decrease in $T_V(N_2)$ at each P. Notably, $T_V(N_2)$ values are also nearly an order of magnitude greater than $T_R(N_2)$ values, suggesting rotational relaxation is more efficient than vibrational relaxation for N_2. Overall, $T_V(N_2)$ displays a wide value range (~2910 – 8940 K) for our studied parameter space, and can be compared to previously reported $T_V(N_2)$ values for a 100% N_2 plasma[10-11] in Figure 7.7b. Comparatively, $T_V(N_2)$ values in 100% N_2 plasmas ranged from ~2250 – 3550 K (p = 150 mTorr) and displayed both pressure and P dependences.

We also evaluated T_R and T_V for CN as functions of P and feed gas composition. Figure 7.6b shows a representative experimental emission spectrum and simulated fit (via LIFBASE[14]) for the CN $B^2\Sigma^+ \rightarrow X^2\Sigma^+$ transition in a 1:1 CH_4/N_2 plasma (P = 125 W), along with the calculated T_R(CN), T_V(CN), and peak correlation (PC) values for that particular spectrum.

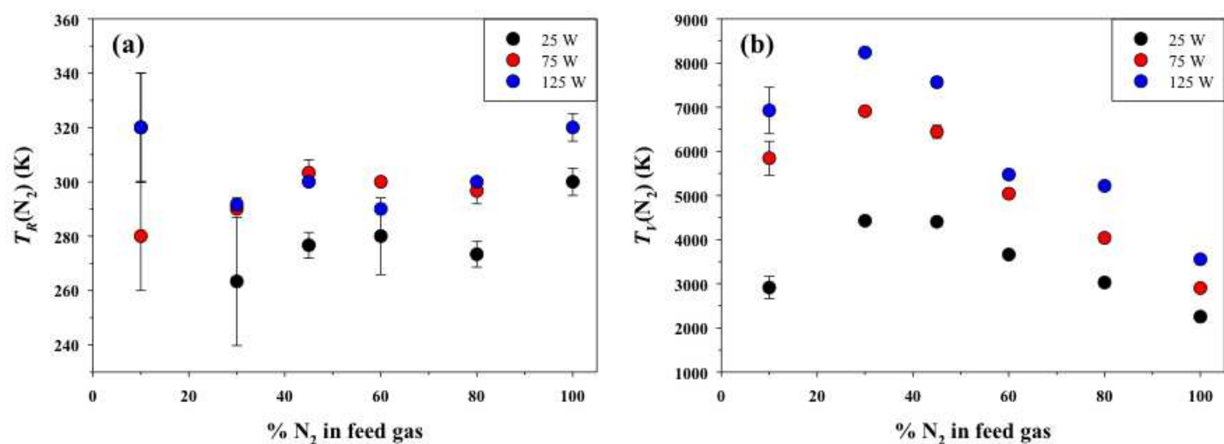

Figure 7.7. (a) $T_R(N_2)$ and (b) $T_V(N_2)$ values as a function of $\%N_2$ in CH_4/N_2 plasmas at three applied rf powers (25 W, 75 W, and 125 W). The $T_R(N_2)$ and $T_V(N_2)$ values shown for a 100% N_2 plasma system were reported previously.[10-11]

Notably, peak correlation values were ≥0.94 for each simulated spectrum at $P \geq 50$ W (PC ≥ 0.77 for $P = 25$ W), indicating good agreement between the experimental data and simulation. Figure 7.8a shows that T_R(CN) values for our CH_4/N_2 plasmas range from ~790 – 1180 K over our parameter space. Although T_R(CN) values do not appear to have a strong P dependence, T_R(CN) generally decreases as N_2 content in the feed gas increases up to a 1:2 CH_4/N_2 ratio. This is followed by a slight increase in T_R(CN) in the 1:8 CH_4/N_2 plasma system. As shown in Figure 7.8b, T_V(CN) ranges from ~3200 to 4930 K and does not appear to have either a strong P or feed gas composition dependence over the studied parameter space.

T_R(CH, H_2) and T_V(CH) values calculated for the 8:1 CH_4/N_2 ratio system are listed in Table 7.2, which also contains T_R(CN, N_2) and T_V(CN, N_2) values. At N_2 contents >8:1 CH_4/N_2, CH was either present in very small amounts or not observed at all and several H_2 rotational transition lines were obscured by emission from the N_2 FPS. Thus, T_R(CH, H_2) and T_V(CH) values were not calculated for other gas precursor ratios. T_R(H_2) values in the 8:1 CH_4/N_2 plasma system ranged from ~540 to 700 K and decreases as P increases. These values and trends are nearly identical to those reported for T_R(H_2) in a 100% CH_4 plasma.[15] Conversely, T_R(CH) values are ~300 K lower than those reported for a 100% CH_4 plasma.[12] Here, T_R(CH) values range from ~1600 to 1720 K for an 8:1 CH_4/N_2 plasma system, with T_V(CH) values significantly higher, ranging from ~2120 to 2830 K. Comparatively, T_V(CH) values measured in a 100% CH_4 plasma ($p = 150$ mTorr) lie a bit higher, ranging between ~2610 and 3310 K.[12] Both T_R(CH) and T_V(CH) values reported herein display no clear trends with respect to P.

Figure 7.9 shows rotational and vibrational temperatures as a function of P for each plasma species examined in the 8:1 CH_4/N_2 system. Notably, these data exhibit a wide range of values for T_R within our system, Figure 7.9a, ranging from ~300 K for N_2 $C^3\Pi_u \rightarrow B^3\Pi_g$ to

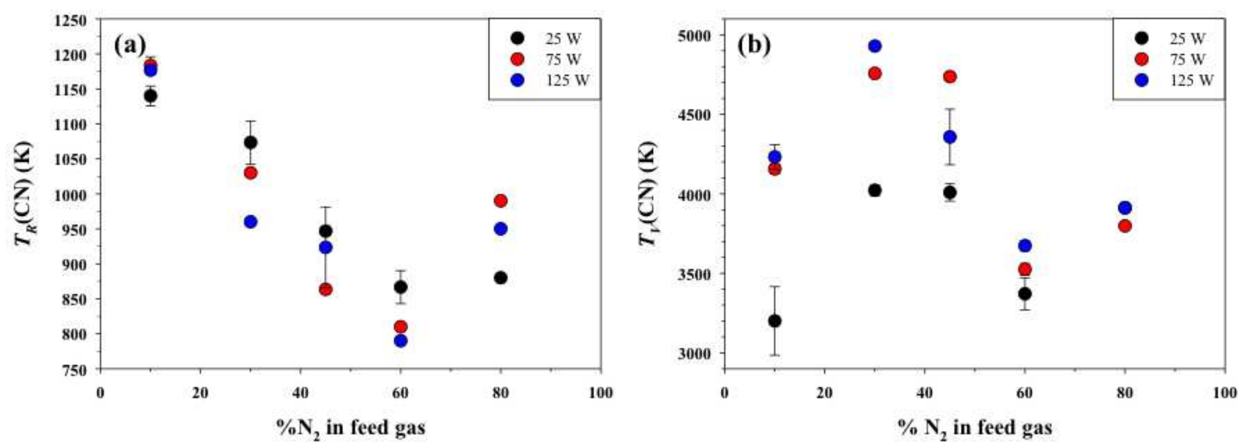

Figure 7.8. (a) T_R(CN) and (b) T_V(CN) values as a function of %N_2 in the feed gas at three applied rf powers (25 W, 75 W, and 125 W).

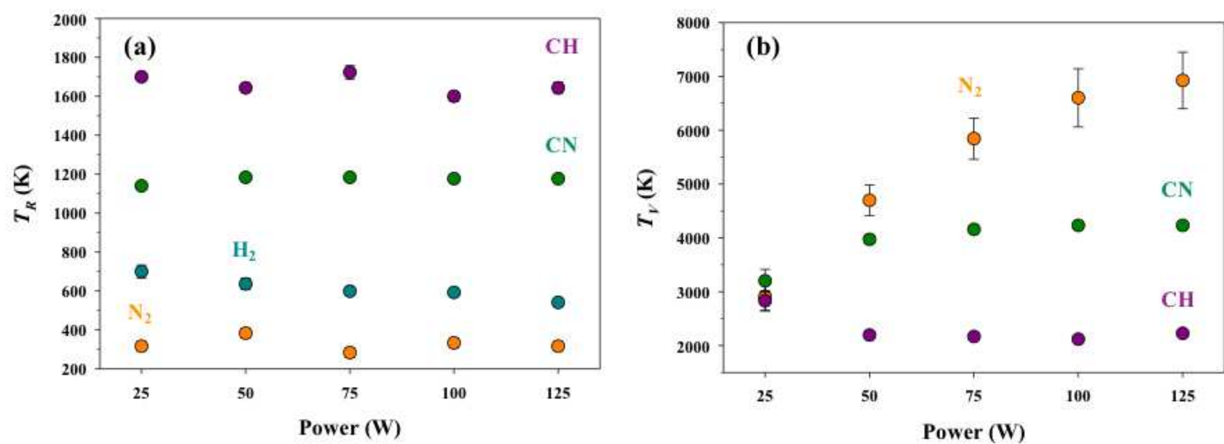

Figure 7.9. (a) T_R and (b) T_V for multiple species plotted as a function of applied rf power in an 8:1 CH_4/N_2 plasma system.

nearly 1750 K for CH $A^2\Delta \rightarrow X^2\Pi$. Values for $T_R(H_2)$ and T_R(CN) lie between these extremes at ~620 K and ~1180 K, respectively. T_V values exhibit much higher values, ranging from ~2100 K for CH $A^2\Delta \rightarrow X^2\Pi$ to ~6920 K for N_2 $C^3\Pi_u \rightarrow B^3\Pi_g$, Figure 7.9b. The vast differences in T_R and T_V values of different species indicate a thermal non-equilibrium and may be inherently related to a combination of species formation mechanisms, excited state lifetimes, or other heating mechanisms (e.g., Franck-Condon heating, charge exchange).[16] These ideas will be explored further below in Section 7.3.

b. *CH_4/H_2O plasma system.* Raw OES spectra in Figure 7.10 show the emitting excited state species in CH_4/H_2O plasmas at two different feed gas ratios. Notably, peaks arising from Ar transitions appear in both spectra. In the 8:1 CH_4/H_2O plasma, species resulting from CH_4 decomposition (i.e., CH, atomic hydrogen, H_2) dominate the spectrum, Figure 7.10a. Additionally, emission from CO $A^1\Pi \rightarrow X^1\Sigma$ and OH $A^2\Sigma^+ \rightarrow X^2\Pi$ also appear in the spectrum for this feed gas ratio. As the feed gas composition shifts to a majority H_2O (1:8 CH_4/H_2O, Figure 7.10b), emission peaks from OH $A^2\Sigma^+ \rightarrow X^2\Pi$, atomic O, and the hydrogen Balmer series clearly emerge.

Inert gas actinometry allows further evaluation of how species densities change as a function of feed gas composition, Figure 7.11. As expected, [OH] and [O] increase concomitantly with H_2O feed gas fraction, whereas both [CH] and [H_2] decrease. The [H_α] (shown in the inset of Figure 11) increases from ~2.3 in an 8:1 CH_4/H_2O plasma to a value of ~25.0 in the 1:8 CH_4/H_2O system. For [CO] we observe a trend similar to [CN] in the CH_4/N_2 system in that [CO] increases to a maximum density at 1:1 CH_4/H_2O and then decreases as the H_2O fraction continues to increase. Similar to formation of CN in the CH_4/N_2 system, CO must be formed from a bimolecular collision between the two precursor gases (CH_4 and H_2O) or their

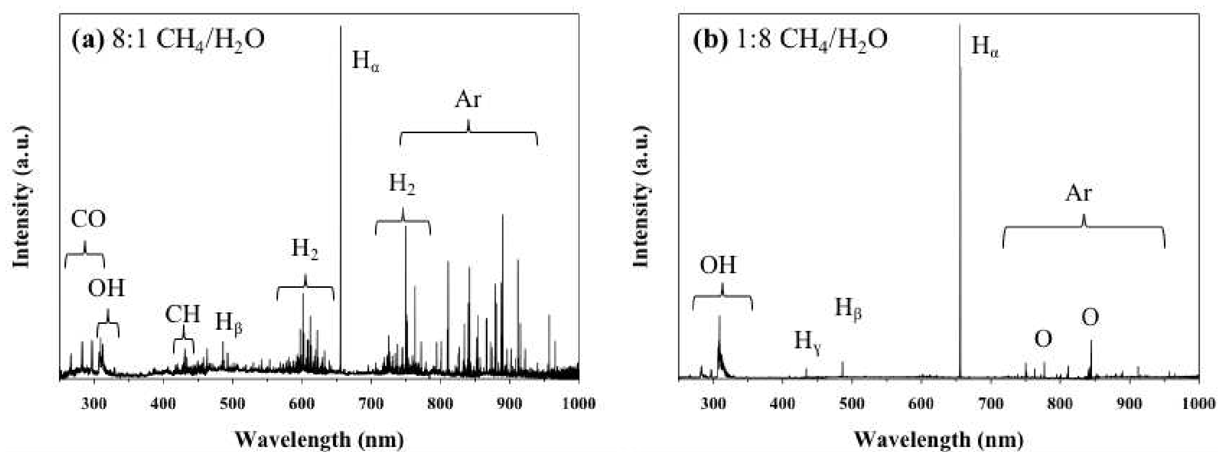

Figure 7.10. Raw OES spectra (P = 125 W) of a (a) 8:1 CH_4/H_2O plasma and a (b) 1:8 CH_4/H_2O plasma. Emission lines and bands attributed to the major emitting species are labeled.

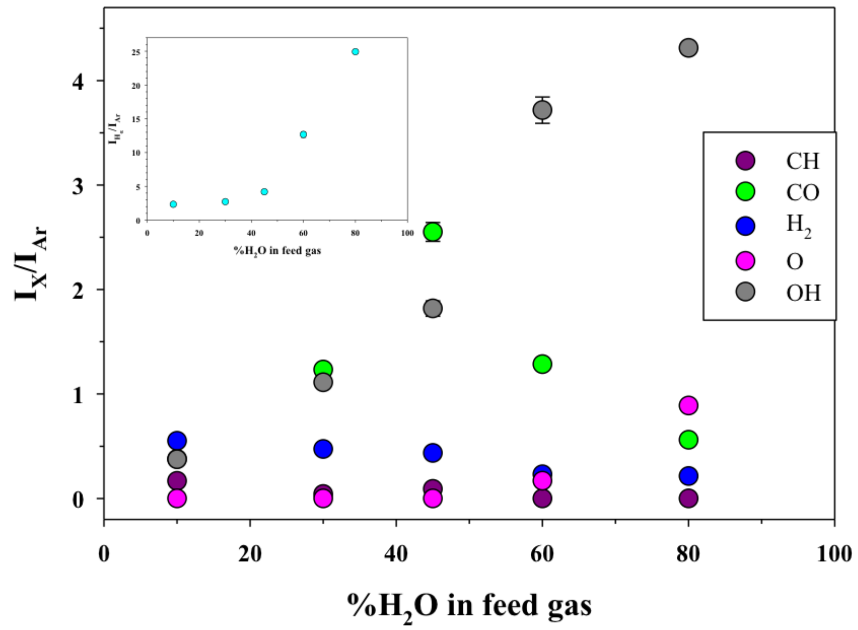

Figure 7.11. Relative densities of excited state species in CH_4/H_2O plasmas as a function of %H_2O in the feed gas (P = 125 W).

decomposition products; thus, decreases in the relative amounts of a precursor gas may significantly hinder formation of species such as CO or CN.

TR-OES provides insight into formation and destruction rates of CO and OH, in CH_4/H_2O plasmas. Figure 7.12a shows a temporal emission profile for CO (296.9 nm) with a clear rise to a steady state emission intensity. Unlike the CN or N_2 emission profiles in Figures 7.3 and 7.5, only a formation profile was present for CO throughout the entire parameter range studied (i.e. no decay curve was observed). The data plotted in Figure 7.12b show that CO k_f values do not change significantly across the parameter space and do not depend on the feed gas composition. For feed gas ratios comprising ≤50% H_2O, CO k_f increases slightly with an increase in P. Overall, CO k_f values range from ~1.6 – 2.5 s^{-1}, Table 7.3.

Table 7.3 also lists OH k_d values, with values ranging from ~1.6 – 14.6 s^{-1}. Notably, only a decay curve is present for OH emission at each parameter (i.e. no formation curves observed), as depicted by the representative OH decay curve in Figure 7.13a. All measured OH k_d values are plotted in Figure 7.13b. In general, OH k_d values decrease with increasing H_2O feed gas fraction. At low H_2O fractions, OH k_d strongly increases with increasing P, whereas at >50% H_2O in the feed gas, no feed gas or P dependence is observed and OH k_d values are ~2.0 s^{-1}.

Rotational and vibrational temperatures were also measured for several of the excited state species present in the CH_4/H_2O system. Figure 7.14a shows a representative emission spectrum for the OH $A^2\Sigma^+ \rightarrow X^2\Pi$ transition and corresponding simulated fit and calculated T_R(OH), T_V(OH), and PC values (1:2 CH_4/H_2O; P = 25 W). PC values were ≥0.80 for each simulated spectrum of OH, indicating fair agreement between experimental data and simulation. Table 7.4 lists all T_R(OH) and T_V(OH) values and Figure 7.14b shows select T_R(OH) and T_V(OH) data as a function of %H_2O in CH_4/H_2O plasmas. T_V(OH) values are elevated compared to

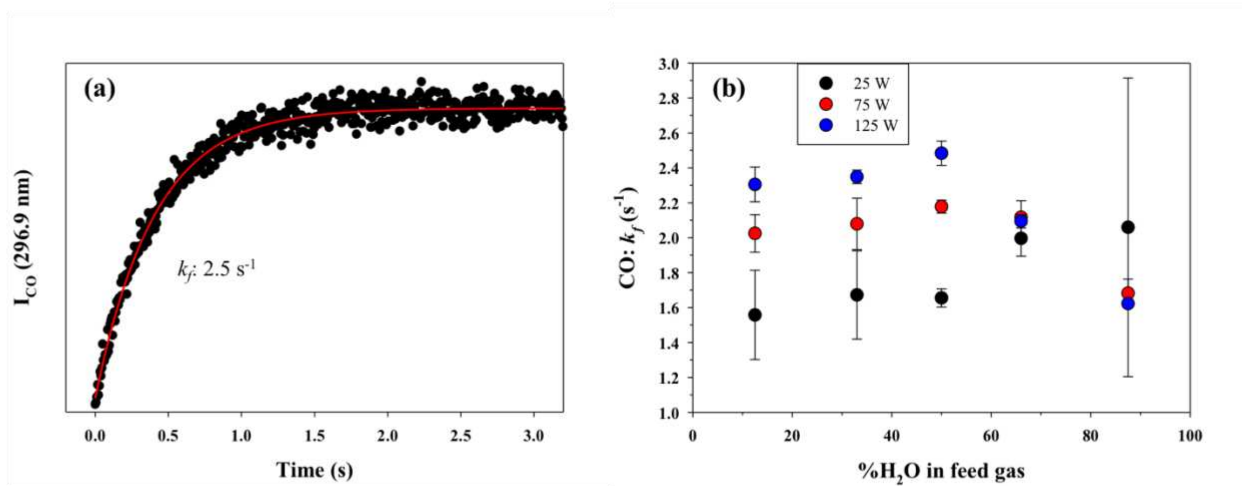

Figure 7.12. (a) Intensity of CO emission as a function of time (1:1 CH_4/H_2O, *P* = 125 W); and (b) CO k_f (s^{-1}) as a function of %H_2O in CH_4/H_2O plasmas at three applied rf powers (25 W, 75 W, and 125 W).

Table 7.3. Calculated CO k_f and OH k_d values.[a,b]

8:1 CH_4/H_2O		
P (W)	CO: k_f	OH: k_d
25	1.6 (0.3)	6.0 (1.3)
75	2.0 (0.1)	14.6 (0.7)
125	2.3 (0.1)	—
2:1 CH_4/H_2O		
P (W)	CO: k_f	OH: k_d
25	1.7 (0.3)	3.0 (0.3)
75	2.1 (0.1)	6.4 (0.1)
125	2.3 (0.1)	9.5 (0.7)
1:1 CH_4/H_2O		
P (W)	CO: k_f	OH: k_d
25	1.7 (0.1)	1.9 (0.1)
75	2.2 (0.1)	2.8 (0.1)
125	2.5 (0.1)	3.2 (0.1)
1:2 CH_4/H_2O		
P (W)	CO: k_f	OH: k_d
25	2.0 (0.1)	1.9 (0.4)
75	2.1 (0.1)	2.2 (0.1)
125	2.1 (0.1)	2.5 (0.1)
1:8 CH_4/H_2O		
P (W)	CO: k_f	OH: k_d
25	2.5 (0.9)	1.6 (0.2)
75	1.7 (0.1)	1.9 (0.1)
125	1.6 (0.1)	2.3 (0.1)

[a] Values in parentheses represent the standard deviation calculated from the mean of n≥3 trials.

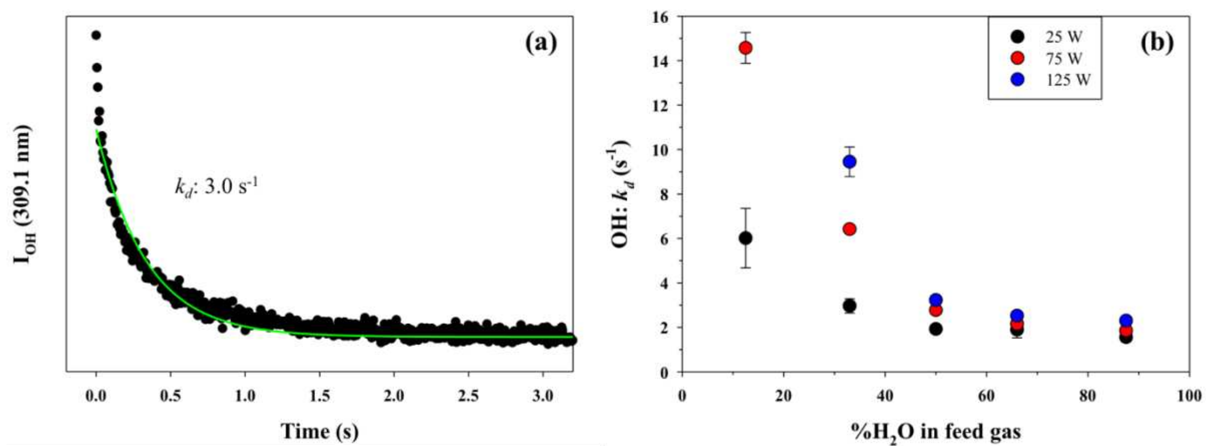

Figure 7.13. (a) Intensity of OH emission as a function of time (1:1 CH_4/H_2O, P = 125 W) and (b) OH k_d (s^{-1}) as a function of %H_2O in CH_4/H_2O plasmas at three applied rf powers (25 W, 75 W, and 125 W).

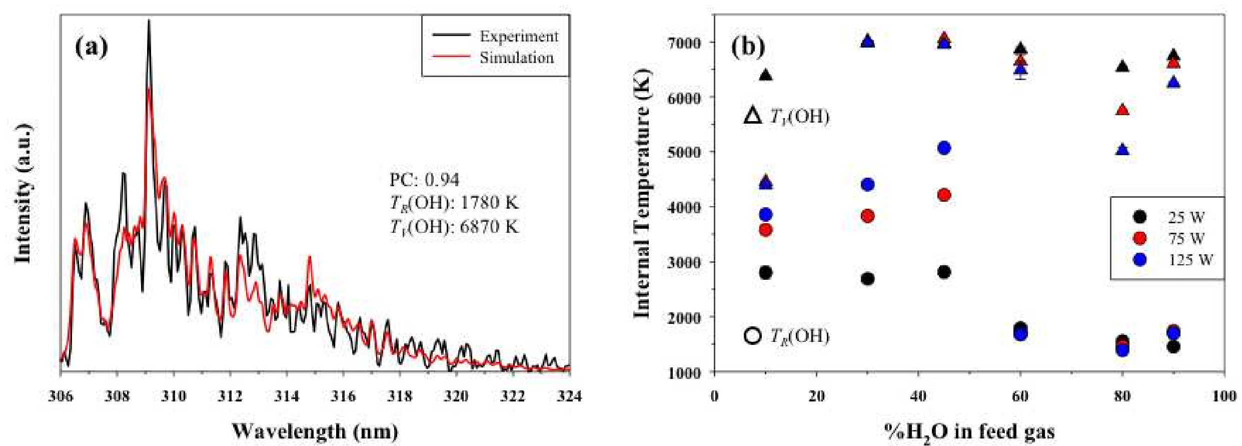

Figure 7.14. (a) Representative emission spectrum and simulated fit of OH $A^2\Sigma^+ \rightarrow X^2\Pi$ (1:2 CH_4/H_2O plasma, P = 25 W) and (b) T_R(OH) (circles) and T_V(OH) (triangles) as a function of %H_2O in CH_4/H_2O plasmas at three applied rf powers (25 W, 75 W, and 125 W).

Table 7.4. T_R (K) and T_V (K) values for CH_4/H_2O plasma systems.[a,b]

8:1 CH_4/H_2O					
P (W)	T_R(CH)	T_V(CH)	$T_R(H_2)$	T_R(OH)	T_V(OH)
25	1480 (30)	2250 (340)	680 (10)	2800 (100)	6380 (10)
50	1610 (60)	2440 (120)	640 (10)	3250 (170)	4520 (20)
75	1500 (20)	2400 (290)	630 (10)	3580 (10)	4450 (20)
100	1580 (10)	2510 (130)	620 (10)	3780 (130)	4440 (20)
125	1540 (60)	2430 (210)	620 (10)	3860 (70)	4400 (10)
2:1 CH_4/H_2O					
P (W)	T_R(CH)	T_V(CH)	$T_R(H_2)$	T_R(OH)	T_V(OH)
25	—	—	—	2690 (40)	7020 (10)
50	—	—	—	3300 (10)	6980 (10)
75	—	—	—	3830 (10)	6980 (20)
100	—	—	—	4190 (10)	7020 (10)
125	—	—	—	4400 (30)	6990 (20)
1:1 CH_4/H_2O					
P (W)	T_R(CH)	T_V(CH)	$T_R(H_2)$	T_R(OH)	T_V(OH)
25	—	—	—	2810 (70)	6970 (20)
50	—	—	—	3550 (40)	7000 (30)
75	—	—	—	4210 (10)	7050 (10)
100	—	—	—	4770 (50)	6910 (20)
125	—	—	—	5070 (10)	6950 (10)

1:2 CH_4/H_2O					
P (W)	T_R(CH)	T_V(CH)	$T_R(H_2)$	T_R(OH)	T_V(OH)
25	—	—	—	1790 (10)	6870 (40)
50	—	—	—	1700 (10)	6790 (10)
75	—	—	—	1690 (10)	6640 (130)
100	—	—	—	1660 (10)	6620 (30)
125	—	—	—	1680 (40)	6480 (160)
1:8 CH_4/H_2O					
P (W)	T_R(CH)	T_V(CH)	$T_R(H_2)$	T_R(OH)	T_V(OH)
25	—	—	—	1550 (10)	6530 (10)
50	—	—	—	1460 (10)	6160 (60)
75	—	—	—	1460 (10)	5740 (10)
100	—	—	—	1430 (10)	5870 (200)
125	—	—	—	1390 (10)	5020 (60)
H_2O					
P (W)	T_R(CH)	T_V(CH)	$T_R(H_2)$	T_R(OH)	T_V(OH)
25	—	—	—	1450 (10)	6740 (10)
50	—	—	—	1610 (10)	6530 (90)
75	—	—	—	1740 (30)	6600 (20)
100	—	—	—	1650 (40)	6190 (10)
125	—	—	—	1690 (20)	6240 (10)

[a] Values in parentheses represent the standard deviation calculated from the mean of n≥3 trials.

[b] "—" represents conditions where species is not present above experimental noise.

T_R(OH), exhibiting different levels of thermalization between T_R(OH) and T_V(OH), depending on feed gas composition. For example, T_V(OH) values for the 8:1 CH_4/H_2O system are generally lower than the other feed gas compositions, except at P = 25 W. Overall, T_V(OH) values range from ~4440 – 7050 K and display little dependence on P or feed gas composition. Nevertheless, T_V(OH) values for the 1:8 CH_4/H_2O plasma appear to display some P dependence, as T_V(OH) decreases with increasing P. Moreover, T_R(OH) values also display interesting trends with respect to feed gas composition. At high H_2O fraction (>~60%), T_R(OH) = ~1390-1790 K and remains relatively constant with P and feed gas. Conversely, T_R(OH) rises to ~2690 – 5070 K and exhibits a P dependence in feed gas compositions comprising ≤50% H_2O. The striking differences in T_R(OH) values and trends suggest the possibility of different formation mechanisms based on the feed gas composition, discussed further in Section 7.3.

T_R(CH, H_2) and T_V(CH) values were calculated for the 8:1 CH_4/H_2O ratio system, Table 7.4. At H_2O content greater than the 8:1 CH_4/H_2O ratio, both CH and H_2 were either present in very small amounts or not observed at all. As such, T_R(CH, H_2) and T_V(CH) values were not calculated for these gas ratios. T_R(H_2) values in the 8:1 CH_4/H_2O plasma system ranged from ~620 – 680 K and decrease as P increases. Overall, these values and trends are similar to those reported for T_R(H_2) in a 100% CH_4 plasma[12] and the 8:1 CH_4/N_2 system described above. Conversely, T_R(CH) values range from ~1480 – 1610 K and are slightly lower than those reported in the 8:1 CH_4/N_2 plasma (Table 7.2). T_V(CH) values, however, generally align with those reported in the CH_4/N_2 system, ranging from ~2250 – 2510 K. Both T_R(CH) and T_V(CH) values reported herein display no clear trends with respect to P. Similar to the Figure 7.9 data, rotational and vibrational temperatures in the CH_4/H_2O system also exhibit a wide range of values. Differences in T_R and T_V values are discussed in detail in Section 7.3.

7.3 Discussion

PAC can be a viable pollution remediation tool; however, the applicability of this technology is inherently hindered by a vast data gap in fundamental, gas-phase chemistry and physics. Examination of kinetic and energetic processes occurring in the gas-phase can provide significant insight into molecule formation mechanisms, decomposition pathways, and the overall plasma chemistry. Importantly, it is essential to simultaneously examine multiple plasma species as different molecules within the same plasma system may exhibit vastly different internal temperatures. One additional consideration is a single plasma species can be produced via different mechanisms (e.g., direct impact excitation, decomposition, recombination, among others), which may result in very different energy partitioning for that species as functions of different plasma parameters. Here, we evaluated kinetic and energetic trends of several plasma species within two environmentally relevant mixed gas plasma systems, CH_4/N_2 and CH_4/H_2O.

a. *CH_4/N_2 plasma system.* Raw OES spectra (Figure 7.1) and actinometry data (Figure 7.2) for the CH_4/N_2 system demonstrate several excited state species are produced with relative densities highly dependent on the feed gas ratio. Over the past several decades, CH_4/N_2 plasmas have been widely employed for production of *a*-C:H:N films.[17-20] As such, several previous studies investigated production mechanisms for gas phase species and film precursors in these systems using OES.[18, 21-23] In particular, CH radicals were identified as an important film growth precursor because they present three "dangling bonds" when incorporated into a growing film and consequently, display a high sticking coefficient.[18] Thus, several studies focused particularly on CH contributions to materials deposited by CH_4/N_2 plasmas.[18, 20] In CH_4-

based plasmas, CH ($A^2\Delta$) is hypothesized to form mainly via a dissociative excitation process, Reaction 7.1,[24]

$$CH_4^* + e^- \rightarrow CH^* + H + H_2 + e^- \quad (7.1)$$

Additionally, excited nitrogen species promote CH_4 dissociation, resulting in the production of CH radicals over CH_3 radicals.[25] OES measurements made over a range of pressure conditions demonstrated that addition of nitrogen to a constant CH_4 flow resulted in enhanced emission of CH and CN.[18, 21] In our systems, an increase in the N_2 fraction is simultaneously associated with a decrease in CH_4. Thus, we observe a decrease in [CH], even if N_2 enhances CH formation. Similarly, the observed decreases in [H_α] and [H_2] with an increase in N_2 content are also expected as these species arise primarily from CH_4 decomposition.

The actinometry trends for CN, however, are quite different from the other species in the system. Although some studies have reported a similar [CN] maximum in a 1:1 CH_4/N_2 mixture followed by a decrease in [CN] as the N_2 fraction further increases,[18] others have shown [CN] increases to a maximum at ~50% N_2 and remains stable with increasing N_2 until the feed gas comprises ~90% N_2.[21, 26] Because CN must be formed via some bimolecular recombination process from the two precursors in our system, we suspect that the rise of [CN] with nitrogen content up to 50% and subsequent decrease at nitrogen contents >50% may be driven by the amount of nitrogen- and carbon-containing precursors available. Thus, a decrease in either of the precursors will result in an overall decrease in [CN].

In a low pressure (100 mTorr) rf CH_4/N_2 plasma, Clay *et al.* also observed both a decrease in the CH emission intensity and an increase in the CN emission intensity as the N_2/CH_4 ratio approached ~0.5.[21] Yet as the N_2/CH_4 ratio was increased to 2, the CN intensity remained stable at the maximum. The authors suggest the increase in reactive nitrogen species in their

system results in a reduction of the molecular $C_xH_y^*$ species necessary for film formation. Consequently, a decrease in CH is observed while the CN emission peaks develop.[21] Importantly, Clay *et al.* also analyzed *a*-C:H:N film growth rates, noting a decrease in film growth rate with an increase in the N_2/CH_4 ratio, providing key insight into how the gas phase species may participate in film growth.[21] We did not perform any film analysis here; thus, future investigations should include film analyses or analysis of catalyst characteristics and plasma-surface interactions for PAC studies to provide further insight into probable mechanistic processes.

OES is a powerful diagnostic tool that provides not only species identification and species density trends, but also temporal emission data (TR-OES), which provides insight into formation and destruction processes. Chatei *et al.* examined temporal concentration trends of CN species using OES to elucidate contributions of gas phase and plasma-surface reactions for production of CN.[27] Their results demonstrate that a cut off of N_2 flow in $CH_4/CO_2/N_2$ plasmas results in an immediate sharp decrease of [CN] to zero within 2 minutes, indicating N_2 flow is essential to CN production. Notably, film growth continues from the still flowing CH_4 precursor and consequently, CN can no longer be removed from the surface as the available nitrogen is buried below the *a*-C:H film continuing to be formed. Conversely, when CH_4 flow is cut off, [CN] decreases sharply at first but then stabilizes. Thus, CN formation cannot be explained exclusively by gas-phase reactions. To further explore this observation, the authors removed their substrate holder from the discharge, observing that [CN] decreased sharply during the two minutes immediately following cut off of CH_4 flow. A slower decrease of [CN] follows until approximately 10 minutes post CH_4 flow cut off when all solid carbon in the reactor is eliminated and [CN] vanishes to zero. This study indicates that reactions involving nitrogen

species are essential to formation of CN as are plasma-surface interactions. Similarly, in our systems, when the glass reactor walls are coated with *a*-C:N:H films, we observe CN emission with a 100% N_2 plasma.[26] The Fisher group has also previously noted, however, that plasma-film interactions are not the only contributor to the CN production as stronger CN emissions are observed with the addition of a hydrocarbon precursor (e.g., CH_4, C_2H_2) to a N_2 plasma.[26]

Our TR-OES studies of CN and N_2 display interesting trends, most notably, their respective temporal profiles (Figures 7.3 and 7.5, respectively) contain nearly opposite behaviors. For example, in the 8:1 and 2:1 CH_4/N_2 systems, a decay in N_2 intensity and a simultaneous rise in CN intensity are observed. In the 1:1 and 2:1 CH_4/N_2 systems, a quick initial decay in N_2 intensity is followed by a rise to a steady state intensity. Conversely, CN intensity first rises to a maximum before decaying to steady state. Finally, in the 1:8 CH_4/N_2 system, we observe no clear destruction curve for N_2 (i.e. only a formation curve is present). Although we note both a formation and destruction curve for CN with this gas ratio, CN k_f values are much higher than those found with other gas ratios. Additionally, we could not obtain a CN k_f value at P = 125 W because no formation curve was observed at the integration time used for these experiments. Indeed, several studies have indicated that CN formation is primarily controlled by the concentration of excited gas-phase nitrogen species because of their high activation energy (>14 eV).[21] In particular, CN is formed from the reaction of these nitrogen species with carbon-containing species, with reaction control arising primarily from the concentration of excited N_2. Thus, production of CN in our systems may be directly related to activated nitrogen species which allow CN to form more rapidly, resulting in the increase in CN k_f with both increased P and nitrogen content in the feed (Figure 7.4, Table 7.1).

Energy partitioning data can further elucidate the chemical reactions that may occur in our plasmas. T_R(CN) data shown in Figure 7.8 generally decrease as the nitrogen content increases to ~60%. This is followed by a slight increase in T_R(CN) in the 1:8 CH_4/N_2 system except at P = 25 W where T_R(CN) values are within error of each other. The >300 K difference in T_R(CN) between the 8:1 CH_4/N_2 and 1:2 CH_4/N_2 plasma systems suggests that different excitation mechanisms may be occurring in the different feed gas ratios. Hu *et al.* hypothesize that CN radical formation in CH_4/N_2 discharges are typically the result of the mechanistic processes described in gas-phase Reactions 7.2 – 7.5.[23]

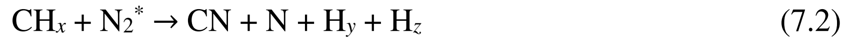

$$CH_x + N_2^* \rightarrow CN + N + H_y + H_z \qquad (7.2)$$

$$N + CH_x \rightarrow CN + xH \qquad (7.3)$$

$$CH_x + N_2^* \rightarrow CNH_y + N + H_z \qquad (7.4)$$

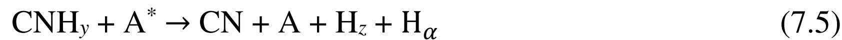

$$CNH_y + A^* \rightarrow CN + A + H_z + H_\alpha \qquad (7.5)$$

Here, $x + y = z$ (Reaction 7.2 and 7.4), $y = z + \alpha$ (Reaction 7.5) and A^* represents excited state N, N_2, or CH_x. In Reactions 7.2 and 7.3, CN radicals are directly formed from reaction with other species (e.g., CH_x, N_2, N). Reactions 7.4 and 7.5 describe a two-step process including the formation of an intermediate compound containing C-N bonding which then yields CN on further reaction with activated plasma species. From Reactions 7.2 – 7.5, CN ($B^2\Sigma^+$) may be formed either via dissociative excitation or electron impact excitation from the ground state. As noted above, plasma-film interactions can also play a significant role in CN formation.[26-27] Both ground state ($X^2\Sigma^+$) and excited state ($B^2\Sigma^+$) CN production has been correlated with plasma-film interactions.[27-28]

Hu *et al.* also observe a link between excited N_2 species and production of CN molecules.[23] These authors observed that trends of CN emission aligned with N_2 SPS emission

trends as a function of CH_4/N_2 feed gas ratio, suggesting that CN production may be tied to excited N_2 ($C^3\Pi_u$). The authors suggest resonant excitation between excited N_2 molecules and CN radicals may occur as the energy of the N_2 $C^3\Pi_u \rightarrow B^3\Pi_g$ transition (3.26 eV) is similar to that of the CN $B^2\Sigma^+ \rightarrow X^2\Sigma^+$ transition (3.19 eV).[23] Additionally, Clay *et al.* suggest the high energy of excited N_2 molecules may favor production of atomic N,[21] which in turn, favors production of CN radicals as reactions between N atoms and carbon species are exothermic.[29] In our OES spectra (Figure 7.1) we do not observe emission from atomic N species, in keeping with many studies that show such emission is not often observed in rf plasmas.[21] Because T_e is much greater in microwave discharges (~8 eV) compared to rf discharges (~1–3 eV), nitrogen is expected to be more highly activated.[21, 30] This highly activated nitrogen leads to atomic nitrogen with a longer radiative lifetime.[21] In contrast, the nitrogen atoms typically produced in rf discharges are short lived and tend to recombine rapidly to produce molecular nitrogen or possibly CN radicals (Reaction 7.3).[23] Hu *et al.* also suggest the lifetime of excited N atoms is shortened by bonding with carbon-containing species, which could reduce the probability of observation in OES data.[23] Additionally, atomic nitrogen peaks can be obscured by the N_2 FPS ($B^3\Pi_g \rightarrow A^3\Sigma_u^+$) emission band.

Hu *et al.* also observed that the intensities of both the N_2 SPS and the N_2^+ FNS increased by a factor of 2 to 10 when CH_4 was added.[23] This enhancement was also reported by Clay *et al.*.[21] Indeed, mass spectroscopic studies indicate there are numerous excited C_xH_y species (radicals and ions) present in CH_4/N_2 plasmas.[31-32] These species tend to undergo collisional reactions rather than deexcitation processes.[21] The addition of CH_4 and other hydrocarbon species (radicals and ions) thus potentially act as Penning collisional agents for nitrogen species activation, Reactions 7.6 – 7.7.[21]

$$CH_x^* + N_2 \rightarrow CH_x + N_2^* \quad (7.6)$$

$$CH_x^{+*} + N_2 \rightarrow CH_x + N_2^* + e^- \quad (7.7)$$

The enhanced nitrogen activation by these processes may be responsible for the elevated $T_V(N_2)$ values observed at high CH_4 content in our CH_4/N_2 plasmas (Figure 7.7b).

Penning collisional processes typically result in a vibrational distribution which deviates from Boltzmann behavior.[33-34] When calculating $T_V(N_2)$, we observed increasing deviation from Boltzmann behavior as the CH_4 fraction in the feed gas simultaneously increased. Bruggeman *et al.* notes that although N_2 vibrational population distributions can deviate significantly from a Boltzmann distribution, the rotational levels tend to equilibrate very quickly with the gas kinetic temperature.[35] Our results indicate that although $T_V(N_2)$ values are dependent on the feed gas composition, $T_R(N_2)$ values are not (Figure 7.7a). Additionally, $T_V(N_2)$ values are approximately an order or magnitude larger than $T_R(N_2)$. Moreover, $T_R(N_2)$ values exhibited the lowest T_R values in our systems (Figure 7.9a). Goyette *et al.* explains that changes in rotational quantum number from inelastic collisions between electrons and molecules are produced by long-range dipole and quadrupole interactions.[36] Because N_2 is a homonuclear molecule with no permanent dipole, the electron exerts a torque through the permanent quadrupole moment of the molecule. Since we hypothesize that N_2 is excited primarily through direct electron impact from a lower-lying level, the rotational distribution of the excited level will reflect the lower-lying level. Thus, the equilibration of the lower-lying level is being indirectly probed in this case.

In general, a non-Boltzmann distribution behavior is expected for excited state species in low pressure plasmas because the collisional timeframe is on the same order as the radiative lifetime.[35] As such, rotational states have little time to relax before undergoing radiative decay. Thus, T_R values measured in our systems can be used to elucidate formation mechanisms because

T_R becomes an image of the formation process rather than the kinetic temperature. Furthermore, some formation mechanisms can favor production of high or low rotational excited states which can drastically change T_R and ultimately provide insight into understanding mechanistic phenomena.[35] Notably, the Figure 7.9 data indicate the rotational and vibrational temperatures of excited state species in our systems are not equilibrated with each other. Insight into formation mechanisms for each of these species may help to explain these observed differences.

Previous studies from our lab examined rotational temperatures of H_2 and CH in CH_4 plasmas and reported similar T_R values and trends for these two molecules as those observed in a CH_4/N_2 system.[12, 15] The significant differences between the $T_R(H_2)$ and T_R(CH) values observed in a 100% CH_4 plasma were ascribed to a combination of differences in the species densities, radiative lifetimes, and consequently their excitation pathways. In our systems, we believe that dissociative electron excitation of a CH_x parent molecule is the primary production mechanism for CH^*. Similarly, dissociative excitation of methane molecules may also contribute to production of H_2^*; yet, several studies have reported that direct electron impact excitation is the primary pathway for H_2^* formation in CH_4 discharges because of the relatively high concentration of molecular hydrogen formed via methane dissociation.[24] Notably, N_2^*, which is also produced primarily via direct electron impact excitation of the N_2 precursor, has $T_R(N_2)$ values near room temperature. $T_R(N_2)$ values within this range (~300 – 400 K) have been reported for a variety of nitrogen plasma systems including N_2/CO_2 DBD[37] and low pressure ICP N_2 plasmas.[11] Moreover, our lab has previously reported similar $T_R(N_2)$ values for both excited and ground state molecules in a 100% N_2 plasma, finding little difference.[10] This bolsters the idea that rotational relaxation and thermalization readily occurs within N_2 rf discharges.

Considering the reported T_R(CN) values in our 8:1 CH_4/N_2 plasma system, T_R(CN) values range from ~790 to 1180 K and are independent of P. Several possible CN^* formation mechanisms were discussed above. Although our reported kinetic and energetic data provide some insight into possible mechanisms for CN formation, information regarding the exact processes cannot be easily disentangled. In a related study, Cruden *et al.* determined rotational temperatures of five molecular species (i.e., CF, CN, C_2, CO, and SiF) from emission spectra of a low pressure (30 mTorr) inductively coupled CF_4 plasma.[16] Four different rotational temperatures were obtained between the five molecules studied. Species produced primarily in the plasma bulk (CF and CN) yielded the lowest rotational temperatures (~1250 K) whereas SiF, an etch product from the reactor walls, had the highest rotational temperature at ~2300 K. C_2 and CO, which are produced both in the plasma bulk and as a product of plasma/surface interactions from the reactor walls had intermediate rotational temperatures (1600 K and 1800 K, respectively). Importantly, differences in internal plasma temperatures have been attributed to differences in spatial variations and concentrations.[38-39] Simulations demonstrate that neither temperature nor concentration is guaranteed to be spatially uniform within the plasma.[40] Future investigations using spatially-resolved emission spectra could provide further insight into CN formation mechanisms and T_R(CN) values and trends.

Vibrational temperatures were also obtained for CF, CN, C_2, and SiF in the study by Cruden *et al.* with values ranging from 1750 K to 5950 K.[16] Similar to the results reported herein (CH_4/N_2 plasma system), species with lower T_R had the highest T_V, a trend not observed here in the CH_4/H_2O plasma system. Our results suggest that different species have achieved different degrees of equilibration between rotational and vibrational modes, and thus, may not be equilibrated with translational temperatures.

b. CH_4/H_2O plasma system. Similar to the results displayed in Figure 7.9, the excited state species in the CH_4/H_2O system also exhibit vast differences in rotational and vibrational temperatures, Table 7.4. $T_R(H_2)$ values align with those reported in a 100% CH_4 plasma (Table 4.1)[15] and in the CH_4/N_2 plasma system (Table 7.2). Interestingly, we observe very little emission from H_2 as the H_2O fraction in the CH_4/H_2O plasma system increases, Figure 7.10b. We were unable to determine $T_R(H_2)$ with the Boltzmann plot method for H_2O fractions greater than 8:1 CH_4/H_2O because of the low intensity of some of the higher rotational transitions in the H_2 $d^3\Pi_u \rightarrow a^3\Sigma_g^+$ (0, 0) Fulcher (α) band. These observations indicate that H_2 formation likely results primarily from CH_4 decomposition rather than H_2O decomposition or from a recombination reaction involving atomic hydrogen species. Chapter 4 includes a more detailed discussion on probable H_2 formation pathways in a CH_4 plasma.[15]

Notably, T_R(CH) and T_V(CH) values for both of the plasma systems discussed in this chapter (CH_4/N_2 and CH_4/H_2O) are slightly lower than those in a 100% CH_4 plasma system (Table 3.1).[12] Although some T_R(CH) values are ~220 K lower in the CH_4/H_2O system than in the CH_4/N_2 system, other T_R(CH) values are within error between the two systems. Additionally, the T_R(CH) and T_V(CH) values in Tables 7.2 and 7.4 generally align with those reported for the CH_4/H_2 system (Table 4.2).[15] Notably, the values reported in Table 4.2 were obtained from different feed gas ratios of a CH_4/H_2 plasma at p = 200 mTorr, and the values reported in this chapter were collected at a total pressure of 150 mTorr. Thus, we cannot make a direct comparison between these systems. Nevertheless, T_R(CH) and T_V(CH) values reported in the Chapter 4 CH_4/H_2 system are also slightly lower than (albeit generally within error of) those reported in a 100% CH_4 plasma at p = 200 mTorr. The combination of these results may suggest

that addition of another feed gas (e.g., H_2, N_2, H_2O) to CH_4 may affect CH formation pathways to varying extents.

The feed gas composition also appears to have a strong effect on T_R(OH) and T_V(OH) values in mixtures of CH_4 and H_2O, Figure 7.14b. In a related study, Sarani *et al.* measured T_R(OH) in an atmospheric pressure plasma jet generated in Ar/water vapor mixtures with varying concentrations of H_2O.[41] T_R(OH) increased with the addition of water to the feed gas from 620 K in a 100% Ar plasma to 1130 K for a mixture comprising 0.76% H_2O. Similarly, Bruggeman and coworkers noted a concurrent increase in T_R(OH) with H_2O concentration in a He/H_2O rf atmospheric pressure glow discharge.[42] They observed formation of a two-temperature Boltzmann distribution for OH ($A^2\Sigma^+$) at ~940 ppm H_2O, indicating a lower rotational temperature for lower rotational states and an elevated rotational temperature for the higher rotational states. In a second publication by Bruggeman and coworkers, the authors determined that excited OH radicals tend to show significant overpopulation of high rotational states in atomic gases and water vapor.[43] The overpopulation of the high OH ($A^2\Sigma^+$) rotational states [and thus, higher reported T_R(OH) values] are explained by a combination of the formation process and quenching rates. H_2O is the most efficient electronic quenching partner of OH ($A^2\Sigma^+$)[43]; however, for high concentrations of water, the quenching time constants become on the same order of magnitude as rotational energy transfer (RET).[42-43] This inhibits the thermalization of OH ($A^2\Sigma^+$) before radiative decay occurs, and consequently, higher T_R(OH) values are observed at high [H_2O] for the systems described by Sarani *et al.*[41] and Bruggeman *et al.*[42]. Additionally, Bruggeman and coworkers observed no change in the rotational population distribution with increasing power, suggesting that the non-Boltzmann behavior in their systems is related to water concentration rather than other plasma parameters.[42]

Our T_R(OH) results clearly display different trends from the studies mentioned above. Namely, T_R(OH) is much lower at high levels of $H_2O_{(v)}$ in the feed gas, and a power dependence is observed for feed gas compositions of ≤50% H_2O (Figure 7.14b). Notably, our system operates at pressures (150 mTorr) much lower than atmospheric pressure; thus, fewer collisions occur in our system than at higher pressures within the same time frame. As collisional time is on the same order as the radiative lifetime, the T_R(OH) values observed in our system are an image of the formation process of OH ($A^2\Sigma^+$). This suggests that, regardless of the feed gas composition, T_R(OH) is more dependent on OH ($A^2\Sigma^+$) formation processes rather than collisional quenching processes (e.g., electronic quenching with H_2O).

The formation of OH ($A^2\Sigma^+$) primarily occurs via direct dissociative electron excitation of water vapor, Reaction 7.8, or direct electron impact excitation of ground state OH, Reaction 7.9.[41]

$$H_2O^* + e^- \rightarrow OH^* + H + e^- \quad (7.8)$$

$$H_2O + e^- \rightarrow H + OH + e^- \quad (7.9a)$$

$$OH + e^- \rightarrow OH^* + e^- \quad (7.9b)$$

Sarani *et al.* characterized T_R(OH) by a two-temperature Boltzmann distribution in their system and suggested that vibrational-rotational populations of OH can be formed via different mechanisms depending on their J level.[41] The authors hypothesize that lower rotational states ($J < 13$) were produced via a combination of Reactions 7.8 and 7.9 resulting in T_R(OH) = 625 K. Conversely, the $13 < J < 25$ rotational levels were characterized by a much higher rotational temperature [T_R(OH) = 5000 K]. Because OH ($A^2\Sigma^+$) radicals produced via Reaction 7.8 result in high rotationally excited levels, the authors suggest that the hydroxyl radicals characterized by the $13 < J < 25$ rotational levels are almost exclusively generated by Reaction 7.8.[41] This

interpretation suggests that the elevated T_R(OH) values observed at low H_2O feed gas concentration may be related to formation of OH ($A^2\Sigma^+$) primarily via Reaction 7.8. In contrast, the lower T_R(OH) values observed at high H_2O feed gas concentration indicate that Reaction 7.9 may also significantly contribute to OH ($A^2\Sigma^+$) formation. Indeed, if the ground state [OH] is sufficiently large as would be expected with a larger concentration of H_2O, then Reaction 7.9 will be important to the formation processes of OH ($A^2\Sigma^+$).[42] One additional consideration for the formation of OH^* is the recombination between H and O atoms which produces rotationally "hot" OH ($A^2\Sigma^+$).[44] This is described in Reaction 7.10, where either the atomic hydrogen or oxygen atom or both atoms may already be in an excited state.

$$H^* + O^* \rightarrow OH^* \qquad (7.10)$$

In our systems, an increase in power leads to greater destruction of OH molecules and consequently, higher atomic H and O densities. Thus, the observed power dependence for T_R(OH) may be related to Reaction 7.10.

Evaluating steady state emission data provides valuable information regarding energy partitioning and further insight into molecular formation mechanisms can be gained when combined with the kinetics data afforded by TR-OES. Figure 7.13a shows OH intensity is high upon plasma ignition, immediately followed by a decrease to steady state at longer times. k_d is highly dependent on the feed gas composition and power (at low H_2O concentrations). The absence of a formation curve for OH suggests that OH^* indicates that the formation process is faster than the time resolution of our experiment. Additionally, the presence of the decay curve suggests that OH^* produced from H_2O decomposition either continues to decompose into atomic hydrogen and oxygen species or participates in further reactions (e.g., formation of CHO, recombination to form H_2O, etc.). Zaima and Sasaki also utilized TR-OES to examine OH

($A^2\Sigma^+$) production processes in a pulsed $CH_4/O_2/Ar$ DBD burner flame.[44] Increases in OH density and decreases in T_R(OH) aligned simultaneously with the plasma current pulses. These authors suggest two reaction processes may be contributing to the pulsed responses of [OH] and T_R(OH), one that produces rotationally "hot" OH and another that produces "cold" OH. They hypothesize that "cold" OH is produced simultaneously with the pulsed high energy electrons. Indeed, further studies probing T_R(OH) as a function of time both in pulsed and continuous wave plasmas could provide useful insight into formation mechanisms of OH ($A^2\Sigma^+$).

Because CO k_f remains relatively constant over the parameter space, the formation of CO does not appear to be directly related to OH formation or destruction processes. Although CO k_f values are generally not dependent on feed gas ratio, there appears to be a slight P dependence at low H_2O concentration. This dependence could be related to the total amount of oxygen species present in the plasma, a clearly essential component for formation of CO. For example, an increase in P corresponds to a decrease in [OH] and an increase [O] and [H] species. Currently, most literature discussing CO formation in plasmas utilizes CO_2 as a feed gas component (e.g., CH_4/CO_2 mixtures). Thus, CO primarily results from CO_2 decomposition, rather than formation though a recombination reaction as is the case in our systems. Moreover, the carbon and oxygen species needed to form CO arise from the two different precursors. As it is difficult to determine exact gas phase formation mechanisms from the CO k_f data presented here, further gas phase investigations including the determination of T_R(CO) and T_V(CO) may be useful.

7.4 Summary

Optical spectroscopy techniques were employed to evaluate kinetic and energetic processes in two environmentally relevant mixed gas plasma systems (CH_4/N_2 and CH_4/H_2O).

Determination of rotational and vibrational temperatures for several molecular species in each plasma system demonstrate that the excited state species in our systems are not equilibrated with each other and that different species have achieved different degrees of equilibration between rotational and vibrational modes. When combined with evaluation of TR-OES data, T_R and T_V values provide insight into molecule formation pathways. Furthermore, our results suggest that formation of some molecular species are dependent on the feed gas composition. For example, our results indicate CN^* formation is dependent on activated nitrogen species in the plasma. Possible formation mechanisms for the excited state species examined in this chapter serve to provide a deeper understanding of the relationship between plasma parameters and kinetic and energy partitioning outcomes as well as the roles of reactive species. Collectively, these data help provide the foundation for increasing the utility of PAC.

REFERENCES

1. Grill, A., *Cold Plasma in Materials Fabrication*. IEEE Press, New York: 1994; Vol. 151.
2. Zhang, W.; Catherine, Y., Deposition of Carbon Films by the Dissociation of Methane in RF Discharge. *Surf. Coat. Technol.* **1991,** *47* (1-3), 69-83.
3. Bogaerts, A.; Tu, X.; Whitehead, J. C.; Centi, G.; Lefferts, L.; Guaitella, O.; Azzolina-Jury, F.; Kim, H.-H.; Murphy, A. B.; Schneider, W. F., The 2020 Plasma Catalysis Roadmap. *J. Phys. D: Appl. Phys.* **2020,** *53* (44), 443001.
4. Hanna, A. R.; Fisher, E. R., Investigating Recent Developments and Applications of Optical Plasma Spectroscopy: A Review. *J. Vac. Sci. Technol., A* **2020,** *38* (2), 020806.
5. Wang, Y.; Craven, M.; Yu, X.; Ding, J.; Bryant, P.; Huang, J.; Tu, X., Plasma-Enhanced Catalytic Synthesis of Ammonia over a Ni/Al_2O_3 Catalyst at near-Room Temperature: Insights into the Importance of the Catalyst Surface on the Reaction Mechanism. *ACS Catal.* **2019,** *9* (12), 10780-10793.
6. Wang, X.; Gao, Y.; Zhang, S.; Sun, H.; Li, J.; Shao, T., Nanosecond Pulsed Plasma Assisted Dry Reforming of CH_4: The Effect of Plasma Operating Parameters. *Appl. Energy* **2019,** *243*, 132-144.
7. Cruden, B. A.; Rao, M.; Sharma, S. P.; Meyyappan, M., Neutral Gas Temperature Estimate in CF_4/O_2/Ar Inductively Coupled Plasmas. *Appl. Phys. Lett.* **2002,** *81* (6), 990-992.
8. Raud, J.; Laan, M.; Jogi, I., Rotational Temperatures of N_2 (C, 0) and OH (A, 0) as Gas Temperature Estimates in the Middle Pressure Ar/O_2 Discharge. *J. Phys. D: Appl. Phys.* **2011,** *44* (34), 345201.
9. Bai, B.; Sawin, H. H.; Cruden, B. A., Neutral Gas Temperature Measurements of High-Power-Density Fluorocarbon Plasmas by Fitting Swan Bands of C_2 Molecules. *J. Appl. Phys.* **2006,** *99* (1), 013308.
10. Hanna, A. R.; Blechle, J. M.; Fisher, E. R., Using Fundamental Spectroscopy to Elucidate Kinetic and Energetic Mechanisms within Environmentally Relevant Inductively Coupled Plasma Systems. *J. Phys. Chem. A* **2017,** *121* (40), 7627-7640.
11. Hanna, A. R.; Van Surksum, T. L.; Fisher, E. R., Investigating the Impact of Catalysts on N_2 Rotational and Vibrational Temperatures in Low Pressure Plasmas. *J. Phys. D: Appl. Phys.* **2019,** *52* (34), 345202.
12. Van Surksum, T. L.; Blechle, J. M.; Fisher, E. R., Determination of Rotational and Vibrational Temperatures of CH in CH_4 Plasmas. *J. Vac. Sci. Technol., A* **2018,** *36* (4), 041302.
13. Laux, C. O., Radiation and Nonequilibrium Collisional-Radiative Models. *von Karman Institute Lecture Series* **2002,** *7*.
14. Luque, J.; Crosley, D. R., Lifbase: Database and Spectral Simulation Program (Version 1.5). *SRI international report MP* **1999,** *99* (009).
15. Van Surksum, T. L.; Fisher, E. R., Gas-Phase Diagnostic Studies of H2 and Ch4 Inductively Coupled Plasmas. *J. Vac. Sci. Technol., A* **2020,** *38* (3), 033010.
16. Cruden, B. A.; Rao, M.; Sharma, S. P.; Meyyappan, Neutral Gas Temperature Estimates in an Inductively Coupled CF_4 Plasma by Fitting Diatomic Emission Spectra. *J. Appl. Phys.* **2002,** *91* (11), 8955-8964.
17. Freire, F.; Lazaro, J.; Franceschini, D.; Achete, C., Nitrogen Incorporation into Hard Amorphous Carbon Films Obtained by RF Plasma Decomposition of CH_4-N_2 Gas Mixtures. *Phys. Status Solidi B* **1995,** *192* (2), 493-502.

18. Pereira, J.; Massereau-Guilbaud, V.; Géraud-Grenier, I.; Plain, A., CH and CN Radical Contribution in the Particle Formation Generated in a Radio-Frequency CH_4/N_2 Plasma. *Plasma Process. Polym.* **2005,** *2* (8), 633-640.
19. Majumdar, A.; Das, G.; Basvani, K. R.; Heinicke, J.; Hippler, R., Role of Nitrogen in the Formation of HC−N Films by CH_4/N_2 Barrier Discharge Plasma: Aliphatic Tendency. *J. Phys. Chem. B* **2009,** *113* (48), 15734-15741.
20. Truscott, B. S.; Kelly, M. W.; Potter, K. J.; Ashfold, M. N.; Mankelevich, Y. A., Microwave Plasma-Activated Chemical Vapor Deposition of Nitrogen-Doped Diamond. II: $CH_4/N_2/H_2$ Plasmas. *J. Phys. Chem. A* **2016,** *120* (43), 8537-8549.
21. Clay, K.; Speakman, S.; Amaratunga, G.; Silva, S., Characterization of a-C:H:N Deposition from CH_4/N_2 RF Plasmas Using Optical Emission Spectroscopy. *J. Appl. Phys.* **1996,** *79* (9), 7227-7233.
22. Seo, H.; Kim, J.-H.; Chung, K.-H.; Kim, J. Y.; Kim, S. H.; Jeon, H., Characterization of Remote Inductively Coupled CH_4–N_2 Plasma for Carbon Nitride Thin-Film Deposition. *J. Appl. Phys.* **2005,** *98* (4), 043308.
23. Hu, W.; Tang, J.-Y.; Wu, J.-D.; Sun, J.; Shen, Y.-Q.; Xu, X.-F.; Xu, N., Characterization of Carbon Nitride Deposition from CH_4/N_2 Glow Discharge Plasma Beams Using Optical Emission Spectroscopy. *Phys. Plasmas* **2008,** *15* (7), 073502.
24. Avtaeva, S.; Lapochkina, T., Characteristics of Molecular Hydrogen and CH^* Radicals in a Methane Plasma in a Magnetically Enhanced Capacitive RF Discharge. *Plasma Phys. Rep.* **2007,** *33* (9), 774-785.
25. Bhattacharyya, S.; Granier, A.; Turban, G., Growth, Microstructure and Electronic Properties of Amorphous Carbon Nitride Films Investigated by Plasma Diagnostics. *J. Appl. Phys.* **1999,** *86* (8), 4668-4676.
26. Liu, D.; Zhou, J.; Fisher, E. R., Correlation of Gas-Phase Composition with Film Properties in the Plasma-Enhanced Chemical Vapor Deposition of Hydrogenated Amorphous Carbon Nitride Films. *J. Appl. Phys.* **2007,** *101* (2), 023304.
27. Chatei, H.; Bougdira, J.; Remy, M.; Alnot, P., Optical Emission Diagnostics of Permanent and Pulsed Microwave Discharges in H_2–CH_4–N_2 for Diamond Deposition. *Surf. Coat. Technol.* **1999,** *116*, 1233-1237.
28. Stillahn, J. M.; Fisher, E. R., CN Surface Interactions and Temperature-Dependent Film Growth During Plasma Deposition of Amorphous, Hydrogenated Carbon Nitride. *J. Phys. Chem. C* **2009,** *113* (5), 1963-1971.
29. Veprek, S.; Weidmann, J.; Glatz, F., Plasma Chemical Vapor Deposition and Properties of Hard C_3N_4 Thin Films. *J. Vac. Sci. Technol., A* **1995,** *13* (6), 2914-2919.
30. Manabe, Y.; Mitsuyu, T., Silicon Nitride Thin Films Prepared by the Electron Cyclotron Resonance Plasma Chemical Vapor Deposition Method. *J. Appl. Phys.* **1989,** *66* (6), 2475-2480.
31. Kareev, M.; Sablier, M.; Fujii, T., Diagnosis of a CH_4/N_2 Microwave Discharge: Ionic and Neutral Species. *J. Phys. Chem. A* **2000,** *104* (31), 7218-7223.
32. Mutsukura, N., Deposition of Diamondlike Carbon Film and Mass Spectrometry Measurement in CH_4/N_2 RF Plasma. *Plasma Chem. Plasma Process.* **2001,** *21* (2), 265-277.
33. Jolly, J.; Touzeau, M.; Ricard, A., Determination of Non-Boltzmann Vibrational Level Populations of Excited Nitrogen Using the Penning Ionisation Technique. *J. Phys. B* **1981,** *14* (3), 473.

34. Piper, L. G.; Marinelli, W. J., Determination of Non-Boltzmann Vibrational Distributions of N_2 (X, V') in He/N_2 Microwave-Discharge Afterglows. *J. Chem. Phys.* **1988,** *89* (5), 2918-2924.
35. Bruggeman, P.; Sadeghi, N.; Schram, D.; Linss, V., Gas Temperature Determination from Rotational Lines in Non-Equilibrium Plasmas: A Review. *Plasma Sources Sci. Technol.* **2014,** *23* (2), 023001.
36. Goyette, A.; Peck, J.; Matsuda, Y.; Anderson, L.; Lawler, J., Experimental Comparison of Rotational and Gas Kinetic Temperatures in and He-Discharges. *J. Phys. D: Appl. Phys.* **1998,** *31* (13), 1556.
37. Khan, M.; Rehman, N.; Khan, S.; Ullah, N.; Masood, A.; Ullah, A., Spectroscopic Study of CO_2 and CO_2–N_2 Mixture Plasma Using Dielectric Barrier Discharge. *AIP Adv.* **2019,** *9* (8), 085015.
38. Abdel-Rahman, M.; Gans, T.; Schulz-Von Der Gathen, V.; Döbele, H., Space and Time Resolved Rotational State Populations and Gas Temperatures in an Inductively Coupled Hydrogen RF Discharge. *Plasma Sources Sci. Technol.* **2005,** *14* (1), 51.
39. Michler, T.; Toedter, O.; Koch, T., Measurement of Temporal and Spatial Resolved Rotational Temperature in Ignition Sparks at Atmospheric Pressure. *Automotive and Engine Technology* **2020,** *5* (1), 57-70.
40. Hash, D.; Bose, D.; Rao, M.; Cruden, B.; Meyyappan, M.; Sharma, S., Impact of Gas Heating in Inductively Coupled Plasmas. *J. Appl. Phys.* **2001,** *90* (5), 2148-2157.
41. Sarani, A.; Nikiforov, A. Y.; Leys, C., Atmospheric Pressure Plasma Jet in Ar and Ar/H_2O Mixtures: Optical Emission Spectroscopy and Temperature Measurements. *Phys. Plasmas* **2010,** *17* (6), 063504.
42. Bruggeman, P.; Iza, F.; Guns, P.; Lauwers, D.; Kong, M. G.; Gonzalvo, Y. A.; Leys, C.; Schram, D. C., Electronic Quenching of OH (A) by Water in Atmospheric Pressure Plasmas and Its Influence on the Gas Temperature Determination by OH (A–X) Emission. *Plasma Sources Sci. Technol.* **2009,** *19* (1), 015016.
43. Bruggeman, P.; Schram, D. C.; Kong, M. G.; Leys, C., Is the Rotational Temperature of OH (A–X) for Discharges in and in Contact with Liquids a Good Diagnostic for Determining the Gas Temperature? *Plasma Process. Polym.* **2009,** *6* (11), 751-762.
44. Zaima, K.; Sasaki, K., Responses of OH ($X^2\Pi$) and OH ($A^2\Sigma^+$) to High-Energy Electrons of Dielectric Barrier Discharge in Plasma-Assisted Burner Flame. *Jpn. J. Appl. Phys.* **2014,** *53* (11), 110309.

CHAPTER 8

RESEARCH SUMMARY AND PERSPECTIVES

This chapter summarizes the major aspects and themes of the research presented within this dissertation. Potential avenues for future directions of research to address current limitations of plasma-assisted catalysis (PAC) applicability are also proposed.

8.1 Research Summary

Low energy requirements and the enormous potential for feed gas decomposition and conversion make plasma-assisted catalysis (PAC) an attractive approach for pollution remediation of waste gas streams;[1-3] however, a lack of knowledge on the fundamental processes contributing to observed plasma-catalyst synergies in PAC systems severely limits its utility.[4-5] To fully utilize the advantages of these plasma systems, an understanding of the roles of the catalyst and the plasma, as well as the interactions occurring at the plasma-surface interface must be understood. Evaluating the contributions of the plasma and catalyst to the observed synergies requires a multi-pronged approach, wherein the fundamental chemistry of each region of the plasma-substrate system is characterized (Figure 1.1). This approach to deciphering key molecular-level processes in plasmas is an emergent theme throughout this dissertation and involves an array of complementary analysis techniques to both probe the gas-phase of the plasma and comprehensively characterize the material of interest.

Plasma diagnostic tools are employed to evaluate kinetic and energetic processes for multiple molecular species in low-temperature, inductively-coupled plasma (ICP) systems with precursors of increasing complexity, including mixed gas systems. A primary goal of this work

has been the determination of internal molecular temperatures within PAC systems. This emphasis comes from the estimation that these values collectively represent a key component to understanding the reactions that drive the chemistry and the mechanisms involved in plasma-surface interactions. Moreover, these data help to establish the relationship between system parameters and energetic outcomes. Specifically, rotational and vibrational temperatures (T_R and T_V, respectively) have been calculated for several excited state diatomic species (e.g., CH, CN, H_2, N_2, OH). Our data indicate that our ICPs generate vibrationally hot species with $T_V > T_R$ for each molecule studied. Importantly, this work has clearly demonstrated differences between T_R values of several molecular species within the same plasma system. For example, in a CH_4/N_2 plasma (8:1 precursor ratio; p = 150 mTorr, P = 75 W), T_R values for CH and CN (~1720 K and ~1180 K, respectively) are significantly elevated compared to $T_R(H_2)$ (~600 K) and $T_R(N_2)$ (~280 K). As N_2 ($C^3\Pi_u$) and H_2 ($d^3\Pi_u$) are typically excited via direct electron impact in N_2 and CH_4 discharges,[6-8] this thermal nonequilibrium between molecular species implies that formation mechanisms play a significant role in resulting rotational temperatures for diatomic molecules. Additionally, studies as functions of various system parameters demonstrate the significant impact of pressure (p), applied rf power (P), and feed gas ratio on fundamental plasma processes. For example, $T_R(H_2)$ increases simultaneously with system pressure and decreases with increasing power in a 100% CH_4 plasma, whereas no clear pressure or power trends appear for $T_R(H_2)$ in a 100% H_2 plasma (Chapter 4). Moreover, T_R(CN) is dependent on the feed gas ratio in a mixed gas CH_4/N_2 plasma system (Chapter 7), indicating that different formation mechanisms may be occurring under different parameter conditions. Time-resolved spectroscopic studies allow us to further probe these complex molecular level processes by measuring species formation and destruction rates as functions of plasma parameters. Time-

resolved optical emission spectroscopy (TR-OES) results presented in Chapter 7 demonstrate that the kinetics of both N_2 and CN formation and destruction are highly dependent on the feed gas ratio while TR-OES studies in Chapters 5 and 6 demonstrate that the presence of a catalyst also impacts kinetic processes.

A second chief component to the work presented throughout this dissertation centers on understanding the effect of the plasma on the substrate properties. A combination of materials analysis techniques were employed to evaluate chemical and morphological properties before and after plasma exposure. X-ray photoelectron data (XPS) data of a TiO_2 catalyst presented in Chapter 5 demonstrates that H_2 plasma significantly reduces titanium from Ti^{4+} to Ti^{3+} and Ti^{2+} oxidation states. Reduction of titanium is also observed to a lesser extent after exposure to CH_4 (Chapter 5) and N_2 (Chapter 6) plasmas. Moreover, an increase of adsorbed oxygen species relative to lattice oxygen post plasma exposure indicates the formation of oxygen vacancies via plasma-surface interactions.

By utilizing a combination of optical spectroscopy and materials characterization techniques to investigate both the gas phase and catalyst characteristics, insight into key molecular-level processes in PAC systems can be constructed. Specifically, the studies presented herein have sought to understand mechanistic phenomena occurring in the gas-phase and at the plasma-surface interface in PAC-relevant systems. Overall, this work offers unique insight into these fundamental processes which are crucial to advancing PAC technology. For research to continue to address PAC implementation limitations, however, future studies should include investigations into systems of increasing complexity and continue to yield important and valuable information about the plasma-surface interface.

8.2 Future Directions

The results presented and discussed herein demonstrate original research that can be used as a foundational basis for PAC applications. The implications of this work are far reaching, and yet, significant additional research must be done to establish full applicability of PAC. To encapsulate the complex chemistry occurring in a PAC environment, further research efforts should include a holistic approach to characterizing the plasma-catalyst environment. Elucidating fundamental chemical processes occurring at the molecular level in (1) the gas phase of the plasma, (2) the catalytic material, and (3) at the plasma-surface interface will provide valuable insight towards understanding the multifaceted environment of PAC systems.

As demonstrated throughout this dissertation, monitoring species emission via OES can provide valuable information beyond species identification. Species densities, plasma temperatures, and kinetics information obtained via OES can afford tremendous insight into the underlying mechanisms at work within our plasma systems. Although OES provides useful data, it is also important to evaluate ground state species, which comprise the majority of species in low temperature ICPs.[9] As a complementary technique to OES, broadband absorption spectroscopy (BAS) is a gas-phase diagnostic tool that can be readily implemented in the Fisher group laboratories to obtain information on ground state species. With the addition of a halogen-deuterium light source interfaced to a second quartz window on the upstream end of the reactor (Figure 2.1b), we can collect absorption data of relevant species within our plasma systems.[10] Preliminary BAS data, Figure 8.1, shows absorption of the CH $A^2\Delta \leftarrow X^2\Pi$ transition in a 100% CH_4 plasma. Fitting this spectrum within LIFBASE gives rise to T_R = 1690 K. Notably, T_R(CH $X^2\Pi$) is significantly lower than T_R(CH $A^2\Delta$) (~2010 K) under the same plasma parameter conditions, indicating that a higher degree of thermalization may be achieved for the ground state

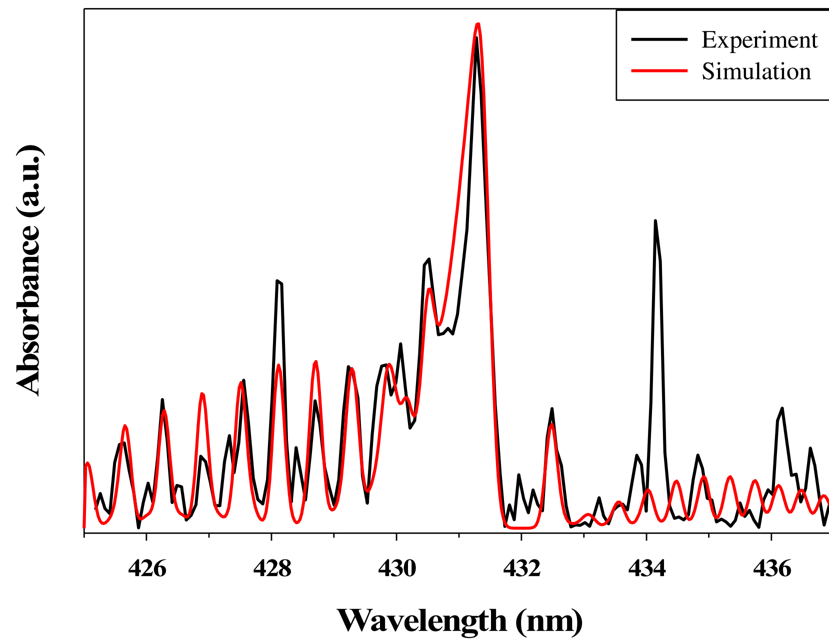

Figure 8.1. Broadband absorption spectrum (p = 150 mTorr, P = 100 W) for CH $X^2\Pi \rightarrow A^2\Delta$ in a CH_4 plasma. Simulation of this spectrum using LIFBASE yields T_R = 1690 K, PC = 0.94.

species compared to the excited state species. Interestingly, the Fisher group has noted the opposite trends for N_2 and NO species in N_xO_y plasma systems. Specifically, T_R(N_2, NO) for ground state species are elevated compared to those for excited state species.[8, 10] Our OES temperature studies of CH_4 and N_xO_y plasmas have demonstrated significant differences in T_R and T_V values and trends between the two types of plasma systems, indicating there are fundamental differences in how these species and plasma systems behave.[8, 10-11] The preliminary BAS spectrum in Figure 8.1 provides a glimpse into the ground state energetics of T_R(CH $X^2\Pi$) in our plasma systems. Clearly, further BAS investigations would provide valuable information that would aid in understanding the key molecular processes that occur in PAC systems.

Future investigations should also include studying plasma systems of increasing complexity. Although we have studied mixed gas plasma systems comprising CH_4 mixtures with either N_2 or $H_2O_{(v)}$ (Chapter 7), real world waste gas streams comprise a vast array of gas-phase species. Several VOCs, NO_x species, and even sulfur contaminants contribute significantly to the overall chemistry of exhaust systems of interest for remediation through PAC. As precursor gases become more complex, the interactions between gas-phase species and catalysts will undoubtably become more complex and convoluted. As such, a thorough understanding of the molecular-level processes occurring in increasingly complex systems will provide valuable information towards increasing the overall applicability of PAC by tailoring the chemistry occurring in the system. It is crucial to investigate the role that each of these component species plays in the overall chemistry, energy, and reactivity of environmentally-relevant plasma systems. Thus, increasing the complexity of the plasma precursors should also include increasing the complexity of the hydrocarbon feed gases (e.g., C_2H_6, C_2H_4, C_6H_6) or utilizing multiple precursors to further probe mixed gas systems. Additionally, studies

performed in Chapter 7 did not include the use of a catalyst. As demonstrated in the work presented throughout this dissertation, a catalyst can significantly change the plasma chemistry. Preliminary investigations of an 8:1 CH_4/N_2 plasma show that $T_V(N_2)$ is reduced for $P > 25$ W ($p = 200$ mTorr) when a TiO_2 substrate is introduced to the discharge, Figure 8.2. With the catalyst, $T_V(N_2)$ values decrease by up to ~1800 K. Moreover, $T_V(N_2)$ data show a linear dependence on P both with and without the TiO_2 catalyst in the plasma. These results mimic $T_V(N_2)$ trends for a 100% N_2 plasma with and without a TiO_2 substrate (Figure 6.2).[12] Although this suggests similar $T_V(N_2)$ trends may exist for the other CH_4/N_2 feed gas ratios studied in Chapter 7, further investigations of other molecular species in this system could provide key insight into PAC processes.

Studies focused on the catalyst in PAC systems are also important to increasing applicability. A host of catalysts have been used in PAC systems including platinum, palladium, zeolites, and several metal oxide materials (e.g., TiO_2, Al_2O_3, SnO_2, ZnO, MgO).[13-15] Numerous studies have focused on optimizing conversion rates of toxic pollutants to clean gas species by comparing various catalyst types and morphologies.[16-17] Although the results presented in this dissertation up to this point have only included TiO_2 nanoparticles as the catalyst material, studies with SnO_2 nanoparticles, ZnO nanoparticles, and ZnO microrods as catalysts were also executed. These preliminary results are presented in Appendix A. As noted elsewhere, the Fisher research group has studied the effect of Pt and zeolite materials on N_2O plasma chemistry.[18] The presence of Pt nanopowder or micro-structured zeolites in the plasma significantly decreased the concentration of NO at high powers, whereas the flat Pt foil substrate did not. Moreover, whereas all catalyst materials decreased $T_V(N_2)$, the Pt materials had a limited effect on $T_V(NO)$. These results along with those presented in this dissertation clearly

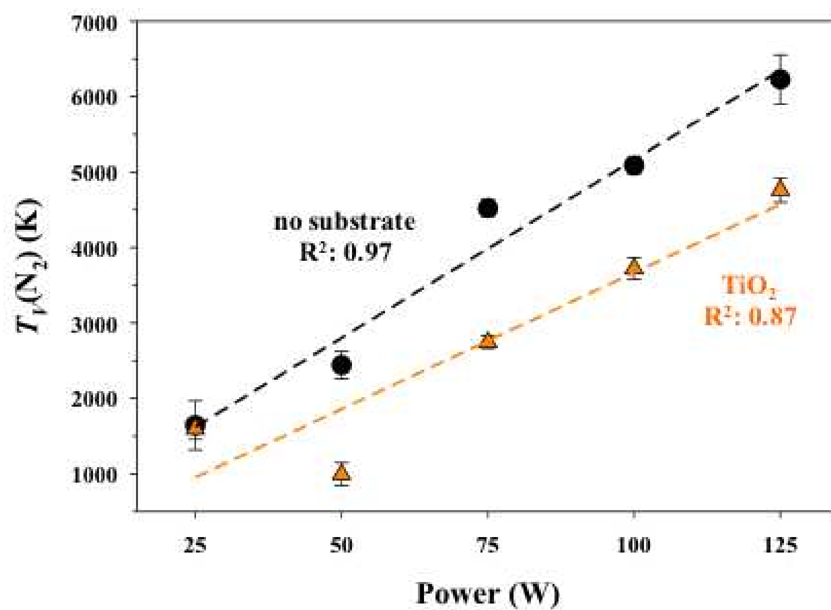

Figure 8.2. $T_V(N_2)$ in an 8:1 CH_4/N_2 plasma (10% Ar, p = 200 mTorr) without a substrate (black circles) and with a TiO_2 substrate (orange triangles). Dashed lines represent linear regression analysis for the two data sets, with the R^2 values shown.

indicate that careful selection of catalysts is important when designing a PAC system for commercial or industrial implementation. Further fundamental studies must be performed to fully understand the impact of different catalysts and morphologies on plasma chemistry.

Notably, in addition to selection of the catalyst material, modification of catalyst surfaces can increase catalytic performance.[19-23] Several studies have shown that pre-treating a catalyst with a reducing plasma environment can create oxygen vacancies in metal oxide catalyst materials.[19, 22-23] This is demonstrated in Chapter 5 where high resolution XPS spectra show the reduction of Ti^{4+} to Ti^{3+} and Ti^{2+} oxidation states with a simultaneous increase in adsorbed oxygen species after exposure to a 100% H_2 plasma. The presence of oxygen vacancies within the metal oxide material can enhance conversion of NO_x and VOC species.[19-21] Notably, the Fisher research group stands uniquely poised to enter this area of research, with significant contributions to plasma-enhanced surface modification techniques. Surface modification via plasma processing could be an invaluable tool towards creating better catalytic materials to be used in PAC systems.

A primary challenge to understanding low-temperature plasma chemistry within the context of PAC systems lies in deciphering plasma-surface interactions.[3, 24-25] Thus, it is critical to distinguish effects arising from (a) different types of species bombarding the surface; (b) synergistic or coupled reactions at the surface (e.g., ion bombardment assisting chemical etching[26-27]) and (c) energy partitioning within molecules. All can impact how molecules interact with a surface, especially because the rates of many surface reactions are likely controlled by molecular vibrational and electronic states.[28] Our unique imaging of radicals interacting with substrates (IRIS) technique utilizes a laser and plasma molecular beam and laser-induced fluorescence images are collected with and without a substrate in the path of the

beam to determine scatter coefficients and the concomitant surface reactivity.[29-30] IRIS allows us to measure plasma-surface interactions during plasma processing of a substrate. Previous Fisher group work showed that that the surface reactivity probability of CH in a CH_4 plasma is near unity and appears independent of several plasma parameters (e.g., pressure, power) and substrate conditions (e.g., substrate temperature and substrate bias).[31] The high surface reactivity of CH implies that almost all incident CH radicals have been lost to the surface of the material. Some studies suggest carbon deposition is mitigated by synergistic effects during PAC,[32-33] and plasma desorption of VOCs from adsorbent catalysts can occur via energetic species bombardment to form CO_2 and other hydrocarbon decomposition products.[34-35] Certainly, it would be of significant interest to use IRIS to study the interaction of CH on catalytic substrates to further elucidate plasma-catalyst synergies. Indeed, studying other radical species (e.g., C_2, CN, N_2, NO, OH) that are prevalent in PAC systems using the IRIS technique is also essential to provide a more complete picture of the processes occurring in a PAC environment by providing foundational information on plasma-surface interactions.

Significant foundational work still remains to be done to understand and increase the future success of PAC systems as a pollution remediation tool. These future directions serve to explore each aspect of the PAC environment (gas phase, catalyst, plasma-catalyst interface) in an effort to elucidate the roles that each component [gas-phase species, catalyst material, or plasma parameter (pressure, power, precursor)] has on the overall chemistry of the PAC system. Understanding the effects that each of these components has on the PAC environment on a molecular level will allow us to control and essentially tune the chemistry of the system as needed for specific applications. Thus, fundamental investigations such as those performed or

suggested throughout this dissertation will ultimately provide the significant foundational advancement necessary for PAC utility.

REFERENCES

1. Feng, X.; Liu, H.; He, C.; Shen, Z.; Wang, T., Synergistic Effects and Mechanism of a Non-Thermal Plasma Catalysis System in Volatile Organic Compound Removal: A Review. *Catal. Sci. Technol.* **2018,** *8* (4), 936-954.
2. Puliyalil, H.; Jurković, D. L.; Dasireddy, V. D.; Likozar, B., A Review of Plasma-Assisted Catalytic Conversion of Gaseous Carbon Dioxide and Methane into Value-Added Platform Chemicals and Fuels. *RSC Adv.* **2018,** *8* (48), 27481-27508.
3. Neyts, E. C., Plasma-Surface Interactions in Plasma Catalysis. *Plasma Chem. Plasma Process.* **2016,** *36* (1), 185-212.
4. Röpcke, J.; Lombardi, G.; Rousseau, A.; Davies, P., Application of Mid-Infrared Tuneable Diode Laser Absorption Spectroscopy to Plasma Diagnostics: A Review. *Plasma Sources Sci. Technol.* **2006,** *15* (4), S148.
5. Whitehead, J. C., Plasma–Catalysis: The Known Knowns, the Known Unknowns and the Unknown Unknowns. *J. Phys. D: Appl. Phys.* **2016,** *49* (24), 243001.
6. Avtaeva, S.; Lapochkina, T., Characteristics of Molecular Hydrogen and CH* Radicals in a Methane Plasma in a Magnetically Enhanced Capacitive RF Discharge. *Plasma Phys. Rep.* **2007,** *33* (9), 774-785.
7. Van Surksum, T. L.; Fisher, E. R., Gas-Phase Diagnostic Studies of H_2 and CH_4 Inductively Coupled Plasmas. *J. Vac. Sci. Technol., A* **2020,** *38* (3), 033010.
8. Hanna, A. R.; Blechle, J. M.; Fisher, E. R., Using Fundamental Spectroscopy to Elucidate Kinetic and Energetic Mechanisms within Environmentally Relevant Inductively Coupled Plasma Systems. *J. Phys. Chem. A* **2017,** *121* (40), 7627-7640.
9. Grill, A., *Cold Plasma in Materials Fabrication*. IEEE Press, New York: 1994; Vol. 151.
10. Blechle, J. M.; Hanna, A. R.; Fisher, E. R., Determination of Internal Temperatures within Nitric Oxide Inductively Coupled Plasmas. *Plasma Process Polym.* **2017,** *14* (12), 1700041.
11. Van Surksum, T. L.; Blechle, J. M.; Fisher, E. R., Determination of Rotational and Vibrational Temperatures of CH in CH_4 Plasmas. *J. Vac. Sci. Technol., A* **2018,** *36* (4), 041302.
12. Hanna, A. R.; Van Surksum, T. L.; Fisher, E. R., Investigating the Impact of Catalysts on N_2 Rotational and Vibrational Temperatures in Low Pressure Plasmas. *J. Phys. D: Appl. Phys.* **2019,** *52* (34), 345202.
13. Zhang, Z.; Jiang, Z.; Shangguan, W., Low-Temperature Catalysis for VOCs Removal in Technology and Application: A State-of-the-Art Review. *Catal. Today* **2016,** *264*, 270-278.
14. Kamal, M. S.; Razzak, S. A.; Hossain, M. M., Catalytic Oxidation of Volatile Organic Compounds (VOCs)–A Review. *Atmos. Environ.* **2016,** *140*, 117-134.
15. Neyts, E. C.; Ostrikov, K.; Sunkara, M. K.; Bogaerts, A., Plasma Catalysis: Synergistic Effects at the Nanoscale. *Chem. Rev.* **2015,** *115* (24), 13408-13446.
16. Patil, B.; Cherkasov, N.; Lang, J.; Ibhadon, A.; Hessel, V.; Wang, Q., Low Temperature Plasma-Catalytic Nox Synthesis in a Packed DBD Reactor: Effect of Support Materials and Supported Active Metal Oxides. *Appl. Catal., B* **2016,** *194*, 123-133.
17. Zhu, X.; Gao, X.; Yu, X.; Zheng, C.; Tu, X., Catalyst Screening for Acetone Removal in a Single-Stage Plasma-Catalysis System. *Catal. Today* **2015,** *256*, 108-114.

18. Hanna, A. R.; Fisher, E. R., Efforts toward Unraveling Plasma-Assisted Catalysis: Determination of Kinetics and Molecular Temperatures within N_2O Discharges. *ACS Catalysis* **2020,** *10*, 6546-6560.
19. Nakamura, I.; Negishi, N.; Kutsuna, S.; Ihara, T.; Sugihara, S.; Takeuchi, K., Role of Oxygen Vacancy in the Plasma-Treated TiO_2 Photocatalyst with Visible Light Activity for NO Removal. *J. Mol. Catal. A: Chem.* **2000,** *161* (1-2), 205-212.
20. Chen, G.; Godfroid, T.; Britun, N.; Georgieva, V.; Delplancke-Ogletree, M.-P.; Snyders, R., Plasma-Catalytic Conversion of CO_2 and CO_2/H_2O in a Surface-Wave Sustained Microwave Discharge. *Appl. Catal., B* **2017,** *214*, 114-125.
21. Chung, W.-C.; Chang, M.-B., Review of Catalysis and Plasma Performance on Dry Reforming of CH_4 and Possible Synergistic Effects. *Renew. Sust. Energ. Rev.* **2016,** *62*, 13-31.
22. Tu, X.; Gallon, H.; Whitehead, J., Plasma-Assisted Reduction of a NiO/Al_2O_3 Catalyst in Atmospheric Pressure H_2/Ar Dielectric Barrier Discharge. *Catal. Today* **2013,** *211*, 120-125.
23. Zhu, B.; Jang, B. W.-L., Insights into Surface Properties of Non-Thermal RF Plasmas Treated Pd/TiO_2 in Acetylene Hydrogenation. *J. Mol. Catal. A: Chem.* **2014,** *395*, 137-144.
24. Thagard, S. M.; Sankaran, M.; Kushner, M. J., Science Challenges in Low Temperature Plasma Science and Engineering: Enabling a Future Based on Electricity through Non-Equilibrium Plasma Chemistry. *arXiv preprint arXiv:1911.07076* **2019**.
25. Adamovich, I.; Baalrud, S. D.; Bogaerts, A.; Bruggeman, P.; Cappelli, M.; Colombo, V.; Czarnetzki, U.; Ebert, U.; Eden, J. G.; Favia, P., The 2017 Plasma Roadmap: Low Temperature Plasma Science and Technology. *J. Phys. D: Appl. Phys.* **2017,** *50* (32), 323001.
26. Van Laer, K.; Tinck, S.; Samara, V.; de Marneffe, J.-F.; Bogaerts, A., Etching of Low-K Materials for Microelectronics Applications by Means of a N_2/H_2 Plasma: Modeling and Experimental Investigation. *Plasma Sources Sci. Technol.* **2013,** *22* (2), 025011.
27. Lee, C. G.; Kanarik, K. J.; Gottscho, R. A., The Grand Challenges of Plasma Etching: A Manufacturing Perspective. *J. Phys. D: Appl. Phys.* **2014,** *47* (27), 273001.
28. Meichsner, J.; Schmidt, M.; Schneider, R.; Wagner, H.-E., *Nonthermal Plasma Chemistry and Physics*. Crc Press: 2012.
29. McCurdy, P. R.; Bogart, K.; Dalleska, N.; Fisher, E. R., A Modified Molecular Beam Instrument for the Imaging of Radicals Interacting with Surfaces During Plasma Processing. *Rev. Sci. Instrum.* **1997,** *68* (4), 1684-1693.
30. McCurdy, P. R.; Butoi, C. I.; Williams, K. L.; Fisher, E. R., Surface Interactions of NH_2 Radicals in NH_3 Plasmas. *J. Phys. Chem. B* **1999,** *103* (33), 6919-6929.
31. Zhou, J.; Fisher, E. R., Surface Reactivity and Energetics of CH Radicals During Plasma Deposition of Hydrogenated Diamondlike Carbon Films. *J. Phys. Chem. B* **2006,** *110* (43), 21911-21919.
32. Chen, H. L.; Lee, H. M.; Chen, S. H.; Chang, M. B.; Yu, S. J.; Li, S. N., Removal of Volatile Organic Compounds by Single-Stage and Two-Stage Plasma Catalysis Systems: A Review of the Performance Enhancement Mechanisms, Current Status, and Suitable Applications. *Environ. Sci. Technol.* **2009,** *43* (7), 2216-2227.
33. Schmidt-Szałowski, K.; Krawczyk, K.; Sentek, J.; Ulejczyk, B.; Górska, A.; Młotek, M., Hybrid Plasma-Catalytic Systems for Converting Substances of High Stability, Greenhouse Gases and Voc. *Chem. Eng. Res. Des.* **2011,** *89* (12), 2643-2651.
34. Xu, X.; Wang, P.; Xu, W.; Wu, J.; Chen, L.; Fu, M.; Ye, D., Plasma-Catalysis of Metal Loaded SBA-15 for Toluene Removal: Comparison of Continuously Introduced and Adsorption-Discharge Plasma System. *Chem. Eng. J.* **2016,** *283*, 276-284.

35. Kuroki, T.; Fujioka, T.; Kawabata, R.; Okubo, M.; Yamamoto, T., Regeneration of Honeycomb Zeolite by Nonthermal Plasma Desorption of Toluene. *IEEE T. Ind. Appl.* **2009,** *45* (1), 10-15.

APPENDIX A

THE IMPACT OF SnO_2 AND ZnO CATALYSTS ON MOLECULAR PLASMA TEMPERATURES WITHIN CH_4 DISCHARGES: PRELIMINARY RESULTS

The discussions in Chapter 5 focus on rotational and vibrational energy partitioning for H_2 $d^3\Pi_u \rightarrow a^3\Sigma_g^+$ and CH $A^2\Delta \rightarrow X^2\Pi$ in H_2 and CH_4 plasmas with a catalytic TiO_2 substrate. In addition to TiO_2, the impact of other metal oxide catalysts on CH_4 plasma chemistry were also explored. This appendix contains preliminary results for the determination of characteristic plasma temperatures within a 100% CH_4 plasma containing several nano-structured and micro-structured catalytic materials.

A.1 Background

A primary goal of the work presented throughout this dissertation has been the determination of rotational and vibrational temperatures within plasma-assisted catalysis (PAC) systems. An understanding of how energy is partitioned into rotational and vibrational modes can provide insight into molecule formation and decomposition pathways. We have examined the impact of a nano-structured TiO_2 catalyst on fundamental gas-phase properties in CH_4 and N_2 plasmas (discussed in Chapters 5 and 6, respectively). Furthermore, we sought to understand the impact of the plasma discharge on the material as PAC processes rely on the synergistic effect between both the catalyst and the plasma. The work presented in this appendix expands on these fundamental studies by examining the impact of several other catalytic materials (i.e., SnO_2 nanoparticles, ZnO nanoparticles, ZnO microrods) on CH_4 plasma chemistry. These materials were chosen because of their photocatalytic nature, which is thought to be advantageous in PAC

systems. Although, plasma-triggered photocatalytic effects are not well understood,[1] UV light generated from plasmas is thought to induce the formation of electron-hole pairs.[2-3] Plasma photocatalysis has been studied as a method of VOC degradation and removal[4-6] and several photocatalysts have been used in PAC studies (e.g., Fe_2O_3, TiO_2, ZnO).[4-6] Nevertheless, TiO_2 is the currently most promising photocatalytic material for PAC applications because of its stability, strong oxidizing power, chemical inertness, non-toxicity, and low cost.[1] Thus, we have also included the TiO_2 data presented in Chapter 5 here to directly compare results between photocatalytic materials.

For these studies, commercially purchased SnO_2 nanopowder (< 100 nm, Aldrich) and ZnO nanopowder (< 50 nm, Aldrich, > 97%) substrates were made by creating a slurry of as received nanoparticles and methanol. The nanoparticles (NP) were suspended in methanol until saturation; then the NP solution was doctor bladed onto glass slides or p-type <100> silicon wafers (Wacker-Chemitronic GMBH, Germany) of ~3 × 3 cm. ZnO microrods (MR) were grown hydrothermally on glass slides and silicon wafers in 0.1 M solutions of zinc nitrate (Alfa Aesar, 99%), $Zn(NO_3)_2 \bullet 4H_2O$, and hexamethylene tetramine (Alfa Aesar, 99+ %), $C_6H_{12}N_4$, in a stopped flask on a hot plate at 95 °C for six hours.[7] Subsequently, the ZnO MR materials were thoroughly washed with water to remove residual salt or amino complex and allowed to dry at room temperature overnight. All substrates used were placed in the coil region of the plasma reactor ~30 cm upstream from the quartz window, as depicted in Figure 2.1.

Of burgeoning interest to the PAC community is the correlation between catalyst properties (e.g., chemical identity, material morphology, pore size) and their influence on plasma characteristics (e.g., species densities, energy partitioning, formation of microplasmas within catalyst pores). This was explored to some extent in Chapter 6 and our related published study

where we examined the effects of nano-structured TiO_2 and micro-structured zeolite on N_2 discharge characteristics.[8] Here, we have chosen to examine the impact of several nano-structured photocatalysts on CH_4 plasma characteristics. Additionally, both nano-structured and micro-structured ZnO catalysts were included in this study to elucidate the influence of material morphology. SEM images, Figure A.1, highlight the size disparity between the nano-structured and the micro-structured materials. The commercially purchased SnO_2 NP and ZnO NP agglomerate into nanoparticle clusters with a porous network when pasted on the silicon wafer substrate (Figure A.1a and Figure A.1b, respectively). The morphological features of the as-prepared ZnO MR are shown in Figure A.1c, where rods of varying lengths extend in all directions across the substrate surface. The inset in Figure A.1c shows a higher magnification image of the rod-like features.

A.2 Characteristic Plasma Temperatures

Within our plasma systems, energy can be transferred from the rf power source to the electrons and internal energy modes (i.e., rotational, vibrational) of the atoms, molecules, and ions of the system. Electrons, in particular, play a crucial role in governing plasma chemistry. Energy from the external electromagnetic field is transferred to the electrons of the system which excite and sustain the plasma.[9] Thus, in addition to elucidating rotational and vibrational energy partitioning trends, we have determined T_e (described in Section 2.5.1), for these systems. Table A.1 lists T_e for a CH_4 (~10% Ar) plasma without and with each of the catalysts in the coil region of the reactor. Notably, T_e values range from ~2 – 3 eV over our studied parameter space, regardless of the presence or nature of the catalyst. Moreover, the lack of pressure and power dependence indicates increasing energy within the system preferentially results in increasing the

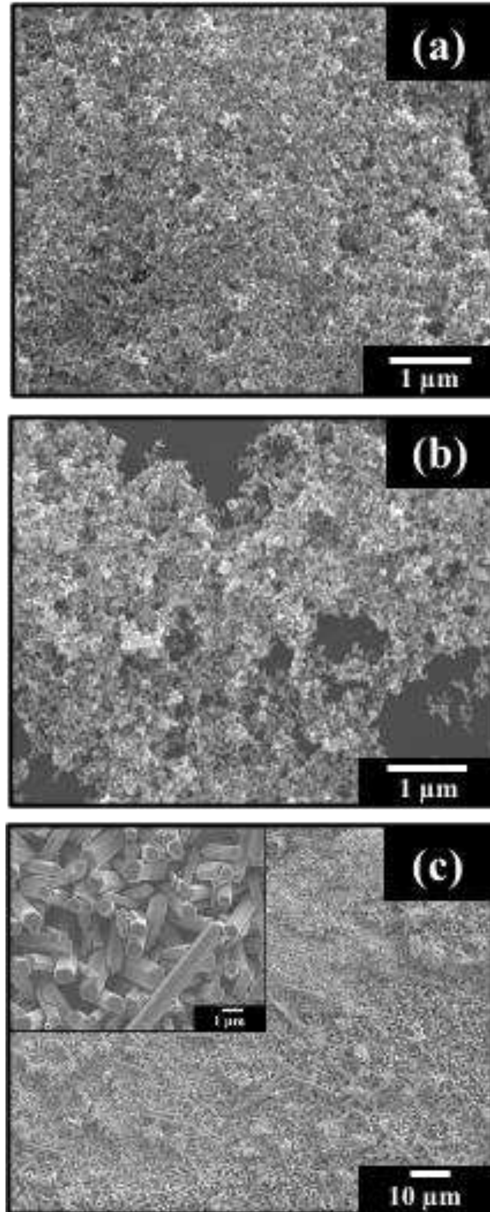

Figure A.1. SEM images of (a) SnO_2 nanoparticles (x20000), (b) ZnO nanoparticles (x20000), and (c) ZnO microrods (x1000). Magnification of inset in (c) is x10000.

Table A.1. T_e (eV) values in a CH_4 plasma without and with substrates.[a]

p (mTorr)	P (W)	no substrate	SnO_2 NP	TiO_2 NP	ZnO NP	ZnO MR
100	25	2.4 (0.3)	3.0 (0.5)	2.8 (0.8)	2.7 (0.4)	2.4 (0.3)
	50	2.6 (0.4)	2.5 (0.5)	2.1 (0.2)	2.7 (0.4)	2.4(0.3)
	75	2.7 (0.4)	2.4 (0.3)	2.2 (0.3)	2.7 (0.4)	2.2 (0.2)
	100	2.7 (0.4)	2.7 (0.4)	2.5 (0.4)	2.8 (0.4)	2.5 (0.4)
	125	2.7 (0.4)	2.4 (0.3)	2.6 (0.4)	2.6 (0.4)	2.9 (0.5)
150	25	2.7 (0.3)	2.6 (0.3)	2.6 (0.4)	2.8 (0.6)	1.0 (0.10
	50	2.7 (0.4)	2.6 (0.3)	2.7 (0.3)	1.9 (0.2)	2.1 (0.1)
	75	2.8 (0.3)	2.9 (0.4)	2.7 (0.3)	2.2 (0.2)	1.9 (0.1)
	100	2.8 (0.4)	2.4 (0.3)	2.7 (0.3)	2.9 (0.5)	2.5 (0.2)
	125	2.9 (0.4)	2.9 (0.4)	2.5 (0.3)	2.7 (0.3)	2.5 (0.3)
200	25	1.7 (0.1)	2.9 (0.2)	2.5 (0.5)	2.6 (0.3)	1.1 (0.1)
	50	2.4 (0.2)	3.0 (0.4)	2.6 (0.3)	2.9 (0.5)	2.5 (0.2)
	75	2.4 (0.2)	2.8 (0.4)	2.7 (0.3)	2.9 (0.2)	2.8 (0.1)
	100	2.6 (0.3)	2.8 (0.3)	2.7 (0.3)	1.4 (0.1)	2.5 (0.2)
	125	2.6 (0.3)	2.7 (0.3)	2.8 (0.4)	2.7 (0.3)	2.5 (0.2)

[a]Values in parentheses represent standard error calculated from the weighted mean of n ≥ 3 trials.

overall energy of the neutral species and ions rather than the electrons. These hypotheses were previously studied in N_xO_y plasmas,[10-11] and are further explored here.

Overall, electrons can play a substantial role in governing molecular-level processes in plasmas. Electron impact reactions lead to the production of excited state atoms and molecules, which are largely governed by T_e.[9] Understanding production mechanisms for a particular species is critical to comprehending molecular plasma temperatures. Moreover, it is important to examine energy partitioning of multiple species within a plasma system to understand the overall character of the plasma. In CH_4 plasmas, electron impact excitation of H_2 from the ground state is the primary route to H_2^* production;[12] however, decomposition and/or recombination reactions and dissociative excitation of methane via collisions with molecules may also contribute to the production of H_2^*. We have previously investigated energy partitioning trends for $T_R(H_2)$ in H_2 and CH_4 plasmas both without a substrate (Chapter 4) and with a catalytic TiO_2 substrate (Chapter 5) to gain further insight into H_2^* formation mechanisms in our systems. Here, we have determined $T_R(H_2)$ values in a 100% CH_4 plasma with three other types of catalytic materials (i.e., SnO_2 NP, ZnO NP, ZnO MR).

Figure A.2 shows $T_R(H_2)$ plotted as a function of P and catalyst material in a CH_4 plasma. Numerical values for all conditions studied are listed in Table A.2 and range from ~400 – 700 K over the parameter space explored. $T_R(H_2)$ data for a CH_4 plasma without a substrate at p = 100 mTorr, Figure A.2a, demonstrate a small decreasing trend with increasing P where $T_R(H_2)$ values at P = 25 W are ~ 580 K and decrease to ~ 500 K at P = 125 W. Addition of the SnO_2 NP, TiO_2 NP, or ZnO NP catalysts to the plasma discharge all result in a decrease in $T_R(H_2)$, with values ranging from ~400 – 480 K and minimal power dependence at p = 100 mTorr. Conversely, the presence of micro-structured ZnO (MR) appears to have a slightly different effect on rotational

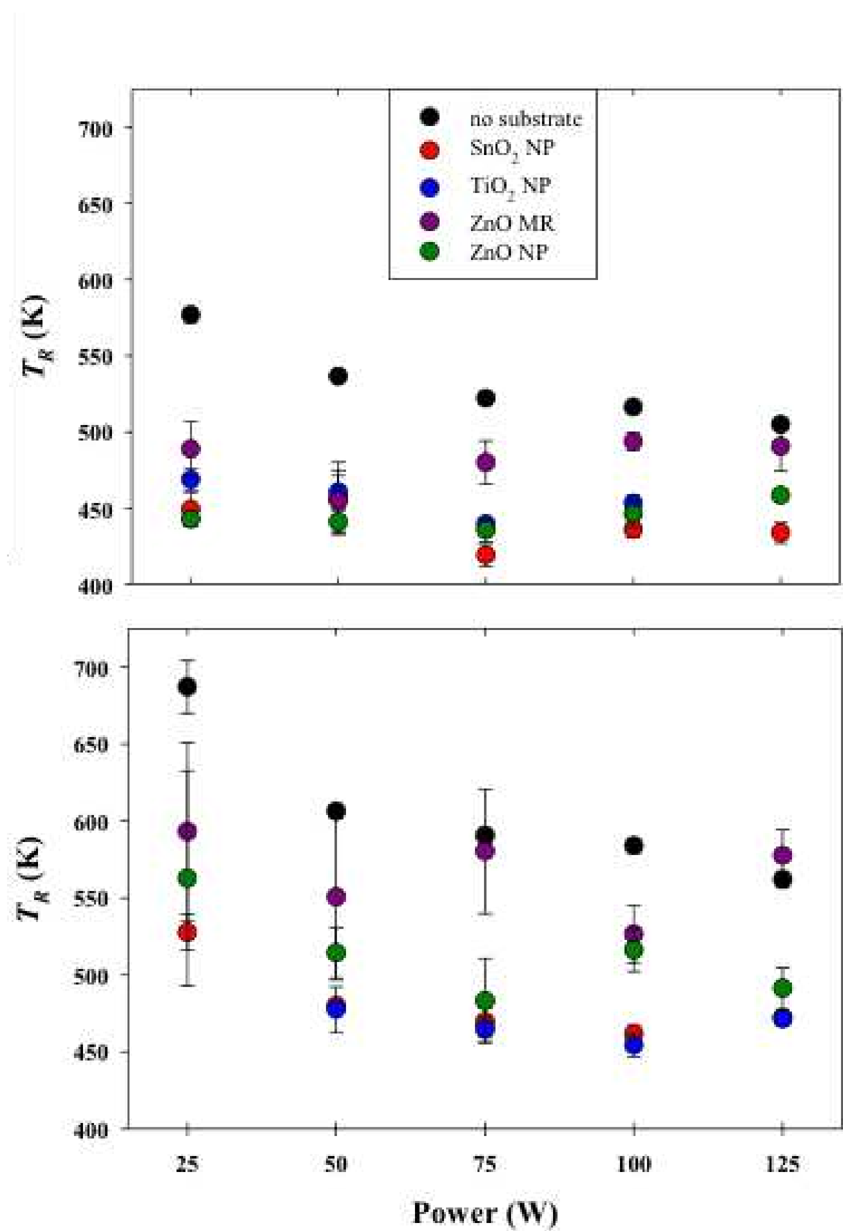

Figure A.2. $T_R(H_2)$ data as a function of applied rf power for a CH_4 plasma without and with substrates at (a) p = 100 mTorr and (b) p = 200 mTorr.

Table A.2. $T_R(H_2)$ (K) values in a CH_4 plasma without and with substrates.[a]

p (mTorr)	P (W)	no substrate	SnO_2 NP	TiO_2 NP	ZnO NP	ZnO MR
100	25	580 (10)	450 (10)	470 (10)	440 (10)	490 (20)
	50	540 (10)	460 (20)	460 (10)	440 (10)	450 (20)
	75	520 (10)	420 (10)	440 (10)	440 (10)	480 (10)
	100	520 (10)	440 (10)	450 (10)	450 (10)	490 (10)
	125	500 (10)	430 (10)	--	460 (10)	490 (20)
150	25	600 (10)	470 (10)	460 (20)	520 (40)	540 (50)
	50	480 (10)	460 (10)	450 (10)	460 (20)	640 (20)
	75	570 (10)	440 (10)	470 (10)	510 (20)	570 (20)
	100	560 (10)	440 (10)	450 (10)	420 (10)	530 (50)
	125	540 (10)	430 (10)	450 (10)	480 (10)	490 (30)
200	25	690 (20)	530 (10)	420 (70)	560 (70)	590 (60)
	50	610 (10)	480 (10)	480 (10)	510 (20)	550 (50)
	75	590 (10)	470 (10)	460 (10)	480 (30)	580 (40)
	100	580 (10)	460 (10)	450 (10)	520 (10)	530 (20)
	125	560 (10)	470 (10)	470 (10)	490 (10)	570 (20)

[a]Values in parentheses represent standard deviation calculated from the mean of $n \geq 3$ trials.

energy partitioning of H_2 compared to the nano-structured materials. Here, there is a notable decrease in $T_R(H_2)$ at $P \leq 50$ W from the no substrate system, and the values align well those reported for the nano-structured materials. However, at $P \geq 75$ W, $T_R(H_2)$ values increase slightly and are closer to the $T_R(H_2)$ values measured for the no substrate plasma system. Similar trends are noted at a higher pressure ($p = 200$ mTorr), Figure A.2b, but $T_R(H_2)$ values are elevated by ~100 – 200 K, regardless of substrate presence or composition. The observed decrease in $T_R(H_2)$ suggests that the catalysts may impact H_2^* formation processes. More discussion on this idea is provided in Section 5.3. Moreover, the elevated $T_R(H_2)$ values for the ZnO MR catalyst compared to the nano-structured catalysts (including ZnO NP) suggest that material morphology may play a more important role in energetics for some plasma species than the material chemistry.

To further demonstrate the impact of the catalyst on energy partitioning, T_R(CH) as a function of P at two different pressures is shown in Figure A.3, and Table A.3 provides T_R(CH) values for the entire parameter space. At $p = 100$ mTorr, Figure A.3a, T_R(CH) values range from ~1780 – 2770 K with minimal power dependence. Moreover, the presence of nano-structured substrates (SnO_2 NP, TiO_2 NP, ZnO NP) in the discharge results in a notable decrease in T_R(CH) (~100 – 200 K) compared to the no substrate system. In contrast, ZnO MR substrates show a slightly different and more complex trend for T_R(CH) at $p = 100$ mTorr. Interestingly, an increase in pressure to 150 mTorr and 200 mTorr (Figure A.3b), results in T_R(CH) values similar to the no substrate system, regardless of the type of catalyst used. Exceptions to this trend are at $P = 25$ W (ZnO MR substrate) and $P = 50$ W (ZnO NP substrate). T_R(CH) values for catalyst-containing systems also decrease concomitantly with an increase in system pressure, regardless of substrate. We have previously discussed this pressure trend for T_R(CH) in 100% CH_4 plasmas

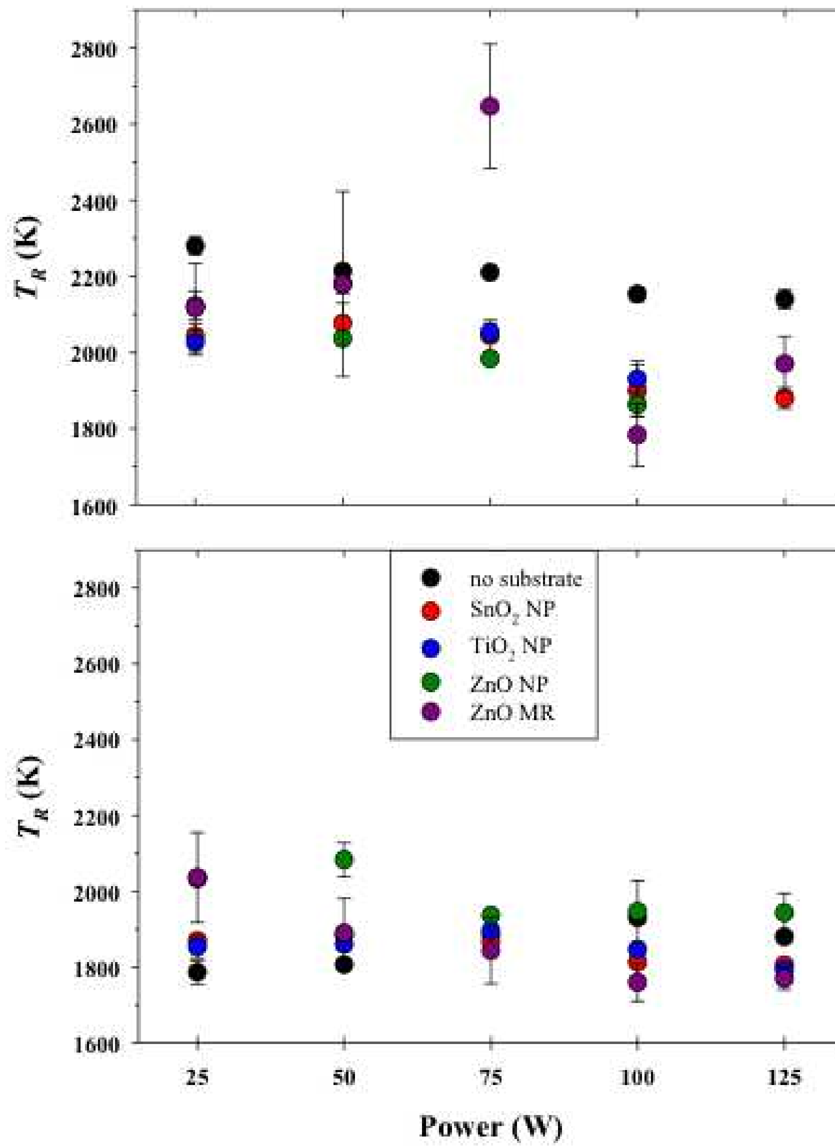

Figure A.3. T_R(CH) data as a function of applied rf power for a CH_4 plasma without and with substrates at (a) p = 100 mTorr and (b) p = 200 mTorr.

Table A.3. T_R(CH) (K) values in a CH_4 plasma without and with substrates.[a]

p (mTorr)	P (W)	no substrate	SnO_2 NP	TiO_2 NP	ZnO NP	ZnO MR
100	25	2280 (20)	2050 (30)	2030 (30)	2120 (40)	2120 (120)
	50	2210 (10)	2080 (50)	2180 (20)	2040 (10)	2370 (110)
	75	2210 (10)	2040 (40)	2050 (20)	1980 (10)	2770 (60)
	100	2150 (20)	1900 (70)	1930 (50)	1860 (30)	1780 (80)
	125	2240 (20)	1880 (30)	--	--	1970 (70)
150	25	1910 (20)	1940 (10)	2030 (30)	1980 (20)	1990 (100)
	50	1960 (10)	1950 (10)	1980 (20)	1980 (60)	1700 (90)
	75	2070 (10)	1960 (10)	1970 (10)	1880 (20)	1730 (50)
	100	2010 (10)	1950 (20)	1930 (40)	1980 (40)	2130 (70)
	125	1980 (40)	1890 (20)	1880 (30)	1900 (50)	2030 (40)
200	25	1790 (30)	1870 (10)	1850 (30)	2030 (20)	2040 (120)
	50	1810 (10)	1880 (20)	1860 (10)	2080 (40)	1890 (90)
	75	1880 (10)	1870 (30)	1900 (10)	1940 (10)	1840 (50)
	100	1930 (10)	1810 (10)	1850 (10)	1950 (80)	1760 (50)
	125	1880 (10)	1810 (10)	1790 (20)	1940 (50)	1770 (30)

[a]Values in parentheses represent standard deviation calculated from the mean of $n \geq 3$ trials.

without a substrate in Chapter 3.[13] The addition of a substrate to the plasma may impact rotational cooling pathways by providing an extra surface for collisional cooling leading to the lower $T_R(H_2)$ and T_R(CH) values. Rotational relaxation is a relatively fast process as fewer than ten collisions are typically required to reach equilibrium.[14] Thus, although T_R(CH) is reduced with the addition of the catalyst to the discharge at p = 100 mTorr, at p = 150 – 200 mTorr T_R(CH) values for the catalyst systems are generally within experimental error of the no catalyst system, indicating that gas-phase rotational cooling processes are likely the principal processes occurring at theses increased pressures.

T_V for excited state CH are listed in Table A.4, and values range from ~2000 – 4000 K over the parameter space. At p = 100 mTorr, Figure A.4a, T_V(CH) is significantly reduced (~300 K – 1200 K) upon addition of a catalyst to the discharge. This trend generally holds true for both SnO_2 NP and TiO_2 NP substrates at each pressure; however, somewhat different trends are noted for both the ZnO NP and ZnO MR catalysts. For the ZnO substrates, as pressure is increased to 200 mTorr, Figure A.4b, T_V(CH) values are generally higher than the no substrate system at $P \leq$ 50 W, but at $P \geq$ 75 W, T_V(CH) values for the ZnO catalyst systems are the same as a system without a substrate. This observed decrease of T_V(CH) with increasing P documented for the ZnO catalysts in Figure A.4b may be related to the plasma mode which shifts from E-mode (low plasma density) to H-mode (higher plasma density) at ~75 – 100 W. A previous study from the Fisher research group noted that the discharge mode and the resulting rotational and vibrational distributions appear to be interrelated for one of the three catalysts included in that study.[15] Although T_V(CH) decreases upon the addition of SnO_2 NP and TiO_2 NP catalysts at all pressures, this vibrational cooling effect is only significant at low pressure (p = 100 mTorr) for the ZnO catalysts. A pressure dependence for T_V(CH) is also worth mentioning for the data presented in

Table A.4. T_V(CH) (K) values in a CH_4 plasma without and with substrates.[a]

p (mTorr)	*P* (W)	no substrate	SnO_2 NP	TiO_2 NP	ZnO NP	ZnO MR
100	25	3440 (20)	2750 (100)	3100 (150)	3070 (60)	2880 (190)
	50	3420 (60)	2970 (140)	3020 (50)	2920 (60)	3000 (180)
	75	3340 (60)	2780 (50)	2980 (60)	2670 (20)	2110 (80)
	100	3180 (60)	2540 (50)	2570 (50)	2390 (20)	2380 (80)
	125	3140 (40)	2680 (30)	--	--	2130 (70)
150	25	2610 (10)	2150 (30)	2680 (70)	3440 (430)	3200 (170)
	50	2910 (20)	2230 (20)	2480 (50)	2930 (130)	3490 (370)
	75	3310 (60)	2330 (30)	2620 (40)	2710 (130)	3690 (290)
	100	3090 (30)	2740 (70)	2690 (30)	2870 (150)	2140 (120)
	125	3010 (110)	2650 (100)	2680 (120)	2440 (30)	2780 (200)
200	25	2280 (10)	2060 (40)	2060 (10)	3560 (210)	3600 (40)
	50	2340 (20)	2140 (40)	2060 (10)	3110 (30)	2940 (330)
	75	2680 (20)	2070 (40)	2230 (10)	2870 (460)	2380 (120)
	100	2790 (20)	2180 (30)	2180 (20)	2550 (90)	2880 (360)
	125	2810 (10)	2060 (20)	2110 (10)	2720 (30)	2500 (40)

[a]Values in parentheses represent standard deviation calculated from the mean of $n \geq 3$ trials.

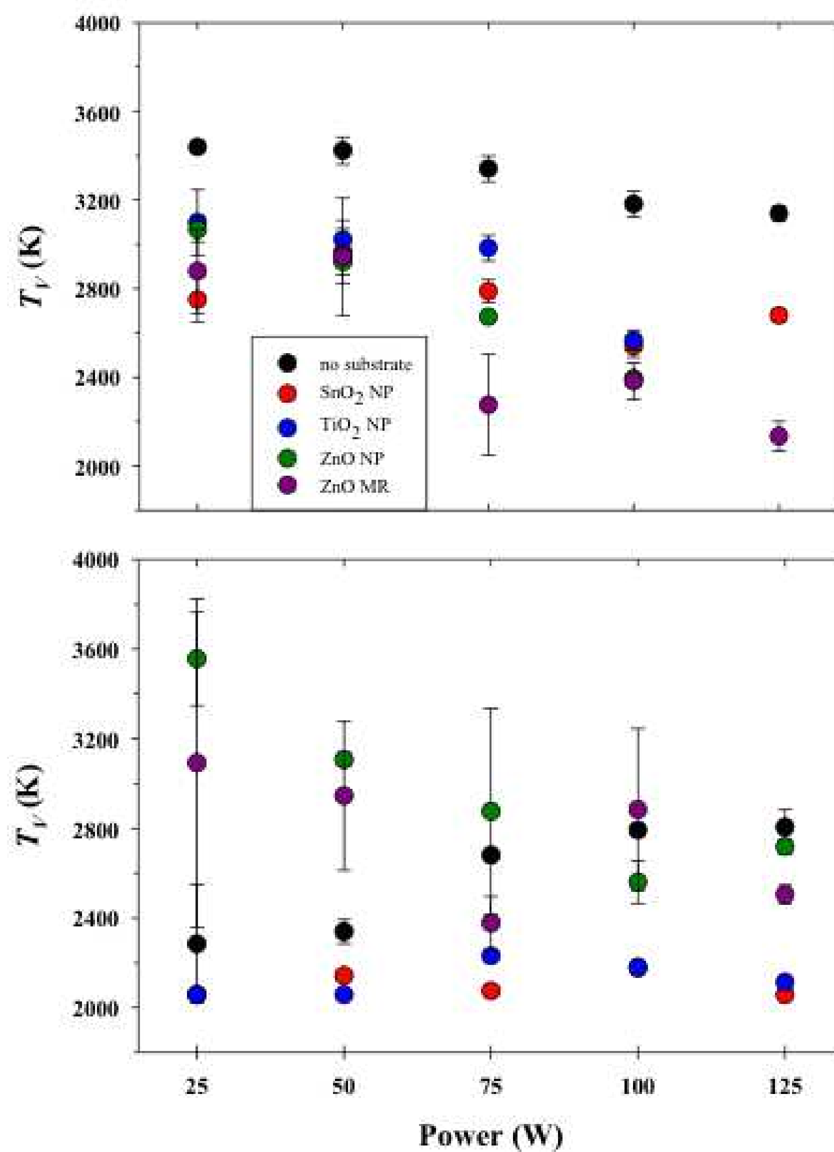

Figure A.4. T_V(CH) data as a function of applied rf power for a CH_4 plasma without and with substrates at (a) p = 100 mTorr and (b) p = 200 mTorr.

Figure A.4a. T_V(CH) values generally decrease with increasing pressure for CH_4 plasma systems without a substrate and with SnO_2 NP or TiO_2 NP whereas ZnO NP and ZnO MR substrates display minimal pressure dependence for T_V(CH). Overall, our data demonstrate that both material morphology (Figure A.2) and chemical identity (Figure A.4) may have a significant impact on gas-phase processes. To gain additional insight into these phenomena, it would be beneficial to characterize the chemical characteristics of the catalysts both before and after plasma exposure and to study the plasma-surface interface.

REFERENCES

1. Van Durme, J.; Dewulf, J.; Leys, C.; Van Langenhove, H., Combining Non-Thermal Plasma with Heterogeneous Catalysis in Waste Gas Treatment: A Review. *Appl. Catal., B* **2008,** *78* (3-4), 324-333.
2. Neyts, E. C., Plasma-Surface Interactions in Plasma Catalysis. *Plasma Chem. Plasma Process.* **2016,** *36* (1), 185-212.
3. Feng, X.; Liu, H.; He, C.; Shen, Z.; Wang, T., Synergistic Effects and Mechanism of a Non-Thermal Plasma Catalysis System in Volatile Organic Compound Removal: A Review. *Catal. Sci. Technol.* **2018,** *8* (4), 936-954.
4. Sano, T.; Negishi, N.; Sakai, E.; Matsuzawa, S., Contributions of Photocatalytic/Catalytic Activities of TiO_2 and γ-Al_2O_3 in Nonthermal Plasma on Oxidation of Acetaldehyde and CO. *J. Mol. Catal. A: Chem.* **2006,** *245* (1-2), 235-241.
5. Abedi, K.; Ghorbani-Shahna, F.; Jaleh, B.; Bahrami, A.; Yarahmadi, R.; Haddadi, R.; Gandomi, M., Decomposition of Chlorinated Volatile Organic Compounds (CVOCs) Using NTP Coupled with TiO_2/GAC, ZnO/GAC, and TiO_2–ZnO/GAC in a Plasma-Assisted Catalysis System. *J. Electrostat.* **2015,** *73*, 80-88.
6. Zhang, F.; Li, X.; Zhao, Q.; Zhang, Q.; Tadé, M.; Liu, S., Fabrication of α-Fe_2O_3/In_2O_3 Composite Hollow Microspheres: A Novel Hybrid Photocatalyst for Toluene Degradation Under Visible Light. *J. Colloid Interface Sci.* **2015,** *457*, 18-26.
7. Vayssieres, L.; Keis, K.; Lindquist, S.-E.; Hagfeldt, A., Purpose-Built Anisotropic Metal Oxide Material: 3D Highly Oriented Microrod Array of ZnO. *J. Phys. Chem. B* **2001,** *105* (17), 3350-3352.
8. Hanna, A. R.; Van Surksum, T. L.; Fisher, E. R., Investigating the Impact of Catalysts on N_2 Rotational and Vibrational Temperatures in Low Pressure Plasmas. *J. Phys. D: Appl. Phys.* **2019,** *52* (34), 345202.
9. Grill, A., *Cold Plasma in Materials Fabrication*. IEEE Press, New York: 1994; Vol. 151.
10. Blechle, J. M.; Cuddy, M. F.; Fisher, E. R., Effect of Ion Energies on the Surface Interactions of NO Formed in Nitrogen Oxide Plasma Systems. *J. Phys. Chem. A* **2013,** *117* (6), 1204-1215.
11. Hanna, A. R.; Blechle, J. M.; Fisher, E. R., Using Fundamental Spectroscopy to Elucidate Kinetic and Energetic Mechanisms within Environmentally Relevant Inductively Coupled Plasma Systems. *J. Phys. Chem. A* **2017,** *121* (40), 7627-7640.
12. Avtaeva, S.; Lapochkina, T., Characteristics of Molecular Hydrogen and CH* Radicals in a Methane Plasma in a Magnetically Enhanced Capacitive RF Discharge. *Plasma Phys. Rep.* **2007,** *33* (9), 774-785.
13. Van Surksum, T. L.; Blechle, J. M.; Fisher, E. R., Determination of Rotational and Vibrational Temperatures of CH in CH_4 Plasmas. *J. Vac. Sci. Technol., A* **2018,** *36* (4), 041302.
14. Brown, M. S.; Forlines, R. A.; Ganguly, B. N., Measurement of CH Density in a Pulsed-DC Hydrocarbon-Gas-Mixture Discharge. *J. Appl. Phys.* **2005,** *97* (10), 103302.
15. Hanna, A. R.; Fisher, E. R., Efforts Toward Unraveling Plasma-Assisted Catalysis: Determination of Kinetics and Molecular Temperatures within N_2O Discharges. *ACS Catal.* **2020,** *10*, 6546-6560.

APPENDIX B

INDEPENDENT RESEARCH PROPOSAL

This appendix contains the entirety of an independent research proposal, entitled *Utilizing Cold Plasma and Polymer Blending to Develop Defect-Free Mixed Matrix Membranes for CO_2 Gas Separations*, prepared by Tara L. Van Surksum in partial fulfillment of the doctoral requirements of the Department of Chemistry at Colorado State University. It details the combined approach of utilizing plasma-based fabrication methods and performance testing to better understand material structure-function relationships with the goal of developing defect-free mixed matrix membranes.

B.1 Abstract

Mixed matrix membranes (MMMs) have the potential to be an efficient and effective method for capturing and removing CO_2 from industrial sources; yet, there are significant limitations currently inhibiting MMM implementation. Particle agglomeration of the inorganic fillers, poor distribution throughout the polymeric matrix, and poor interfacial compatibility between the polymer and filler hinder advances toward increasing both the permeability and selectivity of these membranes. The overarching goal of this proposal is to design and develop MMMs that will address these materials-based limitations with novel fabrication approaches. Our tactics will feature the use of both cold plasma and polymer blending to ultimately develop MMMs with enhanced permeability and selectivity towards CO_2. The use of these techniques during the fabrication process allows for creating a material with highly tunable chemical properties. Importantly, we also seek to understand how to tailor the chemical and physical

properties of the material for enhanced separations performance. Gas permeation experiments will allow us to determine the efficacy of these strategies. Additionally, comprehensive materials characterization will be coupled with performance testing results and fabrication methodologies to better understand material structure-function relationships. Such information will provide insight into understanding how to develop MMMs with the desired chemical and physical properties necessary for industrial scale implementation.

B.2 Background and Motivation

In 2017, global emission of CO_2 through combustion of fossil fuels exceeded 36 billion tons, 15% of which came from the United States.[1] Escalating atmospheric CO_2 concentrations disturb the global carbon cycle causing additional adverse effects such as global warming and ocean acidification.[2] Although renewable energy consumption continues to rise,[3] fossil fuel-based energy sources are expected to remain a vital component to the world's energy resources for the next several decades;[4] thus, mitigation of industrial sources of CO_2 must be addressed. To overcome these increasing environmental concerns, researchers are adopting various technologies to remove and capture CO_2 from flue gases. As most costs associated with carbon capture and storage are associated with the capture component,[5] cost reductions can be achieved through development of innovative separation technologies.

Membrane-based technology is a promising approach towards CO_2 capture and separations development.[6-8] Compared to other conventional separations approaches, membranes are low cost, energy efficient, and environmentally sustainable.[7, 9-10] Gas separation membranes must have high permeability and high selectivity for efficient and economic CO_2 separation. Polymeric membranes have been extensively studied for gas separation;[6, 10-11]

however, there is a tradeoff limit between selectivity and permeability with polymer membranes,[12] constraining their potential for industrial gas separation. Recently, mixed matrix membranes (MMMs), membranes containing a bulk polymer phase and an inorganic filler phase, have gained significant interest for CO_2-based separations. MMMs combine the desirable properties of both polymer membranes (i.e., cost effective, large-scale production) and inorganic membranes (i.e., enhanced selectivity and permeability, chemical and thermal stability) for enhanced material performance. The incorporation of inorganic fillers into the polymer matrix can increase affinity for CO_2 and improve gas diffusivity by increasing the free volume between polymer chains.[5, 7] Moreover, fillers can enhance the physical properties of the membranes including thermal stability, mechanical strength, and stability against physical aging.[5]

Currently, MMM performance requires further improvements for industrial scale implementation. Both permeability and selectivity must be enhanced to improve the overall performance. Challenges inhibiting material development are highlighted in Figure B.1 and include particle agglomeration or sedimentation of the fillers and poor interfacial compatibility between polymer and filler.[5, 8, 13-14] These undesirable filler/polymer interface morphologies can include voids, matrix rigidification, or blocked pores.[7-8] Voids form when there is poor interfacial adhesion between the polymer and the filler. This leads to increased permeability and reduced selectivity by providing a lower resistance pathway for gas molecules. Matrix rigidification occurs when a rigid polymer layer forms around the filler, causing immobilization of the polymer chain, ultimately leading to decreased permeability and increased selectivity. The blocked pore morphology occurs when the inorganic filler is partially or fully blocked by the rigidified polymer. Partial pore blockage has the same effect on MMMs as matrix rigidification, whereas complete pore blockage significantly reduces both permeability and selectivity.

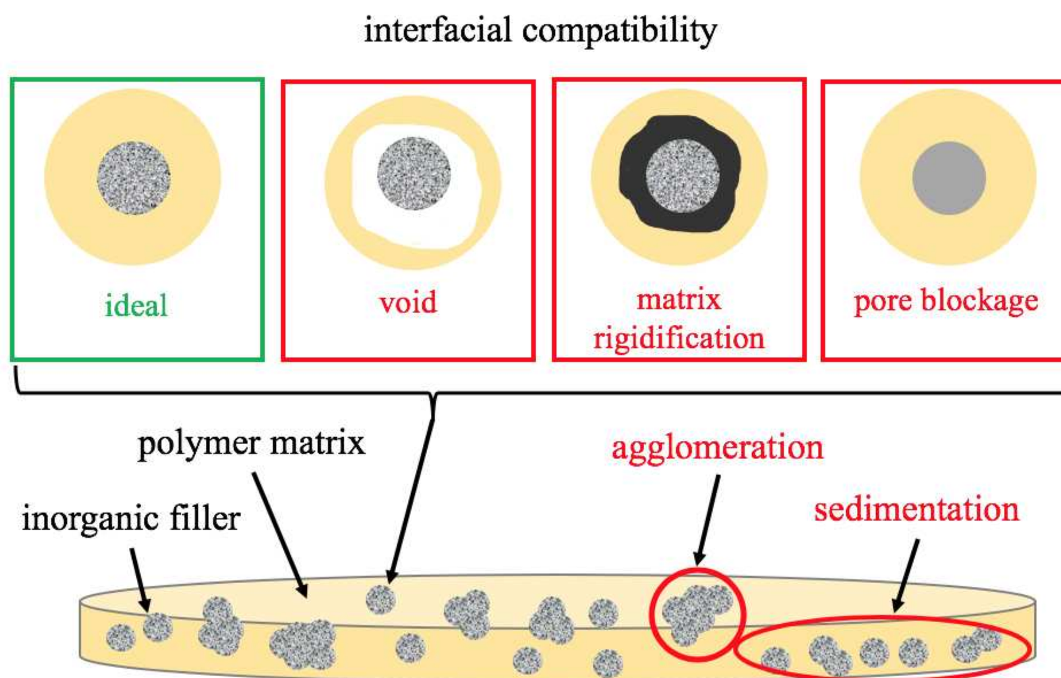

Figure B.1. Diagram illustrating challenges in MMM fabrication.

Typically, fillers are chosen based on their gas sorption behavior and pore sizes;[14] common filler choices include zeolites, silica, carbon molecular sieves (CMS), carbon nanotubes, metal-organic frameworks, and metal oxides.[8, 13-14] Yet, filler selection remains a major challenge in MMM fabrication and design because of the compatibility issues discussed above. Consequently, current efforts towards MMM development have focused on choosing compatible polymers and fillers and utilizing different polymer/filler combinations for creation of novel materials.

Researchers have also utilized chemical modification to alter surface and interfacial properties as a strategy to overcome compatibility challenges. For example, the use of coupling agents has been widely explored to improve interfacial interactions in MMMs.[14-15] Introducing additional agents into the membranes, however, often leads to undesired pore blocking, ultimately reducing gas permeability.[14-15] Hence, alternative approaches, such as plasma surface modification are necessary. Although plasma modification has also been used sparingly in the development of MMMs, it has promising potential as a more efficient and environmentally friendly approach for surface modification compared to wet chemical methods that produce hazardous waste.[16]

Sustainable performance of MMMs remains an important additional consideration for industrial scale implementation purposes. Under high pressure conditions, the dissolution of different penetrants in the material disrupts the polymer structure, rendering the polymeric phase of the membrane susceptible to CO_2-induced plasticization and swelling.[6, 8] Although incorporation of the inorganic component partially aids in overcoming stability issues presented in traditional membranes, MMMs still encounter problems with plasticization and swelling.[6] As plasticization causes a significant loss in gas selectivity, the development of new polymer matrices via grafting, blending, and crosslinking is warranted for overcoming any material

shortcomings. Thus, employing novel fabrication and modification methods for the polymer phase is regarded as a necessary approach for the development of defect-free MMMs.[9]

To address current MMM limitations, new fabrication and modification approaches must be explored. For example, polymer blending has not been widely studied in combination with inorganic filler materials, but has shown promising potential for gas separation applications.[8] Additionally, plasma treatment has shown potential particularly for modification of inorganic fillers. For example, de Clippel *et al.* utilized cold N_2 plasma to impart nitrogen functionalities onto carbon-silica microsphere fillers.[17] They found that plasma functionalization of the filler increased CO_2 gas selectivity in CO_2/H_2 mixtures compared to literature values, with only a slight concomitant drop in membrane permeance. Plasmas offer a wide, tunable parameter space to tailor material surface properties for desired functionalities. Plasma-based methods are an environmentally friendly alternative to other methods and can be scaled up for commercial use. Finally, thoughtful selection of polymers and fillers remains a crucial component to advancing MMM technology as material-environment interactions are highly dependent on the inorganic constituent and polymer matrix properties. Exploration of promising polymer/filler combinations remains vital to MMM research.[8, 14] Our approach will utilize both polymer blending and plasma modification tools, as these are promising, largely unexplored solutions to MMM development.

B.3 Specific Aims

The goal of the proposed research is to fabricate MMMs with high permeability and selectivity for CO_2 gas separations, while maintaining the desirable physical characteristics necessary for industrial scale implementation. Moreover, we seek to understand how the

physical and chemical properties of the membrane can be tuned to optimize material performance. This requires a molecular-level understanding of the material structure-function relationship. To this end, we will address the following three specific aims:

1. Develop fully integrated polymer/inorganic composite membranes. Fabrication of MMMs will focus on creating materials with a uniform distribution of inorganic fillers and high interfacial contact area between fillers and the polymer matrix. Multiple fabrication and surface modification strategies will be employed in conjunction with different polymer/filler combinations to fabricate fully integrated MMMs.
2. Evaluate and optimize chemical and mechanical properties of MMMs. Materials analyses coupled with performance testing will be used to tune and optimize fabrication methodologies for desired physical and chemical properties.
3. Achieve an understanding of material structure-function relationships. Expand fundamental understanding of the relationship between material characteristics and MMM performance.

B.4 Proposed Work

Development of Fabrication Methodologies. The first phase of this project will focus on developing fabrication strategies for producing defect-free MMMs. A combination of fabrication methodologies and surface modification strategies will be employed to tune material properties for improved membrane properties and performance. Importantly, the approach necessitates mindful selection of the polymers and fillers utilized to fabricate MMMs with the desired chemical and physical properties. Thus, we outline below several polymers and fillers

with unique chemical and mechanical properties that may be useful when designing our materials. Additionally, strategic fabrication and modification methods critical to overcoming challenges currently inhibiting MMM implementation will be discussed below.

Selection of Polymers and Inorganic Fillers. Our studies will employ a variety of polymers and polymer blends with well-known gas separation properties. Polysulfones and polyimides are commonly used polymers for gas separation applications. Their high thermal stability, chemical resistance, and excellent gas separation properties allow them to withstand the aggressive feed conditions often found in industrial settings.[6, 8] As such, initial studies will utilize both polysulfones [including polysulfone (PSF) and polyethersulfone (PES)] and polyimides [including polyimide (PI) and polyetherimide (PEI)] in our fabrication investigations. We will also use polyethylene glycol (PEG) polymers in our MMM fabrication process because of its strong affinity towards CO_2 molecules.[8] Each of these polymers has been used in conjunction with various fillers to create MMMs with enhanced performance (i.e., selectivity, permeability) compared to their corresponding traditional membrane.[18-20] Additionally, PEG is commonly studied as an additive to improve gas separation performance in polymeric membranes. Improvements in both selectivity and mechanical strength are reported with these PEG blended membranes.[21] Thus, our studies will include investigations into polymer blending within MMMs as a method to tune material properties. This is discussed in further detail below.

Optimizing filler loading percentage is another key to creating MMMs that are both permeable and selective, yet structurally sound enough to endure the sometimes-harsh conditions required for MMM implementation at the industrial scale. Thus, our fabrication processes will include investigations of different filler loading percentages. Our investigations will include a few common types of fillers that have been used in MMM development for their desirable

chemical properties. Zeolites, in particular, are commonly used in MMMs because their defined pore structure and size-selective nature make them attractive for separations applications. Although various types of zeolites have been used as MMM fillers, zeolite 4A, zeolite NaY, and ZSM-5 appear to be the most promising zeolite choices for CO_2 separations.[7-8, 13] A pore size of 3.8 Å for zeolite 4A, for example, is close to the kinetic diameter of CO_2 (3.3 Å),[7] allowing for ideal separations properties for CO_2 separation and capture. Conversely, the pore size of zeolite NaY is much larger (~9 Å),[7] which can facilitate gas diffusion and increase permeability. Moreover, Y-type zeolites are often chosen over X-type zeolites because their larger Si/Al ratio and lower number of coordinated cations can lead to higher CO_2 adsorption capacity, consequently favoring CO_2 separations.[22] Such information is essential to consider while designing and optimizing our materials.

Silica and CMS, other common filler options, will also be utilized in our MMM fabrication investigations. Both nonporous and mesoporous silica particles have been utilized as the inorganic component in MMMs.[23] Nonporous silica particles do not participate in gas transport. Rather, they change the molecular packing of the polymer chains around the filler particles and consequently, increase free volume in the membrane.[23] If the free volume is too large, however, selectivity substantially decreases. Additionally, the large pore sizes create a major drawback of mesoporous silica, as they are commonly too large to achieve size selectivity.[14] Mesoporous silica, however, exhibits better filler-polymer interaction than most other molecular sieves because of its higher surface area and attached silanol groups which are able to create hydrogen bonds with the polymer chain.[7] Although increased interfacial compatibility is exhibited with mesoporous silica particles, voids still exist within the material, leaving room for improvement in material design.

CMS are highly porous materials with pore sizes similar to gas molecules. These properties ensure high gas permeability and allow discrimination of certain gas species. Vu *et al.* studied the gas separation performance of MMMs comprising CMS and Matrimid® 5218 and reported a 45% increase in CO_2/CH_4 selectivity for the MMM over the Matrimid® matrix alone.[24] The authors also claimed that CMS exhibited better interfacial compatibility with the polymer than the zeolites.

Fabrication and Modification Methods. Although selection of appropriate polymer matrices and inorganic fillers in MMMs can help overcome some challenges associated with material development, often materials properties are still far from ideal for their desired applications. Thus, additional fabrication methods or modifications may be necessary to create defect-free MMMs. As discussed above, substantial work on various approaches to modify both the polymer and inorganic phases of MMMs has been performed to overcome challenges hindering advancement of MMMs. We will employ several strategies to fabricate and modify MMMs, outlined here.

Polymer Blending. One noteworthy approach to combat the permeability/selectivity tradeoff limit of polymer membranes has been to modify membrane properties via blending techniques.[8, 21] Polymer blending yields the benefits of two different polymers to enhance separation properties. Although this approach has also been used extensively to overcome plasticization issues in CO_2 separation membranes,[8, 21] research into using polymer blending in MMMs is limited.[8] A recent review article by Wong *et al.* illustrates that while blending modifications can significantly enhance membrane properties, many polymer blends still fall below the Robeson upper bound limit.[8] Thus, additional research into the separation properties of different polymer blends is needed. Furthermore, other types of modification may be

necessary to surpass the upper bound limit. Incorporating inorganic fillers into polymer blended matrices may help overcome the limitations currently hindering separations properties of both polymer-blended membranes and MMMs. Thus, our fabrication approaches will include creating polymer blended MMMs by using various polymer blends and inorganic fillers. Via blending, we can tune our membrane properties (e.g., CO_2 affinity, polymer rigidity, plasticity resistiveness) by combining different ratios of polymers to create MMMs with more desirable properties than a construct formed from a single polymer. As briefly mentioned above, PEG has been frequently used in blended polymeric membranes to enhance CO_2 affinity. Additionally, PI blends are common for CO_2 separations because PI has excellent thermal and mechanical stability and high selectivity despite its low permeability and plasticization resistance.[21] Thus, we will start with blends that incorporate these polymers and include inorganic fillers, such as zeolites, into the matrix. Although polymer blending may improve MMM permeability or selectivity, we suspect compatibility issues between the polymer and filler may remain, and additional modification methods may be necessary to overcome interfacial compatibility challenges.

Plasma Surface Modification and Plasma-Induced Grafting. Although inorganic fillers can enhance diffusivity and selectivity in membranes, they often suffer from poor compatibility and interfacial adhesion within the polymer matrix. Plasma modification provides an alternative route to modify fillers or polymer matrices and avoid undesirable polymer-interface morphologies. Plasmas can modify surface properties of materials via etching, deposition, or functionalization while still retaining the material's bulk characteristics. Plasma has been notoriously used as a tool for polymer membrane modification;[25-27] yet, its use in MMM modification has been minimal. Advantages of plasma-surface modification include a highly

tunable parameter space (e.g., precursor, pressure, power, substrate placement), low processing temperatures, and the ability to modify virtually any type of material. Proposed experiments will utilize plasma to modify both the polymer and inorganic components of MMMs.

Inorganic filler modification will be performed via a rotating drum radio frequency (rf) plasma reactor. The rotating drum allows for the ability to modify unsupported and unusually shaped materials. A detailed schematic of the design of this reactor has been previously published.[28] Experiments performed by Shearer and Fisher validate an effective reactor design for multiple plasma processes.[28] For example, they utilized the reactor to examine the efficacy of both depositing (plasma polymerized allyl alcohol) and non-depositing NH_3 plasmas to effectively modify the surface of commercially purchased Fe_2O_3 nanoparticles. The viability of the rotating drum reactor to produce customizable surface chemistries for MMMs will be evaluated by exploring a range of plasma parameters. Both continuous wave (CW) and pulsed plasma conditions will be assessed in addition to reactor rotation speed. Furthermore, we will investigate additional plasma parameters (e.g., pressure, power, treatment time) to optimize the filler surface chemistry for incorporation into the polymer matrix.

Our studies will utilize both plasma-induced grafting and plasma surface functionalization techniques to modify the polymer and/or fillers. De Clippel *et al.* plasma treated carbon-silica fillers with cold N_2 plasma to introduce amine functionalities.[17] These modifications resulted in increased mixed gas selectivity. As the introduction of amine functionalities improves affinity towards the acidic CO_2,[29] our initial studies will include use of N_2- and NH_3-based plasmas to functionalize filler surfaces.

Grafting techniques are among the approaches used to overcome both particle agglomeration and interfacial voids within the polymer matrix.[7] Grafting of MMMs can be

performed by 1) grafting the polymer matrix or 2) grafting the inorganic fillers. For example, Liang *et al.* created highly hydrophilic polyvinylidene fluoride ultrafiltration composite membranes by plasma-induced graft copolymerization of poly(methacrylic acid).[30] This approach provided sufficient carboxyl groups as anchor sites for amine-functionalized silica nanoparticles to bind to and ultimately improved membrane performance. Similarly, Mauter *et al.* grafted silver nanoparticles with PEI and combined them with plasma functionalized PSF to create ultrafiltration membranes with improved separation properties over PSF alone.[31] These studies demonstrate the effectiveness of surface grafting techniques for successfully incorporating inorganic particles into polymer matrices and ultimately improving membrane performance. With plasma-induced grafting, rare gas plasma irradiation creates active sites on the material surface and subsequent exposure to a polymerizing monomer results in the formation of the grafted layer. The extent of grafting on a surface can be controlled by plasma irradiation time or grafting time. Thus, this technique allows for controlled modification processes with the additional advantages of low processing temperatures (to avoid damage) and low-cost.

Additional Fabrication Considerations. Challenges associated with interface morphology and particle agglomeration can also be reduced by considering additional fabrication or post treatment methods. Polymer membranes are typically fabricated via casting, wherein the polymer is dissolved in a solvent and then molded to a desired thickness and allowed to dry. With MMMs, how the inorganic fillers are combined with the polymer can affect interfacial properties. For example, to avoid agglomeration, the "prime protocol"[14, 32-33] is utilized, wherein a small amount of polymer solution is first added to the particle suspension to coat the inorganic particles with a thin layer of polymer. Then the remainder of the polymer solution is added to

the primed solution. Mahajan *et al.* demonstrated that "primed" zeolite 4A sieves resulted in higher successful filler loading compared to "unprimed" native zeolite. Thus, priming fillers could be a useful approach for optimizing filler loading.[32] Another approach to achieve good particle dispersion involves adding the inorganic fillers to the solvent rather than the polymer solution before mixing the two separate solutions together.[14] The resulting suspension has a low viscosity which allows for a high shear rate with vigorous stirring and consequently reduces agglomeration of the inorganic fillers.[34-35] Moreover, post treatment methods such as thermal annealing can overcome low adhesion challenges between the fillers and polymer matrix as well as increase plasticity resistance.[6, 14] As such, our approach will include these considerations when designing and optimizing our materials.

Materials Characterization. Materials will be characterized throughout the fabrication and modification processes to determine chemical bulk and surface properties. Filler properties will be assessed before and after surface modification to ensure the desired modification has been achieved. Additionally, MMMs will be characterized after filler incorporation within the polymer matrix to determine the presence of voids or particle agglomeration. Several types of analyses will be performed to comprehensively assess material morphology, chemical properties, and mechanical properties. Scanning electron microscopy will be utilized in conjunction with energy dispersive X-ray spectroscopy to examine material architecture and determine the degree of incorporation of inorganic fillers into the polymer matrix. X-ray diffraction, Fourier transform infrared spectroscopy, and X-ray photoelectron spectroscopy will be employed to determine bulk and surface chemistry before and after modification and fabrication processes. Additionally, mechanical properties essential for MMM commercial implementation will be assessed (e.g., thermogravimetric analysis, tensile strength, Young's modulus). These materials

analyses will be utilized in conjunction with performance testing results to tune and optimize the chemical and mechanical properties of MMMs via our fabrication strategies.

Performance Testing. To address the second specific aim of the project, the performance of the materials will be assessed. Specifically, gas transport properties will be measured via variable pressure/constant volume permeation method, which measures the steady-state gas flux through a membrane of known thickness under a given pressure differential. A permeation chamber will be constructed to house the membrane and perform gas permeation measurements. We will measure the permeability of several gases (e.g., H_2, O_2, N_2, CO_2, CH_4) and gas mixtures chosen based on their relevancy to flue gas composition. Additionally, gas selectivity will be calculated from permeation measurements by using the ratio of the permeability coefficient of gas A over that of gas B.[5] After permeation experiments, membranes will be analyzed using the characterization techniques described above to determine the effects of the permeation experiments on membrane properties. Consequently, permeation and selectivity data will be evaluated in conjunction with materials properties and fabrication techniques. When coupled with materials characterization data, gas permeability and selectivity results will provide insight into material structure-performance. The ability to correlate specific material properties and behavior will allow us to modify and tailor our fabrication approaches to design a material with the desired properties for improved performance.

Initial Experimental Plan. The approach outlined above provides details on several types of polymers, fillers, and fabrication/modification methods that could be explored and combined in many different ways with the goal of developing defect-free MMMs. A list of the materials and fabrication/modification methods described in this proposal are summarized and outlined in Table B.1.

Table B.1. Selection of polymers, fillers, and fabrication and modification approaches for MMMs.

Polymer Selection	Projected Outcome	Initial Studies
PSF, PES	high thermal stability, chemical resistance, and resistance to plasticization	X
PI, PEI	high thermal stability and chemical resistance, excellent gas separations properties	X
PEG	improved selectivity	
Filler Selection	**Projected Outcome**	
zeolite 4A	improved selectivity	X
zeolite NaY	improved permeability	X
mesoporous silica	enhanced interfacial compatibility	
CMS	high permeability and selectivity, good interfacial compatibility	
Fabrication & Modification Approaches	**Projected Outcome**	
polymer blending	tune CO_2 affinity, polymer rigidity, and plasticity resistiveness	X
filler plasma modification (N_2- & NH_3-based plasmas)	incorporate amine functionalities for increased CO_2 affinity and improved interfacial compatibility	X
plasma-induced grafting	enhance interfacial compatibility, reduce particle agglomeration	

Our approach will focus on fabrication methods that utilize plasma modification and polymer blending techniques because these are both promising, yet minimally explored approaches for MMM development. Initial studies will examine polymer blends of PSF and PI as several researchers have reported these blends exhibit good compatibility and increased gas separations performance over the native polymers.[36-38] Additionally, filler selection is a critical consideration to MMM development. Zeolites have been widely studied as the inorganic component in MMMs because of their desirable gas separation properties. As such, zeolites will be the first filler we choose to explore in our studies. Even with careful material selection and polymer blending, however, we anticipate compatibility issues may persist between polymer and filler. Plasma modification of the filler will be the first route towards enhancing polymer/filler compatibility. We will utilize either N_2 or NH_3 plasmas to impart amine functionalities onto filler surfaces, as these systems previously resulted in improved interfacial compatibility and CO_2 separations.[14, 17, 39] Overall, we anticipate these initial studies will result in new MMM fabrication approaches that demonstrate success via enhanced separations performance.

Potential Challenges and Resolutions. We designed our approach with multiple routes to both fabrication and surface tailoring, which should provide alternate routes around obstacles we may encounter. Thus, depending on the outcome of our initial studies, we may choose to examine different polymer blends or fillers based on the desirable properties they hold. Some strategies to overcome the possible challenges we may encounter are highlighted in Figure B.2. This roadmap highlights several fabrication approaches discussed throughout the body of this proposal to overcome challenges relating to both poor interfacial compatibility and particle dispersion. The roadmap will be referenced to adjust fabrication and modification procedures if we encounter MMM fabrication challenges.

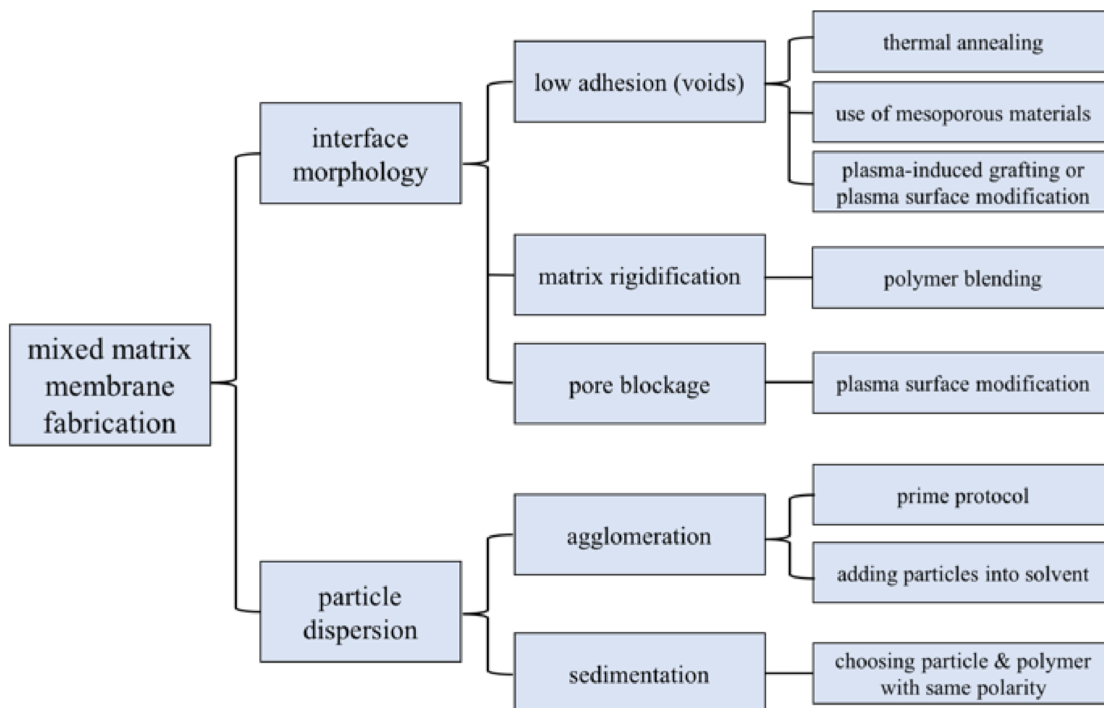

Figure B.2. Strategies to overcome MMM fabrication challenges.

B.5 Summary

The studies presented here offer a unique approach to designing and fabricating MMMs for use in gas separations applications. We anticipate the proposed approach will address current limitations inhibiting MMM development and provide an efficient and environmentally friendly alternative to traditional wet chemical methods typically used in MMM fabrication. Moreover, the tunable parameter space inherent to plasma-based methods will allow us to tailor and optimize materials properties for enhanced performance. Overall, via comprehensive characterization of the material throughout the fabrication, modification, and performance testing processes, our investigations will provide insight into the material-structure function relationships critical to advancing MMM technology.

REFERENCES

1. Ritchie, H.; Roser, M. CO_2 and Greenhouse Gas Emissions. https://ourworldindata.org/co2-and-other-greenhouse-gas-emissions (accessed April 20, 2020).
2. Pachauri, R. K.; Allen, M. R.; Barros, V. R.; Broome, J.; Cramer, W.; Christ, R.; Church, J. A.; Clarke, L.; Dahe, Q.; Dasgupta, P., *Climate Change 2014: Synthesis Report. Contribution of Working Groups I, II and III to the Fifth Assessment Report of the Intergovernmental Panel on Climate Change*. IPCC: 2014.
3. McFarland, A. In 2018, the United States Consumed More Energy Than Ever Before. https://www.eia.gov/todayinenergy/detail.php?id=39092 (accessed April 21, 2020).
4. Bauer, N.; Mouratiadou, I.; Luderer, G.; Baumstark, L.; Brecha, R. J.; Edenhofer, O.; Kriegler, E., Global Fossil Energy Markets and Climate Change Mitigation–An Analysis with Remind. *Clim. Change* **2016,** *136* (1), 69-82.
5. Kanehashi, S.; Scholes, C. A., Perspective of Mixed Matrix Membranes for Carbon Capture. *Front. Chem. Sci. Eng.* **2020**, 1-10.
6. Suleman, M. S.; Lau, K. K.; Yeong, Y. F., Plasticization and Swelling in Polymeric Membranes in CO_2 Removal from Natural Gas. *Chem. Eng. Technol.* **2016,** *39* (9), 1604-1616.
7. Jusoh, N.; Yeong, Y. F.; Chew, T. L.; Lau, K. K.; Shariff, A. M., Current Development and Challenges of Mixed Matrix Membranes for CO_2/CH_4 Separation. *Sep. Purif. Rev.* **2016,** *45* (4), 321-344.
8. Wong, K. K.; Jawad, Z. A., A Review and Future Prospect of Polymer Blend Mixed Matrix Membrane for CO_2 Separation. *J. Polym. Res.* **2019,** *26* (12), 289.
9. Rezakazemi, M.; Amooghin, A. E.; Montazer-Rahmati, M. M.; Ismail, A. F.; Matsuura, T., State-of-the-Art Membrane Based CO_2 Separation Using Mixed Matrix Membranes (MMMs): An Overview on Current Status and Future Directions. *Prog. Polym. Sci.* **2014,** *39* (5), 817-861.
10. Mohshim, D. F.; Mukhtar, H. B.; Man, Z.; Nasir, R., Latest Development on Membrane Fabrication for Natural Gas Purification: A Review. *J. Eng.* **2013,** *2013*.
11. Cong, H.; Radosz, M.; Towler, B. F.; Shen, Y., Polymer–Inorganic Nanocomposite Membranes for Gas Separation. *Sep. Purif. Technol.* **2007,** *55* (3), 281-291.
12. Robeson, L. M., The Upper Bound Revisited. *J. Membr. Sci.* **2008,** *320* (1-2), 390-400.
13. Chawla, M.; Saulat, H.; Masood Khan, M.; Mahmood Khan, M.; Rafiq, S.; Cheng, L.; Iqbal, T.; Rasheed, M. I.; Farooq, M. Z.; Saeed, M., Membranes for CO_2/CH_4 and CO_2/N_2 Gas Separation. *Chem. Eng. Technol.* **2019**.
14. Dong, G.; Li, H.; Chen, V., Challenges and Opportunities for Mixed-Matrix Membranes for Gas Separation. *J. Mater. Chem. A* **2013,** *1* (15), 4610-4630.
15. Li, Y.; Guan, H.-M.; Chung, T.-S.; Kulprathipanja, S., Effects of Novel Silane Modification of Zeolite Surface on Polymer Chain Rigidification and Partial Pore Blockage in Polyethersulfone (PES)–Zeolite a Mixed Matrix Membranes. *J. Membr. Sci.* **2006,** *275* (1-2), 17-28.
16. Zhao, D.; Wu, Y.; Ren, J.; Li, H.; Qiu, Y.; Deng, M., Improved CO_2 Separation Performance of Composite Membrane with the Aids of Low-Temperature Plasma Treatment. *J. Membr. Sci.* **2019,** *570*, 184-193.
17. de Clippel, F.; Khan, A. L.; Cano-Odena, A.; Dusselier, M.; Vanherck, K.; Peng, L.; Oswald, S.; Giebeler, L.; Corthals, S.; Kenens, B., CO_2 Reverse Selective Mixed Matrix

Membranes for H_2 Purification by Incorporation of Carbon–Silica Fillers. *J. Mater. Chem. A* **2013,** *1* (3), 945-953.
18. Kiadehi, A. D.; Rahimpour, A.; Jahanshahi, M.; Ghoreyshi, A. A., Novel Carbon Nano-Fibers (CNF)/Polysulfone (PSF) Mixed Matrix Membranes for Gas Separation. *J. Ind. Eng. Chem.* **2015,** *22*, 199-207.
19. Shindo, R.; Kishida, M.; Sawa, H.; Kidesaki, T.; Sato, S.; Kanehashi, S.; Nagai, K., Characterization and Gas Permeation Properties of Polyimide/ZSM-5 Zeolite Composite Membranes Containing Ionic Liquid. *J. Membr. Sci.* **2014,** *454*, 330-338.
20. Moghadassi, A.; Rajabi, Z.; Hosseini, S.; Mohammadi, M., Fabrication and Modification of Cellulose Acetate Based Mixed Matrix Membrane: Gas Separation and Physical Properties. *J. Ind. Eng. Chem.* **2014,** *20* (3), 1050-1060.
21. Mannan, H. A.; Mukhtar, H.; Murugesan, T.; Nasir, R.; Mohshim, D. F.; Mushtaq, A., Recent Applications of Polymer Blends in Gas Separation Membranes. *Chem. Eng. Technol.* **2013,** *36* (11), 1838-1846.
22. Amooghin, A. E.; Omidkhah, M.; Kargari, A., The Effects of Aminosilane Grafting on NaY Zeolite–Matrimid® 5218 Mixed Matrix Membranes for CO_2/CH_4 Separation. *J. Membr. Sci.* **2015,** *490*, 364-379.
23. Amooghin, A. E.; Mashhadikhan, S.; Sanaeepur, H.; Moghadassi, A.; Matsuura, T.; Ramakrishna, S., Substantial Breakthroughs on Function-Led Design of Advanced Materials Used in Mixed Matrix Membranes (MMMs): A New Horizon for Efficient CO_2 Separation. *Prog. Mater Sci.* **2019,** *102*, 222-295.
24. Vu, D. Q.; Koros, W. J.; Miller, S. J., Mixed Matrix Membranes Using Carbon Molecular Sieves: I. Preparation and Experimental Results. *J. Membr. Sci.* **2003,** *211* (2), 311-334.
25. Liang, C. Z.; Chung, T.-S.; Lai, J.-Y., A Review of Polymeric Composite Membranes for Gas Separation and Energy Production. *Prog. Polym. Sci.* **2019**.
26. Yanling, C.; Yingkuan, W.; Chen, P.; Deng, S.; Ruan, R., Non-Thermal Plasma Assisted Polymer Surface Modification and Synthesis: A Review. *Int. J. Agr. Biol. Eng.* **2014,** *7* (2), 1-9.
27. Hawker, M. J.; Pegalajar-Jurado, A.; Fisher, E. R., Innovative Applications of Surface Wettability Measurements for Plasma-Modified Three-Dimensional Porous Polymeric Materials: A Review. *Plasma Process. Polym.* **2015,** *12* (9), 846-863.
28. Shearer, J. C.; Fisher, E. R., Design and Operation of a Rotating Drum Radio Frequency Plasma Reactor for the Modification of Free Nanoparticles. *Rev. Sci. Instrum.* **2013,** *84* (6), 063904.
29. Lu, C.; Bai, H.; Wu, B.; Su, F.; Hwang, J. F., Comparative Study of CO_2 Capture by Carbon Nanotubes, Activated Carbons, and Zeolites. *Energ. Fuel.* **2008,** *22* (5), 3050-3056.
30. Liang, S.; Kang, Y.; Tiraferri, A.; Giannelis, E. P.; Huang, X.; Elimelech, M., Highly Hydrophilic Polyvinylidene Fluoride (PVDF) Ultrafiltration Membranes Via Postfabrication Grafting of Surface-Tailored Silica Nanoparticles. *ACS Appl. Mater. Interfaces* **2013,** *5* (14), 6694-6703.
31. Mauter, M. S.; Wang, Y.; Okemgbo, K. C.; Osuji, C. O.; Giannelis, E. P.; Elimelech, M., Antifouling Ultrafiltration Membranes Via Post-Fabrication Grafting of Biocidal Nanomaterials. *ACS Appl. Mater. Interfaces* **2011,** *3* (8), 2861-2868.
32. Mahajan, R.; Koros, W. J., Factors Controlling Successful Formation of Mixed-Matrix Gas Separation Materials. *Ind. Eng. Chem.* **2000,** *39* (8), 2692-2696.

33. Mahajan, R.; Burns, R.; Schaeffer, M.; Koros, W. J., Challenges in Forming Successful Mixed Matrix Membranes with Rigid Polymeric Materials. *J. Appl. Polym. Sci.* **2002,** *86* (4), 881-890.
34. Jiang, L. Y.; Chung, T. S.; Cao, C.; Huang, Z.; Kulprathipanja, S., Fundamental Understanding of Nano-Sized Zeolite Distribution in the Formation of the Mixed Matrix Single- and Dual-Layer Asymmetric Hollow Fiber Membranes. *J. Membr. Sci.* **2005,** *252* (1-2), 89-100.
35. Kusworo, T. D.; Ismail, A. F.; Mustafa, A.; Matsuura, T., Dependence of Membrane Morphology and Performance on Preparation Conditions: The Shear Rate Effect in Membrane Casting. *Sep. Purif. Technol.* **2008,** *61* (3), 249-257.
36. Rafiq, S.; Man, Z.; Maulud, A.; Muhammad, N.; Maitra, S., Effect of Varying Solvents Compositions on Morphology and Gas Permeation Properties on Membranes Blends for CO_2 Separation from Natural Gas. *J. Membr. Sci.* **2011,** *378* (1-2), 444-452.
37. Basu, S.; Cano-Odena, A.; Vankelecom, I. F., Asymmetric Membrane Based on Matrimid® and Polysulphone Blends for Enhanced Permeance and Stability in Binary Gas (CO_2/CH_4) Mixture Separations. *Sep. Purif. Technol.* **2010,** *75* (1), 15-21.
38. Fouada, E.; Ahmada, F.; Sawalhac, S., Removal of Carbon Dioxide from Flue Gases Using Polyethersulfone (PES) and Polyimide (PI) Blended Membranes. *Int. J. Chem. Environ. Eng.* **2014,** *5* (2).
39. Nik, O. G.; Chen, X. Y.; Kaliaguine, S., Amine-Functionalized Zeolite FAU/EMT-Polyimide Mixed Matrix Membranes for CO_2/CH_4 Separation. *J. Membr. Sci.* **2011,** *379* (1-2), 468-478.

LIST OF ABBREVIATIONS

Ar	argon
BAS	broadband absorption spectroscopy
C_{1s}	carbon 1s (XPS spectrum)
CCD	charge coupled device
CH_4	methane
CVD	chemical vapor deposition
DBD	dielectric barrier discharge
DLC	diamond-like carbon
e^-	electron
EDS	energy dispersive spectroscopy
EEDF	electron energy distribution function
E mode	inductance or electrostatic mode
FTIR	Fourier transform infrared spectroscopy
FWHM	full width at half maximum
H_2	diatomic hydrogen
HC	hydrocarbon
H_2O	water
H mode	conductance or electromagnetic mode
ICP	inductively coupled plasma
IRIS	imaging of radicals interacting with surfaces
K_B	Boltzmann's constant
k_d	rate of destruction
k_f	rate of formation
LIF	laser-induced fluorescence
LTP	low temperature plasma
min	minute
MR	microrods
N_{1s}	nitrogen 1s (XPS spectrum)
N_2	diatomic nitrogen
NO_x	nitrogen oxides
NP	nanoparticles
NTP	non-thermal plasma
O_{1s}	oxygen 1s (XPS spectrum)
OES	optical emission spectroscopy
P	applied radio frequency power
p	total system pressure
PAC	plasma-assisted catalysis
PC	peak correlation
PECVD	plasma enhanced chemical vapor deposition
rf	radio frequency
s	second
SEM	scanning electron microscopy
SnO_2	tin (IV) oxide

t	time, plasma treatment time
T_e	electron temperature
T_g	gas temperature
T_i	ion temperature
Ti_{2p}	titanium 2p (XPS spectrum)
TiO_2	titanium dioxide
T_R	rotational temperature
T_T	translational temperature
TR-OES	time-resolved optical emission spectroscopy
T_V	vibrational temperature
UT	untreated or no plasma treatment
VOCs	volatile organic compounds
WCA	water contact angle
XPS	x-ray photoelectron spectroscopy
ZnO	zinc oxide